University of Maribor

Faculty of Chemistry and Chemical Engineering

Doctoral dissertation

High-pressure process design for polymer treatment and heat transfer enhancement

May, 2018

Gregor Kravanja

University of Maribor

Faculty of Chemistry and Chemical Engineering

Gregor Kravanja

High-pressure process design for polymer treatment and heat transfer enhancement

Doctoral dissertation

Maribor, 2018

University of Maribor

Faculty of Chemistry and Chemical Engineering

High-pressure process design for polymer treatment and heat transfer enhancement

Doctoral dissertation

Ph.D. candidate: Gregor Kravanja

Supervisor: prof. dr. Željko Knez

Co-supervisor: prof. dr. Mojca Škrget

Co-supervisor: assist. prof. dr. Maša Knez Hrnčič

Maribor, 2018

Table of Contents

Acknowledgments

I would like to express my deep gratitude to my supervisor prof. dr. Željko Knez and my co-supervisors prof. dr. Mojca Škerget and dr. Maša Hrnčič Knez. I highly appreciate all their guidance, inspiration, immense knowledge and especially support during my Ph.D. study.

I thank my fellow colleagues, graduate students, and research technicians from the Laboratory for Separation Processes and Product Design who contributed to my research. Thanks for all the fun we have had in the last years.

I would also like to acknowledge the Slovenian Research Agency (ARRS) as the funding source that made this Ph.D. possible.

Last but not the least, I would like to thank my family and friends for supporting me throughout writing this thesis.

"Whatever you can do or dream you can, begin it. Boldness has genius, power, and magic in it".
(Johann Wolfgang von Goethe)

Abstract

The doctoral thesis presents the design of several high-pressure processes involving »green solvents« so-called supercritical fluids for the eco-friendly and sustainable production of new products with special characteristics, fewer toxic residues, and low energy consumption. The thesis is divided into three main parts: polymer processing and formulation of active drugs, measurements of transport properties form pendant drop geometry, and study of heat transfer under supercritical conditions.

In the first part, special attention is given to using biodegradable polymers in particle size reduction processes that are related to pharmaceutical applications for controlled drug release. The PGSS^{TM} micronization process was applied to the biodegradable carrier materials polyoxyethylene stearyl ether (Brij 100 and Brij 50) and polyethylene glycol (PEG 4000) for the incorporation of the insoluble drugs nimodipine, fenofibrate, o-vanillin, and esomeprazole with the purpose of improving their bioavailability and dissolution rate. In order to optimize and design micronization process, preliminary transfer and thermodynamic experiments of water-soluble carriers (Brij and PEG)/ SCFs system were carried out. It was observed that a combination of process parameters, including particle size reduction and interactions between drugs and hydrophilic carriers, contributed to enhancing the dissolution rates of precipitated solid particles.

In the second part, a new optimized experimental setup based on pendant drop tensiometry was developed and a mathematical model designed to fit the experimental data was used to determine the diffusion coefficients of binary systems at elevated pressures and temperatures. Droplet geometry was examined by using a precise computer algorithm that fits the Young–Laplace equation to the axisymmetric shape of a drop. The experimental procedure was validated by a comparison of the experimental data for the water-CO_2 mixture with data from the literature. For the first time, interfacial tension of CO_2 saturated solution with propylene glycol and diffusion coefficients of propylene glycol in supercritical CO_2 at temperatures of 120°C and 150°C in a pressure range from 5 MPa, up to 17.5 MPa were measured.

Additionally, the drop tensiometry method was applied for measuring systems that are of great importance in carbon sequestration related applications. The effect of argon as a co-contaminant in a CO_2 stream on the interfacial tension, diffusion coefficients, and storage capacity was studied.

In the third part, comprehensive investigation into the heat transfer performance of CO_2, ethane and their azeotropic mixture at high pressures and temperatures was studied. A double pipe heat exchanger was developed and set up to study the effects of different operating parameters on heat transfer performance over a wide range of temperatures (25 °C to 90 °C) and pressures (5 MPa to 30 MPa). Heat flux of supercritical fluids was measured in the inner pipe in the counter-current with water in the outer pipe. For the first time, the heat transfer coefficients (HTC) of supercritical CO_2, ethane and their azeotropic mixture in water loop have been measured and compared. A brief evaluation is provided of the effect of mass flux, heat flux, pressure, temperature and buoyancy force on heat transfer coefficients. Additionally, to properly evaluate the potential and the performance of azeotropic mixture CO_2-ethane, the coefficients of performance (*COP*) were calculated for the heat pump working cycle and compared to a system containing exclusively CO_2.

Keywords: supercritical fluids, PGSS^{TM}, formulation of active drugs, biodegradable polymers, transport and thermodynamic data, pendant drop method, carbon sequestration, heat transfer coefficients

UDK: 536.2:683.97(043.2)

Povzetek

V doktorski disertaciji je predstavljeno načrtovanje visokotlačnih procesov, ki izkoriščajo »zelena topila« t.i. nadkritične fluide. Z njihovo uporabo lahko pridobivamo nove produkte z višjo dodano vrednostjo pri nizki porabi energije. Doktorska dizertacija je razdeljena na tri osrednja poglavja: procesiranje polimerov in formulacija aktivnih zdravilnih učinkovin, merjenje transportnih lastnosti iz geometrije viseče kaplje in študij prenosa toplote pri nadkritičnih pogojih.

V prvem delu smo se osredotočili na uporabo biorazgradljivih polimernih materialov z namenom pridobivanja praškastih delcev in struktur za formulacijo aktivnih farmacevtskih učinkovin. Biorazgradljivi polimerni materiali so pomembni v številnih farmacevtskih aplikacijah pri nadzorovanem sproščanju zdravil. Uporabili smo patentiran visokotlačni PGSS^{TM} postopek za formulacijo netopnih aktivnih zdravilnih učinkovin nimodipina, fenofibrata, o-vanilina in esomeprazola z namenom izboljšanja njihove biološke uporabnosti in hitrosti raztapljanja. Kot nosilni material smo uporabili biorazgradljive polimere polioksietilen stearil eter (Brij 100 in Brij 50) in polietilen glikol (PEG 4000). Preliminarno smo določili transportno-termodinamske parametre polimernima nosilcema polietilen glikolu (PEG) in polioksietilen stearil eteru (Brij S) v sistemih z nadkritičnimi fluidi. Izmerjene parametre smo uporabili za optimalno formulacijo aktivnih učinkovin. Kombinacija zmanjšanja velikosti delcev in medsebojni vpliv med aktivno zdravilno učinkovino in hidrofilnimi nosilci sta pripomogla k povečanju hitrosti raztapljanja dobljenih praškastih delcev.

V drugem delu smo razvili novo visokotlačno merilno tehniko in izpeljali matematični model za določitev difuzijskih koeficientov in površinskih napetosti iz geometrije viseče kaplje. Nastanek asimetrične kapljice fluida smo preučevali z uporabo računalniškega algoritma, ki vključuje iterativno uporabo Young-Laplace-ove enačbe za opis razmerja med gravitacijsko deformacijo kapljice in površinsko napetostjo. Metodo smo umerili z meritvami površinske napetosti in difuzijskih koeficientov v sistemu voda/superkritični CO_2. Določili smo površinsko napetost in difuzijske koeficiente še neraziskanemu sistemu propilen glikola/CO_2 pri temperaturah 120 °C in 150 °C v tlačnem razponu od 5 MPa do 17.5 MPa.

Novo metodo smo nadalje uporabili za preučitev sistemov pomembnih pri geološkem zajemanju CO_2. Z namenom zmanjšanja izpustov toplogrednega CO_2 v ozračje smo preučili in izmerili gostote in površinske napetosti sistemom slanica/CO_2 in preučili vpliv nečistoče Ar na skladiščenje CO_2 v geološke formacije.

V tretjem delu doktorske naloge smo preučevali učinkovitosti prenosa toplote v bližini kritične točke CO_2, etana in njune azeotropne mešanice. Izdelali smo dvocevni prenosnik toplote, ki je omogočil meritve pri povišanih temperaturah (25 °C do 90 °C) in tlakih (5 MPa do 30 MPa). Prenos toplote v sistemu z nadkritičnim fluidom smo merili v smeri iz notranje visokotlačne cevi protitočno na zunanjo cev po kateri se je pretakala voda. Izmerili smo koeficiente prenosa toplote nadkritičnemu CO_2, etanu in njuni mešanici. Preučili smo učinek masnega pretoka, toplotnega toka, vzgona, tlaka in temperature na vrednosti koeficientov prenosa toplote. Za pravilno oceno potenciala in učinkovitosti azeotropne mešanice CO_2 in etana smo izračunali koeficiente zmogljivosti (*COP*) za cikel toplotne črpalke in jih primerjali s sistemi, ki delujejo izključno na CO_2.

Ključne besede: nadkritični fluidi, PGSS^{TM}, formulacija aktivnih učinkovin, biorazgradljivi polymeri, transportni in termdinamski podatki, metoda viseče kaplje, skladiščenje toplogrednega CO_2, koeficienti prenosa toplote.

UDK: 536.2:683.97(043.2)

List of Tables

List of Figures

Symbols and Abbreviations

Symbols

A	heat transfer area (m^2)
A_d	drop surface area ($Ad = 2\Pi \int x\, ds$, m^2)
B	Buoyancy number (/)
B_0	Bond number ($\frac{\Delta\rho g R_0^2}{\gamma}$, /)
c	concentration (mol/L)
c_0	initial concentration of the diffusing CO_2 (mol/L)
c_1	concentration of the diffusing CO_2 on the sample surface (mol/L)
c_p	specific heat (J/kg K)
De	equivalent sphere diameter ($\frac{6\,V_d}{S_d}$, m)
D^2/t	slope of the plot (/)
Dab	diffusion coefficients (m/s^2)
D_{eff}	effective diffusion coefficient ($\varphi D_{ab}/\epsilon$, m/s^2)
dr	distance from the center of the droplet equivalent sphere to the phase boundary (m)
e_f^z	vertical squared residual component (m)
e_i^r	horizontal squared residual component (m)
F	regression function of certain type of particle morphology (/)
g	acceleration constant (m/s^2)
Gr	Grashof number ($g\,\beta d^3(T_{wall}-T_f)/v^2$)
H	enthalpy (J/kg)
H_{CO2}	maximum height of the injected CO_2 column beneath the caprock seal (m)
K	characteristic constant (/)
L	length (m)
M	mass stored fluid per unit surface of the geological formation (Mt/km^2)
m_{BAL}	recorded balance mass (m)
m_{eq}	mass of gas CO_2 absorbed in the polymer at equilibrium (g)
m_{SC}	mass of a sample container (g)
m_t	mass of gas CO_2 absorbed in the polymer at time t (g)
$\dot{m}$	mass flux (kg/ m^2 s)
n	empirical constant for calculation effective diffusion coefficient (/)
$N_{b,r}$	flux of dense gas in to a drop surface ($-C\,D_{AB}\frac{dy_B}{dr}$, $mole/sm^2$)
Ne	Newton number (/)
Nu	Nusselt number (/)
P	power (W)
P_{cp}	critical capillary pressure (MPa)
P_c	critical pressure (MPa)
Pr	Prandtl number (Cp μ/λ)
Q	heat transfer rate (kW/m^2)
r	distance from the center of the droplet equivalent sphere to the phase boundary (m)

R	size of the largest cylindrical pore radius in the porous seal (m)
R_0	radius of curvature at the apex of the drop (m)
R_1	principal radii of the curvature (m)
R_2	principal radii of the curvature (m)
Re	Reynolds number (/)
s	arc length (m)
S	solubility (g/g)
Sd	surface area of the droplet ($S_d = \pi\, D^2$, ml)
S_w	residual saline water saturation in the reservoir (%)
t	time (s)
T_c	critical temperature (°C)
ΔT	logarithmic mean temperature difference (K)
U	total heat transfer coefficient (W/m^2 K)
v	velocity (m/s)
V_d	volume of a drop ($Vd = \Pi \int x^2 sin\ \phi$ds, ml)
V_K	volume of a drop ($\frac{\pi D^3}{6}$, ml)
V_S	volume of polymer sample (ml)
V_{SC}	volume of a sample container (ml)
$W_{b,r}$	molar flow ($4\,\pi\, r^2\, C\, D_{AB}\, \frac{dy_B}{dr}$, mol/s)
y_B	fluid phase equilibrium data upper phase (g/g)
x_B	fluid phase equilibrium data in the lower phase (g/g)
Z	compressibility factor (/)
$\sum_{i=1}^{n} e_i^2$	minimum Euclidean distance between the data point (r_i, z_i)

Greek Symbols

α	heat transfer coefficients on the supercritical fluid side
β	coefficient of thermal expansion (1/K)
λ	thermal conductivity (W/m K)
ϵ	tortuosity factor of the rock (/)
θ	contact angle (°)
Φ	porosity factor of the rock (/)
ρ	density (kg/m^3)
γ	interfacial tension (mN/m)
η	kinematic viscosity (m^2/s)
σ	surface tension (mN/m)
E	loading efficiency (%)
μ	dynamic viscosity (Pa s)
τ	oscillating time (s)

Abbreviations

APR	Aqueous Phase Reforming
ASES	Aerosol Solvent Extraction Systems
BRIJ	Polyoxyethylene Stearyl Ether
CCS	Carbon Capture and Storage
CCU	Carbon Capture and Utilization
CFC	Chlorofluorocarbon
COP	Coefficients of Performance
CR	Capillary Rise
DME	Diethanolamine
EFB	Empty Fruit Bunch
EOR	Enhanced Oil Recovery
ESEM	Environmental Scanning Electron Microscopy
GAS	Gas Antisolvent Process
GF	Gas Foaming
GTF	Gas, Used as a Solvent
GTG	Hydrothermal Gasification
GWP	Global Warming Potential
HCFC	Hydro-chlorofluorocarbon
HT	Hydrothermal Processes
HTC	Hydrothermal Carbonization
HTF	Heat Transfer Fluid
HTL	Hydrothermal Liquefaction
IPCC	Intergovernmental Panel on Climate Change
LC-MS	Liquid Chromatography-Mass Spectrometry
MSB	Magnetic Suspension Balance
NIST	National Institute of Standards and Technology
NMR	Nuclear Magnetic Resonance
NWA	New Way of Measurements
ODE	Zero Ozone Depletion Potential
PD	Pendant Drop
PEG	Polyethylene Glycol
PGSS	Particles from Gas-Saturated Solution
PLA	Polylactide
PTAC	Petroleum Technology Alliance Canada
RESS	Rapid Expansion of Supercritical Solutions
SAS	Supercritical Antisolvents
SCE	Supercritical Extraction
SCF	Supercritical Fluid
SEDS	Solution Enhanced Dupercritical Dispersion processes
SFE	Supercritical Fluid Extraction
SFEE	Supercritical Fluid Extraction of Emulsions

SRC	Supercritical Rankine Cycle
TCI	Total Capital Investment
TRR	Total Annual Revenue Requirement

The doctoral thesis is mainly based on the following paper published by the candidate:

KRAVANJA, Gregor, ZAJC, Gašper, KNEZ, Željko, ŠKERGET, Mojca, MARČIČ, Simon, KNEZ HRNČIČ, Maša. Heat transfer performance of CO_2, ethane and their azeotropic mixture under supercritical conditions. *Energy*, ISSN 0360-5442. [Print ed.], June 2018, vol. 152, Pages. 190-201, Impact Factor: **4.520**

KRAVANJA Gregor, KNEZ Željko, KOTNIK Petra, LJUBEC Barbara, KNEZ HRNČIČ, Maša**,** Formulation of nimodipine, fenofibrate, and o-vanillin with Brij S100 and PEG 4000 using the PGSS™ process, *The Journal of Supercritical Fluids*, ISSN 0896-8446, vol. 135, 2018, Pages 245-253, Impact Factor: **2.991**

KRAVANJA Gregor, KNEZ Željko, KNEZ HRNČIČ, Maša**,** The effect of argon contamination on interfacial tension, diffusion coefficients and storage capacity in carbon sequestration processes, *International Journal of Greenhouse Gas Control*, ISSN 1750-5836, Volume 71, 2018, Pages 142-154, Impact Factor: **4.380**

KRAVANJA, Gregor, ŠKERGET, Mojca, KNEZ, Željko, KNEZ HRNČIČ, Maša. Diffusion coefficients of water and propylene glycol in supercritical CO2 from pendant drop tensiometry. *The Journal of supercritical fluids*, ISSN 0896-8446., March 2018, vol. 133, part. 1, Pages 1-8, Impact Factor: **2.991**

KRAVANJA, Gregor, KNEZ HRNČIČ, Maša, ŠKERGET, Mojca, KNEZ, Željko. Interfacial tension and gas solubility of molten polymer polyethyleneglycol in contact with supercritical carbon dioxide and argon. *The Journal of supercritical fluids*, ISSN 0896-8446. [Print ed.], Feb. 2016, vol. 108, Pages. 45-55, Impact Factor: **2.991**

KNEZ HRNČIČ, Maša, **KRAVANJA, Gregor**, KNEZ, Željko. Hydrothermal treatment of biomass for energy and chemicals. *Energy*, ISSN 0360-5442., Dec. 2016, vol. 116, part 2, Pages. 1312-1322, Impact Factor: **4.520**

KEGL, Tina, **KRAVANJA, Gregor**, KNEZ, Željko, KNEZ HRNČIČ, Maša. Effect of addition of supercritical CO2 on transfer and thermodynamic properties of biodegradable polymers PEG 600 and Brij52. *The Journal of supercritical fluids*, ISSN 0896-8446, April 2017, vol. 122, Pages. 10-17, Impact Factor: **2.991**

KNEZ HRNČIČ, Maša, **KRAVANJA, Gregor**, ŠKERGET, Mojca, SADIKU, Makfire, KNEZ, Željko. Investigation of interfacial tension of the binary system polyethylene glycol/CO2 by a capillary rise method. *The Journal of supercritical fluids*, ISSN 0896-8446., Jul. 2015, vol. 102, Pages. 9-16, Impact Factor: **2.571,** award: The Journal of supercritical fluids **Editor-in-chief's featured article**, July 2015,

1. Introduction

High-pressure processes involving sub and supercritical fluids offer ways to develop new products with special physical characteristics, less toxic residues, low energy consumption, and which are eco-friendly and sustainable. Supercritical fluids show potential as solvents in boosting green chemistry by replacing environmentally harmful conventional organic solvents [1].

Supercritical fluids (SCFs) were discovered in 1822 by Baron Charles Cagniard de la Tour, who proved the existence of a critical point by conducting an acoustics experiments in a sealed cannon. He noticed that a splashing sound generated by a solid ball in a liquid phase inside the cannon ceased above a certain temperature and pressure. That indicates no liquid-gas phase boundary and surface tension in a supercritical fluid phase [2]. Compared to these pioneering experiments, today's industrial process involving supercritical fluids operate at pressures of several magnitudes higher, ranging from 10 MPa in extraction and formation processes up to 20 000 MPa in the production of artificial diamonds [3]. In nature, SCFs can occur below the Earth's ocean floor, on the planet Venus, and probably on exoplanets such as Super-Earths. They can also considered to be life-sustaining solvents, since some bacteria species have been shown to be tolerant of SFCs [4].

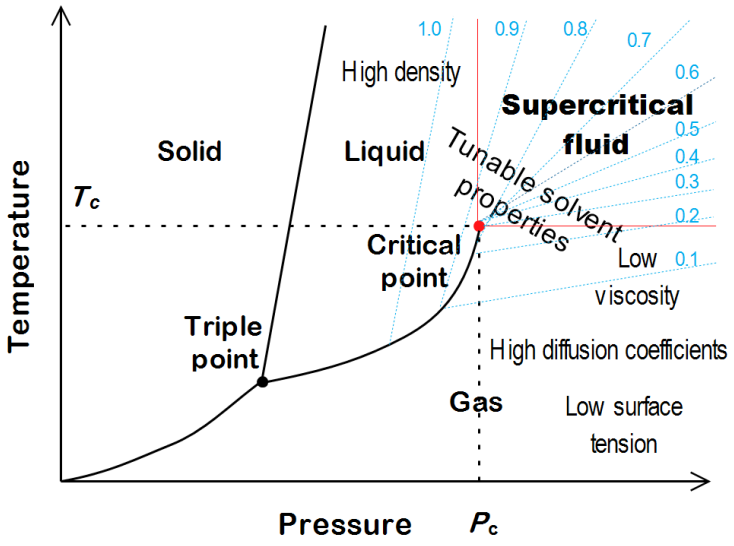

Figure 1-1: *P-T* diagram for supercritical fluid with the lines of constant density.

SCFs are defined as any substances whose temperature and pressure are above their critical values. The phase behaviour of pure compounds is presented in a P-T diagram (Figure 1-1). The physical and chemical properties of these fluids are in between of those of liquids and gases. They can diffuse through solids like a gas, and dissolve materials like a liquid [5]. Near the critical point, a small variation in pressure and temperature can result in tunable solvent properties that make them ideal for several high-pressure extraction and separation processes. SCFs have a density comparable to those of liquids, values of viscosity relatively equivalent to gases, and diffusion coefficients intermediate between those of liquids and gases [6]. Typical values for the range of variation of density ρ, viscosity μ, thermal conductivity λ and diffusion coefficients D_{ab} of liquids, gases, and SCFs are presented in table 1-1. SCFs have excellent heat transfer properties and have been studied as heat transfer fluids (HTF). Around the critical point

of fluids, the specific heat c_p increases greatly with increasing temperature, while thermal conductivity λ, density ρ, and viscosity μ decrease.

Table 1-1: Characteristic values of gas, liquid and supercritical state.

Properly	Liquid	Supercritical fluid	Gas
ρ (kg / m^3)	1000	200-900	0.6-1
η (kg m^{-1} s^{-1})	10^{-3}	10^{-5}-10^{-4}	10^{-5}
D_{ab} (m^2 s^{-1})	$<10^{-9}$	10^{-7}-10^{-8}	10^{-5}
λ (W/mK)	$<10^{-1}$	10^{-3}-10^{-1}	10^{-3}

SCFs can be easily removed from a product by depressurization since they are gaseous under atmospheric pressure. That means there are no solvent residues in the final product and consequently lower processing costs. The choice of which supercritical fluid is used for chemical and industrial processes must be determined by a compromise of practical factors. Carbon dioxide (CO_2) is the most commonly used supercritical fluid because of its moderate critical constants (T_c = 31.0°C, P_c = 7.38 MPa), non-flammability, and non-toxic, non-corrosive nature [7]. It's available on the market for low prices and is considered to be the second cheapest solvent after water. Hot compressed water has attracted attention as an excellent green reaction and processing media for the conversion of biomass into biobased chemicals and biofuels. However, water has a relatively high critical point (T_c=374.14°C, P_c=22.12 MPa) and energy requirements are high. A possible solution to reduce the operating temperature and consequently energy requirements of processing biomass with water is to process at higher pressures or by adding supercritical CO_2 to the reaction mixture [8]. Among other supercritical fluids, argon is used in polymer processing and as a potential reaction media for natural substances because of its inactivity, easy accessibility, very low thermal conductivity and easily accessible critical point (T_c= -122.46°C, P_c=48.63 bar) [9]. Some of the frequently used SCF are listed in Table 1-2, together with their critical properties.

Table 1-2: Some of the often used SCF in high-pressure applications.

Supercritical solvent	T_c (°C)	P_c (MPa)	ρ_c (g/cm^3)
Carbon dioxide (CO_2)	31.03	7.38	0.469
Water (H_2O)	377.00	22.06	0.322
Methane (CH_4)	-82.55	4.60	0.162
Ethane (C_2H_6)	32.15	4.87	0.203
Propane (C_3H_8)	92.05	4.25	0.217
Ethylene (C_2H_4)	9.35	5.04	0.215
Propylene (C_3H_6)	91.75	4.60	0.232
Methanol (CH_3OH)	239	8.09	0.272
Ethanol (C_2H_5OH)	240	6.14	0.276
Acetone (CH_3COCH_3)	235	4.70	0.278
Nitrous oxide (N_2O)	33.42	7.35	0.452
Argon (Ar)	122.46	48.63	0.526
Sulfur hexafluoride (SF_6)	295.80	2.49	0.755

In order to obtain the data fundamental for the design of high-pressure processes and to fulfill consumer economic requirements, basic thermodynamic and transport data like phase equilibria, density, viscosity, dielectric constant, diffusion coefficients and interfacial tension are the topic of intense research. SCFs have a great potential in many areas and new applications are developing daily. Several high-pressure applications involving SCFs have already found a way to industrial scale production. In the following subsection, new applications of supercritical fluids will be presented. Additionally, techno-economic analyses of several high-pressure processes will be systematically overviewed.

1.1 Applications of Supercritical fluids

High-pressure technology involving SCFs is German in origin, with the first large-scale application in the food industry (decaffeination of coffee or tea and hop extraction) mainly oriented toward the production of natural products. Without the advent of competitors in the 1980s, the German companies extended their activities to new areas including smaller-scale applications for extracting aromas, colorants, diet lipids, cosmetics etc. [10]. Today, many new SCF applications have been developed worldwide with an extensive potential for increase in capacity as new high-quality products are required.

SCF technology can be used as a new reaction media for chemical reactions, in large-scale operations in petrochemical plants [11], for biochemical reactions in the pharmaceutical industry for production of intermediate and final products [12], for powder coatings [13], for polymer processing including particle formation and encapsulation [14], for jet cutting [15], dry cleaning [16], for sterilization processes, virus inactivation in plasma fractions [17] and bone implants [18], for separation process in supercritical chromatography [19], as an alternative refrigerants in power cycles [20] and for extraction of value added products and by-products [21]. There is also great potential in the treatment of sewage wastes with SCFs and generated value products from waste streams [22]. Several SCF applications will be briefly presented from the perspective of their environmental and economic benefits.

1.1.1 Supercritical fluid extraction (SFE)

Supercritical fluid extraction (SFE) has been successfully introduced in many fields, from decaffeination of coffee beans and black tea leaves, isolation of some flavouring from hops, fatty acid refining, to the production of herbal production [23]. Tuneable physical properties of the most frequently used SCF, CO_2, enables selective extraction purification and fractionation [23]. Lipids and carotenoids can be easily isolated from the natural source (algae, microalgae, dairy production) [24]. Since CO_2 is a non-polar solvent, a small amount of ethanol can be added to extend the range of its solvating strength to extract polar components like phenolic and metal-ligand complexes [25]. Recently, new processes have been developed to recover components from wastes ranging from manure to packing residuals. In the food industry, SFE can be used to extract value products from by-products that are generated during food manufacturing. Another interesting field is the removal of heavy metals from solid matrices and liquids, where using SFEs presents an excellent option [26].

SFE can be carried out in different modes of operation; the most frequently used is extraction from solids, which is carried out in batch and single stage mode since solids are difficult to handle continuously in pressured vessels. The size of vessels used in industry today varies from $1m^3$ up to 40 m^3 volume. The maximum throughput of a single industrial plant for extraction from solids is above 10 000 t/a. [5]. Like many other processes, SFE has to be properly adjusted before every single run. Extraction yield depends on temperature, pressure, amount and type of modifier, amount and particle size of a sample and use of a dispersing agent. One option is experimental design and proper statistical analyses with a small number of trials [27].

Most companies believe that supercritical extraction is too expensive and because of high investment costs in comparison with classical methods, should be restricted only to high-quality products. Hoverer, that is far from true when a very large amount of material is treated, as in the case of coffee and hops processing and waste treatment [10]. Reported costs for production of solid feed with a capacity around 1000 t/a are around 3 EUR/kg. The economy of scale may bring the cost down to less than 0.5 EUR/kg for batch operation. In the case of continuous operation, the cost can be reduced even more [5]. Figure 1-2 presents an economy of a scale for SCE of solids using CO_2 as a solvent. The lower line represents continuous operation where an increase in productivity is proportional to throughput feed.

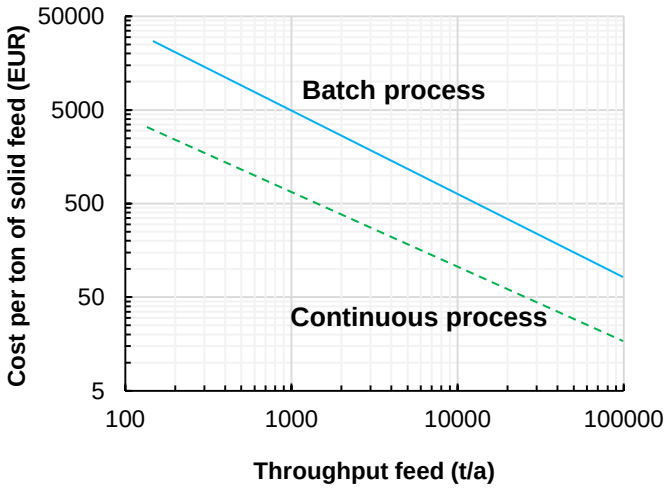

Figure 1-2: Economy of scale for SCE of solid using CO_2 [5].

1.1.2 High-pressure application for polymer processing

Absorption of compressed gas in polymer matrices results in a wide spectrum of possible applications in the field of sustainable polymer processing, for example, production of fibers, microparticles and foams; polymer impregnation; and separation of gas mixtures through polymer membranes. Several modifications of polymers take place since CO_2 dissolution and polymer swelling can be expected. SCF addition is reflected in the modification of several physical properties of the polymer, such as glass transition temperature that influences the plasticising effect, melting temperature, surface tension and viscosity, which are changed depending on the solubility of SCF in the polymer.

In the field of polymeric foams, supercritical CO_2 is used as blowing agent. To obtain polymer or composite foams, the substrate is saturated with SC CO_2, followed by rapid depressurization at a constant temperature (pressure quench) [28]. This method takes advantage of the large depression of the glass transition temperature (T_g) observed for many polymers in the presence of dense CO_2 [29]. In the polymer industry, polyurethane (PU) foams comprise the largest segment of the foams market in many products, followed by polystyrene (PS) foams. The replacement of ozone-depleting foaming agents like R12 and R22 by CO_2 has the potential to create a great impact in the foam industry [30]. Nucleation growth can be optimized by changing the saturation pressure, temperature and the rate of release gas. At higher temperature, less gas is dissolved in the polymer matrix; therefore, low growth of pores is expected. When pressure is increased, CO_2 solubility in polymer matrices increases, creating more small size nuclei available for the formation and growth of pores. Rate of gas release also significantly influences the size of porous structures. At higher rates, more nuclei are generated with a smaller size compared to lower rates [31].

Another interesting application is in the field of particle production using supercritical fluids. Particles have been obtained with rapid expansion of supercritical solutions (RESS) [32], the gas antisolvent process (GAS) [33], supercritical antisolvents (SAS) [34], solution enhanced supercritical dispersion processes (SEDS) [35], aerosol solvent extraction systems (ASES) [36], supercritical fluid extraction of emulsions (SFEE) [37] and particles from gas-saturated solutions (PGSS^{TM}) [38].

High-pressure particle production can be summarized by three main processes (table 1-3). In the RESS process, the product is dissolved in a compressed fluid and rapidly extruded through a nozzle, causing rapid nucleation of the product into a dispersed powder. In this process, large amounts of gas are needed. In the GAS/SAS/SEDS process, the product is first dissolved in an

organic solvent and the precipitation of particles is performed by reducing solubility through adding a dense CO_2 as antisolvent, which dissolves partly into the solvent [39]. In the PGSS process, the polymer to be powdered must be converted into sprayable form by liquefaction/dissolution. This can be achieved by melting or dissolving the substance in a liquid solvent, followed by saturation of the melt or solution with gas, where the formation of fine droplets after spraying through a nozzle is driven by reduced surface (interfacial) tension and low viscosity.

Table 1-3: High-pressure technologies for producing powder particles [1].

	RESS	**GAS/PCA/SAS/ASES/ SEDS/SA**	**PGSS^{TM}**
SCF used as	Solvent	Antisolvent	Dissolved
Gas quantity	High	Medium	Low
Organic solvent	Absent	Present	Absent
Pressure	High	Medium	Medium
Separation of gas	Easy	Easy	Easy

The basis for scale-up and cost estimation of PGSS^{TM} processes for industrial production is related to the production capacity and depends on the annual hours of operation and the amount of CO_2 required to generate 1 kg of powder. Weidner [40] has considered an economic evaluation of a PGSS^{TM} plant with a capacity of 1.5 t/h (Figure 1-3). The process features low operating costs, as low as 0.20 €, including investment, personal, consumables (incl. gas), maintenance and interest. Feasibility of a plant of that size can be increased by installing a CO_2 recovery capability. However, processing costs can increase up to 1.2 €/kg in the case of short processing time and high GTF (gas, used as a solvent, to feed) ratios. Low GTF ratios contribute significantly to reducing processing costs. For a plant with a capacity of 1,500 kg/h, processing costs decrease from 1.2 €/kg to 0.4 €/kg in the same operation time. For a plant of the same capacity, extending processing time from 3,000 h/y up to 8,000 h/y can reduce operating cost by almost 50%.

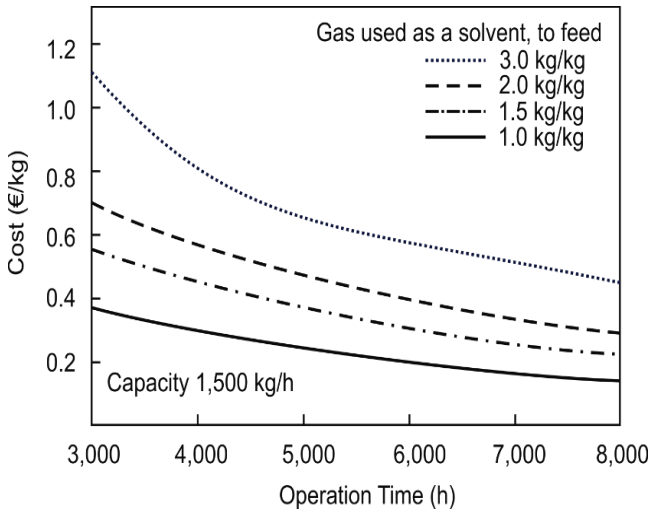

Figure 1-3: Economic evaluation of PGSS plant with a capacity of 1.5 t/h [40].

1.1.3 Supercritical fluid technology in the energy domain

SCF was first introduced in the energy domain in steam cycles in order to increase the thermal efficiency of fossil-fired power plants. Steam at supercritical conditions was used for recovering heat from flue gases and transforming the energy into kinetic and electrical energy [41]. Recently, SCFs have been studied as heat transfer fluids (HTF) in refrigeration systems, advanced power cycles, solar collectors, as a processing media in fuel cell applications, in carbon capture and storage (CCS) processes and as reactants in biofuel production. As a heat transfer fluid, supercritical CO_2 has been reintroduced as an environmentally friendly refrigerant in heat pumps, car radiators, and air conditioning systems [42]. It has zero ozone depletion potential (ODE), low global warming potential (GWP), and non-toxicity when compared to conventional chlorofluorocarbon (CFC) and hydrochlorofluorocarbon (HCFC) freons.

The Supercritical Rankine Cycle (SRC) has been widely studied in terms of efficiency and conversion of energy at lower temperatures. Compared to the organic Rankine cycle, there is a better thermal match between the working fluid and the heat source at the pinch point. In SRC, fluid is heated directly from the liquid phase into the supercritical region, bypassing the two-phase region, which results in less energy loss [43]. As an HTF, supercritical CO_2 can also be integrated with solar energy in power cycles. Over the past several years, there has been a significant amount of research done on supercritical Brayton cycles. Thermal efficiency above 50% can easily be achieved. The main advantages lie in significantly reduced compressor work. Supercritical CO_2 Brayton is present in many applications, ranging from nuclear, geothermal to solar-thermal [44]. There are many opportunities in the development of turbomachines for supercritical power cycles, in research for heat transfer near the critical condensation and evaporation points, and also in recovery processes for hydrocarbons, and in enhanced oil recovery processes at great depths [41].

Global warming and air pollution resulting from the use of enormous quantities of fossil fuels can be significantly reduced with the appliance of carbon sequestration processes. Carbon capture and storage (CCS) technology includes capturing CO_2 emissions at industrial combustion sources (coal power plants, cement factories or biomass refineries), compressing it to liquid or supercritical phases, transporting it (mainly with pipelines and ships), and injecting it into suitable geological storage sites (e.g. depleted oil or gas reservoirs, saline aquifers, ocean and coal seams). Today, CCS projects are capable of capturing up to 28 Mt of CO_2 per year, and they providing critical information for delivering technological cost reductions and for refining policy. The main obstacles preventing CCS technology from becoming even more important in the electric power sector are the substantial amounts of energy needed in the CO_2 capture process that considerably reduce net power capacity, large retrofit capital costs and increased operation costs [45].

One way of making CCS more economically attractive, while at the same time contributing to energy security, is to use captured CO_2 to maximize production from declining oil fields with a process known as enhanced oil recovery (EOR) [46]. Globally, CO_2-EOR has the potential to produce 470 billion barrels of additional oil and to store 140 billion metric tons of CO_2, which are equivalent to the greenhouse gas emissions from 750 large one GW size coal power plants over 30 years [47]. When CO_2 is turned into a supercritical phase at 7.38MPa and 31.1°C, it is soluble in oil [48]. The resulting solution has lower interfacial tension, viscosity, and density; thus, recovery of oil can be enhanced (EOR). Overall, 1t of injected CO_2 enables extraction of 1.5t of oil with carbon emission reduction of 25-60% compared to conventional production. The energy requirement of the capture process can be reduced to approximately 60% with proper optimization of the absorbent/gas ratio of capture process and the utilization of an energy integration option that recovers the heat content of the regenerated hot absorbent. The economic factor demonstrates that the most economical process is uncontrolled CO_2 release. The social

factor shows a preference for the CCS option based on renewables, while from a technological point of view, the preferable technology is the improved CCS alternative because of its lower heat energy demand. The optimal option, from an environmental aspect and overall from total factors, is the application of CCS with renewable energy [49]. Another option is to store captured CO_2 through utilization processes (CCU-Carbon capture and utilization), where waste CO_2 can be transformed into valuable products such as chemicals, building materials and fuels. The required energy can be provided by highly-energetic reactants such as hydrogen, by heat, electricity, sunlight or microwaves. Many of the reduction reaction products, especially methane, methanol and formic acid, can be used as a chemical storage option for renewable energies [50].

In order to make a good comparison between the environmental impacts of different CCS and CCU processes, global warming potential (GWP), with units defined as the mass of CO_2 produced divided with 1 ton of CO_2 removed, is presented [51]. Average GWP through the entire life cycle of a CCS process is estimated near 250 kg CO_2 eq./t CO_2; in a CCU process GWP appears at a significantly higher level (Figure 1-4). The best CCU option, from an environmental point of view, is the production of methanol by a reaction between captured CO_2 and H_2 produced from a photovoltaic energy source. GWP is estimated to be 450 kg CO_2 eq./t CO_2, which is approximately twice better than fuel production from microalgae cultivation with CO_2, which has an average GWP near 1100 kg CO_2 eq./t CO_2. Direct utilization of CO_2 for supercritical extraction of coffee beans has an average GWP near 1.20 kg CO_2 eq./t CO_2. Utilization through enhanced oil recovery might be a better option, from an economic perspective, to store CO_2 rather than CCS, but the environmental impact is clearly higher (average value around 500 kg CO_2 eq./t CO_2). Carbon utilization for production diethanolamine (DME) is the worst option, with a GWP near 600 t CO_2/t CO_2, which is almost 100 times higher than other options presented in Figure 1-4. Carbon mineralization is an interesting option, since storage of CO_2 is considered for a long period of time: in the case of production of fuel and chemicals, CO_2 is stored for a limited time and then is released back into the atmosphere.

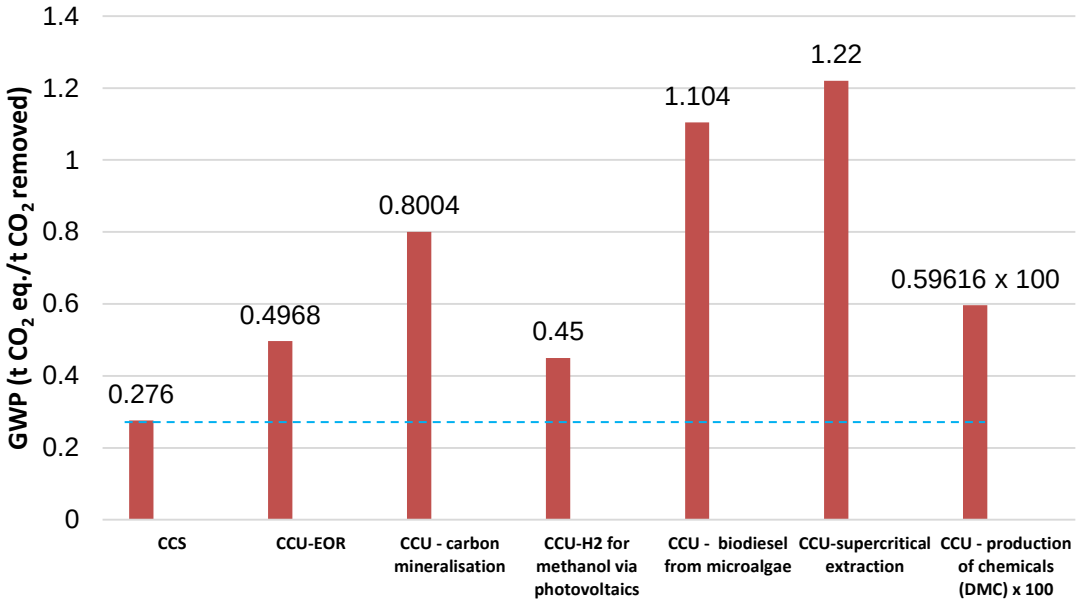

Figure 1-4: Average GWP (global warming potential) for different CCS (Carbon Capture and Storage) and CCU (Carbon Capture and Utilization) process**.**

1.1.4 Hydrothermal reactions and technology

Hydrothermal (HT) processes are promising technologies for the conversion of waste biomass into biobased chemicals and biofuels, using sub- and supercritical water as processing media. Subcritical water is pressurized water at temperatures above boiling point at ambient pressure and below the critical point (343 °C, 22.1 MPa). Within a region close to the critical conditions, system properties become more sensitive to pressure and temperature changes. By increasing temperature, the density of the liquid phase decreases as the density of the vapour increases, and becomes more similar and finally identical at a critical point. Water above the critical point is named supercritical water and has properties between liquid-like and gas-like phase [52].

Generally, HT processes can be divided into four main processes: carbonization (HTC), aqueous phase reforming (APR), liquefaction (HTL), and gasification (HTG). In these processes, water has the role of reactant, solvent, and catalyst. The main advantage over other processing methods includes the ability to use wet biomass without prior dewatering thus enabling the production of versatile chemicals and fuels in the gaseous, liquid, or solid state. The four main HT reactions of biomass conversion into desired energy products and different operating parameters [52] are presented in Figure 1-5.

As demonstrated in Figure 1-5, hydrothermal carbonization is performed at mild temperatures, usually up to 250 °C. Solid products with a high content of carbon are obtained. Such products have high energy contents and are suitable chemicals for different applications. Hydrothermal liquefaction is demonstrated as a process that is typically carried out at temperatures between 250 °C K and 375 °C. The product is a highly viscous liquid - pyrolysis oil which can be applied as a pure chemical or can be added to diesel fuel. It is also demonstrated that at higher temperatures, above 375 °C, supercritical water gasification is performed. Gaseous products with a high content of hydrogen and carbon monoxide are obtained. CO_2 and other hydrocarbons are present in lower concentrations. This gas could be used as a source of energy or as “syngas” for the synthesis of higher value chemicals.

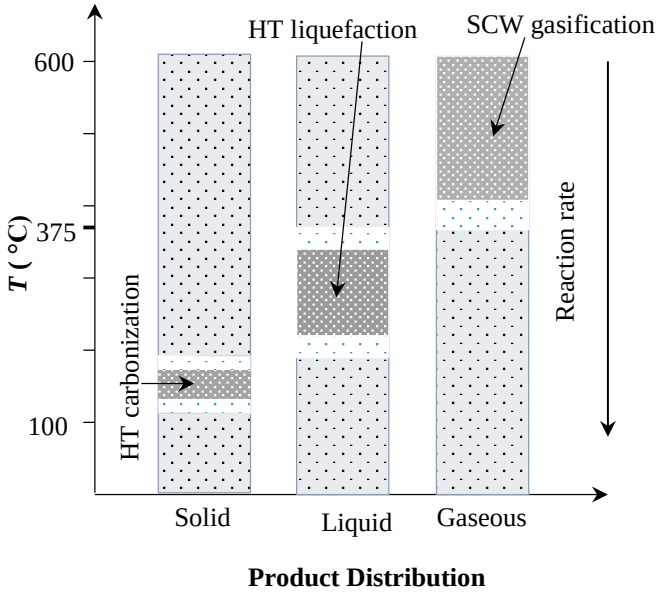

Figure 1-5: Diagram of water with an area of application for hydrothermal treatment; (*T*c - critical temperature, *P*c - critical pressure) [53].

The operating conditions of biomass treatment by hot compressed water effect, both product distribution and characterization. The physicochemical properties of the target products (gas,

HO, aqueous phase, and SR) are influenced by hydrothermal temperature and residence time [54].

A brief techno-economic analysis of the hydrothermal process is presented in table 1-4. The data is based on lab-scale experiments using certain assumptions scaled up with modeling software. When considering a new hydrothermal industrial plant [55], reactor cost may represent about 8.5 to 21.3% of the total capital investment (TCI), depending on plant capacity and feedstock used. Additionally, the overall costs of the hydro char or bio-based fuel produced decrease with increasing plant capacity because of economies-of-scale effects. As can be observed for HT carbonization processes, the capacity of the plants varies from 0.468 t/h up to 83.33 t/h depending on the feedstock type and operating conditions. Different products such as hydrochar, pyrolysis oil, biofuel or "syngas" are obtained. The main advantage of these processes is that they are carbon neutral, which results in low environmental impact. Stemann and co-authors [70] calculated investment, operating, and total production cost of HT production of hydrochar based on computer simulations.

Two different scale-up plants, one with a processing capacity of 5.7 t/h EFB (Empty Fruit Bunch) and the other with 13.8 t/h EFB, were studied. The production cost was 19% lower when model systems were used to perform calculations. Facing the challenge of sustainable algae biofuel production, hydrothermal liquefaction (HTL) certainly presents a good alternative to wet lipid extraction and the secretion of oils or alkanes. There are still several constraints to be overcome before the technology can be made market ready. Gasafi and co-authors report [78] the annual costs of the sewage sludge gasification process based on the method of total annual revenue requirement (TRR) which corresponds to the amount of money that must be obtained from selling one or several products in a given year to cover the investment and operation costs of the current year and to provide economic efficiency of the process. The solution to lowering the energy requirements of these processes could be the application of pressures exceeding conventional ones (up to 30.0 MPa) and applying much higher pressures, up to 100.0 MPa. Three main limitations affecting material consideration are corrosion, pressure resistance, and hydrogen aging [53].

Table 1-4: Economic evaluation of scale-up hydrothermal processes reported in the literature [53].

Process	Capacity (t/h)	Feedstock	Investment (M€)	Product cost (€/GJ)	Environmental impact
HT carbonization				Hydrochar	
Plant 1	5.7	Empty fruit branches	9.01	9.67	Carbon neutral
Plant 2	13.8	Empty fruit branches	16.47	7.94	Carbon neutral
Plant 3	48.6	Waste wood	20.719	5.27	Carbon neutral
HT liquefaction				Biofuel	
Plant 4	0.468	Microalgae	1.6	65.9	Carbon neutral
Plant 5	83.33	Microalgae	468	/	Carbon neutral
HT gasification				Syngas	
Plant 6	5	Sewage sludge	2.915	7.1	Carbon neutral

1.1.5 Supercritical drying and aerogels

Supercritical drying is used for cleaning processes of microelectrochemical systems [56], in the preparation of biological specimens for scanning electron microscopy [57], and in nanotechnology for the production of aerogels [58].

Aerogels are regarded as one of the most promising high-performance thermal insulation materials, with a thermal conductivity down to 13 mW/mK for commercial products in building applications [59]. They were discovered and synthesized almost one hundred years ago in a low-temperature sol-gel environment driven by evaporation. In recent years, several biocompatible aerogels have been obtained using supercritical drying technology. The pharmaceutical industry is highly interested in using biocompatible aerogels, especially in drug delivery systems. Silica aerogels are the most common synthesized inorganic aerogels, with a wide spectrum of potential applications as additives, free flow agents, and drug carriers. As surface area/volume ratio is one of the key variables in controlling drug release, different aerogel characteristics can be obtained by changing the types and degrees of esterification and concentration of encapsulated drugs [60]. However, silica aerogels can present certain problems, mostly as a result of their fragility. Most supercritical dried inorganic aerogels can easily crack and form fragile monoliths. Polysaccharide aerogels usually don't have those limitations and they can improve production in many applications [61]. Polysaccharide is a promising material for hydrogels, the first step in areole preparation production because of their biodegradability, nontoxicity and natural origin. Several polysaccharide aerogels have been loaded with drugs such as ibuprofen, paracetamol and nicotinic acid [62].

2. Polymer processing and formulation of active drugs

Supercritical fluids (SCFs) are well established for use as a green processing solvent in polymer applications such as polymer modification, the formation of polymer composites, polymer blending, microcellular foaming, polymerization and particle production [63]. In particular, special attention is dedicated to using biodegradable polymers in particle size reduction processes that are related to pharmaceutical applications for controlled drug release [64]. One of the most frequently used biodegradable polymer is polyethylene glycol (PEG), which is a water-soluble polymer, psychological acceptable and biocompatible [65].

2.1 Theoretical part

2.1.1 Biodegradable polymer/supercritical fluid

Polymer processing considering compounding and mixing of polymers requires previous knowledge of S-L-G phase equilibria, density, viscosity, interfacial tension, gas solubility, and diffusivity in multipolymer and supercritical fluid (SCF) systems. In recent years, many experimental and numerical investigations of various molecular weight polyethylene glycols (PEGs) using carbon dioxide [66, 67], argon[68], nitrogen and propane [68] as an SCF have been done. Furthermore, supercritical carbon dioxide acting as a plasticizer was used in investigations of polycaprolactone [69]. polypropylene, polystyrene [70], poly(β-hydroxybutyrate) [71], poly(3-hydroxybutyrate-co-3-hydroxy valerate) [72], and polyethylene glycol nonyl phenyl ether [73].

Weidner et al. [74] studied phase equilibrium (solid-liquid-gas) in polyethylene glycol (PEG)-*c*arbon dioxide systems that has been lately frequently employed in the preparation of solid dispersions. Phase behavior with a negative dp/dT slope is desirable, where the SCF is highly soluble in the molten heavy component [75]. In particular, the solubility of the SCF biodegradable carrier PEG of different molar weights was found to increase significantly with pressure [76, 77]. Maša H. Knez et al. [78] measured the solubility and diffusivity of CO_2 in PEGs of different molecular weight. Results indicated that solubility of CO_2 in PEG increases with increasing pressure. In contrast, diffusion coefficients in the system are mostly influenced by the amount of CO_2 already present in PEG. The same research group has also reported on density and viscosity of the binary polyethylene glycol/CO_2 systems [79]. They found out that increase of dissolved CO_2 in the polymer matrix is related to viscosity reduction and density increase. Fanovich and Jaeger [69] published a research on determining solubility and diffusivity of CO_2 within polycaprolactone and thus on the swelling of the polymer using magnetic suspension balance. Sorption measurements indicate that a higher amount of gas is absorbed when pressure is increased, meanwhile, this amount usually decreases when the temperature is raised. Sato [70] addresses the behavior of the CO_2 and N_2 in the polypropylene and polystyrene. The solubility of CO_2 and N_2 in polypropylene were measured at temperatures from 160 °C to 200 °C and pressure up to 17 MPa. The solubility of CO_2 decreased with increasing temperature, while the solubility of N_2 increased with increasing temperature. The solubility of both gases in polypropylene is much higher than in polystyrene. Khosravi et al. [71] investigated the effect of pressure and temperature on the solubility of CO_2 in polyhydroxybutyrate. Results clearly demonstrate that solubility increases with increasing pressure and temperature at a pressure above 18.2 MPa, meanwhile, below this pressure, the solubility increases with increasing pressure but decreases with increasing temperature. Cravo et al.[72] report on the determination of diffusion coefficient of CO_2 in natural biodegradable poly (3-hydroxybutyrate-co-3-hydroxy valerate). A maximum diffusion coefficient has been achieved at lower temperatures and higher pressures. Dimitrov et al. [73] report on the solubility

of CO_2 within polyethylene glycol nonyl phenyl ether of molecular weight of 1980 g/mol, 2420 g/mol, and 2860 g/mol. The results show, that the solubility increases with increasing the pressure for all molecular mass of polyethylene glycol nonyl phenyl ether at a constant temperature.

Review by Nalawade et al. [80] provides extensive information on useful processing aspects and applications of polymers melts at high pressures, where the high diffusivity of CO_2 and the low interfacial tension are key factors in determining a wide range of applications. It is well known that polymer-gas mixture exposed to high pressure and temperature has a lower interfacial tension than pure polymers. Mahmood et al. [81] investigated the interface of molten polylactide (PLA) by analyzing sessile drops in high-pressure and high-temperature visualization chamber from 6.89 to 20.68 MPa and from 463 to 473 K, respectively. Harrison et al. [13] studied the effects of various surfactants on the interfacial tension between 600 molar weight polyethylene glycol (PEG) and supercritical CO_2 at 318 K on the basis of measurements by a pendant drop. Interesting work was carried out by Carbone et al. [82] were interfacial tension, solubility, diffusivity and specific volume of molten poly(caprolactone)/CO_2 solutions were simultaneously measured to reduce errors by using costume-designed measurement device consisting of a rod to which polymer-gas solution is stuck (by patent drop method) and placed in a magnetic suspension cell. Gutierrez et al. [83]studied interfacial tension and glass transition of polystyrene in scCO_2 within the pressure range from vacuum to 9 MPa, and temperatures from 30.15 °C to 40.15 °C by the pendant drop method. Although it is difficult to achieve accurate and comparable data in modelling of thermodynamic properties of molten polymers at high pressures with experimental ones Enders et al. [84] presented the Chan-Hilliard theory with equations of state (the original statistical associating fluid theory, the perturbed-chain statistical associating fluid theory or the Sanchez–Lacombe lattice theory) in order to describe both, the solubility of carbon dioxide in polystyrene, and the interfacial properties between the liquid mixture and the pure gas phase. Operating pressure during processing with supercritical fluids is of fundamental importance considering morphology of the prepared materials. In some cases, operating pressure showed a linear relation to the porosity of the matrices [85]. A theoretical approach to describing the experimental data on the sorption and diffusion of gaseous mixtures in polymers under high pressures has been developed by Kiran [86]. Markočič et al. [87] investigated the effect of pressure on a system of polycaprolactone and CO_2. Temperature and pressure influence foam morphology through their effect on gas solubility in the polymer and on the viscosity of the substrate. The number of pores and their size depends on nucleation and growth rates. At higher gas concentration, the influence of nucleation predominates, therefore higher solubility enables more pores with smaller diameters. The results show that supercritical CO_2 is suitable to obtain the desired porosity of polycaprolactone. Gutierez et al.[83] shows the behavior of the system polystyrene /CO_2 in the presence of terpene oil limonene in the pressure range from 5 MPa to 15 MPa and concentration from 0.05 g to 0.2 g polystyrene/mL limonene at a temperature of 30 °C and 40 °C. At the pressure of 80 bar, the limonene is fully miscible with CO_2, which results in lower absorption of CO_2 into polystyrene at a further increase of pressure. The most suitable condition to foam polystyrene from limonene solution of 0.1 g polystyrene /mL limonene is a pressure of 90 bar, the temperature of 30 °C, contact time of 240 min, and depressurization time of 30 min. Nalawade et al. [88] investigated phase behavior of PEGs with molecular weight 6000 g/mol and 10 000 g/mol with a goal to produce micron size particles from gas-saturated solution (PGSS). They report that particle size, shape, morphology and particle size distribution depending on the molecular weight of polymer, pressure, and temperature and nozzle diameter.

2.1.2 Formulation of active pharmaceutical drugs

Approximately 70% of new drug candidates possess poor aqueous solubility and about 40% of the immediate release oral drugs on the market are considered to be practically insoluble in water [89]. The pharmaceutical industry is interested in obtaining the successful formulation of poorly soluble active compounds in order to increase their bioavailability and dissolution rate. The current delivery options for improving the dissolution properties of drugs are particle size reduction, crystal modification, pH modification, self-emulsification, amorphization and the formulation of drugs with surfactant carriers and amorphous polymers [90]. Particle size reduction and drug formulation with polymeric carriers incorporate the most promising options in this regard. A number of conventional methods have been developed to improve the dissolution properties of drugs [91]. Many of these methods possess drawbacks, such as thermal and chemical degradation of drugs, large quantity organic solvent use, broad particle size distribution and low drug load [92].

To overcome these limitations, supercritical fluid technology promises to be an excellent option. The reasons for the widespread use of supercritical fluids mainly lie in the simplicity of the processes, high purity of products, no organic solvents in the process, no communication steps in drug preparation, mildness of operating conditions and the possibility of obtaining non-contaminated fine particles with narrow size distributions [31, 93]. Production of fine particles with improved characteristics using supercritical fluids has been obtained with rapid expansion of supercritical solutions (RESS) [32], the gas antisolvent process (GAS) [33], supercritical antisolvents (SAS) [34], solution enhanced supercritical dispersion processes (SEDS) [35], aerosol solvent extraction systems (ASES) [36], supercritical fluid extraction of emulsions (SFEE) [37] and particles from gas-saturated solution (PGSS^{TM}) [38]. In particular, the PGSS^{TM} used in our study is an organic solvent-free process in which polymeric carriers with the target pharmaceutical drug to be micronized and encapsulated are loaded into a high-pressure autoclave together with supercritical CO_2. By heating the autoclave, the content is melted and then, after saturation with the supercritical CO_2 solution, rapidly expanded through a nozzle. Fine particles with irregularly shaped morphology, which normally release the active compound in a very short period of time, are produced [94].

Several bioactive substances, including active pharmaceutical drugs, flavors, and vitamins, have been successfully micronized and encapsulated using the PGSS^{TM} process (Table 2-1). Weidner et al. [95] studied particle precipitation of polyethylene glycol (PEG) of different molar weights that has been frequently employed in the preparation of solid dispersions. Chen et al. [96] successfully micronized the non-steroidal anti-inflammatory drug ibuprofen with PEG 6000 as a carrier material. Božič et al. and Kerč et al. [97, 98] used PEG 4000 for the powder generation of the practical water-insoluble calcium-channel blockers nifedipine and felodipine and the hypolipidemic agent fenofibrate. Meanwhile, Marizza et al. [99] report on the drug release of ketoprofen from polyvinylpyrrolidone (PVP) using supercritical CO_2. Pestieau et al. [89] developed a formulation containing fenofibrate and Gelucire 50/13 as a career in order to improve the bioavailability of the insoluble drug. García-González et al. [100] investigated the encapsulation efficiency of solid lipid hybrid particles prepared using the PGSS technique with ketoprofen, glutathione, and caffeine. Knez et al. [101] measured phase equilibria and performed micronization of the flavors vanillin and ethyl-o-vanillin in the presence of various compressed gases, where vanilla was mainly used to mask the unpleasant flavors of drugs. Couto et al. [94] encapsulated vitamin B_2 in solid lipid nanoparticles using supercritical CO_2 with the aim of protecting active substrate and longer shelf-life.

Production of ultrafine (micro- or nano-sized) particles with desired properties and precise control of particle size and morphology is one of the objectives of many industries.

Table 2-1: Some PGSS^{TM} applications for the formulation of active substances [102].

	Carrier	**Active substrate**	***P* (MPa)**	***T* (°C)**	**Mixing time**	**Morphology**
Experimental [102]	Brij 100	Nimodipine, Fenofibrate, O-vanillin	10-25	60 45	1 h	Irregular/Porous
Experimental [102]	PEG 4000	O-vanillin	10-25	60	1 h	Irregular/Porous
Experimental [76]	Brij 52	Esomeprazole	15	45-60	1 h	Irregular
Weidner et al. [95]	PEG 2000-35000	/	15-40	60 - 90		Spheres
Couto et al. [94]	PEG 2000-35000	Vitamin B2	10-25	65	2h	
Sousa et al. [103]	Glyceryl monostearate	Caffeine	13	62		Needle aggregates
Varona et al. [104]	PEG	Lavadin oil	5-9	70 -90	2h	Spheres
Pestieau et al [89].	Gelucire 50/13	Fenofibrate	80-240	60-80	1h	Spheres
Kerč et al. [97]	PEG 4000	Nifedipine, Felodipine, Fenofibrate	10-20 20 19	50-70 150 65-90	1h	Irregular/porous
González et al. [100]	Glyceryl monostearate, Waxy triglyceride	Glutathione, Ketoprofen	13	72	1h	Needle aggregates
Paz et al.[105]	Polycaprolactone	B-carotene	11-15	50-70	1h	Spheres

2.1.3 The aims

The PGSS^{TM} process was applied to the biodegradable polymeric materials polyoxyethylene stearyl ether **(**Brij 100 and Brij 50) and polyethylene glycol (PEG 4000) for the incorporation of insoluble drugs nimodipine, fenofibrate, o-vanillin, and esomeprazole with the purpose of improving their delivery. Additionally, Brij52/CO_2 is presented as a model system for gas foaming, since polymer foams are ubiquitous in modern life, used everywhere from medicine to pharmaceutical industry. Before starting particle precipitation, preliminary thermodynamic experiments of water-soluble carriers polyoxyethylene stearyl with molar weights of 683 g/mol (Brij 50) and 4670 g/mol (Brij 100) and polyethylene glycol of molar weights from 600 g/mol up to 1000 g/mol were carried out. The diffusion coefficient, density, interfacial tension and solubility of CO_2 saturated Brij 52 were studied at different pressure and temperature conditions. Similarly, for Brij 100, the melting points in the presence of various gases, CO_2 solubility in polymer matrixes and interfacial tension of gas-saturated solutions were determined. Influence of the polymer molar weight on the gas solubility and interfacial tension was measured in the system of PEG/CO_2 and PEG/Ar. Measured interfacial tension and viscosity of CO_2 saturated PEG 6000 at different spraying pressure and temperature conditions were correlated with particle shape and morphology.

In the second part, particle generation and formulation of the above-mentioned drugs with Brij 50, Brij 100 and PEG 4000 were studied. The influence of the main process parameters, including the pre-expansion conditions and polymer-drug ratio, on product characteristics such as the yield of collected particles, drug content (loading efficiency), particle size distribution, morphology, and dissolution rate profile of the microparticle, is presented. [76, 77]. The objective of this work was to carry out a comparative evaluation of substance release from polymeric carriers in gastric pH media for a compound of interest. In order to investigate a

consistent drug release, it was necessary to maintain similar conditions as while dosage form travels across the physiological pH range. The dissolution rate measurements are therefore performed using two different dissolution means, depending on the drug considered: 0.1 M HCl in water and distilled water.

To the best of the authors' knowledge, PGSS formulation of nimodipine, fenofibrate, esomeprazole and o-vanillin using Brij 50, Brij 100 and PEG 4000 as carrier material has not been previously described in the literature.

2.2 Experimental part

2.2.1 Materials

Active substrate nimodipine, fenofibrate, o-vanillin, and esomeprazole were provided by XI'AN Health Biochemical co., LTD. Polyethylene glycol (PEG) of molar weight from 600 g/mol up to 1000 g/mol 1were purchased by MERCK (Germany). Polyoxyethylene stearyl ether (Birj) of molar weight 683 g/mol and 4670 g/mol were bought from Sigma-Aldrich. Moisture content in the polymers, determined gravimetrically by means of an HB43-S Compact Halogen Moisture Analyzer, was lower than 0.10 wt. % of each polymer. Disposable capillary pipettes with borosilicate glass resistant to thermal shock were provided by Hirschmann (Germany). CO_2 (99.998%) and Ar (99.998% purity) were supplied by Messer (Slovenia). Structural formulas of materials used in the formulation processes are presented in Figure 2-1 and Figure 2-2.

Table 2-2: Materials used in the formulation processes.

active substrate or carrier	Mw (g/mol)	Melting temperature	Solubility in water at 25 °C
Nimodipine	418.4	125 °C	Low, 0.01 mg/mL
Fenofibrate	360.8	80 - 81 °C	Low, 0.25 mg/mL
O-vanillin	152.1	40 - 42 °C	Medium, 10 mg/mL
Esomeprazole	345.2	155 °C	Low, 0.35 mg/mL
Brij 50	683	38 °C	High, 66 mg/mL
Brij 100	4670.0	51 - 54 °C	High, 55 mg/mL
PEG 4000	4000.0	58 - 61 °C	High, 50 mg/mL

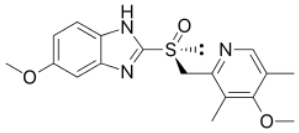

Fenofibrate

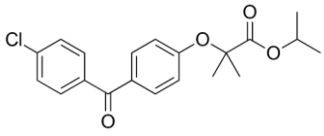

Esomeprazole

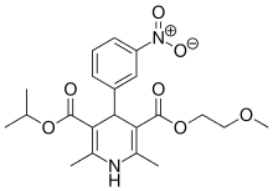

Nimodipine

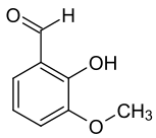

O-vanillin

Figure 2-1: Structural formula of active drugs fenofibrate, esomeprazole, nimodipine, and o-vanillin.

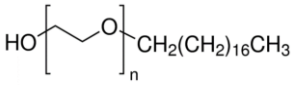

Polyoxyethylene stearyl ether

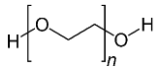

Polyethylene glycol (PEG)

Figure 2-2: Structural formula of biodegradable polymers polyoxyethylene stearyl ether (Birj S) and polyethylene glycol (PEG).

2.2.2 Equipment and methods

In sub-sections, 2.2.2.1 – 2.2.2.9 the methods to determine physical-chemical and transport properties of a binary system of a selected polymer and SCF are presented. Melting points were determent in a high-pressure view cell by means of glass capillary method. Density was determined by a technique using a density meter with a U-tube. Interfacial tension was determined by a modified capillary rise method. A gravimetric technique based on gas sorption measurement by a magnetic suspension balance was used to determine diffusion coefficient and solubility of supercritical CO_2 in the polymer. Viscosity was determined in a high-pressure visual cell, where values are derived from Reynolds number that was calculated from the Newton number. As recent breakouts of polymer processing, two different methods were described: the one for obtaining particles of a reduced size, Particles from Gas Saturated Solutions (PGSS^{TM}), and the one for production of microcellular polymeric foams, Gas Foaming (GF).

2.2.2.1 Modified capillary method for determination of melting points

The melting points of the carrier Brij 100 in contact with dense gases CO_2 and propane were determined by the modified capillary glass method. A detailed description of the method can be found in the literature [75]. Briefly, a capillary made of glass was placed in an optical cell NWA (Germany) equipped with two sapphire windows (operating up to 90 MPa and 460°C). Dense gas was introduced via a high-pressure pump and then the temperature was continuously increased until the last solid particle of polymer melted. The pressure was measured using a digital pressure gauge (WIKA, Germany: 0.1 ± %). Measurements for creation S-L curves were performed up to 60 MPa. The melting points of polymer were observed using a digital camera by upward strategy (pressure/temperature increase).

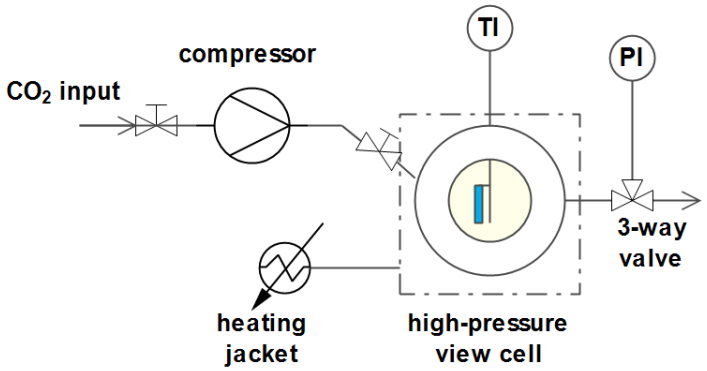

Figure 2-3: A scheme of a high-pressure optical cell for determination of melting points.

2.2.2.2 Gravimetric method involving Magnetic suspension balance (MSB)

Diffusion coefficients, density, and solubility of the carbon dioxide and argon saturated solutions of molten polyethylene glycols were measured by a gravimetric method involving magnetic suspension balance (MSB, Rubotherm). The applied MSB is design for the maximum operating pressure of 35 MPa and operating temperature of 253 °C with a mass uncertainty $u_{c,m}$ = 20 µg, pressure uncertainty $u_{c,p}$ = 0.5 MPa and temperature uncertainty $u_{c,t}$ = 2 °C [67]. Such an accuracy is possible due to the location of the balance outside the measuring cell, under normal conditions of pressure and temperature. The measuring force is transmitted contactless from the measuring chamber to microbalance by magnetic suspension coupling. The measuring cell of MSB is also provided with a window, which allows observation of the sample and estimation of volume modifications during the sorption measurements (Figure 2- 4). A detailed description of the device and of working procedure can be found in the literature [67, 106].

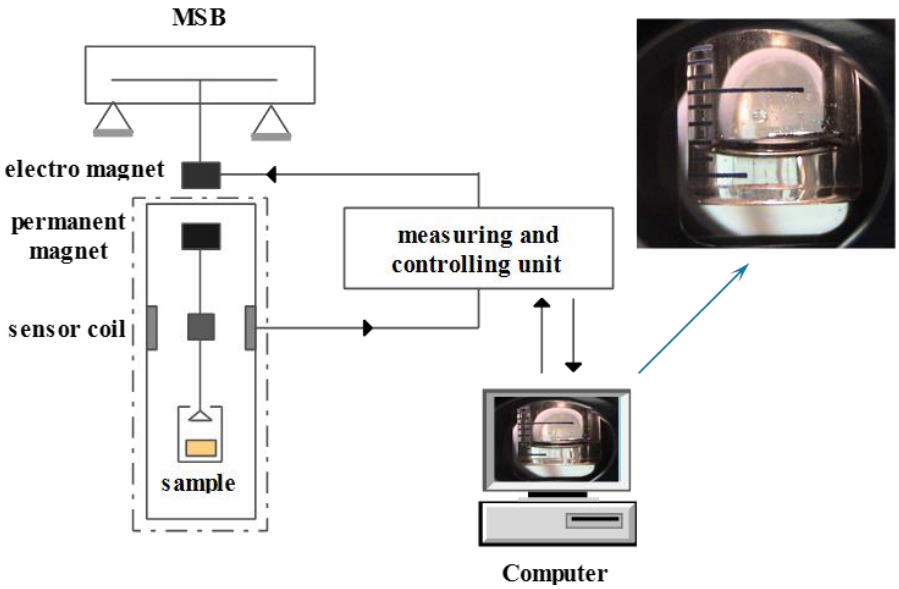

Figure 2-4: A scheme of measuring density and solubility by a gravimetric method involving magnetic suspension balance (MSB).

In the present work, density, solubility, and diffusion coefficients were measured for each investigated binary system by increasing the pressure step by step from 0.0 MPa up to 30.0 MPa at constant temperatures (55 °C, 70 °C and 90 °C) for approximately 2.0 MPa increments. Before applying next pressure step, the software MassPro recorded conditions (mass temperature, pressure) inside measuring cell. After approximately an 80 min period of time, the equilibrium was reached and the volume of the sample could be analyzed by digital photo camera. Calculations of volume were made with Image J software with a measurement uncertainty of u_c = 0.01 cm^3, using the diameter of the sample container as an internal reference. Results were compared with those from the literature. The accuracy was better than 2 %.

2.2.2.2.1 Density and solubility calculations

The density of binary system was expressed in mass (g) of polymer with absorbed gas per volume of sample (polymer with absorbed gas) (mL). The solubility of a gas in the polymer was expressed in mass gas (g) absorbed per gram polymer. First, the mass (m_{SC}) and volume (V_{SC}) of the sample container and of other parts of the suspension coupling were determined by measurements in the absence of the polymer sample. Then the mass of the polymer sample,(m_S), was calculated from difference between the recorded balance mass (m_{BAL}) and the mass of sample container (m_{SC}) [107]:

$$m_S = m_{BAL-\,m_{SC}} \tag{2.1}$$

The recorded balance mass reading (m_{BAL}) during density and solubility measurements was corrected due to the buoyancy effect acting on the sample and the sample container [108]:

$$m_{BAL,CORR} = m_{BAL} + \rho(V_{SC} + V_S) \tag{2.2}$$

where (ρ) is the density of the pure gas inside the measuring cell, obtained from the NIST Chemistry WebBook [109], (V_{SC}) and (V_S) are volumes of the sample container and the sample volume [107]. During the absorption of gas, the volume of polymer sample changes according to equation:

$$V_S = \Pi \cdot r^2 \cdot h_S \tag{2.3}$$

The values of the sample volume were used for determining the mass of polymer with absorbed gas (m_{PG}):

$$m_{PG} = m_{BAL,CORR-}\, m_{SC} \tag{2.4}$$

The density (ρ) of binary system and solubility (S) of gas in polymers were then determined from:

$$\rho \text{ (g PEGs + gas/ml sample)} = \frac{m_{PG}}{V_S} \tag{2.5}$$

$$S \text{ (g gas/g PEG)} = \frac{m_{PG-}\, m_S}{m_S} \tag{2.6}$$

2.2.2.2.2 Diffusion coefficients calculation

The diffusion coefficients were calculated on the basis of Fick's second law for one-dimensional diffusion process which has been considered for a limited environment with two parallel plates $x = 0$ and $x = l$ [110]:

$$\frac{\partial c}{\partial t} = D\frac{\partial^2 c}{\partial x^2} \tag{2.8}$$

where c is the concentration of the diffusing CO_2 (mol/L), x is the position of diffusion direction (mm), t istime (s) and D represent the diffusion coefficient (m^2/s). When the sample is exposed to the CO_2 only on one side of the plate, Fick's second law can be solved by considering the following boundary conditions:

$$\begin{array}{lll} c = c_0 & t = 0 & 0 \le x \le l \\ \frac{\partial c}{\partial x} = 0 & t \ge 0 & x = 0 \\ c = c_1 & t > 0 & x = l \end{array} \tag{2.9}$$

where c_1 is the concentration of the diffusing CO_2 on the sample surface (mol/L), c_0 is the initial concentration of the diffusing CO_2 (mol/L) and l resprisents the thickness of sample plat (mm). After considering the boundary conditions, the solution of Fick's second law can be expressed in the simplified form as[110]:

$$\frac{m_{\mathrm{t}}}{m_{\mathrm{eq}}} = \frac{2}{\sqrt{\pi}}\frac{\sqrt{D}}{l}\sqrt{t} \tag{2.10}$$

where $m_{\mathrm{t}}$is the mass of gas CO_2 absorbed in the polymer at time t (g) and m_{eq} is the mass of gas CO_2 absorbed in the polymer at equilibrium (g). From the initial gradient of the plot $\frac{m_{\mathrm{t}}}{m_{\mathrm{eq}}} = f\left(\sqrt{t}\right)$ the diffusion coefficient (D) can be determined as follows:

$$D = \frac{\pi}{4}\, I^2 l^2 \tag{2.11}$$

where $I$is the initial gradient of the plot ($s^{-1/2}$).

2.2.2.3 Viscosity measurements in high-pressure view cell

The viscosity of CO_2 saturated solutions of PEG 6000 was measured using a high-pressure variable-volume view cell (NWA Gmbh, Lorrah, Germany) with a capacity of 120 ml. The cell consists of two Safire windows, an opening for inserting and emptying the CO_2 gas, and for placing a thermocouple. The cell is designed for a maximum operating pressure of 700 bars and a maximum operating temperature of 200 °C (Figure 2-5). Viscosity is measured using a step-by-step procedure at temperatures higher than the melting point of an investigated polymer. Approximately 10 g of the sample was placed inside the high-pressure view cell. The pressure was increased with an inlet CO_2 gas powered by a high-pressure liquid pump (NWA PM-101). The pressure was measured by an electronic pressure gauge (WIKA to within ± 0.1%), and the cell was electrically heated by a heating jacket accurate to within ± 0.5 °C. After 1h, when the system reached thermodynamic equilibrium, mixing was turned on. Temperature, pressure, voltage, mixing rate and electric current were observed for every experiment. From the data obtained, Re and Ne nondimensional numbers were calculated. Re and Ne curves were also obtained for pure CO_2, under the same conditions as the polymer samples, from the variation of voltage, mixing rate and electronic current [111].

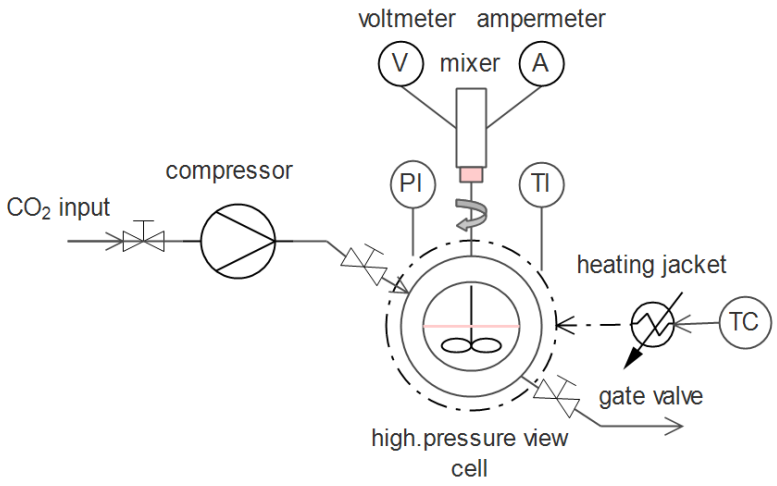

Figure 2-5: A scheme of a high-pressure apparatus for viscosity determination.

Viscosity was derived from the Reynolds number calculated from the Newton number provided in the equation below:

$$Ne = \frac{P}{\rho \cdot \omega^3 \cdot d^5}, \tag{2.12}$$

Where P (W) presents power (a function of experimentally determined electric current and voltage), ρ (kg/m3) is the density of the fluid at certain conditions, ω (s-1) is rotation speed, d (m) is the diameter of the propeller mixer. Viscosity is calculated from the equation for the Reynolds number according to:

$$\mathrm{Re} = \frac{\rho \cdot \omega \cdot d^2}{\eta}, \tag{2.13}$$

$$\eta = \frac{\rho \cdot \omega \cdot d^2}{\mathrm{Re}}, \tag{2.14}$$

where Re is the Reynolds number determined (from Ne vs Re curves for pure CO_2) at each operating condition. Each data point represents the average of at least three measurements at a certain voltage.

2.2.2.4 High-pressure vibration tube *density meter*

The density of CO_2 saturated polymer solution was measured by vibrating an Anton Paar DMA 602 U-tube densitometer with an Anton Paar DMA 60 electronic control unit. Nitrogen and Milli Q water were used as calibration fluids (Figure 2-6). Based on the oscillating time of nitrogen $\tau_{N_2}$and Milli Q water$\tau_{\text{Milli Q water}}$, determined experimentally, and known densities ρ_{N_2} and $\rho_{\text{Milli Q water}}$, the characteristic constant K of the device has been calculated:

$$K = \frac{\rho_{N_2} - \rho_{\text{Milli Q water}}}{\tau_{N_2}^2 - \tau_{\text{Milli Q water}}^2} \tag{2.15}$$

When the U-tube was filled with a sample under the same experimental conditions, the oscillating times $\tau_{\text{polymer}/CO_2}$ were measured and the density of the sample $\rho_{\text{polymer}/CO_2}$ determined by:

$$\rho_{\text{polymer}/CO_2} = K\left(\tau_{\text{polymer}/CO_2}^2 - \tau_{N_2}^2\right) + \rho_{N_2} \tag{2.16}$$

In order to reach equilibrium, approximately 10 minutes was needed at each pressure to stabilize the system. Detail operating procedure can be found in the literature. The U-tube was thermostated by means of an external temperature controlled circulating bath, which controls the temperature within ± 5 x 10^{-3} K. The temperature and pressure inside the U-tube were measured with an Anton Paar CKT 100 platinum resistance thermometer with an uncertainty of ± 0.01 K and a Nuova Fima EN837-1 manometer with an accuracy of 0.25% for pressures lower than 600 bar. The reported uncertainty in the density of reference fluids is generally less than 0.1% with an estimation of ± 0.05 kg/m [112]. Detailed operating procedure can be found in the literature [76].

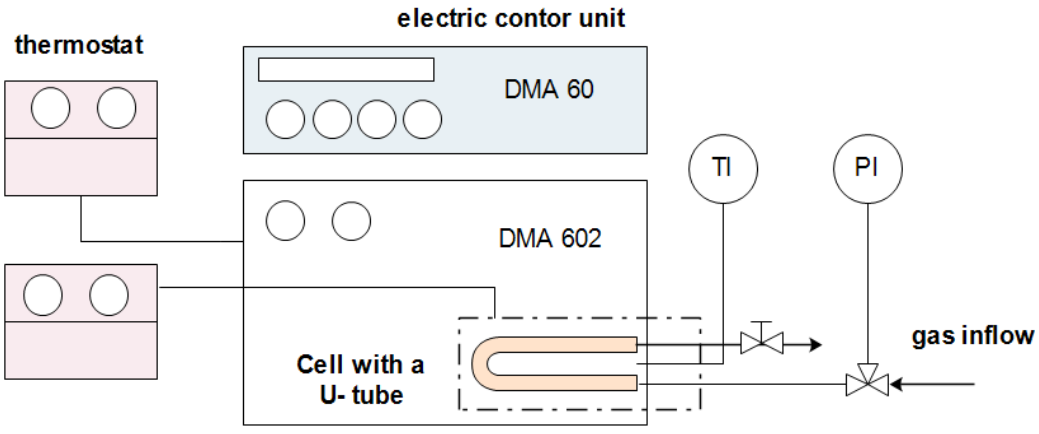

Figure 2-6: A scheme of a high-pressure cell with a vibrating U-tube for density determinations.

2.2.2.5 High-pressure device for determination of interfacial tension

By means of the capillary rise method, accurate data of the equilibrium height of molten biodegradable polymers were measured in a high-pressure view equilibrium cell made of stainless steel (Sitec AG, Zurich). The cell volume is 500 mL and is designed for a pressure of 50 MPa and temperature of 150 °C. The pressure inside the cell was measured by an electronic pressure gauge (WIKA Alexander Wiegand GmbH & Co. KG, Alexander-Wiegand-Straße, Klingenberg, Germany). The temperature of the cell was kept constant using a heating jacket and was observed using calibrated thermocouple immersed in the cell. The uncertainty of the pressure was 0.01MPa and the total uncertainty of the temperature was 0.1 °C.

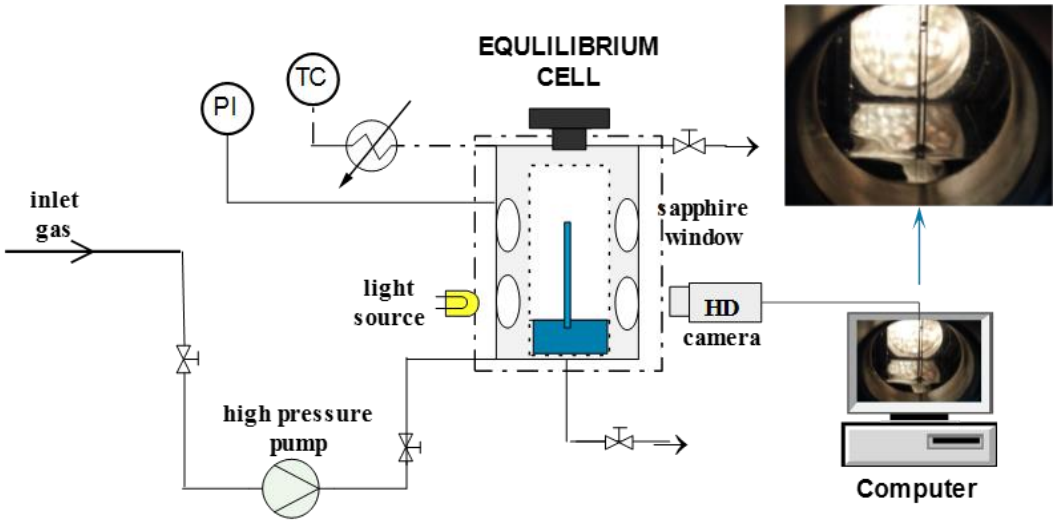

Figure 2-7: A scheme for measuring the equilibrium heights by capillary rise (CR) method in a high-pressure equilibrium view cell.

2.2.2.6 Capillary rise method

The capillary rise technique is a well-established technique used to measure surface (interface) tension. When a glass capillary tube with known inner diameter is immersed in a wetting liquid, the liquid rises due to the action of surface tension forces (Figure 2-8). Equilibrium height (h) occurs when the force of gravity on the volume of liquid ($\rho \cdot h \cdot (\Pi r^2) \Delta g$)) balances the force due to surface tension ($\gamma(2\Pi r)$). Since some of the liquid remains above the meniscus (the surface is not flat), equilibrium height h should be replaced with correlation ($h+r/3$) that results in well-known equation for surface tension:

$$\gamma = \frac{1}{2} \cdot r \cdot g \cdot \left(h + \frac{r}{3} \right) \cdot \left(\rho_{p/CO_2} - \rho_{CO_2} \right) \tag{2.16}$$

where r is the radius of the applied capillary, $\Delta\rho$ is the is the difference in density of the interfacing components (gas-saturated liquid in equilibrium with the CO_2 phase), g = 9.8 m/s2 is the acceleration due to the gravity and since it is experimentally evident that liquid fully wets the glass of capillary tube, the contact angle is assumed to be zero if $\theta < 8°$. Two different sizes of capillaries were placed vertically inside the measuring cell on a stillness holder. One was with a radius of 0.1500 mm and other with a radius 0.4780 mm. First, equilibrium height was determined of a water rise inside a capillary at ambient and also at elevated pressure, followed by the determination of equilibrium height of the melted polymer rise under the pressure of CO_2 and argon. While equilibrium height of a water rise inside a capillary, was reached approximately in 5 min, equilibrium height of the melted polymers needed more time: approx. 30 min due to the higher viscosity of the system. However, with increasing pressure due to

viscosity reduction of polymers, lower time was needed to establish equilibrium inside a capillary.

Second, the capillary rise method was validated by measuring surface tension at the CO_2 + water interface within a pressure range from 0.1 MPa to 20 MPa at a constant temperature 318.25 K. The obtained experimental results were compared to the data available in the literature. At least three measurements were performed at a certain pressure and temperature, and the relative standard deviation between the experimental data and the literature data ranged below 5 %.

The main difficulties of the method lie in determining the uniform capillary diameter and ensuring system cleanliness [113]. However, recent progress in the manufacturing of glass tube and laser techniques allow knowledge of the capillary diameter up to a high precision ($\mp$ 0.001 mm). In our research, the radii of capillaries, at both ends, were determined by a laser coordinate measuring Machine Zeiss, UMC Zeiss UMC 850 located at the Laboratory for Production Measurement, Faculty of Mechanical Engineering, University of Maribor (UM-FS/LTM) [114].

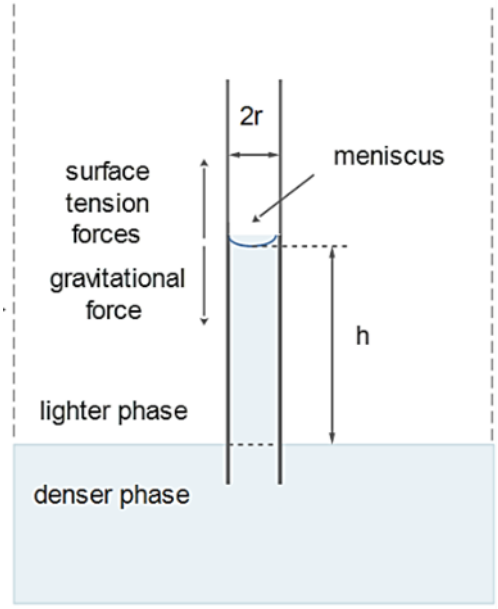

Figure 2-8: Equilibrium height (*h*) occurs when the force of gravity on the volume of liquid balances the force due to surface tension.

2.2.2.7 Design of porous polymeric scaffolds by gas foaming of Brij52

Approximately 1 g of polymer was placed in a high-pressure optical cell (Sitec AG) and saturated with supercritical CO_2 at preliminary determined pressure and temperature, 15 MPa and 60 °C for 6 hours. As determined experimentally, this period of time is required to reach equilibrium. Saturated solution was later released through the valve with a depressurization rate of 1 bar/s. When foaming was completed, the vessel was opened and foam was stored at 25 °C before being subjected to further analyses.

Low interfacial tension is desired in the polymer foaming processes due to the increase of the nucleation rate and production of small and uniform cells. By adding gas into the polymer, nucleation rate can be controlled by parameters like pressure (P) and temperature (T). According to classical nucleation theory nucleation rate (N) is defined

$$N = Sf exp\left[\frac{16\pi\gamma^3}{3kT\Delta P^2}\right] \tag{2.18}$$

where f is the frequency of gas molecules joining the nucleus, S is gas concentration, γ is an interfacial tension between polymer phase and nucleation bubble phase, T is temperature and ΔP is pressure difference across the polymer-gas interface [115]. Another field requiring knowledge of predicting interfacial properties between polymers and supercritical fluids involves particle formation.

2.2.2.8 PGSS™ process

The PGSS™ process, first introduced by Weidner et al. [116], was used for the formulation of three drugs, nimodipine, fenofibrate, and o-vanillin, into two carrier materials (Brij100 and PEG 4000) by using the inert gas CO_2. Experiments were performed at four different pressures (10, 15, 20, 25 MPa) and a constant temperature of 60 °C, with an exception for one experiment at 45 °C. The mass ratio between drug and carrier material was 0.10 and 0.20, respectively.

A high-pressure reactor (IPIM, Croatia) with a volume of 130 ml was filled with a mixture of active substance and carrier material. The reactor, capable of operating at 30 MPa and 200°C, was heated with an electronic heating jacket (Melter, Slovenia, HSN 260/10 M250 to the desired temperature. After the mixture reached its melting point, CO_2 was introduced by a liquid high-pressure pump (NWA PM 101) and the content saturated for 1 hour by mixing in order to establish equilibrium. The gas-saturated solution was then expanded through a nozzle with a diameter of 1 mm and spraying angle 60° into a spray tower with a volume of 50 L or 200 L. During rapid gas expansion, fine particles were formed as a result of the strong reduction of temperature as a consequence of the Joule-Thomson effect. The pressure was monitored using a Nova Fima EN837-1manometer. The scheme of batch PGSS™ process is presented in Figure 2-9.

In process of breaking up a liquid into a spray of fine droplets, which is commonly termed as an atomization process; several factors influence particle size and morphology beside the thermodynamics. These factors include numerous types of atomizers using high-pressure air or steam for effecting micronization, different nozzles, and their performance.

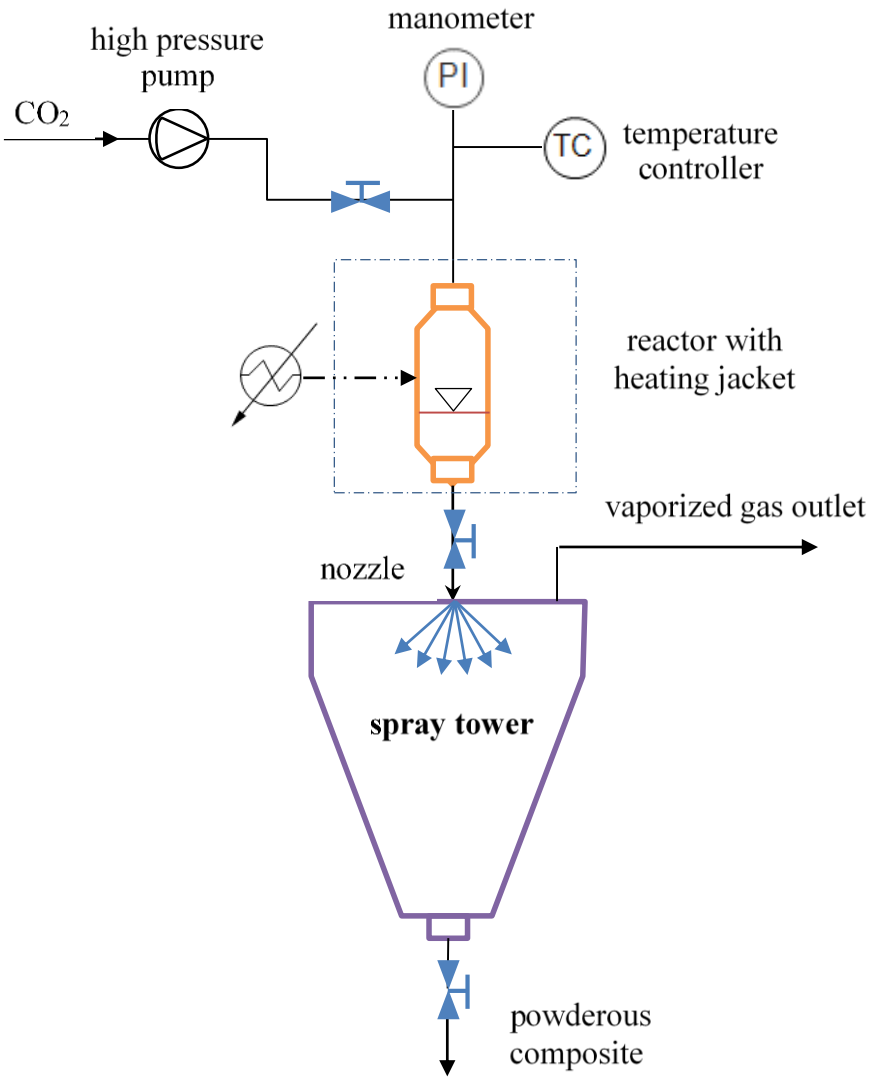

Figure 2-9: Scheme of a batch PGSS™ process [76].

2.2.3 Methods for characterization of precipitated powder

For the analysis of obtained microparticles and foam, Cilas particle distribution analyses, Environmental Scanning Electron Microscopy (ESEM) and Liquid Chromatography/Mass Spectroscopy (LC/MS) have been applied. Dissolution studies of formulating particles have been carried out at Dissolution apparatus Agilent 708-DS.

2.2.3.1 Yield of collected particles

The yield of particles precipitated by the PGSS^{TM} process was calculated using equation 1, where the number of particles obtained after micronization (m_2) was divided by the amount of mass initially introduced into the high-pressure reactor (m_1).

$$Yield(\%) = \frac{m_2}{m_1} \cdot 100 \qquad (2.19)$$

2.2.3.2 Particle size distribution

The mean particle size and size distribution of the precipitated product were measured using a CILAS 1090 diffraction laser particle size analyzer in dry dispersion mode. With two lasers permanently mounted on a short optical bench, it can analyze particles ranging in size from 0.2 to 500 µm in a single measurement with reproducibility of better than 1%. The CILAS 1090 is designed to comply with the ISO 13320 standard for measurement accuracy and repeatability.

2.2.3.3 Particle morphology analyses by ESEM

Precipitated samples were observed at a low vacuum by Environmental Scanning Electron Microscopy (ESEM) Quanta 200 3D (FEI Company, Hillsboro, OR) that allows observation of translation and non-sample without prior preparation (polymer materials, biological and medical samples).

2.2.3.4 Particle morphology analyses by ESEM

Precipitated samples were observed at a low vacuum by Environmental Scanning Electron Microscopy (ESEM) Quanta 200 3D (FEI Company, Hillsboro, OR) that allows observation of translation and non-sample without prior preparation (polymer materials, biological and medical samples).

Figure 2-10: Environmental Scanning Electron Microscopy (ESEM).

2.2.3.5 Loading efficiency of drugs

Loading efficiency of drugs in Brij100 and PEG 4000 was determined by liquid chromatography-mass spectrometry (LC-MS/MS). The LC-MS/MS was used to detect the possible degradation products of the active drug during PGSS^{TM} formulation.

An Agilent 1200 HPLC system, equipped with a quaternary pump (maximum pressure of 400 bar), an autosampler, and a column thermostat (maximum 80 °C), in tandem with an Agilent 6460 Triple quadrupole MS system with JetStream technology ionization source, was used for analysis of the investigated drugs. The apparatus was controlled by Agilent MassHunter Workstation software version 6.0, by which the qualification and quantification of the investigated drugs were performed. Samples dissolved in organic solvents were filtered through 0.2 μm syringe filter and injected (volume of 5 μL) onto an analytical column (Agilent Eclipse Plus, 50 mm x 2.1 mm i.d., 1.8 μm particle size). The column was maintained at 35°C. The separation was achieved with a 5 min isocratic run with flow rate 0.2 mL/min of the mobile phase. Detailed data for each analysis are shown in Table 2-3. The MS acquisition method applied the following parameters: 3500 V capillary voltage, 500 V nozzle voltage, a sheath gas flow of 11 L/min of nitrogen, at a temperature of 250 °C, a drying gas flow of 5 L/min at a temperature of 300 °C, nebulizer gas flow at 45 psi, and Q1 and Q3 (Q stands for quadrupole) set to a unit resolution of 0.7 full width at half maximum (FWHM) with a dwell time of 200 ms and fragmentor at 45 V in positive mode.

Figure 2-11: LC-MS/MS.

Table 2-3: Chromatographic parameters for quantitative analysis of investigated drugs on LC-MS/MS.

	Nimodipine	**Fenofibrate**	**O - vanillin**
Solvent	Methanol	Methanol	Methanol
Mobile phase	Acetonitrile:20mmol Ammonium acetate = 65:35	Methanol:Water = 80:20	Acetonitrile: 0.1% Formic acid in water = 80:20
MRM transitions (Collision Energy)	419 ->343 (CE 4), 301 (CE 24)	361 -> 233 (CE 10), 138.8 (CE 32), 110.9 (CE 64)	167 -> 139 (CE 8), 93 (CE 16)
Calibration range (ng/mL)	55.7 – 557.0	5.1 – 505.0	4.8 – 240.1

Loading efficiency of drugs (E_{drug}) was calculated with equation 2-20:

$$E_{drug}(\%) = \frac{m(analyzer) \times K \,/\, m(weighted)}{m(drug) \,/\, m(drug) + m(carrier)} \tag{2.20}$$

Where E_{drug} is loading efficiency, expressed as mass ratio (in %) of drug loaded on the carrier, *m(analyzer)* is mass which was provided by the LC-MS analyzer based on the analysis, *K* is dilution factor, *m(weighted)* is the weighted mass for LC-MS analysis, *m*(drug) is mass of the drug (active substrate) and *m*(carrier) is mass of the carrier material.

2.2.3.6 Dissolution rate experiments

Dissolution experiments were performed using an Agilent 708-DS Dissolution apparatus configured for a 2 paddle USP apparatus with a capacity of eight 900 mL vessels. The temperature in the vessels is controlled using a water bath vessel heater. In the vessels with 900 ml of 0.1 M HCl in water, 50 mg of nimodipine and 50 mg of fenofibrate were added, respectively. Similarly, 180 mg of o-vanilla was added to 900 ml of distilled water. The temperature in the vessels was maintained at 37°C and the stirring rate of the paddles was set to 100 rpm. At the same time, four samples were tested, three encapsulated precipitated drugs and one sample for comparison of a non-processed drug. Sampling was performed manually by sampling cannulas, and 2 mL of sample was taken at given time intervals. The samples were filtrated using a 0.45 µm syringe filter before analysis on the spectrophotometer. The concentration of nimodipine, fenofibrate, and o-vanillin were determined at 335 nm, 287 nm and 265 nm, respectively.

Figure 2-12: 708-DS Dissolution apparatus.

2.3 Results and discussion

2.3.1 Preliminary studies of biodegradable polymers

Results of experimentally obtained melting points, solubility and interfacial tension on biodegradable polymeric carriers in the presence of dense gases are presented in the following subsections.

2.3.2 Melting points of polymers

The Brij S100/CO_2 binary system showed a melting point depression from 53.4°C at ambient pressure to 35.8°C at 35 MPa, with a local minimum around 10 MPa. S-L-G (solid-liquid-gas) curves have negative *dP/dT* slopes, which indicates high CO_2 solubility in the molten heavy component. Similar observations were made by Weidner et al [74] for PEG 4000, where S-L-G lines were determined by the capillary method. The results show that at a pressure higher than 1 MPa, the liquefaction temperature decreases considerably. The S-L-G curve poses a global temperature minimum of 42°C at 9.4 MPa. By comparing PEG 4000 with Brij S100 in presence of dense CO_2, it can be concluded that Brij S100 has the highest liquefaction temperature depression over the entire pressure span (figure 2). In particular, systems with a negative *dP/dT* slope and/or with a temperature minimum in S-L-G curve are desirable for PGSS^{TM} processes [31]. Another binary system investigated was Brij S100/propane, which has a positive S-L-G curve. This can be explained by the low solubility of propane in the molten heavy component. Propane molecules tend to move more slowly between polymer chains because of their much larger size (5 A) than CO_2 molecules. Trupej et al. [77] obtained melting temperatures for a PEG 4000/propane system where the S-L-G curve shows exactly the same behavior with a positive *dP/dT* slope. As in the presence of dense CO_2, Brij S100 carrier has a lower liquefaction temperature than PEG 4000 in dense propane over the entire pressure range.

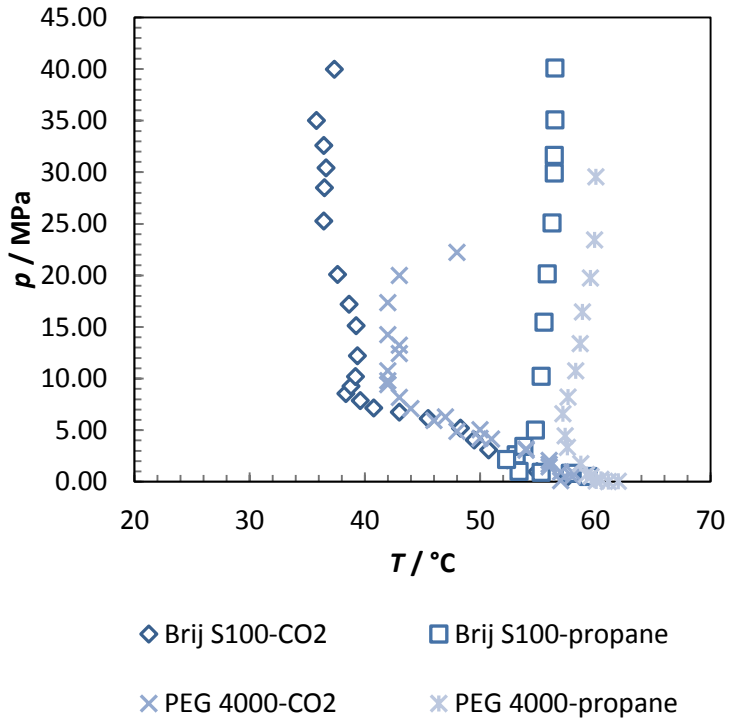

Figure 2-13: *P-T* diagram of Brij100-CO_2, Brij100-propane systems and PEG 4000-CO_2 Weidner et al. [74], and PEG 4000-propane, Trupej et al. [77] systems.

High melting temperature depression in the presence of dense CO_2 makes Brij S100 carrier suitable for the formulation of a large number of thermally instable active drugs. Also, if after precipitation the particles stay in contact with the dense gas, the high decrease of melting temperature can promote agglomeration and other variations in particle morphology [117]. To avoid agglomeration, the precipitation experiments were carried out at temperatures slightly higher than melting point.

2.3.2.1 Gas solubility in system PEG 600/CO_2, Brij 52/CO_2 and Brij 100/CO_2

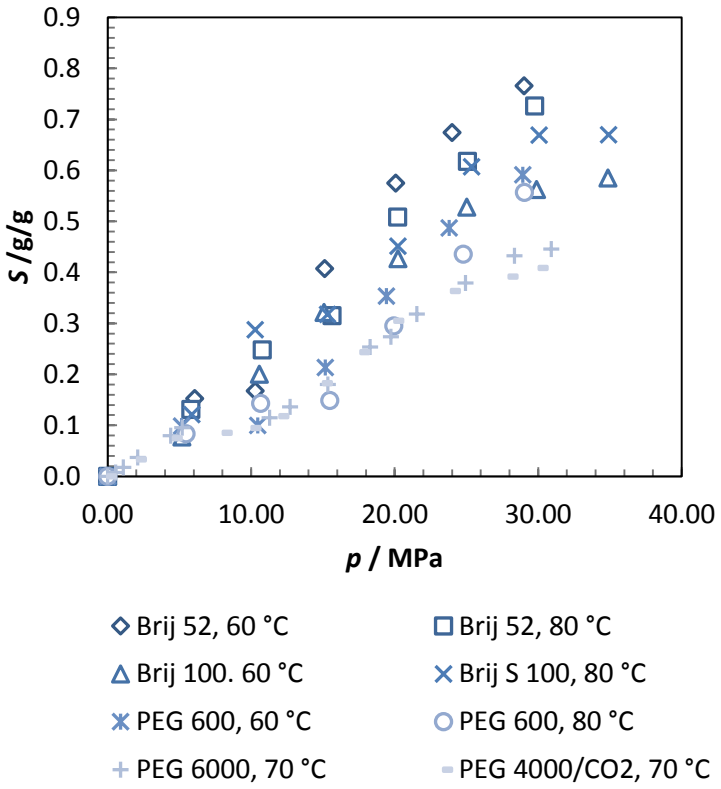

Figure 2-14: Gas solubility as a function of pressure at different temperatures for the systems Brij52/CO_2, PEG 600/CO_2, PEG 1000/CO_2 [6] and PEG 4000/CO_2 [118].

A comparison of solubility as a function of pressure at various temperatures fis shown in Figure 2-14. It can be observed that for all systems at a constant temperature solubility increases with increasing pressure. For all systems, solubility increases slowly at pressures below 12 MPa but increases significantly as the pressure rises above this value. The results show that the highest solubility of CO_2 is in a polymer melt of Brij52 in the entire range of investigated conditions. The solubility of CO_2 in PEG 600 is 0.59095 g/g and, whilst on the other hand, the solubility of CO_2 in Brij52 is for about 25 % higher, 0.76584 g/g at 29 MPa and 60 °C. Influence of temperature in both systems at lower pressures is negligible, meanwhile, at higher pressures, solubility is higher at a lower temperature. This deviation is a consequence of different temperatures and molecular weights of PEG.

$$\frac{\left|S_{\exp} - S_{lit}\right|}{S_{lit}} \tag{2.21}$$

Obtained results show that solubility of gas in the compound increases with increasing pressure due to increased density of CO_2. This effect is more noticeable at pressures above the critical point of CO_2 because the density of CO_2 increases and therefore interaction between molecules

of CO_2 and polymer is even more intense. Pressure elevation enables penetration of gas molecules between polymer chains, thereby increasing the free volume between the molecules and mobility of polymer chains and as a consequence also CO_2 absorption rate is increased. At lower pressures, absorption may be described as a process of filling the free volume between the polymer chains. At higher pressures, absorption represents a process of dissolving CO_2 in the polymer. The influence of the temperature on the solubility is more significant at higher pressures. At constant pressure, higher temperature results in lower solubility both systems. This is because increasing temperature lowers the density of CO_2 which results in a reduced intensity of dissolution of CO_2 in the polymer melt. Finally, the differences in solubility of CO_2 in PEG 600, Brij 100, and Brij 52 is certainly affected by the structure of the polymer molecules (the length and branching of the polymer molecule), which results in various interactions between the gas and the polymer [108]. Measurements were carried out for three times at the same operating conditions. The deviation of the results was about 5 %.

2.3.2.2 Diffusion coefficients for the systems PEG 600/CO2 and Brij52/CO2

A comparison of diffusion coefficient as a function of pressure at various temperatures for PEG 600/CO_2 and Brij 52/CO_2 systems is shown in Figure 2-15. At low pressures, the diffusion coefficient is higher at lower temperatures and at higher pressures; higher temperature enables higher diffusion rate, which is more visible for Brij 52/CO_2 system. For both systems, diffusion coefficient increases up to a certain maximum value at a pressure of 15 MPa and then decreases by further increase of pressure. The maximum diffusion coefficient, which has been observed at a pressure of 15 MPa and a temperature of 60 °C, is $8.0993 \cdot 10^{-4}$ cm^2/s for the system of PEG 600/CO_2 and $1.9293 \cdot 10^{-3}$ cm^2/s for Brij 52/CO_2. Deviation of diffusivity coefficients for the systems of PEG/CO_2 between the experimental results and the literature data [119] is lower than 4 % and can be explained by the differences in temperature. It was already demonstrated [8] that different values of polymer molecular weight influence only to a small extent the diffusivity coefficient.

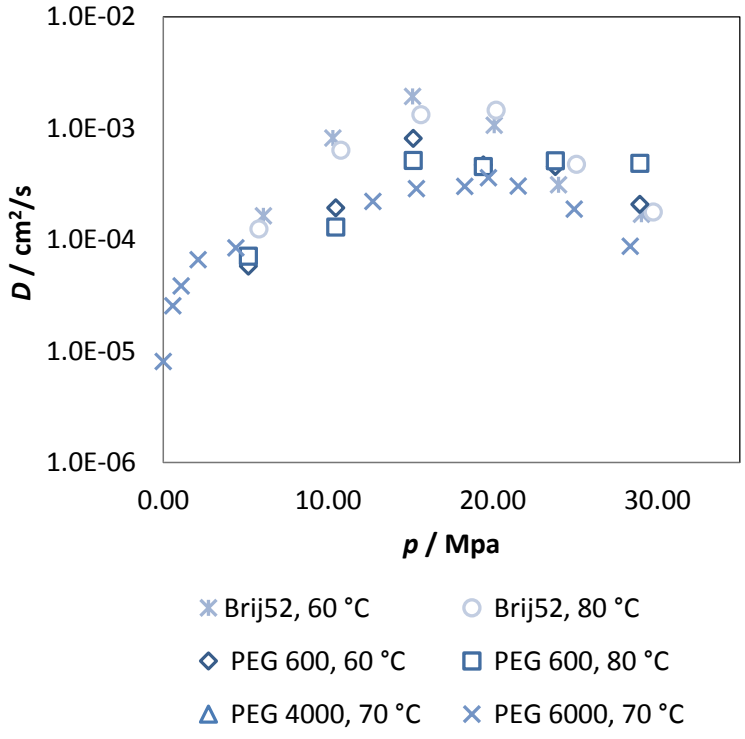

Figure 2-15: Diffusion coefficient as a function of pressure at various temperatures for the systems of Brij52/CO_2, PEG 600/CO_2, PEG 1500/CO_2 [119] and PEG 6000/CO_2 [119].

The increase of the diffusion coefficient with increasing pressure up to 15 MPa in PEG 600/CO_2 and Brij52/CO_2 system and reduction of the diffusion coefficient with further increasing of the pressure can be explained by the fact that CO_2 acts as a plasticizer and additionally by the effect of hydrostatic pressure. When a polymer absorbs CO_2, its molecules are distributed in a new equilibrium state. At lower concentrations of absorbed CO_2, which coincides with the lower pressures, the plastic effect of CO_2 causes higher mobility of the polymer chains and leads to higher diffusion coefficient. At higher concentrations of CO_2, the hydrostatic pressure plays a more important role. This pressure reduces free volume between chains of the polymer, thereby reducing the diffusion coefficient [119]. The obtained diffusion coefficients at pressures up to 15 MPa are higher at lower temperatures, meanwhile, at pressures above 15 MPa, higher diffusion coefficients are obtained at higher temperatures. This temperature effect is more explicit for the system of the Brij 52/CO_2 system. Differences are also observed between both systems concerning the dependence of the diffusion coefficient on the density of CO_2 as well as on CO_2 solubility in the polymer. Lower diffusion coefficients of CO_2 at a higher density of gas may be explained by an increase in the number of collisions between molecules of CO_2 due to their mutual proximity which prevents the movement of CO_2 molecules [68]. It has to be pointed out, that the differences in diffusion of CO_2 into the polymer as a function of pressure, density and solubility of CO_2 at different temperatures also depends on orientation of polymer chains, differences in the morphology of the polymer and the different molecular weight distribution, degree of polymer branching and on the dependence of diffusion on the quantity of previously absorbed gas. Diffusivity of CO_2 influences the bubble growth and the cell size. The narrow cell size distribution, good plasticizing ability, and high diffusivity are advantages of using supercritical CO_2 in microcellular foaming processes [64].Micronization by PGSS process is based on the formation of the particles that absorb supercritical CO_2 at high concentration. High diffusivity along with the moderate solubility in polymer combined with plasticization of the polymer provides the proper environment for guest materials to migrate into the polymer matrix to generate the active ingredient-loaded particles with reasonable loadings.

2.3.2.3 Validation of modified capillary rise method in water/CO_2 system

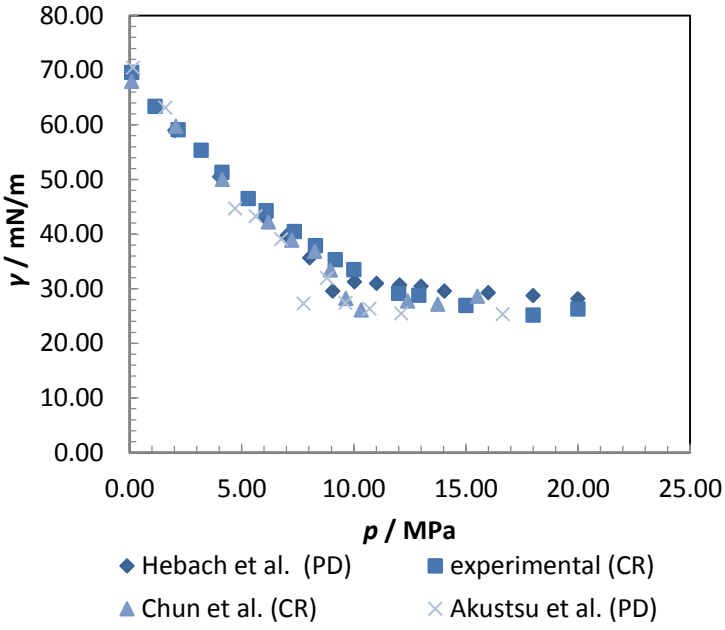

Figure 2-16: Interfacial tension at the CO_2 + water interface as a function of pressure at T=45 °C. Comparison of experimental data by capillary rise method to the literature one. Acronyms: CR- capillary rise method, PD- pendant drop.

The modified capillary rise method was validated by conducting the measurements of the interfacial tension between CO_2 and pure water at a temperature of 45 °C within a pressure range from 0.1 MPa to 20.00 MPa (Figure 2-16). The experimental data obtained by the capillary rise method was compared with the published data by Hebach et.al [120], Akustsu et.al [121] which were determined by the pendant drop (PD) method and by Chun et al. [113] which were determined by the capillary rise method. The density of the CO_2 rich phase was calculated from the NIST database [109] without correlation for a dissolved solution since it is known there is no measurable difference between the density of the CO_2- rich phase and that of pure CO_2. The accuracies of the obtained results with the ones found in the literature were better than 5 %. However, major deviations could be found around the critical point of CO_2 (7.39 MPa and 45 °C) where the densities varied strongly with small changes in pressure and temperature.

2.3.2.4 Density and interfacial tension of CO_2 saturated Brij 50, Brij 100 and PEG 600

A comparison of density and interfacial tension in dependence of pressure at 60 and 80°C up to 30 MPa for the Brij 100, Brij S50 and PEG 600 systems is shown in Figures 2-17 and 2-18. Density was measured by vibrating U-tube densitometer with an Anton Paar DMA 60 electronic control unit. measured by vibrating an Anton Paar DMA 602 U-tube densitometer with an Anton Paar DMA 60 electronic control unit. On the other hand, interfacial tension of the systems at a constant temperature decreases with increasing pressure and reaches constant values at pressures above 15 MPa. Dependence of the on interfacial tension on the temperature is relatively small. Higher temperatures at constant pressure lead to larger free energy and improve mixing of molecules across the surface area by increasing surface area and decreasing interfacial tension. The values of interfacial tension for the Brij 100/CO_2 system are approximately 50% of those of the PEG 4000/CO_2 system [122].

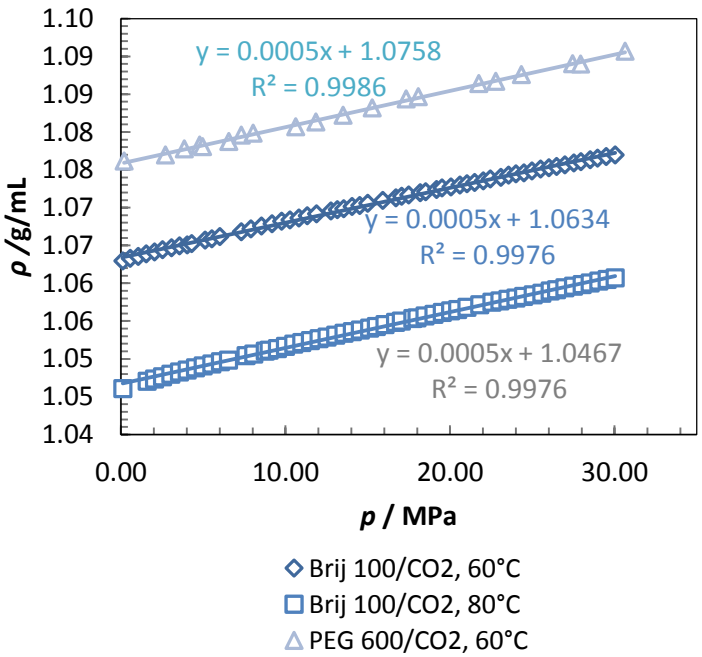

Figure 2-17: The difference in the density of CO_2 saturated biodegradable Brij 100 and PEG 600.

Because interfacial tension can be obtained from a derivative of the free energy with respect to surface area, the resulting dependence of the interfacial tension on the pressure and temperature can be explained by free energy or Helmholtz energy $E = U - TS$, where E is free energy, U is internal energy and S is entropy [35]. The internal energy U increases the segregation of molecules of CO_2 and polymer, while entropic contribution improves the mixing of molecules

of CO_2 and polymer. Higher temperatures of the polymer/CO_2 system lead to a reduction in the effective interaction between the molecules of CO_2 and polymer, consequently the internal energy decreases. The reduction in internal energy makes entropy a relatively larger contributor in the free energy and improves mixing of molecules of CO_2 and polymer across the surface area, the surface area is increased and so the interfacial tension is reduced.

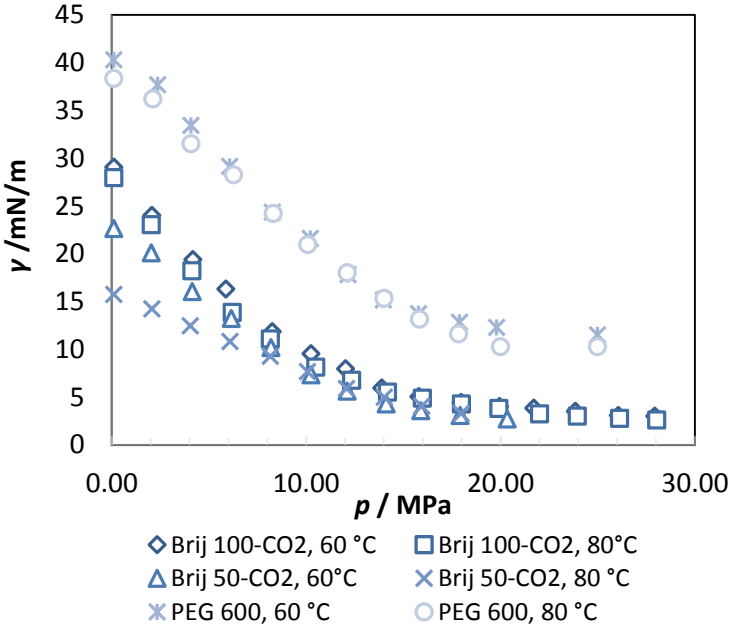

Figure 2-18: Interfacial tension dependence of pressure at 60 and 80°C temperatures up to 30 MPa for the Brij 100, Brij S50 and PEG 600 systems

This effect is especially decisive at lower pressures when the interfacial tension is smaller at a higher temperature. At higher pressures, interfacial tension is practically independent of the temperature; on the one hand, a higher temperature reduces the interfacial tension and on the other hand, higher temperatures reduce the solubility and thus increase the interfacial tension. With increasing pressure, the interfacial tension decreases due to the reduction of the difference in density between CO_2 and polymer, because the density of the CO_2 in the supercritical area approaching the density of the polymer.

2.3.2.5 The effect of molar weight of PEG on argon and CO_2 sorption

Composition and density of of CO_2 and Ar saturated solutions of polyethylene glycols of different molar mass were measured in the pressure range from 0.1 MPa up to 30.0 MPa at a constant temperature of 70 °C by magnetic suspension balance (Figure 2-19). The reasonable choice to use argon under supercritical conditions as an alternative instead of carbon dioxide in polymer processing is due to its inactivity, easy accessibility, very low thermal conductivity and also the easily accessible critical point (T_c= -122.46 °C , P_c=4.86 MPa) [123].

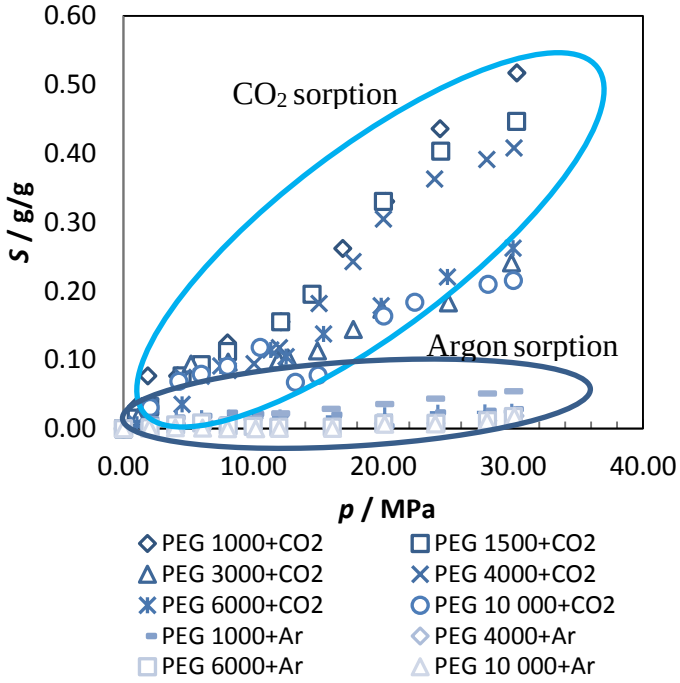

Figure 2-19: The effect of molecular weight of polyethylene glycol on carbon dioxide and argon solubility.

In Figure 2-19, it can be seen that solubility increases with increasing pressure at constant temperature and depends on the type of gas and molecular weight of the polymer. The highest gas solubility at 70 °C in pressure range up to 30 MPa was observed for the CO_2 in the lower molecular weight of polymer samples. For example, the maximum value of solubility was 0.5710 g CO_2 per g of PEG 1000 at 30.00 MPa what is approx. 10 times higher in comparison to the solubility of argon in the same molecular weight of PEG. In case of PEG 10000, maximum solubility of CO_2 is twice lower than in PEG 1000. However, CO_2 absorption in PEG 10000 at 30 MPa is still approx. 5 times higher (0.2156 g) in comparison to the maximum absorption of argon in PEG 1500 at 30 MPa (0.054 g).

One explanation for the lower solubility of argon could be in its molecular structure. In comparison to CO_2, it has no functional groups and there is no cross association between the polymer and gas. CO_2 has two lone electron pairs for interaction with polymer functional groups that result in higher gas solubility [68]. Lower solubility in PEGs was also determined for other gases like nitrogen and propane by Weidner et al. [124] and for oxygen, hydrogen, and helium by B.D Freeman et al. [125] compared to CO_2. It was found that absorption of CO_2 into polymer results in swelling and increasing of volume of polymer sample [68]. The maximum volume variation determined experimentally in our study for system PEG-CO_2 was approx. 60 % and for PEG-Ar only 10 %. In literature, volume variation of other binary systems was investigated. For example, very high volume variations were observed (up to 120 °C) in PLLA samples exposed to CO_2 [119]. Volume variation, in general, depends on solubility rate of gas in polymer and type of polymer, which results in chain rearrangement.

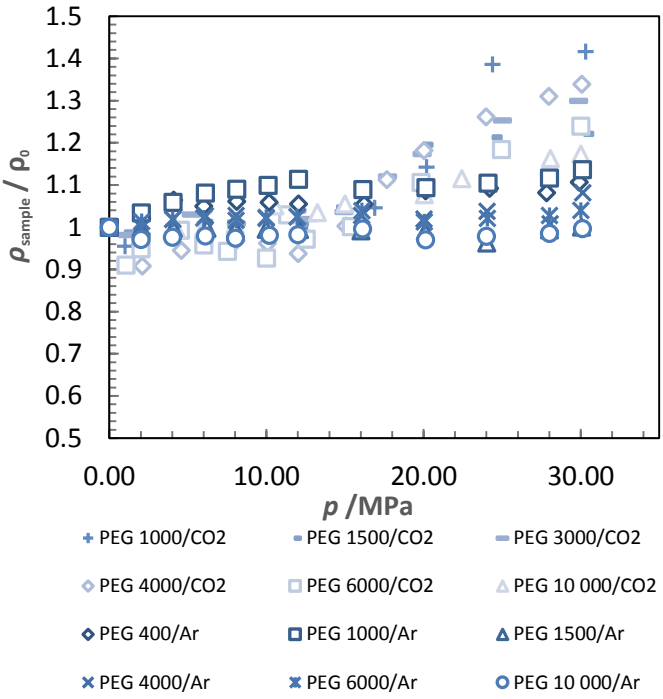

Figure 2-20: Impact of molecular weight of PEG on the densities of gas saturated polymer at 70 °C.

The effects of molecular weight on the densities of the sample in contact with CO_2 and argon is shown in Figure 2-20. The obtained results are presented as a ratio between sample density and the density within the vacuum. Similar as reported in the previous study of the CO_2 + PEG system [79] the density of sample increased with increasing pressure for all of the studied systems, but the impact of molecular weight was almost negligible. In our study, CO_2 saturated PEG 1000 with the lowest molecular weight had the in highest density of the sample. For example, the density of system CO_2 + PEG 1000 rose from 1.1421 g/mL at 0.00 MPa up to 1.6175 g/mL at 30.00 MPa. This can be explained by the low molecular masses of PEGs that have matrixes with more empty spaces and can accept more gas molecules. Similar findings have been obtained when investigating the impact of molecular weight on the densities of argon saturated solutions of polyethylene glycols. However, the densities of those samples in contact with argon showed lower values of density rise in comparison with the samples in contact with CO_2. This is related to different absorption of CO_2 and argon into the polymer [45].

2.3.2.6 The effect of molecular weight on interface between PEG melts and dense gas

The interfacial tension of PEG's melts in contact with CO_2 and argon at temperatures from 318 up to 343 K and pressures up to 30.00 MPa was studied by the capillary rise method, as well as the solubility of CO_2 and Ar (Appendix A1-12 and A1-13).

Interfacial tensions for all molecular weights of PEG's melts at constant temperature was strongly affected by pressure increases when adding CO_2 and argon (Figure 2-21). It was observed for both systems that pressure had a stronger effect in the range below 10.00 MPa. For example, interfacial tension between PEG 6000 and CO_2 decreased within the pressure range from atmospheric up to 10 MPa from 44.88 mN/m to 18.01 mN/m and ended at a pressure of 30.00 MPa at a value of 12.09 mN/m. In the case of argon saturated solutions of PEGs, the effect of pressure on interfacial tension was less pronounced and resulted in 3 times higher values at pressure 30.00 MPa in comparison to CO_2 saturated solutions of PEGs. The discrepancies between both systems can be explained by the solubility of the gases.

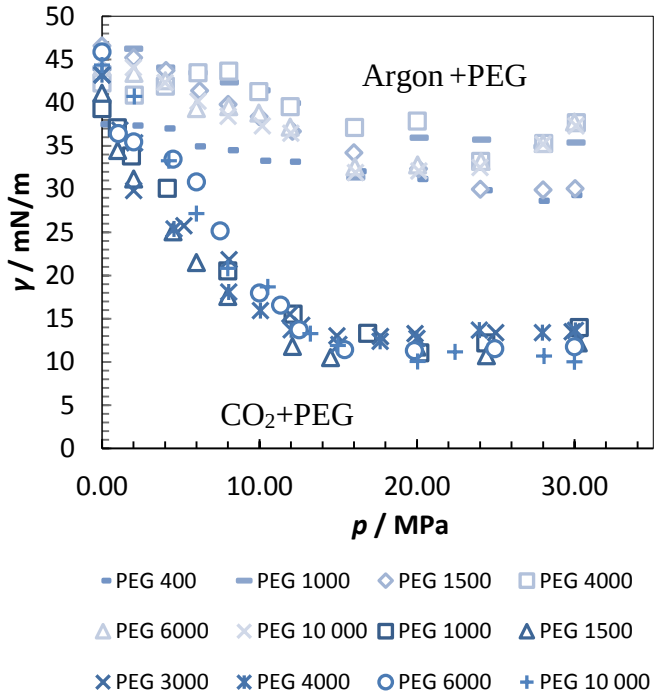

Figure 2-21: Influence of pressure and molecular weight on the interfacial tension between PEG melts and CO_2 within a pressure range from atmospheric pressure up to 30.00 MPa at 70 °C.

2.3.2.7 Density, interfacial tension, and viscosity of PEG 6000 and supercritical CO_2

Investigation of thermodynamic properties of binary systems biodegradable polymer/CO_2 is a topic under an intense research. Kappler et al. [126] developed a regression function (F) that can provide a certain type of PEG 6000 particle morphology as follows:

$$F = 6.9 \cdot 10^{-11} \cdot \frac{T[K]^{4.247}}{p[bar]^{0.403} \cdot GTP^{0.105}} \qquad (2.21)$$

where T is processing temperature, p is processing pressure and GTP is gas to product ratio (CO_2 mass flow/polymer mass flow). Relative deviation of results obtained was 14 %, at a temperature range of $323 < T < 383$ and pressure range of $5\ bar < p < 350\ bar$. Different particle shapes are formed, shapes are formed, depending on the processing conditions applied. In our study, a PEG 6000/CO_2 system was used as a model in order to investigate the basic thermodynamic and transport data including density, viscosity, and interfacial tension of a CO_2 saturated PEG 6000 solution; our will provide better insights for the design of a particle formation process.

Density, viscosity, interfacial tension of CO_2 saturated PEG 6000 solution were determined at four temperatures: 60 °C, 70 °C, 80 °C and 90 °C in the pressure range from ambient pressure up to 35 MPa. Additionally, particle size and particle morphology (obtained by PGSS^{TM}) were correlated for the first time with the interfacial tension and viscosity of a PEG 6000 CO_2 saturated solution.

2.3.2.7.1 Density of CO_2 saturated PEG 6000 solution

To ensure the reliability of the measurements, the density of pure carbon dioxide was determined beforehand at different temperatures and compared with NIST values [109]. The deviation was about 2 % over the entire pressure range from 5 MPa up to 20 MPa. Density for all observed systems increases linearly with increasing pressure as a consequence of liquid compression and low gas solubility in the polymer matrix [127]. Oppositely, density is significantly reduced with the increasing temperature at isobaric conditions. To illustrate the dependence of pressure and temperature on the density, a three-dimensional plot is presented in Figure 2-22. A polynomic function was used to describe the trend with more than 95 % confidence bounds at the temperature range of 50 °C < T < 90 °C and pressure range of 5 MPa < p < 35 MPa (equation 2.22). Aforementioned constants of a simple polynomic function for calculating of density CO_2 saturated PEG 6000 solution are shown in Table 2-4.

$$\rho\left[g/ml\right] = a + b \cdot T + c \cdot p + d \cdot T^2 + e \cdot T \cdot p \qquad (2.22)$$

Table 2-4: Constants a polynomic function for density calculations, R^2 of a function is 0.9838.

a	b	c	d	e
1.09	$-6.78\ 10^{-3}$	$4.96 \cdot 10^{-3}$	$4.66 \cdot 10^{-4}$	$7.49 \cdot 10^{-4}$

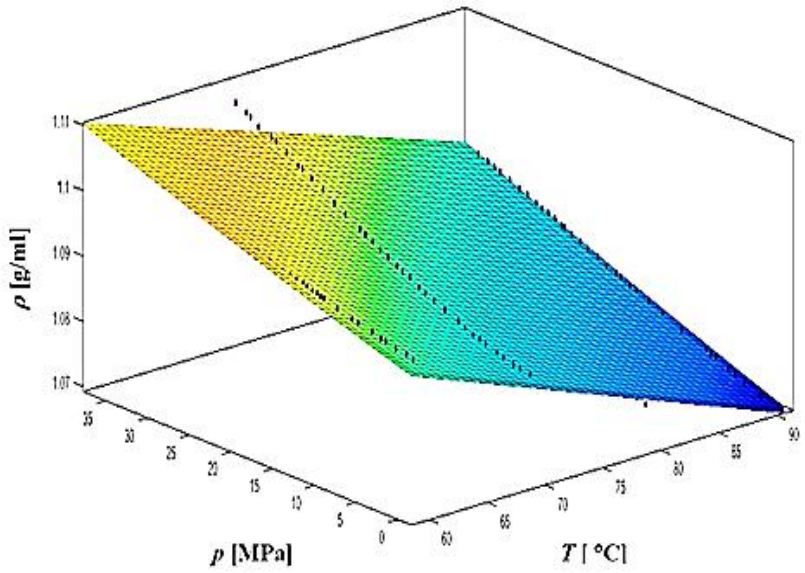

Figure 2-22: Denisty of CO_2 saturated PEG 6000 as a function of temperature and pressure.

The results obtained by the vibrating U-tube densitometer show patterns that are consistent measurements of densities by the external balance method [79] and by other gravimetrical methods involving a magnetic suspension balance. Additionally, densities obtained in our study fit closely to those of recently published by Avelino et al. [128] and by Gourgouillion [129]. The difference in results could be due to the different method used for density measurements.

2.3.2.7.2 Interfacial tension of CO_2 saturated PEG 6000 solution

Calculation of interfacial tension using experimental data obtained by the capillary rise method requires previous data on the density of CO_2 saturated PEG 6000 and the density of pure CO_2. It can be seen that pressure has a significant effect on interfacial tension reduction, on the other hand, the temperature effect is minimal. Interfacial tension is reduced by elevated pressure. For instance, at a constant temperature of 80 °C, interfacial tension decreases from 21.28 mN/m at 4.2 MPa to 3.46 mN/m at 30 MPa. This could be a consequence of CO_2 solubility in the polymer matrix as pressure increases. At lower pressures, the decrease was sharper, and the opposite was observed at higher pressures (p>10 MPa); the interfacial tension decrease became slower and finally vanished and inclined asymptotically to a constant value (p>15 MPa).

The interfacial tension values presented are in good agreement with those of Harrison et al [130], measured by the pendant drop method. To illustrate the dependence of pressure and temperature on interfacial tension, a three-dimensional plot is presented in Figure 2-23. A polynomic function (equation 2.23) was used to describe the trend with more than 95 % confidence bounds at the temperature range of 50 °C < T < 90 °C and pressure range of 0.5 MPa < p < 35 MPa. The aforementioned constants for calculating the interfacial tension CO_2 saturated PEG 6000 solution by a polynomic function are shown in Table 2-5.

$$ITF\left[mN/m\right] = a - b \cdot T - c \cdot p + d \cdot T \cdot p + e \cdot p^2 + f \cdot T \cdot p^2 \qquad (2.23)$$

Table 2-5: Constants for interfacial tension of calculations, R^2 of a function is 0.997.

a	b	c	d	e	f
64.77	$-9.627 \cdot 10^{-2}$	-0.3067	$8.56 \cdot 10^{-5}$	$9.57 \cdot 10^{-4}$	$4.941 \cdot 10^{-8}$

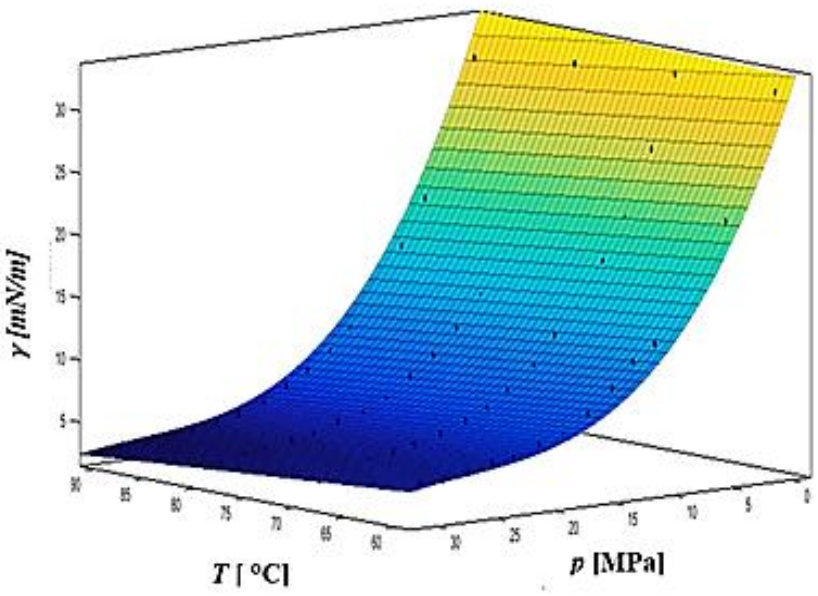

Figure 2-23: Interfacial tension of CO_2 saturated solution of PEG 6000 as a function of temperature and pressure.

2.3.2.7.3 Viscosity of CO_2 saturated PEG 6000 solution

Viscosity measurements were conducted at four temperatures: 60 °C, 70 °C, 80 °C and 90 °C at a pressure range from 10 MPa up to 35 MPa for PEG 6000 in carbon dioxide. After PEG 6000 is saturated with CO_2 at 90 °C, its viscosity decreases from 652 mPas at atmospheric pressure to 2.24 mPas mPas at 20 MPa. Further addition of CO_2 and increasing pressure result in even lower viscosity. As expected, the highest viscosity reduction was reached at the highest investigated pressure and temperature; at 35 MPa and 90 °C the viscosity of the system, PEG 1,500/CO_2 is only 0.995 mPas. Temperature variation has a significant effect on viscosity. With increasing temperature, a rapid reduction in viscosity can be achieved. However, that is not an optimal choice for viscosity reduction since it leads to polymer degradation. The highest viscosity reduction was achieved at the lowest temperatures.

To illustrate the dependence of pressure and temperature on viscosity, a three-dimensional plot is presented in Figure 2-24. A polynomic function (equation 9) was used to describe the trend with more than 95 % confidence bounds at the temperature range of 50 °C < T < 90 °C and pressure range of 0.5 MPa < p < 35 MPa. The above-mentioned constants for calculating the viscosity CO_2 saturated PEG 6000 solution with a polynomic function are shown in Table 2-6.

$$viscosity[mPas] = a + b \cdot T + c \cdot p + d \cdot T \cdot p + e \cdot p^2 \qquad (2.24)$$

Table 2-6: Constants of a polynomic function for viscosity calculations, R^2 of a function is 0.9877.

a	**b**	**c**	**d**	**e**
12.62	$2.78 \cdot 10^{-2}$	$7.5 \cdot 10^{-3}$	$5.08 \cdot 10^{-6}$	$3.48 \cdot 10^{-6}$

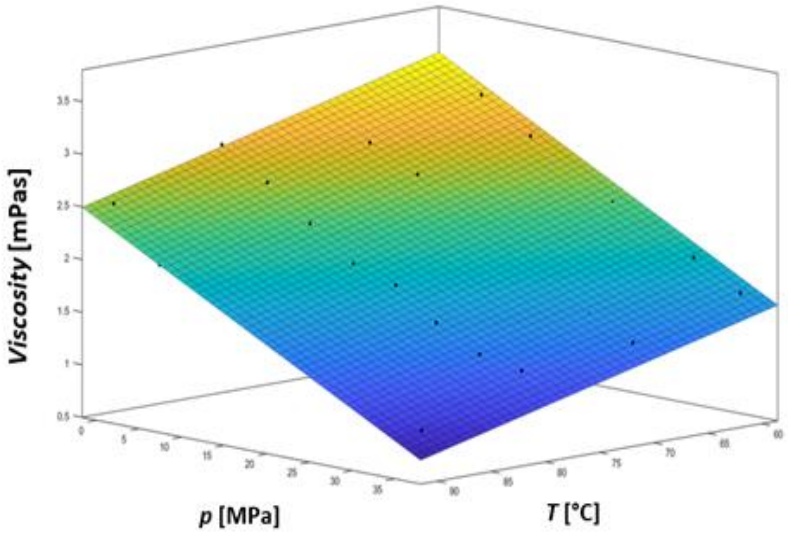

Figure 2-24: Viscosity of a CO_2 saturated solution of PEG 6000 as a function of temperature and pressure.

These data provide a good comparison with our previously published results after testing a PEG/CO_2 system of different molecular weight at 70 °C using the same method [79]. The high-pressure method is considered as rigorous, but there are still problems relating to accuracy. The mixing rate deviated to a small extent and as in several other methods, accurate viscosity measurements and the prevention of gas leakage are still major challenges.

2.3.2.7.4 Interfacial tension and viscosity at different spraying pressure and temperature

Figure 2-25 presents the interfacial tension of CO_2 saturated PEG 6000 solution at different spraying pressure and temperature conditions. It can be seen that interfacial tension is significantly low, varying from 13.43 mN/m at 10 MPa down to 5.02 mN/m at 25 MPa. The interfacial tension of a CO_2 saturated PEG 6000 solution is reduced to 37% with a pressure change from 10 MPa up to 35 MPa at a constant temperature of 60 °C. Effect of a temperature on interfacial tension is minor. On the other hand, the pre-expansion temperature has a strong influence on morphology [39]. Spheres are formed at high pre-expansion temperatures and at lower mixing pre-expansion pressures. When obtaining micro-foams, at lower temperatures around 70 °C the pressure range is much larger. Particle size is reduced when the temperature is decreased and pressure is increased [131]. That indicates that higher interfacial tension boosts the formation of smaller particle droplets after spraying through the nozzle.

Compared to interfacial tension, the pre-expansion temperature has a great effect on viscosity, as it does for particle morphology and size. Figure 2-26 presents the viscosity of CO_2 saturated PEG 6000 solution at different spraying pressure and temperature conditions. Viscosity is significantly low, varying from 2.8 mPas at 10 MPa down to 2.0 mPas. Additionally, when the pre-expansion temperature is increased, viscosity decreases even more. Spheres are formed under pressure and temperature conditions that are related to the highest viscosity of the system. As the viscosity is reduced particles of smaller mean size are expected. Like interfacial tension and viscosity, the density of CO_2 saturated PEG 6000 solution is also reduced when the pre-expansion temperature is increased.

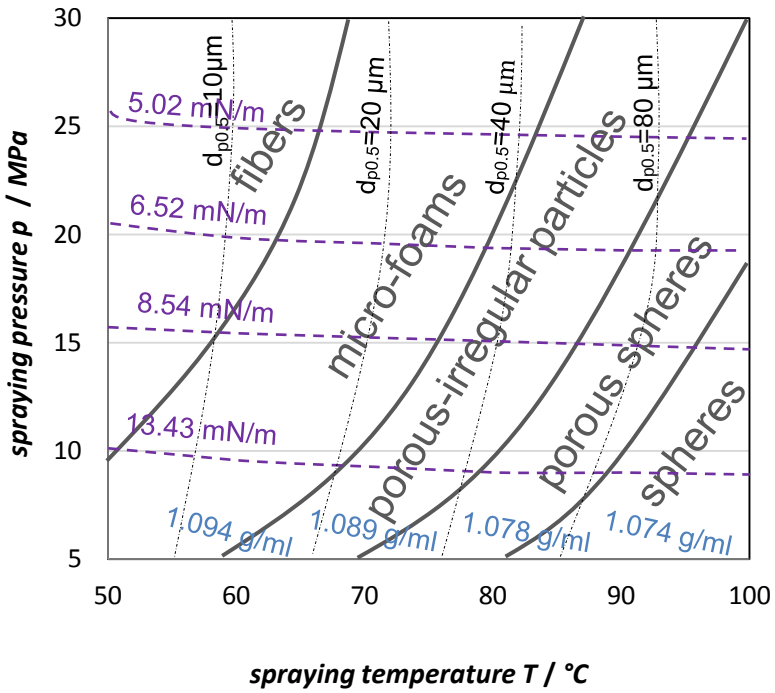

Figure 2-25: Influence of interfacial tension of CO_2 saturated PEG 6000 solution at different spraying pressure and temperature on particle shape and size, GTP (Gas to Product) =1.

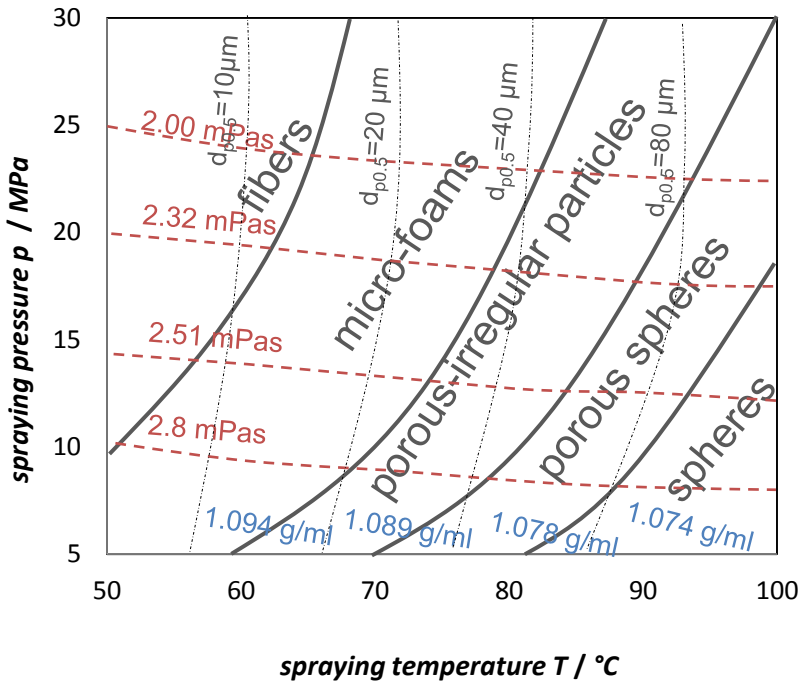

Figure 2-26: Influence of viscosity of CO_2 saturated PEG 6000 solution at different spraying pressure and temperature on particle shape and size, GTP (Gas to Product) =1.

2.3.3 Precipitated product

The second part of this chapter presents particle precipitation and loading efficiency of fenofibrate, nimodipine o-vanillin and esomeprazole with biodegradable Brij 100, Brij 52 and PEG 4000, In the case of Brij 100 and PEG 4000 the influence of the main process parameters (pressure, temperature and active substance/carrier ratio) on the precipitated yield, the particle size distribution, loading efficiency, and dissolution rates have been invesitgated
On the other hand, micronization of Brij52 without/with esomeprazole as the active compound has been carried out at process conditions (15 MPa and 60 °C), where the highest diffusion coefficients and CO_2 solubility in the polymer were measured. The microcellular foam Brij 52 was created with a supercritical CO_2.

2.3.3.1 Yield and mean particle size analysis

As shown in Table 2-7, the yield of collected particles in the particle collector vessel was between 15 % and 83 %. The decrease in average yield in the experiments was a result of discontinuous operation procedure, where a fraction of the initial drug/polymeric carrier mixture remained in the reactor and/or on the walls of the spraying tower. A higher yield of collected particles was obtained at higher pressures as a result of the viscosity reduction of the mixture and higher CO_2 saturation.

Table 2-4: Yield of collected particles after micronization with discontinuous PGGS^{TM} process at 60 °C.

		Yield of collected particles (%)			
Pressure (MPa)	**Drug/Polymeric carrier mass ratio**	**Nimodipine/Brij S100**	**Fenofibrate/Brij S100**	**Vanillin/Brij S100**	**Vanillin/PEG 4000**
10	0.10	54.62	56.56	15.71	16.16
10	0.20	26.44	43.08	19.85	/
15	0.10	54.24	19.63	39.87	66.85
15	0.20	48.31	31.19	54.37	/
20	0.10	41.96	77.61	54.33	83.87
20	0.20	65.62	77.61	22.32	/
25	0.10	43.78	78.48	76.78	73.88
25	0.20	75.73	69.35	34.93	/

The mean particle size of precipitated mixtures of drug/carrier is presented in Table 2-6. Hydrophilic carriers Brij S100 and PEG 4000 were added to nimodipine, fenofibrate, and o-vanillin to avoid agglomeration of micronized particles and thermal degradation. With increasing pre-expansion pressure, the mean particle size of nimodipine/Brij S100, vanillin/Brij S100, and vanillin/PEG 4000 decreased. This can be explained by a shorter solid-liquid equilibrium condition time after spraying when pressure is increased [132]. The melted droplet mixture becomes solid after spraying because of the Joules-Thomson effect, and lower pressures resulted in a coalescence phenomenon causing larger mean particle size. In a mixture of fenofibrate/Bij S100, anticipated effective surface areas were probably slightly reduced with pressure because of agglomeration and resulted in increased mean particle size of precipitated particles. The influence of drug/carrier ratio on particle size distribution was investigated in a nimodipine/Brij S100 system. The mean particle size at pressures higher than 15 MPa increased with increasing drug/carrier ratio. For example, at a pressure of 20 MPa, mean particle size decreased from 61.28 μm at 0.20 drug/carrier ratio and up to 47.92 μm at 0.1 drug/carrier ratio.This can probably be explained by the fact that the viscosity of Brij S100 carrier depends on the amount of nimodipine dissolved within it. The effect of temperature was investigated in the o-vanillin/PEG 4000 system. After the temperature increased from 45 °C to 60 °C at 15 MPa, particle size increased from 41.45 to 59.5 μm.

Table 2-5: Mean particle size (μm) after PGGS^{TM} process at 60 °C.

		Mean particle size (μm)			
Pressure (MPa)	**Drug/Polymeric carrier mass ratio**	**Nimodipin/Brij S100**	**Fenofibrat/Brij S100**	**Vanillin/Brij S100**	**Vanillin/PEG 4000**
10	0.10	51.54	69.99	35.93	69.99
10	0.20	59.94	/	/	/
15	0.10	51.51	60.06	59.5	60.06
15	0.20	61.28	/	/	/
20	0.10	47.92	47.62	61.79	47.62
20	0.20	54.97	/	/	/
25	0.10	45.51	70.56	50.89	45.56
25	0.20	48.63	/	/	/

2.3.3.2 Particle morphology

Figure 2-27 shows ESEM micrographs of particles of nimodipine/Brij S100, o-vanillin/Brij S100 and fenofibrate/Brij S100 processed by PGSS^{TM} at 15 MPa and 60 °C. The morphology of obtained particles was irregular and according to the ESEM pictures, it can be assumed that the particles are porous. The spherical parts appearing in the nimodipine/Brij S100 system could be obtained as a result of the simultaneously occurring evaporation of CO_2 from the melt upon gas expansion. It can be observed that in the case of fenofibrate/Brij S100, some agglomerates are formed because fenofibrate binds particles together via capillary forces.

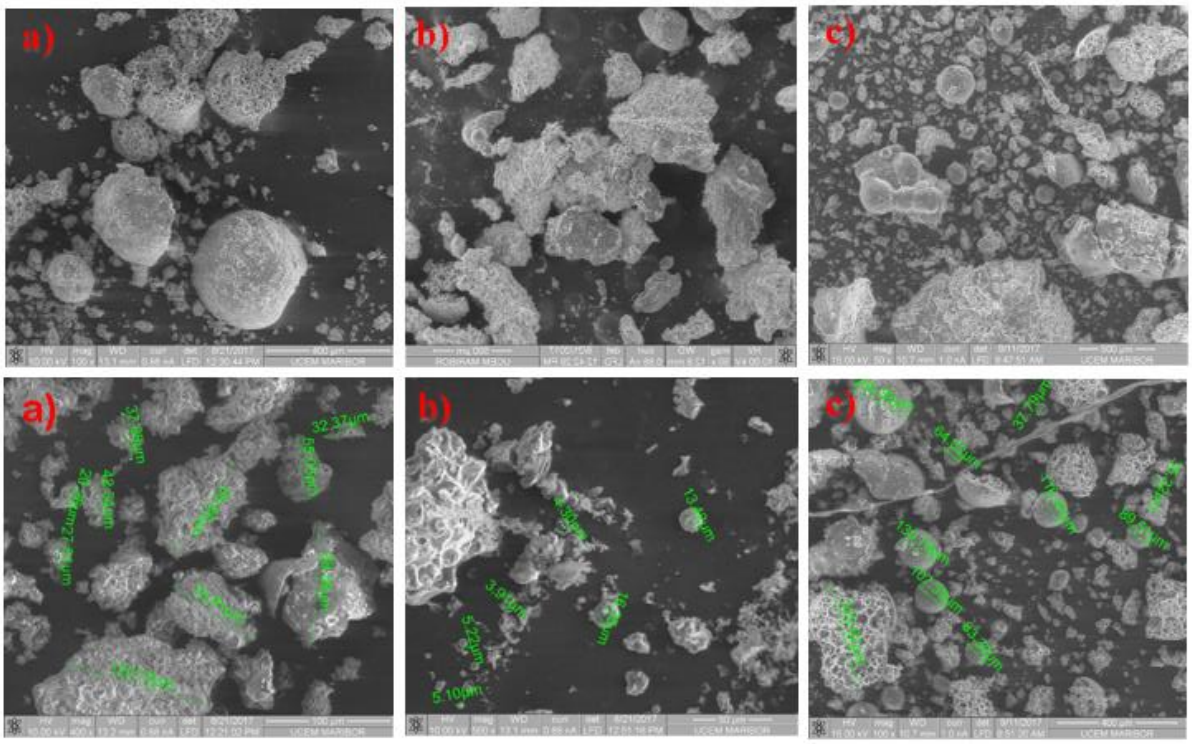

Figure 2-27: ESEM micrographs of composite particles: a) nimodipine/Brij S100, b) o-vanillin/Brij S100 and c) fenofibrate/Brij S100 processed by PGSS^{TM} at 15 MPa and 60°C.

2.3.3.3 Loading efficiency of drugs

The loading efficiency of drugs in carriers observed by PGSS^{TM} was high in all experiments, ranging up to 99 % (Table 2-9 and Figure 2-28). A small proportion of an average decrease of loading efficiency with pressure may have been caused by the increased solubility of nimodipine, fenofibrate, and o-vanillin in supercritical CO_2, where part of the drug was carried away with the CO_2 gas during depressurization.

It was observed for all systems that at lower pressure, loading efficiency was larger than at higher pressures. At higher pressures, more CO_2 is dissolved in the liquid phase, which causes better atomization into smaller droplets, resulting in less of the drug being encapsulated [94]. Loading efficiency varies significantly with changing drug/carrier ratio, despite the fact it was expected that by increasing drug to carrier ratio, loading efficiency would be higher. After increasing nimodipine/Brij S100 ratio at 10 MPa from 2 g to 4 g of nimodipine in 20 g of Brij S100, loading efficiency after particle precipitation decreases from 98.82 % to 79.42 %. On the other hand, at 15 MPa with an increasing nimodipine/Brij S100 ratio, the loading efficiency was increased from 89.90 % to 95.06 %. Similar variations were also observed in other systems. As can be seen in Table 2-9, loading efficiency in o-vanillin/PEG 4000 system increased slightly with increasing temperature. The LC-MS/MS analysis of the formulations, showed that no degradation products were formed, so further analysis was performed using a spectrophotometer.

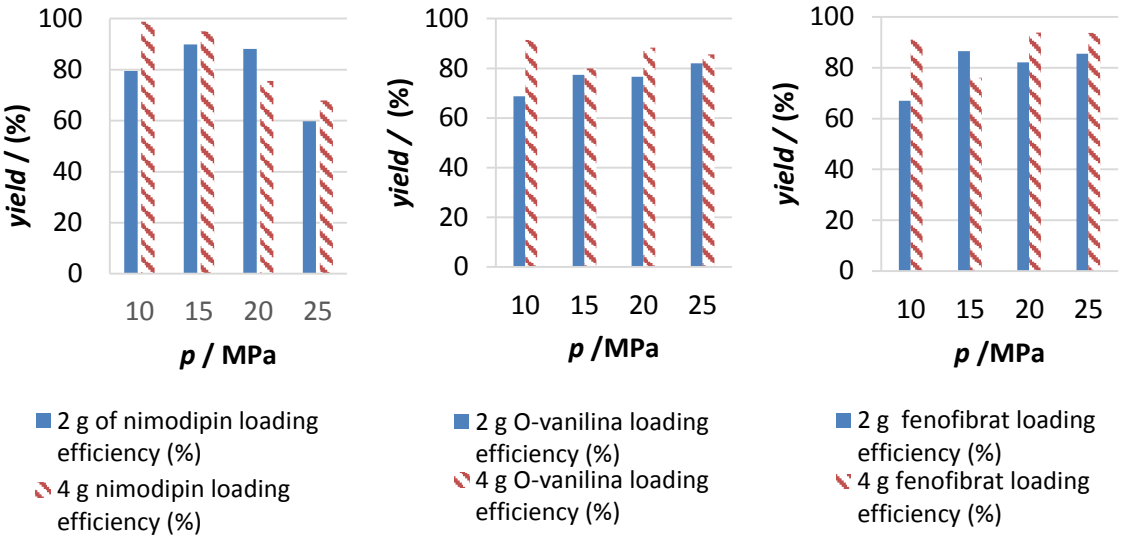

Figure 2-28: Loading efficiency of nimodipine, o-vanillin, and fenofibrate in Brij S100.

Table 2-6: Loading efficiency (%) of drugs in polymeric carriers at 60°C.

		Loading efficiency (%)			
Pressure (MPa)	**Drug/polymeric carrier mass ratio**	**Nimodipin/Brij S100**	**Fenofibrat/Brij S100**	**Vanillin/Brij S100**	**Vanillin/PEG 4000**
10	0.10	98.82	91.10	68.78	89.55
10	0.20	79.42	67.00	91.47	/
15	0.10	89.90	76.06	77.43	93.01
15	0.20	95.06	86.56	79.92	/
20	0.10	88.16	93.77	76.58	99.31
20	0.20	75.50	82.09	88.35	/
25	0.10	59.70	93.66	82.05	86.01
25	0.20	67.87	85.54	85.68	/

Table 2-7: Effect of a temperature of o-vanillin/Brij S100 system on Yield of collected particles (%), Loading efficiency (%) and Mean particle size (µm).

Pressure (MPa)	**Temperature (°C)**	**O-vanillin/ Brij S100 ratio**	**Yield of collected particles (%)**	**Loading efficiency (%)**	**Mean particle size (µm)**
15	45	0.10	78.21	73.68	41.35
15	60	0.10	39.8	77.43	59.5

2.3.3.4 Dissolution rate experiments

The dissolution profiles obtained were compared using two factors: difference factor f_1 (equation 2.25) and a factor of similarity f_2 (equation 2.26), as recommended by the FDA Canter for Drug Evaluation and Research [133]:

$$f_1 = \frac{\sum_{j=1}^{n} \left| R_j - T_j \right|}{\sum_{j=1}^{n} R_j} \tag{2.25}$$

$$f_2 = 50 \times \log \left\{ \left[\left(1 + \left(\frac{1}{n} \right) \sum_n \left(R_t - T_t \right)^2 \right)^{-0.5} \times 100 \right] \right\} \tag{2.26}$$

where R_t and T_t are the percentages of drug dissolved at time t for the formulation. In general, dissolution profiles were taken as similar with an f_1 value lower than 15 and an f_2 value between 50 -100. Dissolution rate profiles of pure unprocessed nimodipine and corresponding physical mixtures of the drug and the carrier (mass ratio 1:5) were compared to loaded nimodipine within Brij S100 carrier at pressures from 15 MPa up to 25 MPa in 0.1 M HCl aqueous solution (Figure 2-29).

Comparing the drug, physical mixtures, and the loaded substance, the loaded substance showed highest intrinsic dissolution rate. The physical mixture of nimodipine and Brij S100 showed somewhat higher drug release rate compared with the unprocessed substance. It was observed that mean particle size is in good correlation with dissolution profiles. The best profile was reached with the highest pre-expansion pressure, 25 MPa.

With the particle size reduction, the dissolution rate increased with the increased effective surface area. On average, a 3.5 time's higher amount of dihydropyridine calcium channel blocker nimodipine was dissolved in 1 h from solid dispersions, compared to unprocessed nimodipine. In order to compare the similarity of unprocessed particles with processed ones, we used difference factor f_1 and similarity factor f_2 as presented in equations 3 and 4. The difference factor f_1 was higher than 15; it was 68.51. Similarity factor f_2 was lower than 50; it was 3.48. This confirms that the dissolution character of nimodipine processed by PGSS^{TM} was different from that of unprocessed nimodipine. Figure 2-30 shows the dissolution rate of pure unprocessed fenofibrate, corresponding physical mixture and processed fenofibrate loaded within Brij S100. With particle size reduction, the dissolution rate increased to some extent, but the effective surface area was probably reduced by the drugs' hydrophobicity and agglomeration effect during micronization. The difference factor f_1 was 10.41, indicating that the dissolution character of processed fenofibrate is similar to that of pure unprocessed fenofibrate. The physical mixture of fenofibrate and Brij S100 showed similar drug release rate as the unprocessed substance. Figure 2-31 presents the dissolution profile of pure unprocessed o-vanillin, a physical mixture prepared with both polymers, Brij S100 and PEG 4000, and processed loaded o-vanillin within Brij S100 or PEG 4000 at 15 MPa. A better dissolution profile with a small difference was reached with the formulation of 2 g o-vanillin with a PEG carrier, compared to with Brij S100. The best profile was obtained by the formulation of 4 g of o-vanillin in Brij S100. The similarity factor f_2 of 0.46 indicates that a different dissolution character between unprocessed o-vanillin and processed loaded o-vanillin was obtained. The physical mixtures of vanillin and Brij S100 showed higher drug release rate compared with the unprocessed substance which was similar in the case of both polymers.

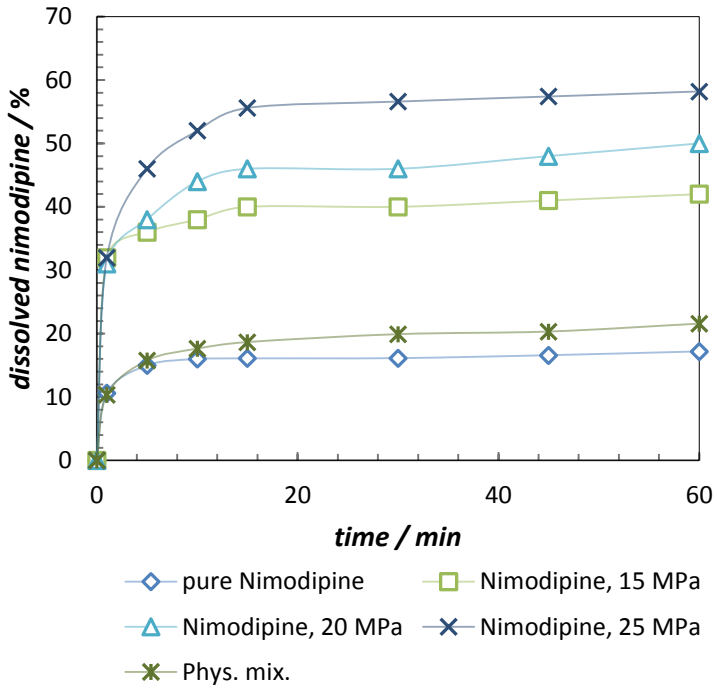

Figure 2-29: Dissolution rate of pure unprocessed nimodipine compared to processed nimodipine encapsulated within Brij S100.

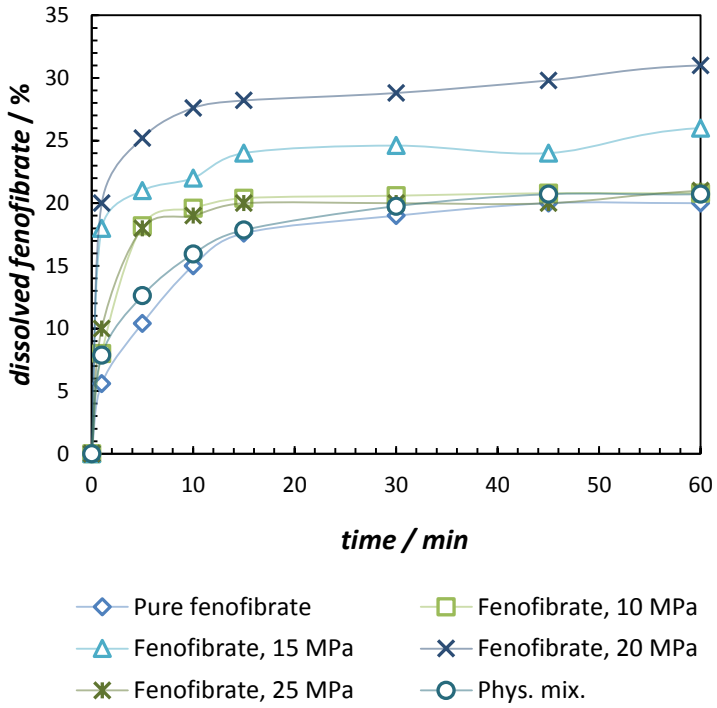

Figure 2-30: Dissolution rate of pure unprocessed fenofibrate compared to processed fenofibrate within Brij S100.

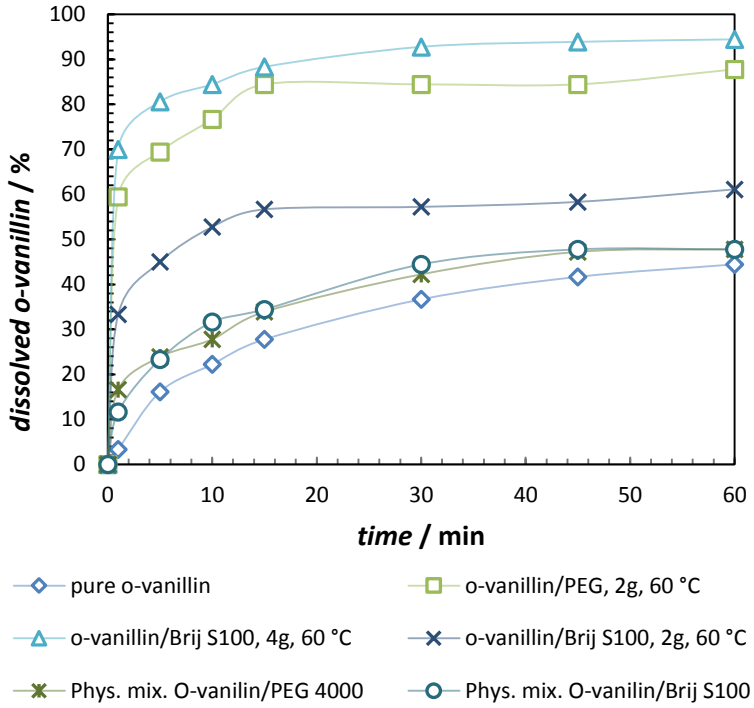

Figure 2-31: Dissolution rate of pure unprocessed o-vanillin compared to processed o-vanillin within Brij S100 or PEG 4000 at 15 MPa.

2.3.3.5 Micronization of Brij 52 and Brij 52/esomeprazole

Micronization of polymer Brij 52 without/with active compound was carried out. High pressure vessel was loaded with a mixture of esomeprazole and Brij52 (2 g esomeprazole/10 g Brij52). ESEM photomicrographs (Figure 32 a and b) prove that it was not possible to obtain particles with a well-defined structure, since massive agglomeration of the particles took place. ESEM photomicrograph with a higher magnification is presented and the microparticle morphology is not clearly shown. The size of the particles presented in Figure 32 (a) pure Brij 52 and b) Brij 52 with esomeprazole) varies between 5 µm up to 35 µm. These results could be explained by solvation of polymer blocks that caused swelling of the particles and the corresponding increase of their mean diameter. Narrowing of the standard deviation might be achieved by enrichment of a solvation equilibrium of the suspended microparticles, similar to the one of micellar systems [26, 40].

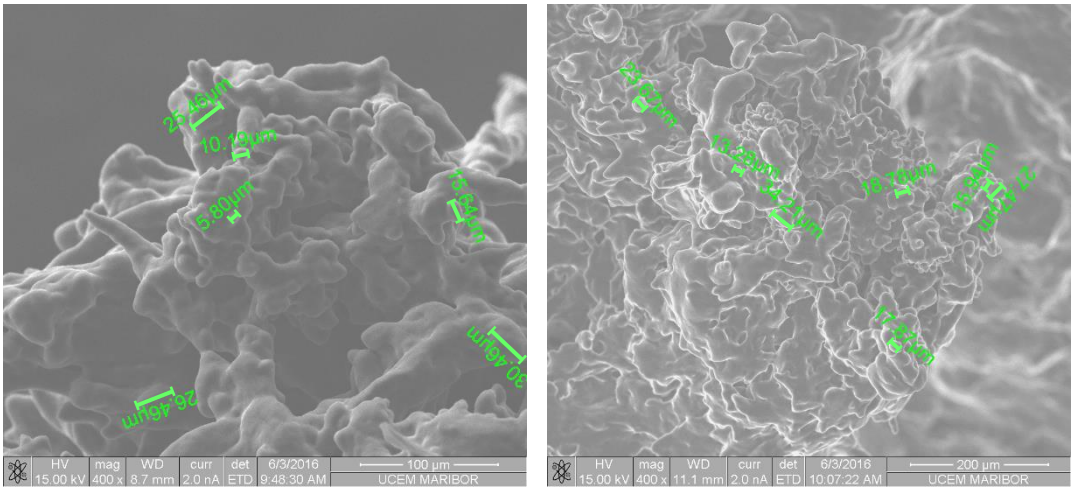

Figure 2-32: a) Small particles of Brij52 b) particles of composite Brij 52/ esomeprazole.

2.3.3.6 Foam of Brij 52

Figure 2-33 presents an enlarged ESEM micrograph of Brij 52 foamed with supercritical CO_2 at 15 MPa and 60 °C. ESEM analysis showed that obtained porous material has a closed cell structure which enables better isolating properties because of higher stiffness and toughness and lower permeability. The diameters of the pores are greater than 100 µm; so they are considered to be macro pores.

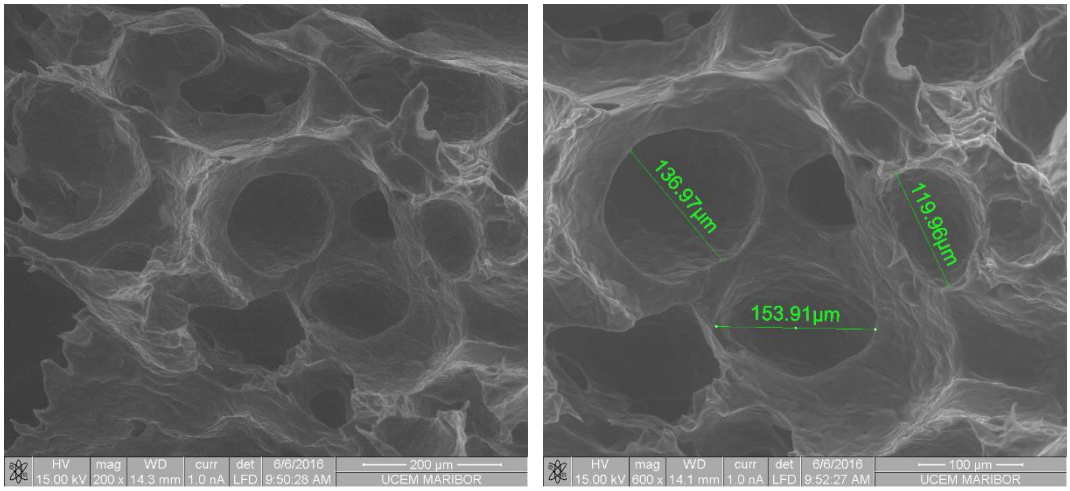

Figure 2-33: Foam of Brij52: a) closed cell structure b) macro pores S100 or PEG 4000 at 15 MPa.

2.4 Conclusion

The presented chapter contributes to a better understand of polymer behaviour in processes with supercritical fluids. The PGSS^{TM} (Particles form Gas saturated Solution) was applied to the biodegradable polymeric materials polyoxyethylene stearyl ether **(**Brij 100 and Brij 50) and polyethylene glycol (PEG 4000) for the incorporation of insoluble drugs nimodipine, fenofibrate, o-vanillin, and esomeprazole with the purpose of improving their delivery. Before starting particle precipitation, preliminary thermodynamic experiments of water-soluble carriers polyoxyethylene stearyl with molar weights of 683 g/mol (Brij 50) and 4670 g/mol (Brij 100) and polyethylene glycol of molar weights from 600 g/mol up to 1000 g/mol were carried out. Different methods for determination of melting points, gas solubility, diffusion coefficient, density, viscosity and interfacial tension, which were either developed or modified to the processing conditions by the authors of the present chapter, were applied for determination of physical-chemical and transport properties of a binary systems of polymer and a SCF with the aim of choosing optimal processing conditions for further polymer processing. Melting points were determinate by modified capillary glass method. The solubility and diffusivity of CO_2, which determine the mass-transfer rate of CO_2 from the matrix to the bubbles, were measured by magnetic suspension balance. The interfacial tension was determined by the capillary rise method. Density of binary systems biodegradable polymer/CO_2 were determined by the density meter with a U-tube and with a magnetic suspension balance, while viscosity was determinate by the use of available experimental data and a simple viscosity mixing rule, results obtained previously for the viscosity of pure compounds have been extended to mixtures.

Determination of melting points at elevated pressures has indicated high CO_2 solubility in the molten heavy component since it was observed that, the Brij 100/CO_2 binary system has an S-L-G (solid-liquid-gas) curve with a negative *dP/dT* slope, which indicates high CO_2 solubility in the molten heavy component. Sorption of CO_2 in Brij 100 and Bij 52 is about 25 % higher than in PEG of different molar weights under similar conditions. In the case of argon saturated solutions of PEGs, the effect of pressure on interfacial tension was less pronounced in comparison with CO_2 saturated solutions of PEGs which resulted in up to 3 times higher values at pressures above 10 MPa. A possible explanation is that the solubility of carbon dioxide in polymer was up to 10 times higher than the solubility of argon, most probably due to the differences in the molecular structures of the gases. The highest solubility and consequently densities of CO_2 and argon were determined in PEGs of lower molecular masses due to the fact that a PEG with a low molecular mass has a matrix with more empty spaces and can accept more gas molecules. Additionally obtain data on interfacial tension and viscosity of CO_2 saturated solution with PEG 6000 were for the first time correlated with particle size and particle morphology. With viscosity reduction particles of the gas-saturated solution is expected to have smaller mean size. Increased pre-expansion temperature has a strong influence on PEG 6000 viscosity and morphology of obtaining particles. Higher interfacial tension boosts the formation of smaller particle droplets after spraying through the nozzle.

The second part of a chapter presents particle precipitation and loading efficiency of fenofibrate, nimodipine, o-vanillin and esomeprazole with biodegradable Brij 100, Brij 52 and PEG 4000. In the case of Brij 100 and PEG 4000 the influence of the main process parameters (pressure, temperature and active substance/carrier ration) on the precipitated yield, mean the particle size distribution, loading efficiency, and dissolution rates are presented. With increasing pre-expansion pressure, the mean particle size of nimodipine/Brij S100, vanillin/Brij S100, and vanillin/PEG 4000 decrease. In the case of a mixture of fenofibrate/Brij S100, anticipated effective surface areas were slightly reduced with pressure as a result of agglomeration. The loading efficiency of drugs in carriers observed by PGSS^{TM} was high in all experiments. It was observed that at lower pressure loading efficiency was greater than at higher pressures and that

efficiency varies significantly with changing drug/carrier ratio. The morphology of particles obtained was irregular and, according to the ESEM pictures, porous. It was observed that a combination of factors, including particle size reduction and interactions between drugs and hydrophilic carriers contribute to enhance the dissolution rates of precipitated solid particles. On average, a 3.5 x greater amount of the dihydropyridine calcium channel blocker nimodipine was dissolved in 1 h from solid dispersions, compared to unprocessed nimodipine. Dissolution profiles were compared with a different f_1 factor and a similarity factor f_2. It was confirmed that the dissolution character of processed o-vanillin and nimodipine by PGSS^{TM} was different from that of unprocessed o-vanillin and nimodipine.

On the other hand, micronization of Brij 52 without/with esomeprazole as the active compound has been carried out at one process condition (15 MPa and 60 °C), where the highest diffusion coefficients and CO_2 solubility in the polymer were measured. It was not possible to obtain particles with a well-defined structure, since massive agglomeration of the particles took place. However, the formation mechanism of the cellular structure has been fully achieved and investigated from the viewpoint of the morphology and viscosity of the blend polymer Brij52 and the mass-transfer rate of the physical foaming agent in polymer

3. Measuring transport properties from drop geometry

3.1 Theoretical part

With increasing usage of supercritical fluids in industry, knowledge about transport properties for binary systems involving supercritical fluids, such as the diffusion coefficient D_{12}, interfacial tension γ, thermal conductivity λ and viscosity η, has become of great importance in designing, analyzing and optimizing high-pressure processes. In this chapter, a new experimental technique for obtaining diffusion coefficients and interfacial tension by means of pendant drop tensiometry is described, along with a mathematical model designed to fit the experimental data used for determining the diffusion coefficients of binary systems at elevated pressures and temperatures. This technique can be used for measurements of several new binary and ternary systems that are relevant in chemical and carbon sequestration applications.

3.1.1 Mass transfer and diffusion coefficients

Accurate prediction of diffusion coefficients, D_{ab}, is fundamental in various engineering and industrial operations and design processes involving mass transfer (e.g. conventional and supercritical extractions, multiphase chemical reactions, distillation, carbon sequestration, membrane separation processes, absorption and adsorption) [134]. Mass transfer data, measured at ambient conditions, can be found in the literature for numerous binary and ternary systems. Data in the literature that reports on the diffusion coefficients of liquids in supercritical fluids are still relatively scarce [135]. In addition, most of the extant experimental techniques for determining diffusion coefficients at high pressures are either expensive or time-consuming and have considerable scatter, with relative uncertainties [136, 137].

Several methods have been developed to study the mass transfer properties of different systems of components. Those are divided into direct, when the composition of the liquid samples with gas absorbed is analysed during the test, and indirect, when the composition of the liquid phase after diffusion is correlated with a measured system property. The main disadvantage of such methods is that they are time consuming and require expensive equipment and subsequent analysis of the composition of system components. Besides, these methods are susceptible to experimental errors [138]. Therefore, there is interest in developing simple, quick and economical methods that would give accurate results.

Frequently used experimental methods for measuring diffusion parameters that do not require measuring compositions include the pressure decay (PD) method, which takes a long period of time to attain the equilibrium state of the mixture [139, 140] and the constant pressure dissolving gas volumes (CPDGV) method, in which volume–time data is recorded with constant pressure and temperature [141, 142]. Another method based on NMR spectra changes caused by changes in the mixture's properties with the diffusion process is the low-field nuclear magnetic resonance (NMR) method [143]. X-ray computer assisted tomography (CAT) is used in reservoir rock characterization [144]; however both methods, nuclear magnetic resonance (NMR) and computer assisted tomography, require expensive devices. The gas permeation through immobilized liquid membrane (ILM) method is used to determine the pressure decay of gas entering a closed chamber with a thin layer of ionic liquid [145].

The dynamic pendant drop volume analysis (DPDVA) method is used to calculate the swelling coefficient of the liquid phase and is based on measuring the change in volume of a pendant drop in a cell surrounded by a gas absorbed by the drop. This is the method used in the frame of the present study and modified to enable measurements at elevated pressures. The special property of the model developed is the ability to determine diffusion of liquid in a supercritical phase.

Diffusivity measurements using drop tensiometry have been done by Espinoza et al. [146], where a sessile droplet of water on a substrate was surrounded by supercritical CO_2. The diffusion model was solved numerically using the Crank-Nicolson implicit scheme for evaporating sessile droplets. Yang et al. [147] presented a method that determines the solvent diffusion coefficient and the oil swelling factor from dynamic measurements of pendant oil drop volumes. This model was numerically solved by applying the semi-discrete Galerkin finite element method. Bellen et al. [148] validated the diffusion coefficients and the thermal diffusion factors of naphthalene in CO_2 from levitated drops. Hirai et al. [149] estimated the diffusion coefficient in a CO_2-water system, where a liquid CO_2 droplet without CO_2 clathrate was placed in the flow of a uniform velocity profile. The diffusion coefficient was obtained by measuring the liquid CO_2 droplet-dissolution rate and using the empirical mass transfer coefficients. Erbil et al. [150] performed fully spherical liquid drop evaporation experiments in still air, where diffusion coefficients were calculated from the decreasing mass of the droplets. Drop tensiomentry has primarily been established for measurements of the surface tension of a system at ambient pressures. Recently, the pendant and sessile drop methods have been applied to perform measurements at elevated pressures and the system of water and CO_2 has been frequently used as a model to verify the reliability of the method and provide repeatability of the results [151-154].

3.1.2 Interfacial tension

In multiphase systems, knowledge of interfacial properties is important in modelling and design of both conventional and supercritical-fluid extraction processes, in formation of microemulsions or colloids, in polymer processing, and especially in enhanced oil recovery (EOR). It has been shown that high-pressure interfacial phenomena govern the migration and recovery of oil and gas from hydrocarbon reservoirs. These phenomena are of particular relevance to phase separation and mass transfer in light hydrocarbon fractionation plants and in lubricating oil refining [155]. The knowledge of interfacial and surface properties can also be helpful in delay life. For example, when water is contaminated by a chemical agent, the surface tension usually decreases. Therefore, surface tension measurements can serve for water quality testing [156]. Several methods have been developed for determination of surface and interfacial tension. They can be classified into five categories. In the first are those involving detachment techniques, where the force needed to break away a different shape body for the liquid-liquid interface is measured using a microbalance (Wilihelmy Plate, Du Nouya ring). The second category of techniques includes those in which interfacial tension can be determined from direct measurement of capillary pressure (Maximum Bubble Pressure, Growing Drop). The next two categories present techniques where analysis of equilibrium between capillary and gravity forces is applied: the third relies on capillary effects, which are the results of a pressure difference between fluids on either side of an interface (Capillary rise method and Drop Volume), while the techniques in the fourth category fix the volume of a liquid drop and measure the distortion of the drop under the influence of gravity (Pedant drop and Sessile Drop). The last category includes techniques where the shape of fluid drops is distorted by centrifugal forces; these are used to measure ultralow interfacial tension (Spinning Drop method) [157].
However, not all techniques are suitable for measurements at high pressures. The most commonly used are those involving analyses of drop shape and capillary rise, because of their simplicity and the possibility to obtain results at the curved interface of drops or rise of meniscus inside the high-pressure and high-temperature environment as results of pressure difference between fluids. Interfacial tension can be also determined inside a high-pressure cell by analysing the curved interface of levitation elevated drops [158]. The importance of knowing the exact interfacial tension and wettability properties at elevated conditions is relevant to carbon sequestration.

3.1.3 Interfacial tension and diffusivity relevant in carbon sequestration

Excessive production of carbon dioxide (CO_2) by the burning of fossil fuels has led to growing concentrations of greenhouse gas in the atmosphere [159]. Along with green renewable energy sources and better energy efficiency, carbon capture and storage are estimated to play a major role in reduction of CO_2 emissions. The subsurface formations that could serve as geological sites for CO_2 storage are depleted oil and gas reservoirs, deep saline aquifers and coal seams. Deep saline aquifers are the most promising future sinks for carbon dioxide, with potentially high storage capacity [160]. Storage safety in a geological formation is related to several CO_2 trapping mechanisms: structural or stratigraphic trapping, capillary or residual trapping, solubility trapping and mineral trapping. Studies have shown that capillary trapping of CO_2 is a very important short-term storage mechanism, with a considerably low risk of leakage [161]. In capillary trapping, injected CO_2 is expected to rise buoyantly to the top of the first physical barrier (caprock) where it becomes trapped in the micropores. Interfacial tension causes the non-wetting CO_2 phase to be retained between narrow pore throats filled with saturated formation water [162]. Interfacial tension and wettability properties affect the multiphase flow properties of the porous formation, such as the relative permeability and CO_2 capillary breakthrough pressure. Consequently, they set a limit on both the operating (i.e. injection) pressure and the maximum height of CO_2 that can be stored in a given cap rock (storage capacity) [163].

Interfacial properties during the contact of saline water (brine) and pure CO_2 under conditions relevant to carbon sequestration have been recently studied by many authors [159, 164-169]. In contrast, little is found in the literature about the presence of other gases, called co-contaminants, that are present in small quantities in all injected CO_2 streams and can significantly affect the physical properties (bounce, interfacial tension, contact angle, diffusivity etc.) and consequently the capillary breakthrough pressure (safety) and storage capacity. The impurities found in both the flue and the separated CO_2-rich gas vary between each power plant design [170]. Table 3-1 shows that the percentage of argon is non-negligible in oxy-combustion CO_2 capture and might affect storage capacity and safety in the subsurface. The idea of co-injected higher amounts of other gasses in CO_2 stream is interesting in order to avoid the high cost of the separation process (purifying CO_2 streams).

The effects of SO_2 co-contaminants in the CO_2 stream on the interfacial properties and dynamic contact angles of equilibrated CO_2 and brine on a quartz surface at high pressures have been studied by Seraj et al. [160]. They concluded that co-injection of SO_2 in the subsurface may increase the risk of gas leakage through the caprock. Al-Yaseri et al. [171] investigated interfacial tension under storage conditions for a 50 mol% CO_2 and 50 mol% N_2 mixture. They noted that the measured N_2-brine interfacial tension was higher than that for CO_2-brine or N_2/CO_2-brine interfaces. Measurements of water/acid gas interfacial tension were done by Shah et al. [172]. They observed a strong decrease in water/H_2S interfacial tension with an increase in H_2S content and therefore a decrease in gas column height in a given subsurface.

Argon is one of the light gases that are poorly soluble in water; therefore it has been concluded that aqueous phase density change caused by dissolution can generally be neglected. The interfacial tension of the Ar/ H_2O system was first measured by Masterton et al. at 30°C in the pressure range from 0.1 to 12 MPa using the capillary rise method [173]. Massoudi and King [174] measured interfacial tension in the same system at a lower temperature of 25°C in a narrower range of pressures (up 8 MPa), also using the capillary rise method. Wiegand and Franck were the first authors to report utilizing the pendant drop method for determination of interfacial tension in the Ar/ H_2O system [175]. Two data points were reported at T = 100°C.

The interfacial tension for various compositions of the ternary mixture containing CO_2, N_2, and H_2O have been measured by several authors, mostly by means of the capillary rise method, pendant drop method and the rising bubble. There is still a lack of data on the interfacial tensions

of binary and ternary component systems involving CO_2, gas, and water or brine, under conditions pertaining to those of reservoirs [176].
An excellent overview on the interfacial behavior of the binary systems N_2/H_2O, Ar/H_2O, and H_2/H_2O and ternary systems $CO_2/N_2/H_2O$, $CO_2/Ar/H_2O$ and $CO_2/H_2/H_2O$ is offered by Chow [177]. The measurements were carried out using the pendant drop method. Data are reported in the pressure range from 0.5 up to 50.0 MPa at temperatures from 25°C to 200°C [178]. Empirical predictions of the ternary systems were introduced. SGT + SAFT-VR Mie was used to model the data on interfacial tensions of binary and ternary systems in the wide range of pressures and temperatures investigated. The authors report average absolute relative deviations of 3.6% - 7.9%.

Table 3-1: Reported impurities in CO_2 stream from different capture type processes by IPCC Intergovernmental Panel on Climate Change (IPCC) [179], Petroleum Technology Alliance Canada (PTAC) [180] and Osterkamp and Ramsen (O&J) [181] studies. Values are presented in vol %.

Capture Type	Study	CO_2	Ar	N_2	O_2	NOx	H_2S	CH_4	H_2	CO
Oxyfuel	IPCC	95.9	4.1			≤0.01				
	PTAC	91.8	3.9	2	2.3					
	O&R	≥90	5	7	3			trace	trace	trace
Pre-combustion	IPCC	95.6	1.3	-	-	-	0.01	2	1	0.04
	PTAC	95						0.5	4	0.5
	O&R	95.9	0.05	0,6	trace		3.4		3	0.4
Post-combustion	IPCC	99.9	0.01			≤0.01		-	-	-
	PTAC	99.8	-	0.02						
	O&R	≥99	trace	0.17	0.01					

3.1.4 The Aims

The aim of this chapter was to describe a new, reliable experimental technique for obtaining diffusion coefficients and interfacial tension by means of pendant drop tensiometry, and a mathematical model designed to fit the experimental data used for determining the diffusion coefficients of binary systems at elevated pressures and temperatures. The experimental procedure was validated by a comparison of the experimental data for the mixture water-CO_2 with data from the literature. For this purpose, the interfacial tension at the water/CO_2 interface and diffusivity of water in CO_2 were measured at 25°C and 45°C in the pressure range from 0.1 MPa up to 60 MPa. Droplet geometry was examined by using a precise computer algorithm that fits Young–Laplace equation to the axisymmetric shape of a drop.
For the first time, interfacial tension of a CO_2 saturated solution with propylene glycol and diffusion coefficients of propylene glycol in supercritical CO_2 at temperatures of 125 °C and 150 °C in a pressure range from 5 MPa up to 17.5 MPa were measured. Knowledge about the diffusivity of volatile liquids, such as propylene glycol in supercritical fluids, especially in CO_2, which is most widely applied, is essential for several applications. The results of the present research serve as a good framework for further development in the processing of poly (propylene fumarate) [182]. Propylene glycol is also used in various edible items, as a vaporizer in the delivery of pharmaceuticals, and in personal-care products.
Secondly, the drop tensiometry method has been applied to measuring systems that are of great importance in carbon sequestration related applications. The effect of argon as a co-contaminant in a CO_2 stream on the interfacial tension, diffusion coefficients and storage capacity was studied. Measurements were performed at the pressures and temperatures at which most of the deep saline aquifers are found, and where CO_2 has the highest density (a maximum mass of

CO_2 can be stored) Finally, the potential implications of observed trends on geological storage capacity and safety with the effect of argon presence in the CO_2 stream are presented.

3.2 Experimental part

3.2.1 Materials

Carbon dioxide (3.5), Argon (4.5) and mixtures of carbon dioxide and argon with 5 vol. %, 10 vol. % and 50 vol. % of argon content were obtained from Messer (Slovenia). Propylene glycol with 99.5 % purity was purchased from Sigma (Germany) and was used without further purification. Brine-salty water relevant to (Gorgon, Australia) the geological side, with a concentration of 23.26 g/L was prepared in the laboratory by mixing 10.88 g/L KCl, 6.68 g/L $NaHCO_3$, 3.14 g/L NaCl, and 2.38 g/L KCO_3. The needles used fin the pendant drop method were made of stainless steel (SITEC-Sieber Engineering AG), with a nominal outer diameter of 1. 56 mm.

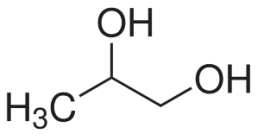

Figure 3-1: Propylene glycol.

3.2.2 Equipment and methods

3.2.2.1 Installation of high-pressure drop tensiometry apparatus

The central part of the experimental setup comprises an optical high-pressure cell (NWA GmbH, Germany) equipped with two stainless steel heaters (mod. Firerod, Watlow, USA). Liquid phase was injected by a high-pressure manual pump (mod. 750.1100, SITEC, Zurich, Switzerland). Pendant drops of adequate size were formed on a stainless steel tip that was placed vertically in the cell between two sapphire windows.

Measurements of dynamic drop volume were filmed with a Basler Aca1300-200um digital camera equipped with a CCTV lens (Tamron, Japan), connected to a computer by using the OpenDrop algorithm [183]. To avoid optical aberrations and the fake reflections from other sources that can occur at the drop edge, the drop was lit from the other side with a diffusion light, which was achieved by placing a glass diffuser between the light source and the hanging drop. The undesirable effect of droplet oscillation was minimized with an anti-vibration Table. Pressure inside the cell was increased with inlet gas by a high-pressure pump (NWA PM-101) or Gas Buster (DLE 75-1-GG-H2), depending on the type of gas. Pressure was monitored during the entire experiment by an electronic pressure gauge (WIKA Alexander Wiegand GmbH & Co. KG, Alexander-Wiegand-Straße, Klingenberg, Germany) with an uncertainty of 0.01 MPa. Total uncertainty of the temperature measurement was 0.1 °C. The entire experimental setup is presented in Figure 3-2.

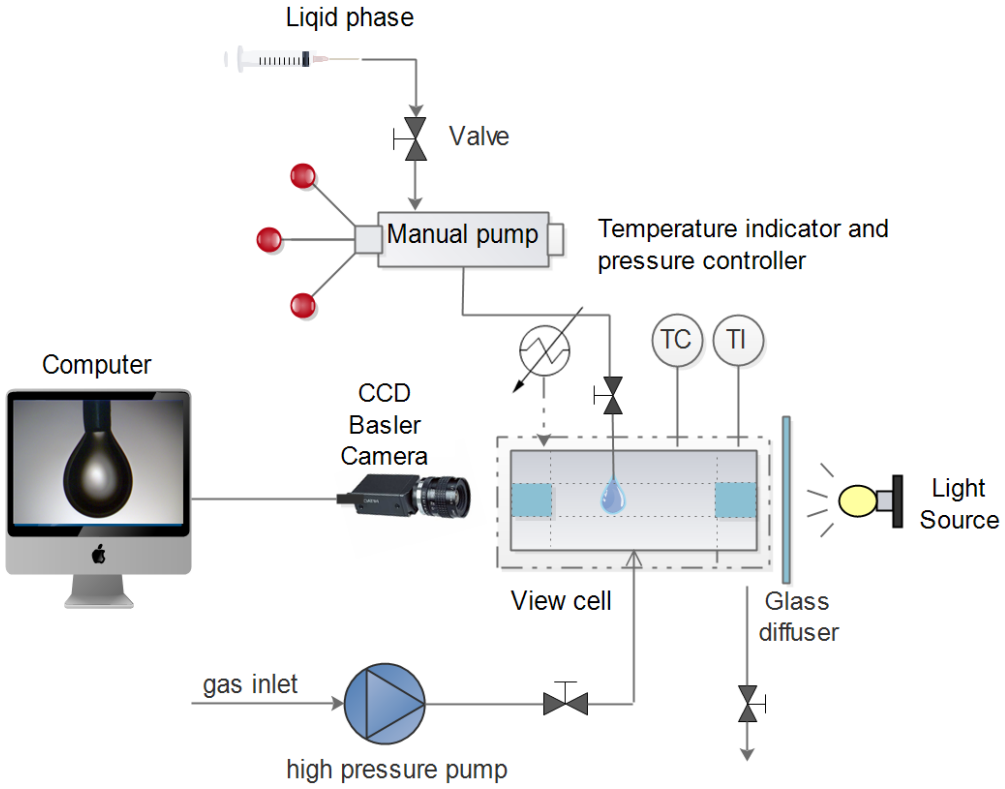

Figure 3-2: Scheme of the experimental setup for measuring interfacial tension and diffusion coefficients by a high-pressure view cell [171]

3.2.2.2 Pendant drop method

Recently, drop tensiometry has been the subject of intensive research by many authors [184-187]. The method has been significantly improved in recent years, and newly accrued algorithms have been developed for fitting the Young-Laplace equation to the digitized axisymmetric shape of a drop [183]. Briefly, Young-Laplace describes the pressure difference between the areas inside and outside a curved liquid surface/interface:

$$\Delta P = \gamma(1/R1 + 1/R2)\Delta P, \tag{3.1}$$

where γ is the interfacial tension and R_1 and R_2 are the principal radii of the curvature. Because of the hydrostatic pressure caused by gravitation across the z-axis, the pressure difference (Laplace pressure) ΔP (z) at a distance z from a subjective reference plane with Laplace pressure ΔP_0 is given by $\Delta P = \Delta P_0 + \Delta\rho gz$, where $\Delta\rho$ is the density difference between the two phases. As can be seen in the geometrical arguments illustrated schematically in Figure 3-3, the Young-Laplace equation becomes a set of three ordinary differential equations:

$$\frac{dx}{ds} = \cos\phi \tag{3.2}$$

$$\frac{dz}{ds} = \cos\phi \tag{3.3}$$

$$\frac{dx}{ds} = 2 - \beta \cdot z - \frac{\sin\phi}{x}, \tag{3.4}$$

where x and y are cylindrical coordinates, ϕ the tangent angle of rotation measured from the apex, and s is the arc length. B_0 represents the Bond number with associated boundary conditions:

$$Bo \equiv \frac{\Delta\rho g R_0^2}{\gamma} \tag{3.5}$$

$$x = 0, z = 0, \phi = 0 \; at \; s = 0 \tag{3.6}$$

If the Bond number can be determined with R_0 which represents the radius of curvature at the apex of the drop, interfacial tension can be solved using equation 3.5. Furthermore, by fitting the Young–Laplace equation to the axisymmetric shape, drop volume and drop surface area can be obtained from 3.7 and 3.8:

$$Vd = \Pi \int x^2 sin \; \phi ds \tag{3.7}$$

$$Ad = 2\Pi \int x \, ds \tag{3.8}$$

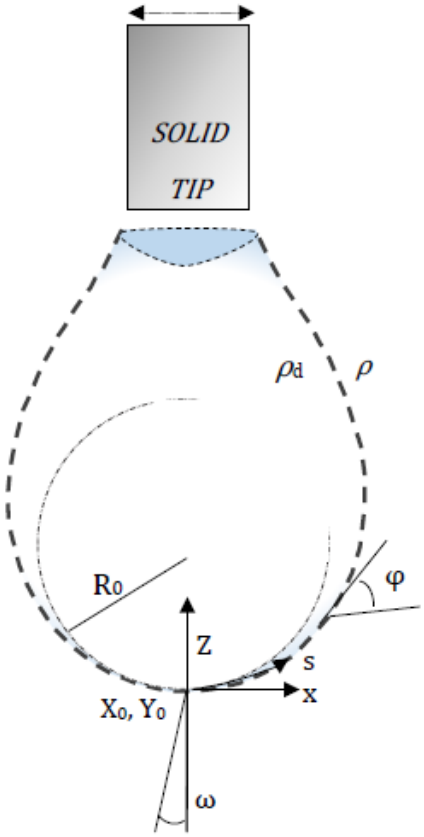

Figure 3-3: Pendant drop on the solid tip with suitable geometrical arguments.

3.2.2.3 Density and fluid phase equilibria determination

For density measurements propylene glycol/CO_2, brine/CO_2/Ar systems, a density meter with U-tube Anton Paar DMA and an Anton Paar DMA 60 electronic control unit were used. Knowledge of the density difference between phases is required as an input value when using OpenDrop software for calculating interfacial properties.

For obtaining diffusion coefficients under supercritical conditions from dynamic changes in equivalent drop diameter by the mass transfer model presented in section 3.3.3.5, knowledge of phase equilibria is essential. High-pressure phase equilibrium data can be found in the literature and have been reviewed by Fonseca [188], Dohrn and Brunner [189] and Škerget [190]. A variety of methods can be used [118, 191, 192] for determining phase equilibria in multi-compound systems at elevated pressures and temperatures. In our study, phase equilibrium data was determinate by variable-volume stainless steel cell by SITEC – Sieber Engineering AG, Zurich, Switzerland). After equilibrium was reached, the sample was taken into a trap with a solvent by opening a valve. The mass of gas released was calculated based on the ambient pressure, temperature and measured volume of the gas.

3.2.2.4 Mass transfer model

Assumptions made for the mass transfer model for diffusion of the solute in the surrounding medium of the droplet were as follows:

- Drop diameter decreases with time, so a pseudo-steady state is assumed, since the path length r increases slowly with time.
- Mass transfer is carried out with equimolar countercurrent diffusion.
- Equivalent sphere diameter is calculated from $D = \frac{6\,V_d}{S_d}$, where ($V_k = \frac{\pi D^3}{6}$) is the volume and ($S_d = \pi\, D^2$) is the surface area of the droplet.
- Subscript A denotes a solute (droplet medium) in the surrounding medium (dense gas), and subscript B denotes the surrounding medium (dense gas) that surrounds the droplet medium, The flux of dense gas in (mol/m^{2}s) to a drop surface can be expressed by Fick's 1st law of diffusion (equation 3.9):

$$N_{B,r} = -C\, D_{AB} \frac{dy_B}{dr}, \tag{3.9}$$

where y_B mole fraction of gas in the gas phase, D_{AB} is the diffusion coefficient, r is the distance from the center of the droplet equivalent sphere to the phase boundary, and C is the molar concentration. Because in the present case the cross-sectional area through which diffusion is taking place varies with the distance r, the molar flux Nb,r is not constant. Therefore, it is more convenient to define the molar flow ($W_{B,r}$). The molar flow of dense gas to the drop is constant and is expressed by equations 3.10 and 3.11:

$$W_{B,r} = 4\,\pi\, r^2 N_{B,r}, \tag{3.10}$$

$$W_{B,r} = -4\,\pi\, r^2\, C\, D_{AB} \frac{dy_B}{dr}. \tag{3.11}$$

Equations 3.12 and 3.13 represent boundary conditions, where the first one proposes that at a distance sufficiently far from the surface of the droplet, the surrounding medium is composed of pure gas only, and second one assumes established boundary conditions on the drop surface.

$$r = \infty \qquad y_B = 1 \tag{3.12}$$

$$r = R, \qquad y_B = y_B^*, \tag{3.13}$$

By integration of equation 3.11 and considering the boundary conditions (equation 3.12 and 3.13):

$$W_B = 2\,\pi\,c\,D\,D_{AB}\,(y_B^* - 1) \tag{3.14}$$

The droplet medium (A) dissolves in dense gas, which affects the mass of pendant drops, which decreases. The solute A diffuses in the direction opposite to that of the gas:

$$W_B = W_A, \tag{3.15}$$

$$W_A = \frac{dm_A}{dt}\,\frac{1}{M_A} = \frac{d(\rho_A\,V)}{M_A\,dt} \tag{3.16}$$

The density of the droplet medium (solute A) ρ_A, is assumed to be constant:

$$W_A = \frac{\rho_A}{M_A}\,\frac{dV}{dt} = \frac{\rho_A}{M_A}\,\frac{dV}{dD}\,\frac{dD}{dt} \tag{3.17}$$

When taking into account the equivalent sphere diameter($\frac{dV}{dD} = \frac{3\,\pi\,D^2}{6}$), mole flow can be expressed by equation 3.18 as:

$$W_A = \frac{3\,\rho_A\,\pi\,D^2}{6\,M_A}\,\frac{dD}{dt} \tag{3.18}$$

After equating the molar flows of solute and gas, *d*t can be expressed by equation 3.19:

$$dt = \frac{\rho_A\,D}{4\,M_A\,C\,D_{AB}\,(y_B^* - 1)}\,dD \tag{3.19}$$

Taking into account the boundary conditions in equations 3.20 and 3.21, *t* can be further expressed in general form as:

$$t = 0 \ldots\ldots\ldots D = D_1 \tag{3.20}$$

$$t = t \qquad D = D_2 \tag{3.21}$$

$$t = \frac{\rho_A}{4\,M_A\,C\,D_{AB}\,(y_B^* - 1)}\,\frac{D^2}{2} \tag{3.22}$$

taking into account the following relationship:

$$C_A = x_A\,C = \frac{\rho_A}{M_A} \tag{3.23}$$

t can be expressed as:

$$t = \frac{x_A}{8\,D_{AB}\,(y_B^* - 1)}\,D^2 \tag{3.24}$$

The diffusion coefficient can be calculated from equation 3.25:

$$D_{AB} = \frac{(1 - x_B)}{8\,(y_B^* - 1)}\,\frac{D^2}{t}, \tag{3.25}$$

Where, $\frac{D^2}{t}$ is obtained experimentally by measuring equivalent drop diameter depending on time, x_B and y_B^* are fluid phase equilibrium data in the lower and upper phases.

3.2.2.5 Software environment and OpenDropR algorithm

Drop geometry was measured by using precise computer algorithm OpenDrop that fits Young-Laplace equation (3.1) to the axisymmetric shape of a drop. Knowledge of the exact capillary tip diameter and density difference between phases are required as an input values when using OpenDrop software for calculating drop shape parameters. Software environment is presented in Figure 3-4.

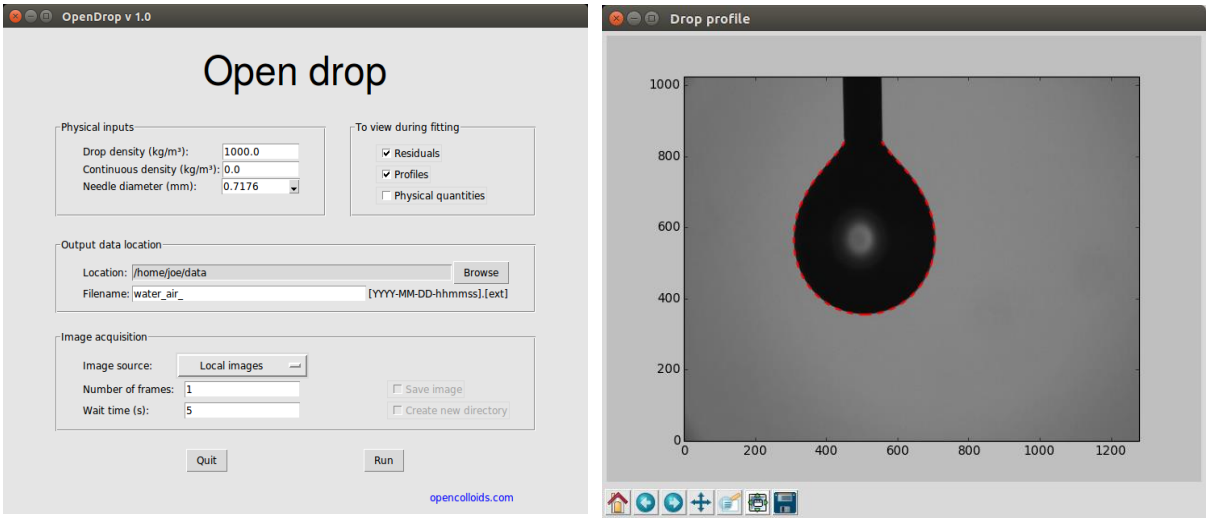

Figure 3-4: Computer algorithm OpenDrop.

The procedure of fitting Young-Laplace equation to the axisymmetric shape of a drop can be divided into two subroutines. Firstly, the drop profile is extracted form an experimental image, and secondly, the Young-Laplace equation is iteratively solved to find the physical parameters that the most precisely describe the extracted drop profile using optimization techniques. The schematic of the pendant drop tensometry process is presented in Figure 3-5. Several methods have been reviewed and discussed about determination of the edge detection of drop profile from an experimental image [193-195].The Canny edge [196] detector using multi-pass approach, is widely used to its robust nature over a range of contrast conditions. When the experimentally drop profile is obtain without aberrations and reflections at r, z coordinates, the theoretical droplet profile is fitted to the extracted experimental data by minimizing the sum of squared residuals:

$$S = \sum_{i=1}^{n} e_i^2 = \sum_{i=1}^{n} \min_{\bar{s}} \left\{ e_i^r(\bar{s}) + e_i^z(\bar{s})^2 \right\}, \tag{3.26}$$

where the i_{th}, e_i, is defined as the minimum Euclidean distance between the data point (r_i, z_i) and any point on the theoretical drop profile (r(s), z(s)). The squared residual can be expressed in terms of a horizontal e_i^r and a vertical e_f^z component. The fitting routine can be expressed as a minimization of non-linear function $S(\beta)$, where:β =(X_0, Y_0, ω, R_0, B_0) are geometrical parameters of the theoretical drop profile, presented in Figure 3-3. Parameters X_0,Y_0 presents coordinates of the drop apex, is ω the rotational angle of the experimental image in relation to gravity, R_0 is the drop radios, and B_0 is the Bond number. If a small Bond number is obtained, the interfacial forces prevails over gravitational forces, with the resulting drop profile only slightly deformed from spherical shape.

The fitting routine of non-linear function can be expressed with automated optimization (LMF- AO) procedure [197] that combines the speed of Gauss-Newton least square method with the stability of steepest descent. LMF-AO informs the parameter set β according to

$$\beta^{(k+1)=}\ \beta_{(k)} + \delta \tag{3.27}$$

where δ is derived by solving the Jacobian matrix:

$$J^T J + \lambda diag(J^T T)\delta = -J^T e\,, \tag{3.28}$$

where e is the vector of residuals, λ parameter is chosen at each step to ensure convergence according to Fletchers criteria [198]. Convergence criteria how to update the parameters $\beta^{(k)}$, and how Jacobian matrix is calculated with detailed procedure of the iteration optimization is described in details by Berry et al. [175].

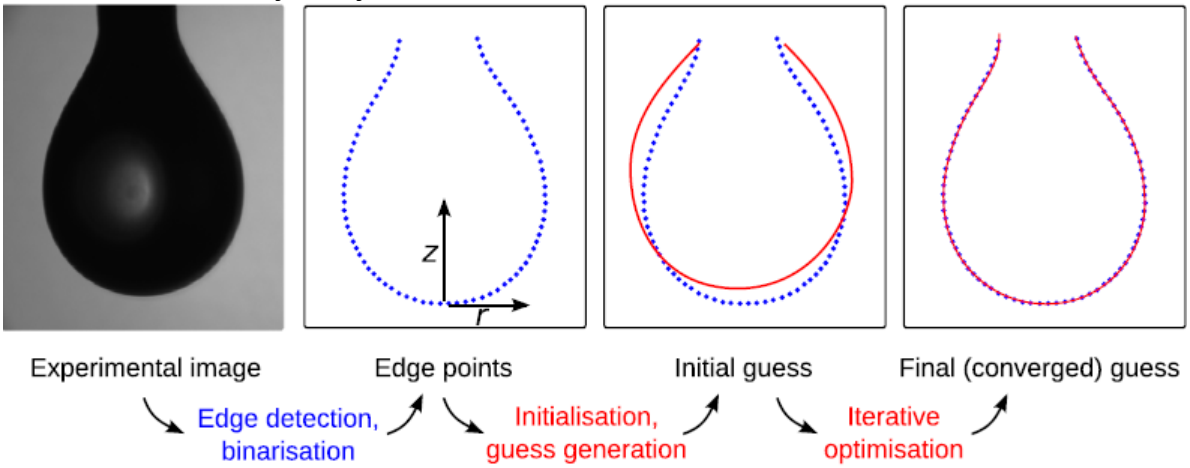

Figure 3-5: Schematic of pendant drop tensometry process, going form a raw experimental image to a fitted solution from which interfacial tension can be calculated.

3.3 Results and discussion

3.3.1 Validation of the experimental technique

New experimental technique for measuring diffusion coefficients and interfacial tension by pendant drop tensiomentry was validated in the water-CO_2 system.

3.3.1.1 Diffusion coefficients measurements in the water-CO_2 system

The experimental technique was validated by conducting the measurements of diffusion coefficients from decreasing equivalent drop diameter in the water-CO_2 system at 25 °C within a pressure range from 5 MPa up to 60 MPa. The experimental results obtained by the tensiometry method were compared with those from data in the literature published by Espinoza et al. [146] and Xu et al. and were correlated with simple models by Takahashi et al. [199] and He Lu et al. [200]. Densities of pure water and CO_2 were found in NIST database [44]. Solubility data for upper and lower phases in the water-CO_2 system were obtained from the literature by Zhao et al. [201] and by Duan et al. [202]. Agreement of the obtained diffusion coefficients with those found in the literature is sufficiently high (Figure 3-6).

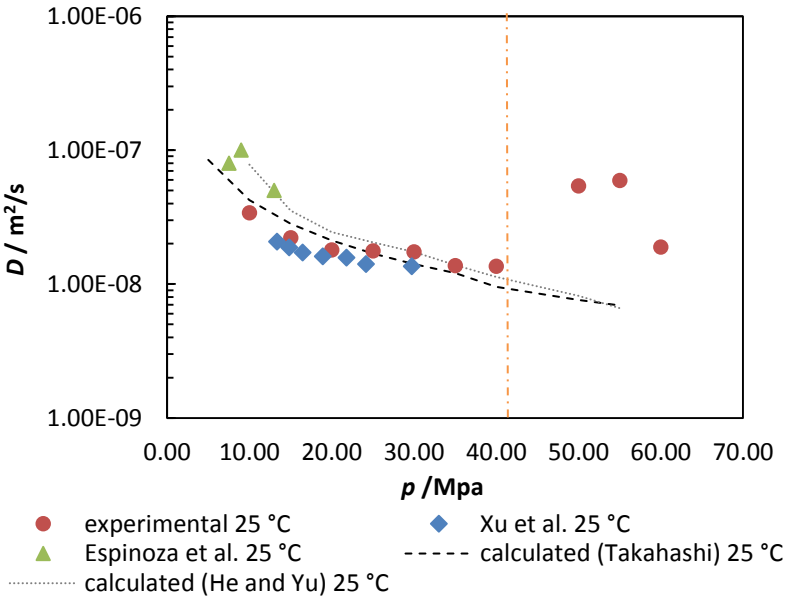

Figure 3-6: Comparison of experimentally obtain diffusivity of water in liquid CO_2 at 25 °C in pressure range up to 60 MPa with literature data and calculated by correlations. The vertical line represents a point where a CO_2 became denser of a water.

The measured values of Xu et al. are 40 % lower, but those of Espinoza et al. are 60 % higher than the model by Takahashi et al., whereas the diffusion coefficients measured in the present study are in fair agreement with the model. The average absolute relative deviation (AARD) was less than 20 %. However, major deviations were found at relatively high pressures, above 40 MPa, probably due to the instability of phases, which caused the water droplets to drip in the opposite direction, towards the ceiling of the optical high-pressure cell. The vertical line in Figure 3-6 represents the point where CO_2 became denser than water. The accuracy of results below 40 MPa was provided by measuring more than 1000 points of equivalent drop diameter as a function of time (Figure 2-7).

With increasing pressure, the slope of the plot of equivalent drop diameter depending on time (D^2/t) has been changed from the negative to almost zero. This can be explained by the higher absorption of the surrounding CO_2 at higher pressure and lower evaporation of the drop. The effect of absorption of a gas phase in a water phase was observed at the beginning of every measurement, where the slope of the plot of equivalent drop diameter depending on time (D^2/t) was zero or even positive. In contrast, after a few minutes, when a water drop was sufficiently saturated with a gas phase, and the evaporation effect was dominant, the slope of the plot of equivalent drop diameter depending on time became negative. Consequently, drop diameter decreased linearly. With increased pressure at a constant temperature in the binary mixture, the slope of the plots D^2/t was slightly increased (Table 3-2).

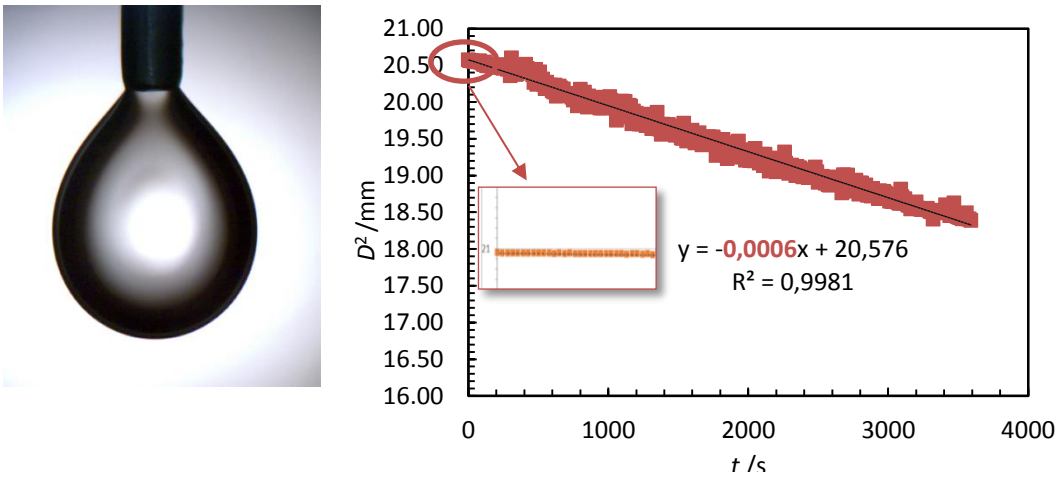

Figure 3-7: The accuracy of results provided by measuring more than 1000 points.

Table 3-2: Solubility data for the system of CO_2 and water [23]: - mole fraction of CO_2 in liquid rich phase- lower phase (S-LP), - mole fraction of CO_2 in gas-rich phase-upper phase (S-UP), diffusion coefficients of water in CO2 and corresponding slope of line in the diagram $D^2 = f(t)$.

***p* (MPa)**	***T* (K)**	**Δ*ρ* (g/ml)**	***S*-LP (g/g)**	***S*-UP (g/g)**	**D^2/t**	**D_{AB} (m2/s)**
5.01	25	870.23	0.9989	0.0011	-0.0006	6.66E-08
10.05	25	186.07	0.9978	0.0022	-0.0006	2.36E-08
15.04	25	129.33	0.9966	0.0034	-0.0007	2.44E-08
20.01	25	93.76	0.9965	0.0035	-0.0006	2.16E-08
25.08	25	67.12	0.9965	0.0035	-0.0005	1.39E-08
30.02	25	45.68	0.9964	0.0036	-0.0005	1.60E-08
35.08	25	27.69	0.9964	0.0036	-0.0004	1.22E-08
40.09	25	12.20	0.9963	0.0037	-0.0004	1.22E-08
50.05	25	1.50	0.9962	0.0038	-0.0020	5.40E-08
55.01	25	13.70	0.9962	0.0038	-0.0022	5.94E-08
60.04	25	36.80	0.9962	0.0038	-0.0007	1.89E-08
20.00	45	186.15	0.994	0.0232	-0.0025	5.42E-08
25.01	45	143.76	0.9938	0.0243	-0.0016	3.26E-08
30.10	45	112.67	0.9938	0.0253	-0.0007	1.56E-08
35.03	45	87.78	0.9935	0.0262	-0.0007	1.32E-08
40.02	45	67.35	0.9934	0.0271	-0.0006	1.10E-08

It has been observed, that the most important parameter for the diffusion determination is the change of the equivalent drop diameter as a function of time. Namely, the density of the drop surrounding phase is changing by increasing pressure and temperature and therefore the size and geometric shape of the drop changes considerably. At higher pressure, the interfacial tension is decreased, due to the lower force of the surrounding phase on the drop surface, a pendant drop of a higher volume is formed.
Agreement of the experimentally obtained diffusion coefficients of water in CO_2 with the ones calculated by the model of Takahashi et al. [20] under the same conditions, is presented in Figure 3-8. Agreement is adequate and is presented for diffusion coefficients measured at a range of pressures from 20 MPa, up to 40 MPa at two different temperatures, 25 °C and 45 °C. In the case of the first isotherm, CO_2 is liquid and supercritical at the higher temperature conditions.

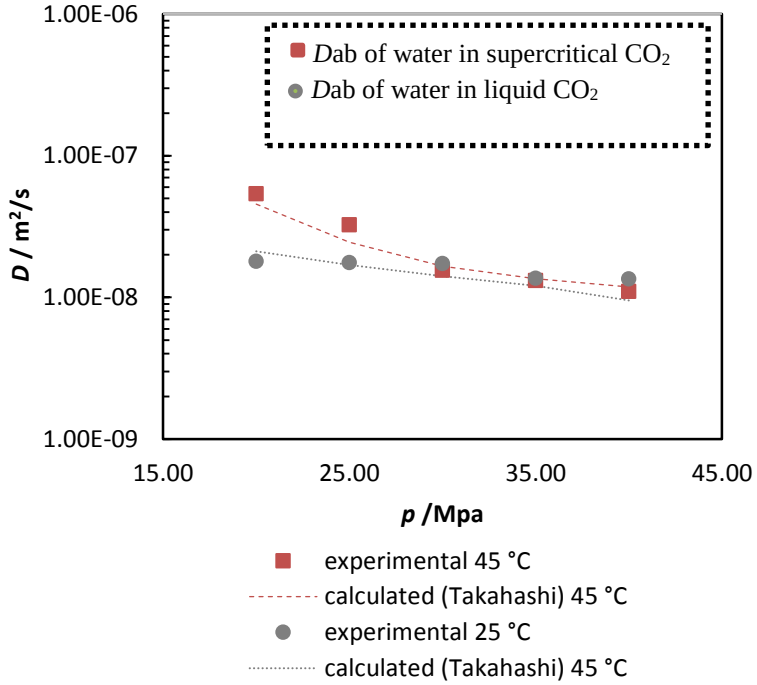

Figure 3-8: Comparison of experimentally obtained and calculated [199] diffusion coefficients of water in supercritical CO_2 at 45 °C and in liquid CO_2 at 25 °C in the pressure range from 20 MPa to 40 MPa.

As reported in the literature, the measured rate of water diffusion in CO_2 is much faster (3 x 10^{-8} up to 7 x 10^{-8} m^2/s) than the opposite, diffusion of CO_2 in water (2 x 10^{-9} to 5 x 10^{-9} m^2/s), despite the higher density of CO_2 compared to H_2O at the same conditions [149, 203]. Similarly, the measured rate of water diffusion in CO_2 a is much faster than diffusion of acetone in CO_2 [146] A possible reason is that the diffusion coefficient decreases as the mass and size of an evaporating molecules increase [204]. Experimental values for the diffusion of CO_2 in H_2O at even higher temperatures (468 °C $\leqslant T \leqslant$ 688 °C) were reported to have considerable scatter and relative uncertainties (38 % to 66 %). This fact clearly indicates that it is necessary to research and develop reliable experimental procedures for obtaining diffusion rates in different systems of compounds at even higher temperatures.

3.3.1.2 Interfacial tension measurements in water-CO_2 system

The pendant drop method was validated by conducting measurements of the surface tension of water droplet at 25 °C and 40 °C in surrounding air and ethyl acetate phase. The measured surface tension values are in a close agreement with the literature (Table 3-3).

Table 3-3: Validation and comparison of surface tension data with literature values at a moderate conditions [205][a] and [183][b].

Temperature	Droplet phase	Surrounding phase	Exp. *ITF* (m/Nm)	Lit. *ITF* (mN/m)
25 °C	Water	Air	71,73±0.18	71.99±0.05[a]
40 °C	Water	Air	69.71±0.11	69.60±0.30[a]
25 °C	Water	Ethyl acetate	6.78±0.30	6.63±0.02[b]

The accuracy of the experimental technique at elevated pressures was justified by comparing the experimentally obtain an interfacial tension of the (H_2O-CO_2) systems at 25 °C and 40 °C to literature values (Table 3-4). From the Figure 3-9, it can clearly be seen that interfacial tension decreases as CO_2 pressure increases, and it remains nearly constant once the CO_2 vapor-liquid boundary (at 25 °C and 6.43 MPa) is reached. Such a dependence on pressure has been attributed to the isothermal compressibility of CO_2 and its impact on the Helmholtz energy density (Chiquet et al., 2007).

Table 3-4: Water-CO_2 interfacial tension at 25 °C and 40 °C in pressure range up to 25 MPa.

T (°C)	P (MPa)	ρ_{Brine} (kg/m^3)	ρ_{CO2} (kg/m^3)	γ (mN/m)
25 ± 0.10	0.10	997.05	/	71.73 ± 0.18
	1.82	997.90	35.78	61.30 ± 0.33
	3.94	998.80	91.74	47.43 ± 0.25
	6.14	999.69	199.80	35.10 ± 0.13
	7.98	1000.60	779.28	31.20 ± 0.08
	10.02	1001.50	817.63	29.16 ± 0.17
	12.00	1002.30	845.47	27.10 ± 0.36
	14.02	1003.20	867.12	26.86 ± 0.21
	16.00	1004.10	885.09	26.42 ± 0.31
	18.00	1005.00	900.56	25.87 ± 0.09
	19.90	1022.80	913.59	25.08 ± 0.04
40 ± 0.10	0.10	992.21	/	69.71 ± 0.11
	2.00	995.60	37.13	60.07 ± 0.23
	4.01	998.77	83.76	49.40 ± 0.62
	5.59	1001.77	149.26	41.78 ± 0.15
	8.05	1003.93	277.90	35.65 ± 0.47
	10.01	1006.36	628.61	31.41 ± 0.18
	12.01	1008.26	717.76	30.65 ± 0.56
	14.06	1009.88	763.27	29.80 ± 0.17
	16.22	1011.14	794.90	29.49 ± 0.36
	18.35	1012.09	819.51	29.37 ± 0.18
	20.01	1012.72	839.81	29.08 ± 0.22
	25,00	1012.90	879.49	27.68 ± 0.29

Expanded uncertainties at 95% confidence are $u(T)$=0.06 °C , $u(p)$=0.06 MPa $u_{25°C}(\gamma)$=0.0098 y *and* $u_{40°C}(\gamma)$=0.014 y.

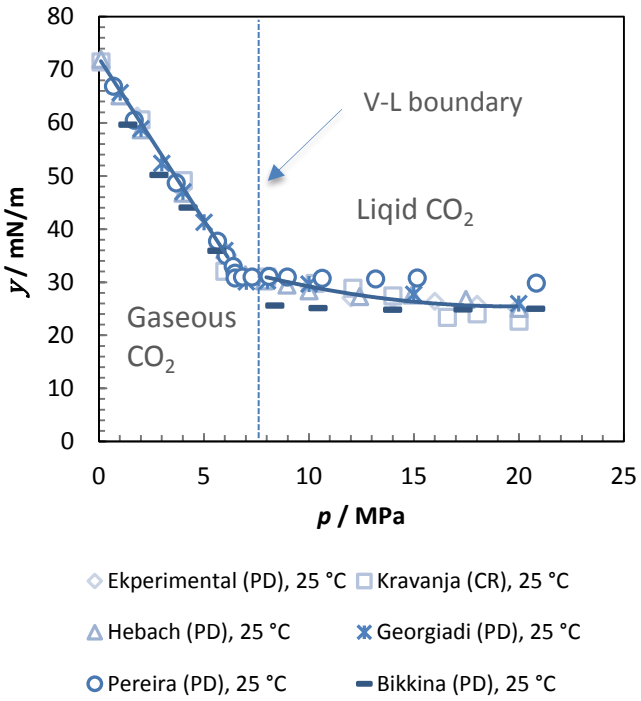

Figure 3-9: Comparison between water-CO_2 interfacial tension determined experimentally and literature data [118] (%AAD is 4.01 %), [206] (%AAD is 2.78 %), [162] (%AAD is 2.23 %), [166] (%AAD is 5.23 %), [207] (%AAD is 7. 34 %) at 25 °C.

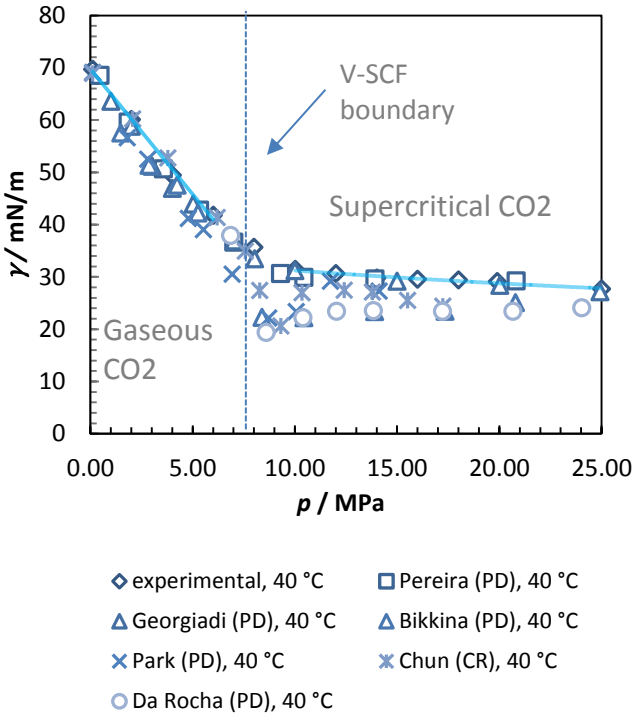

Figure 3-10: Comparison between water-CO_2 interfacial tension determined experimentally and literature data [166] (%AAD is 3.28 %), [162] (%AAD is 3.09 %) [207] (%AAD is 14.83 %), [208] (%AAD is 12.92 %), [155] (%AAD is 7.24 %), [209] (%AAD is 18.5 %) at 40 °C.

In order to calculate the absolute relative deviation between the measured points and those from literature, interfacial tension values at 25 °C were fitted with linear function in the region of low pressure (p>6.43 MPa) and with polynomial function at high pressure (p<6.43 MPa):

$$\gamma / (mNm^{-1}) = a_1 - b_2 \cdot (p / MPa) \tag{3.29}$$

$$\gamma / (mNm^{-1}) = a_1 - b_2 \cdot (p / MPa) + c(p / MPa)^2 \tag{3.30}$$

where p is the pressure and a_1, b_1, and c are fitting parameters. For the isotherm, at 40 °C, more gradual change of slope with increasing pressure is observed (transition of the CO_2 vapor-supercritical phase, 31.10 °C, and 7.38 MPa) (Figure 3-10). The experimentally obtained values were fitted with a polynomial function of third order:

$$\gamma / (mNm^{-1}) = a_1 - b_2 \cdot (p / MPa) + c \cdot (p / MPa)^2 - d \cdot (p / MPa)^3 \tag{3.31}$$

where p is the pressure and a_1, b_1, c, and d are fitting parameters. For both isotherms, the parameters and correlation coefficients with corresponding absolute average deviation and the standard error are presented in Table 3-5.

Table 3-5: Fitting parameters of the interfacial tension for (H_2O/CO_2) system, where p_i* values correspond to the intersection pressure of the two lines in linear-polynomial correlation.

	Linear correlation $p<p_i^*$				**polynomial correlation** $p>p_i^*$				
***T* (°C)**	a_1	b_1	σ	Δ_{AAD}	a_1	b_1	c_1	σ	Δ_{AAD}
25	72.222	6.1117	0.18	0,78	40.338	1.5782	0.0401	0.18	1,14
	polynomial correlation								
***T* (°C)**	a_2		b_2	c_2	d	σ		Δ_{AAD}	
40	71.406		7.042	0.3868	0.007	0.29		1.49	

The absolute average deviation and standard error were calculated by $\Delta_{AAD} = \sum_{i=1}^{N} \frac{|(\gamma_i - \gamma_f)/(\gamma_i)|}{N}$ and $\sigma = \sum (\gamma_1 - \gamma_f)^2 / (j - n)$, where γ_1 is measured interfacial tension, γ_f is fitted interfacial tension, j is number of state points, and n is number of fitting parameters.

The experimental values, obtained in our research differ from those, reported by Chun (for approx. 7.24 %), where CO rise method was utilized and those of Da Rocha, obtained by the PD method, where the discrepancy is even greater (% AAD is 18.5 %). In this case, the deviation may be derived from a differing approximation of the CO_2 water saturated densities to those of pure water at certain conditions. The water-CO_2 interfacial tension reported by Bikkini is questionable since the omission of the saturated density which is usually utilized for calculation of the interfacial tension. Equilibrium is, therefore, crucial to obtain reliable results. In this case, the composition of the gaseous phase remained constant at a certain pressure and temperature due to the absence of solubility change. Figure 3-11 presents plotted values of an average absolute deviation of the fitted interfacial tension function with experimental points and literature at 25 °C and 40 °C. Our results are in good agreement with data from the literature. Slightly deviation of results is observed in the vicinity of the critical point of CO_2, where small changes in pressure and temperature results in large changes in density. Many of the published (H_2O-CO_2) interfacial tension values are inferred from measured capillary lengths, not efficient system cleanness, and from the approximation of the CO_2 saturated water densities to that of pure water. The values of interfacial tension linearly depend on the density difference between the two fluids. Required CO_2 saturated water densities were obtained experimentally using vibrating tube densitometer. Measured CO_2 saturated water densities are in good agreement

with data from literature at 25 °C in the pressure range up to 20 MPa with low relative deviation compared to those from Hebach et al.[210] (%AAD of 0.18 %) and Efika et al. [211] (%AAD of 0.24 %). The density values of the water phase saturated with CO_2 were assumed to be that of pure CO_2 under the same pressure and temperature conditions since there is no substantial influence on interfacial values [109]. Pereira et al. [166] reported that approximation of the CO_2 saturated water densities to that of pure water would result in lower values of density difference and therefore, in underestimation of the interfacial tension values.

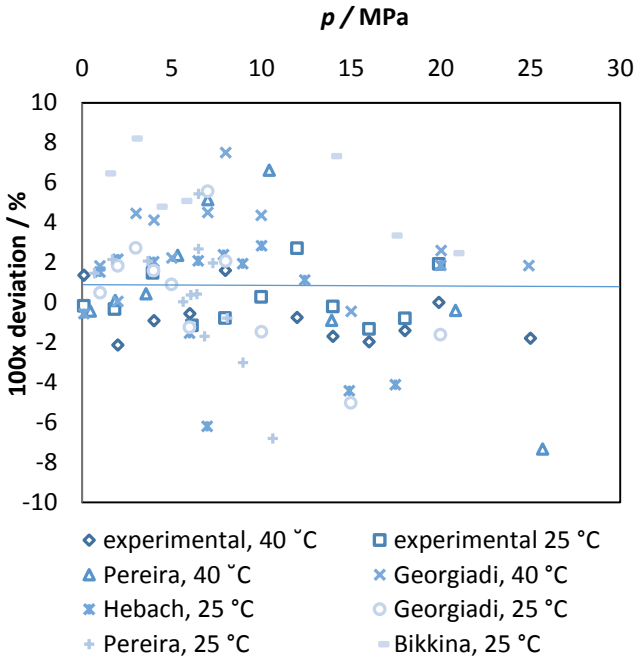

Figure 3-11: Average absolute relative deviation (AAD) of the experimental interfacial tension to fitted values. Average absolute relative deviation (AAD in %) of the fitted interfacial tension to literature values [166], [162, 206] to fitted interfacial tension.

The overall relative standard uncertainty u_r of γ was calculated by combining the standard uncertainties δT, δp and $\delta \Delta\rho$ in the temperature, pressure and density difference respectively with the largest values of the corresponding partial derivatives found in the ranges investigated (equation 3.32).

$$u_r^2 = \left[\frac{1}{\gamma}\left(\frac{d\gamma}{dt}\right)_p \delta T\right]^2 + \left[\frac{1}{\gamma}\left(\frac{d\gamma}{dp}\right)_T \delta p\right]^2 + \left[\frac{u\Delta\rho}{\Delta\rho}\right]^2 + \left[\frac{\sigma(\gamma)}{\gamma}\right]^2 \tag{3.32}$$

For (H_2O-CO_2) interfacial tension at 25 °C and 40 °C in pressure range up to 25 MPa expanded uncertainties at 95 % confidence are u(T)=0.06 °C, u(p)=0.06 MPa, $u_{25°C}(\gamma)$=0.0098 γ and $u_{40°C}(\gamma)$=0.014 γ. Absolute relative deviation of the density difference between both phases obtained in this study was compared to the values of Efika et al. [211] and was less than 0.4 %.

3.4 Measurements in propylene glycol/CO_2 system

The high-pressure tensiometry method was further tested at higher temperatures by measuring a synthetic organic compound, propylene glycol, in supercritical CO_2.

3.4.1 Diffusion coefficient measurements of propylene glycol/CO_2 system

Diffusion coefficients of propylene glycol in supercritical CO_2 were measured at 125 °C and 150 °C and at pressures ranging from 5 MPa, up to 17.5 MPa. The evaporation of propylene glycol and its concomitant shorter observation time (a drop was fully evaporated in approximately 20 min) was assumed to result in lower accuracy compared to water measurements. Nevertheless, similar general trends were observed for the diffusion coefficients measured at different combinations of temperature and pressure, which affected the mixture density; these were compared to the available literature [212] [204] with a satisfactory degree of congruence.

As illustrated in Table 3-6 and Figure 3-12, diffusivity decreases as the pressure increases under isothermal conditions, where the decrease is more noticeable at lower pressures. For example, the diffusivity of propylene glycol in CO_2 varies from 1.35E-09 (m^2/s) at 150 °C at 5 MPa up to 9.67E-10 (m^2/s) at 17.5 MPa. This can be explained as the result of a high number of molecular collisions and the smaller mean free path between them. On the other hand, diffusivity increases as the temperature increases at constant pressure, where greater dependence on the temperature is observed at a lower pressures. Results show that the diffusivity of propylene glycol in CO_2 increases with a temperature gradient of 25 °C at 5 MPa by more than 30%.This may be linked to the decrease in the solvent density of CO_2 with the temperature increase and consequently be related to the propylene glycol molecule's more rapid movement (diffusion), due to the high kinetic energies [212]. It was found that the diffusivity of water in CO_2 is higher in comparison to propylene glycol, probably because the diffusivity decreases as the mass and size of an evaporating molecules increase [204].

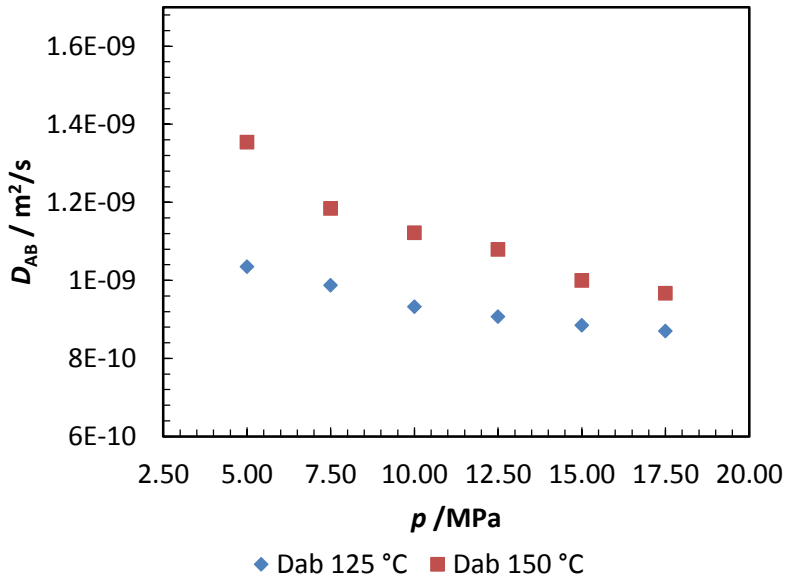

Figure 3-12: Diffusion coefficients in propylene glycol saturated the solution with CO_2 at 125 °C and 150 °C in the pressure range from 5 up to 17.5 MPa.

Additionally, solubility was determined for the systems of propylene glycol in supercritical CO_2 at 125 °C and 150 °C at pressures ranging from 5 MPa, up to 17.5 MPa in relation to the diffusion coefficient, as presented in Table 3-6. In general, for the binary system, it was observed that solubility of CO_2 in the heavier propylene glycol reached phase increases with

increasing pressure at a constant temperature. In contrast, the composition of the gaseous phase is not influenced by pressure or temperature. On average, the solubility of propylene glycol in the light phase of CO_2 is about 30 wt. % [182]. Even small changes in pressure and temperature in the range of investigated conditions are reflected in significant changes in solvent density.

Table 3-6: Solubility data for the system of CO_2 and propylene glycol [7]: - mole fraction of CO_2 in propylene glycol rich phase- lower phase (S-LP), - mole fraction of CO_2 in gas rich phase-upper phase (S-UP), diffusion coefficients of propylene glycol in CO_2 atmosphere with the corresponding slope of a line in the function $D^2 = f(t)$.

p (MPa)	T (K)	$\Delta\rho$ (kg/m^3)	S-LP (g/g)	S-UP (g/g)	D^2/t	D_{AB} (m^2/s)
5.02	125	963.27	0.6998	0.0440	-0.0026	1.03E-09
7.50	125	945.48	0.7061	0.7130	-0.0025	9.87E-10
10.00	125	927.73	0.7074	0.9010	-0.0024	9.33E-10
12.51	125	910.06	0.7074	0.1072	-0.0024	9.07E-10
15.03	125	892.52	0.7259	0.1178	-0.0022	8.85E-10
17.50	125	875.13	0.7009	0.1208	-0.0021	8.70E-10
5.03	150	909.269	0.7021	0.0374	-0.0035	1.35E-09
7.51	150	873.34	0.7124	0.0452	-0.003	1.18E-09
9.98	150	834.64	0.7124	0.0667	-0.0027	1.12E-09
12.52	150	793.29	0.7193	0.0798	-0.0027	1.08E-09
15.00	150	749.77	0.7124	0.0975	-0.0027	1.01E-09
17.51	150	704.97	0.7098	0.1118	-0.0025	9.67E-10

3.4.2 Density and interfacial tension of a CO_2-saturated propylene glycol solution

Interfacial tension and density of a CO_2-saturated propylene glycol solution were obtained using the pendant drop method, simultaneously with drop diameter measurements. Density and interfacial tension as functions of pressure and temperature are illustrated in Figures 3-13 and 3-14. Density for all observed systems increased linearly with pressure as a consequence of liquid compression and low solubility [187, 213].

In the case of interfacial tension, significantly lower values were attained for binary system propylene glycol-CO_2 in comparison to those measured for the water-CO_2 system [118]. This could be due to the lower attraction between molecules and the corresponding surface energies. Additionally, as pressure increased, a consequent decrease in interfacial tension was noted. The deviation of interfacial tension by our measurements is lower than 1 %, even though a drop diameter rapid decrease due to the evaporation effect. Tableted values of density and interfacial tension measurements are provided in Appendix-Table A2-2.

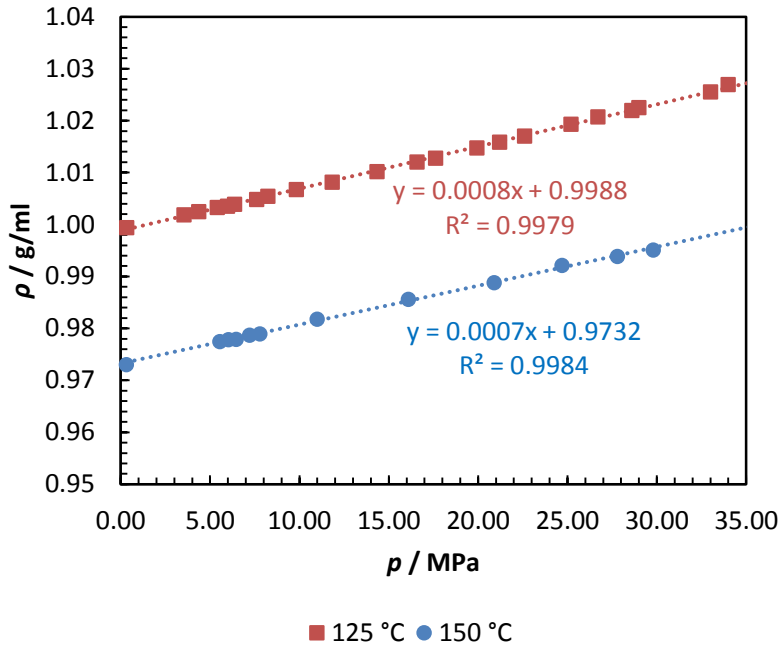

Figure 3-13: Density of the propylene glycol saturated the solution with CO_2 at 125 °C and 150 °C in the pressure range from 5 up to 17.5 MPa.

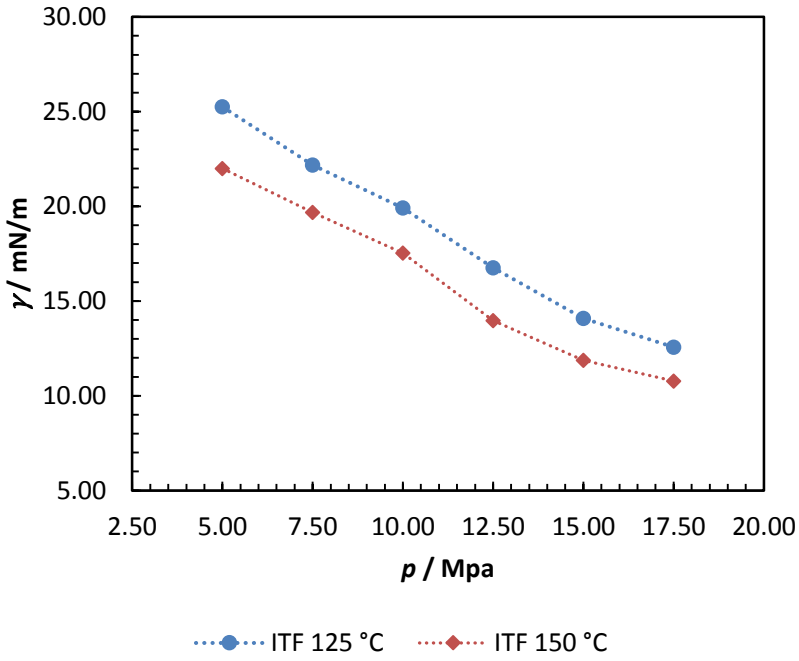

Figure 3-14: Interfacial tension (IFT) of the propylene glycol saturated the solution with CO_2 at 125 °C and 150 °C in the pressure range from 5 up to 17.5 MPa.

3.5 The effect of argon contaminant on interfacial tension, diffusion coefficients and storage capacity in carbon sequestration

The effect of argon as a co-contaminant in a CO_2 stream on interfacial tension (ITF), diffusion coefficients and storage capacity was studied using the pendant drop method. ITF measurements were performed at the pressures and temperatures at which most of the deep saline aquifers are found, and where CO_2 has the highest density (a maximum mass of CO_2 can be stored) (Figure 3-15). Earth's surface temperature variation is considered as ranging from 10 up to 20 °C/km, and the geothermal pressure gradient between 10 MPa/km. The selected temperature and pressure range corresponds to a depth between 0.7 and 3.5 km. For pressures greater than 35 MPa (or reservoirs deeper than 3.5 km), the density change is found to be minimal, and compression and injection costs become uneconomic [214].

The phase diagram of CO_2 can be seen in Figure 3-15. It is clear that CO_2 is most likely to be in a supercritical state in underground aquifers. Additionally, the diffusional mass transfer of injected gases in brine is of major importance in order to understand pore behaviour, the risk of diffusive CO_2 loss through cap rock, dispersion during flow and convection of CO_2-saturated brine in the subsurface reservoir [215]. In our study, the diffusion coefficients of geological water in a CO_2/argon system were measured by using the new method based on reliable pendant drop tensiometry [216].

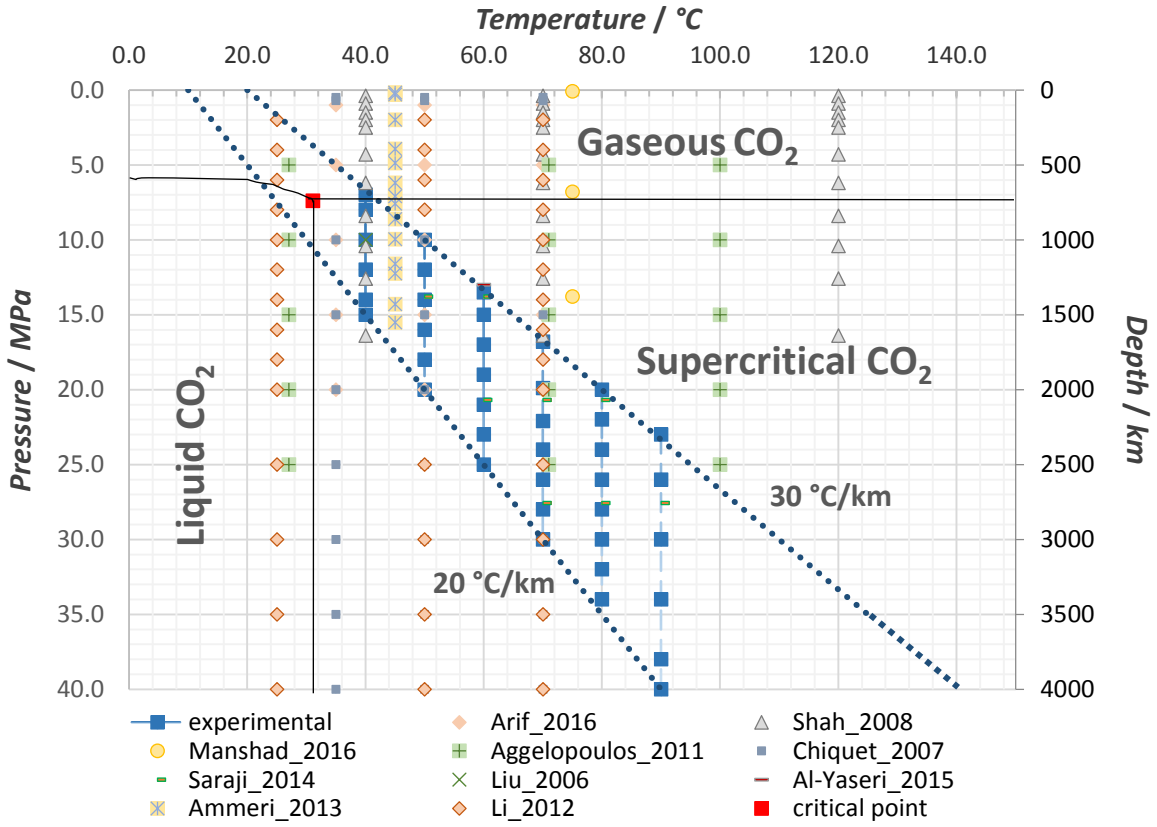

Figure 3-15: Experimental conditions used in this study compared to the literature one Arif et al. [217]; Shah et al. [172]; Manshad et al. [218]; Aggelopoulos et al. [164]; Chiquet et al. [163]; Saraji et al. [160]; Zhang et al. [219]; Al-Yaseri et al. [171]; Ameri et al. [220] and Li et al. [169].

3.5.1 Effect of an argon co-contaminant on interfacial tension at 45 °C

The strong increase in isothermal interfacial tension properties at 45 °C was observed with an increase in Ar co-contaminant from 5 vol. % to 100 vol. %. The measured brine-Ar interfacial tension was significantly higher than the figures for brine-CO_2 or brine-50 vol. % CO_2+50 vol. % Ar interface (Figure 3-16 and Table A2-2). At 10 MPa, interfacial tension increases from 30.91±0.54 mN/m in the presence of 5 vol. % Ar up to 46.99±0.27 mN/m in the presence 50 vol. % Ar content and finally up to 60.42± 0.60 mN/m when pure Ar is used. The low impact of pressure on the interfacial tension in the presence of pure Ar is due to lower gas density at the gas-brine interface. In the presence of the argon, density difference was higher, since Ar has a lower density than CO_2 at investigated conditions. When the interfacial tension data of saline water and pure Ar are compared with those of the literature [178] at comparable pressure range, the agreement is found to be within 2 mN/m (Figure 3-16). A similar decreasing trend is reported for the viscosity of brine-CO_2+Ar systems [221]. The effect of 5vol. % and 10 vol. % Ar impurities on IFT is minor and is in the same order of magnitude as a brine-CO_2 IFT. A similar effect on the IFT of brine-CO_2 in the presence of another non-condensable gas (N_2) has also been reported [171].

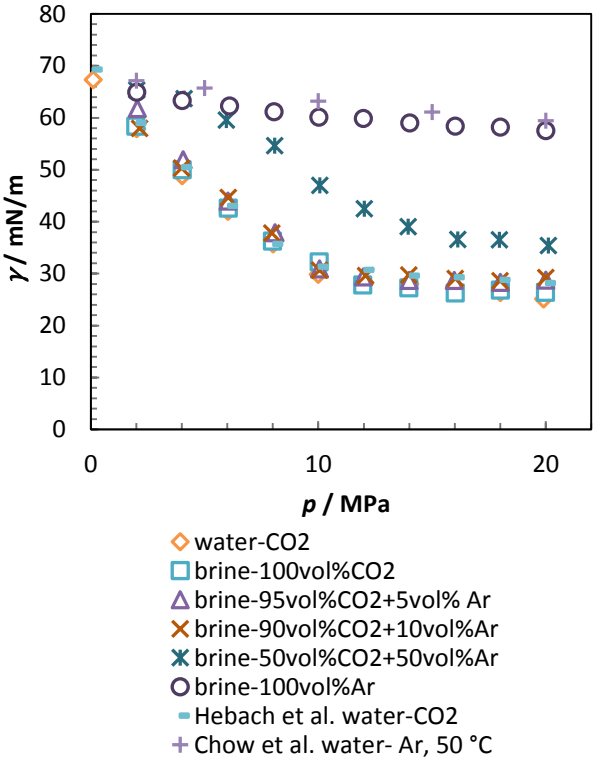

Figure 3-16: Increase in brine-CO_2+Ar interfacial tension with an increase in Ar content at 45 °C in pressure range up to 20 MPa. Comparison of the experimental points at the interface of brine-Ar to the [178] water-ar at 50 °C.

3.5.2 Brine-supercritical fluid interfacial tension and density

Chemically inert argon will be present in most injected CO_2 streams at small concentrations ranging up to 5 vol. % [170]. In our study, we focused on measuring brine-CO_2 interfacial tension and brine mixture (CO_2 and Ar) interfacial tension with 5 vol. % and 10 vol. % of argon content at pressures from 7.5 MPa up to 40MPa, and in a temperature range from 40 °C up to 90 °C. These conditions have not previously been explored, despite their importance for carbon sequestration processes.

In order to obtain the desired interfacial tension, knowledge of the accurate density difference between the brine-rich phase and the CO_2 rich phase is needed. The density of the CO_2 rich phase was calculated from the NIST database [109], since it is known that there is no measurable difference between the density of the CO_2- rich phase and that of pure CO_2 [214]. On the other hand, the density of the brine-rich phase, being a strong function of pressure and temperature, was obtained experimentally. The effect of pressure and temperature on the density of the brine-rich phase (brine saturated solutions with CO_2) is presented in Figure 3-17 and Appendix-Table A2-4, 5 and 6. Density increased linearly with pressure as a consequence of the penetration of gas molecules into the brine solution (increased solubility) and decreased considerably with a rise in temperature from 40 °C up to 90 °C for all systems in the investigated pressure range. It has to be highlighted that density will correspond to the molar solubility. For a wider pressure range, this relationship is not linear. Furthermore, the density of the brine-rich phase additionally decreased when 5 vol. % Ar and 10 vol. %. Ar was introduced to all investigated systems. This is the consequence of the lower solubility of Ar in brine/water. The alteration of density when performing measurements with the densitometer was taken under consideration since equilibrium has been waited.

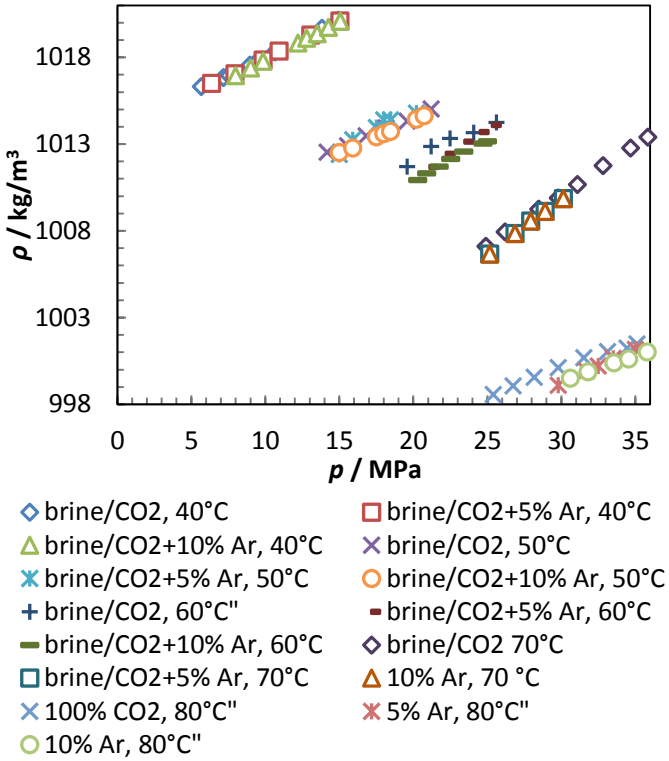

Figure 3-17: Density of brine saturated solution with CO_2 and CO_2/Ar mixtures with 5 vol. % and 10 vol. % of argon content.

As shown in Figure 3-18 and 3-19, at a constant temperature, interfacial tension decreases as a function of pressure. This could be linked to an increase in CO_2 or to Ar solubility in brine as pressure increases. At lower pressures, the decrease was sharper, and the opposite was true at higher pressures (p>10MPa); the rate of interfacial tension decrease became weaker and finally vanished and inclined asymptotically to a constant value (p>15MPa). Under constant water salinity, the dependence of interfacial tension on the pressure at isothermal conditions was similar to that reported in the literature for a CO_2/NaCl solution and CO_2/$CaCl_2$ [162, 164].

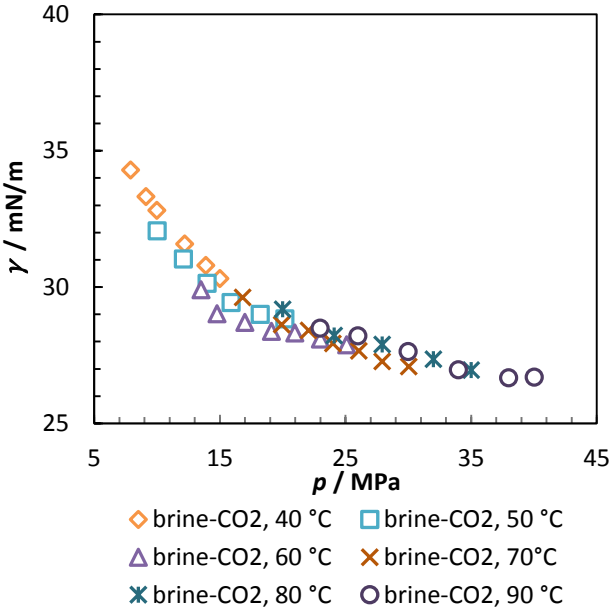

Figure 3-18: The Interfacial tension of brine-CO_2 at conditions relevant to carbon sequestration.

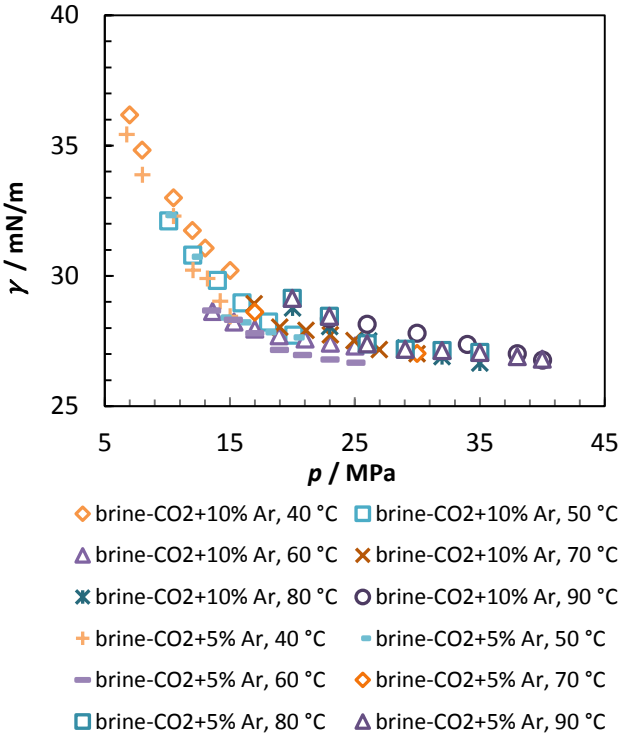

Figure 3-19: The interfacial tension of Brine-mixture (CO_2+Ar) with 5 vol. % and 10 vol. % of argon.

3.5.3 Solubility data and diffusion coefficient

Knowledge about the equilibrium solubility data for the lower and upper phases was required for calculating diffusion coefficients. Equilibrium solubility data were determined for the system water-supercritical argon at 45 °C and at pressures ranging from 5 MPa to 30 MPa in relation to the diffusion coefficient, as presented in Table 3-4. In general, for the binary system, it was observed that the solubility of Ar in the heavier water phase increased with increasing pressure at a constant temperature. In contrast to the CO_2-water binary system, the solubility of the Ar-water system is substantially less. The composition of the gaseous phase is not influenced by pressure or temperature It was established that even small changes in pressure and temperature in the range of the conditions being investigated were reflected in significant changes in solvent density. Equilibrium has been attained after a certain time, therefore the composition of the gaseous phase remained constant at certain pressure and temperature.
Many studies in the literature cover the diffusion coefficients of dense gases in liquids, but little is found about the contrary phenomenon of liquid diffusion into CO_2 and nothing about liquid diffusion in argon. As reported in the literature, the measured rate of water diffusion in CO_2 is much faster (3×10^{-8} up to 7×10^{-8} m^2/s) than the opposite process, the diffusion of CO_2 in water (2×10^{-9} to 5×10^{-9} m^2/s), despite the higher density of CO_2 compared to H_2O under the same conditions [149, 203]. As illustrated in Figure 3-20, diffusivity decreases as the pressure increase under isothermal conditions, with the decrease being sharper at lower pressures. It was found that the diffusivity of water in Ar is higher in comparison to that for water in CO_2, probably because the diffusivity decreases as the mass and size of the surrounding gas molecules increase [204]. The measured brine-CO_2 system at 45 °C showed no significant difference to the water-CO_2 system. Small quantities of salt in water had a minor effect on diffusion coefficients, as in Table 3-7.

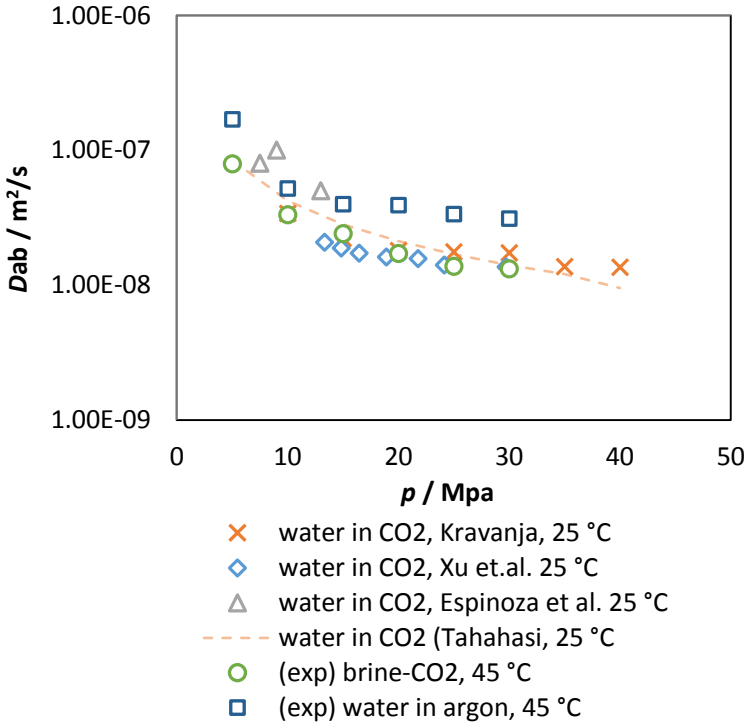

Figure 3-20: Diffusivity of brine in CO_2 and diffusivity of water in Ar at 45 °C compared to literature data (Kravanja et al. [222], Xu et al.[222], Takahashi et al.[199] and Espinoza et al. [146].

Table 3-7: Solubility data (experimental) for the system of Ar and water: - mole fraction of Ar in liquid-rich phase- lower phase (S-LP), - mole fraction of Ar in gas-rich phase-upper phase (S-UP), diffusion coefficients of water in Ar and corresponding slope of line in the diagram $D^2 = f(t)$.

***p* (MPa)**	***T* (°C)**	***S*-LP (g/g)**	***S*-UP (g/g)**	D^2/t	D_{AB} (m_2/s)
Water+Ar					
5	45	0.9995	0.0321	-7.00E-04	1.69E-07
10	45	0.9993	0.0323	-3.00E-04	5.18E-08
15	45	0.9991	0.0461	-3.00E-04	3.97E-08
20	45	0.9988	0.0593	-4.00E-04	3.92E-08
25	45	0.9986	0.0587	-4.00E-04	3.36E-08
30	45	0.9985	0.0653	-7.00E-04	3.12E-08

Table 3-8: Solubility data [223] for the system of CO_2 and saline water (0.1 M NaCl): - mole fraction of CO_2 in liquid-rich phase- lower phase (S-LP), - mole fraction of CO_2 in gas-rich phase-upper phase (S-UP), diffusion coefficients of saline water (brine) in CO_2 and corresponding slope of line in the diagram $D^2 = f(t)$.

***p* (MPa)**	***T* (°C)**	***S*-*LP* (g/g)**	***S*-UP (g/g)**	D^2/t	D_{AB} (m_2/s)
brine+CO_2					
5	45	0.9972	0.0134	-1.80E-03	7.93E-08
10	45	0.9963	0.0190	-1.00E-03	3.31E-08
15	45	0.9949	0.0202	-1.00E-03	2.40E-08
20	45	0.9943	0.0212	-8.00E-04	1.72E-08
25	45	0.9938	0.0220	-7.00E-04	1.38E-08
30	45	0.9935	0.0228	-7.00E-04	1.32E-08

3.5.4 Potential implications for geological sequestration

The interfacial interaction (safe storage capacity) and diffusion measurements (effective diffusion coefficients) reported in this chapter have important potential implications for CO_2 geological sequestration and are a step forward in the interaction of argon presence in co-injection scenarios.

3.5.4.1 Critical capillarity threshold pressure and storage capacity

The undesirable CO_2 breakthrough in a geological formation may occur when the overpressure (the pressure difference between the injected fluid and the geological saline water) overcomes the critical threshold capillary pressure required for the saline water/fluid meniscus to go through a pore throat in the porous caprock seal [164]. Critical capillary pressure (*P*c) is estimated by the Laplace law:

$$Pc = Pf - Pw = \frac{2IFTcos\phi}{R}, \tag{3.29}$$

where ITF is the interfacial tension between the saline geological water and the injected fluid (CO_2 and Ar), ϕ is the contact angle of the seal mineral/saline water/injected fluid system, and *R* the size of the largest cylindrical pore radius in the porous seal. The maximum injected fluid overpressure that the caprock can hold is easily expressed as a storage capacity. The maximum height H of the injected CO_2 column beneath the caprock seal and underlying aquifer is obtained by dividing the critical capillary pressure (*P*c) by the buoyancy effect:

$$H = \frac{2ITF_{w,f}\cos\varphi}{(\rho_w - \rho_f)gR} \tag{3.30}$$

where ρ_w and ρ_f are the saline water and injected fluid densities at the desired pressure and temperature. Furthermore, the storage capacity can also be expressed in terms of mass stored fluid per unit surface of the geological formation:

$$M = \rho_f H\varphi(1 - S_w) \tag{3.31}$$

where φ is the porosity and S_w is the residual saline water saturation in the reservoir. We used a reasonable porosity of 20 % and a residual water saturation of 30 %. Critical capillary pressure, the maximum height *H* of injected fluid and the storage capacity were calculated for caprock depths ranging from 0.68 km to 3.5 km temperature and pressure conditions typical for carbon sequestration. In the calculations, the wettability of a shale mineral/geological saline water/CO_2 system was taken from data in the literature [224]. Since only a small amount of Ar (5 vol. % and 10 vol. %) was present in the investigated injection fluid, we assumed the wettability to be about the same as for the system with pure CO_2. The cylindrical pore radius R in the porous seal was assumed to be the same at all depths, while in reality, R decreases with depth [163]. Consequently, storage of a pure CO_2 beneath a caprock seal should increase with depth.

The results obtained by this calculation are presented in Appendix-Table A2-4, A2-5, and A2- 6. Interfacial tension was only slightly increased or was the same when 5 vol. % and 10 vol. % Ar were co-injected. As a result, there was no significant difference or increase in critical capillary threshold pressure. However, the maximum height *H* and storage capacity did change considerably. This can be explained by the fact that maximum storage capacity also depends on the injected fluid density and consequently on the buoyancy effect. Storage capacity decreased from the scenario where pure CO_2 was injected, down to the scenario where 5 vol. % and 10

vol. % Ar were co-injected into the CO_2 stream (Figure 3-21). The decrease was considerable at all depths tested. For example, at a depth of 2 km, the maximum decrease in storage capacity was observed. Storage decreased from 27.75 Mt/km^2 for the pure CO_2 stream to 23.12 Mt/km^2 for 5 vol. %, and finally to 20.44 Mt/km^2 for 10 vol. % Ar. In the case of 5 vol. % and 10 vol. % Ar, the contamination buoyancy effect prevailed over the interfacial properties and decreased storage capacity [112].

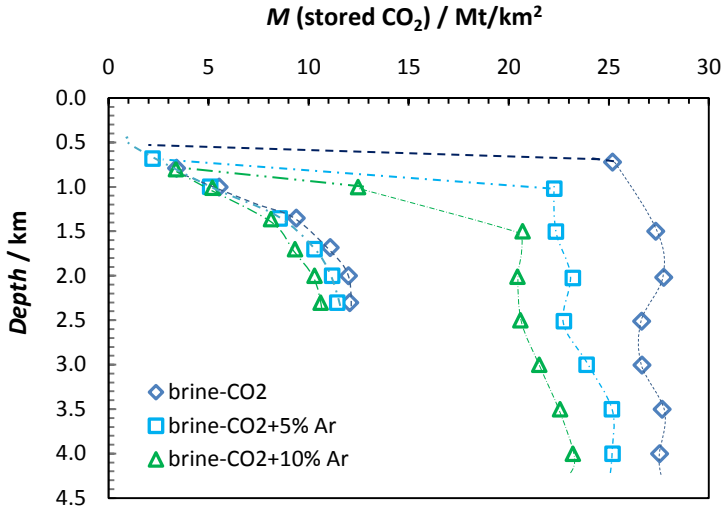

Figure 3-21: Storage capacities for a scenario when pure CO_2 was injected and when 5 vol. % and 10 vol. % Ar were co-injected in CO_2 stream [112].

Table 3-9: Effect of common impurities in CO_2 stream on ITF (interfacial tension, bouncy, pressure threshold security and storage capacity.

Impurity in CO_2 stream	Interfacial tension	Contact angle	Density (bouncy effect)	Pressure threshold security (p_c)	Storage Capacity (Mt/km^2)
Ar (this study)	Increased (50 vol. %) /negligible (5 vol. % in 10 vol. % Ar)	Assumed to have no or negligible effect (sandstone surface)	Increased	Increased (50 vol. %)/negligible (5 vol. % in 10 vol. % Ar)	Decreased considerably (5 vol. % in 10 vol. % Ar)
N_2 [171]	Increased (100 % N2), small increase (50 moll % N_2)	Negligible effect (core from Gipps land Basin)	Increased	Increased slightly/ negligible (50 moll % N_2)	Decreased considerably
SO_2 [160]	Decreased linearly (from 1wt. % up to 6 wt. %)	Not affected (quartz substrates)	decreased	May increase the risk of gas leakage through the cap rock	Increased
H_2S [172]	Decreased considerably	Assume complete wetting of the cap rock	Increased slightly	May increase the risk of gas leakage through the cap rock	Depend on H_2S content (100 % H_2S decreased capacity)

A similar conclusion can be reached when other non-condensable fluids like N_2 and O_2 and H_2 are co-injected. Although critical capillary threshold pressure is slightly increased, overall storage capacity decreased. On the other hand, contaminants that are more condensable than CO_2 can increase storage capacity but may also increase the risk of gas leakage through the caprock, since interfacial tension decreases when SO_2 or H_2S is co-injected (Table 3-9).

3.5.4.2 Effective diffusion coefficient

When the porosity and the tortuosity factors of the sedimentary rock are known, the effective diffusion coefficient (D_{eff}) of saturated geological water in CO_2 can be correlated with the experimentally obtained diffusion coefficient (D_{ab}):

$$D_{eff}=\varphi D_{ab}/\epsilon \quad (3.32)$$

where φ is the porosity factor, ϵ is the tortuosity factor of the rock, and D_{ab} is the diffusion coefficients of saturated geological water in supercritical CO_2 and Ar. To simplify, the tortuosity factor can be expressed as a function of total porosity:

$$D_{eff}=\varphi^{n}Dab \quad (3.33)$$

where n is an empirical constant, generally between 1.3 and 4.5 [215]. To evaluate effective diffusion coefficients relevant to CO_2 sequestration conditions, we assumed a porosity factor φ=0.2, an empirical constant n=2.2 and a cap rock thickness of 100 m at a reservoir depth of 1000 m (corresponding to temperatures of 45 °C and a fluid pressure of 10 MPa). Based on these assumptions, the effective diffusion coefficient of saturated geological water in supercritical CO_2 was approximately 9.02 x 10^{-10} m^2/s, and the effective diffusion coefficient of saturated geological water in supercritical Ar was around 1.48 x 10^{-9} m^2/s. Lu et al. [215] calculated the opposite effective diffusion coefficient of CO_2 in bulk water (2.17 x 10^{-11} m^2/s). With the knowledge of the effective diffusion coefficient, the risk of CO2 diffusion loss through cap rock can be assessed. Busch et al. [225] estimated that diffusive gas breakthrough at the top boundary of the cap rock occurs after a time of 0.3 MPa, but the sealing integrity could be even lower, owing to geochemical alteration. In the case of co-injecting Ar with CO_2, diffusive gas breakthrough of the caprock could be enhanced.

3.6 Conclusion

New experimental technique for obtaining diffusion coefficients and interfacial tension by means of pendant drop tensiometry was developed. A mass transfer model based on pendant drop tensiometry phenomena was developed to measure the diffusivity of liquids in supercritical fluids by fitting the Young-Laplace equation to an experimentally determined droplet geometry.

Experiments to determine diffusion coefficients were performed at high pressure. Changes in evaporating drop geometry (volume and surface area) were observed. Diffusion coefficients have been determined based on assumptions made for a mass transfer model describing diffusion of a solute in the surrounding medium of a droplet that can be expressed with Fick's 1st law of diffusion. Equilibrium solubility has been established in the literature and determined experimentally by our research group using the static-analytic method. A specific feature of the method is its relative simplicity: the resulting model serves to determine the diffusivity coefficients of liquids in the gas phase, based on equilibrium solubility data and drop diameter change over time. The method was validated by measuring the diffusivity of water in CO_2 at 25 °C and 40 °C and at pressures from 5.0 to 60.0 MPa. Agreement of the resulting diffusion coefficients with those found in the literature and correlated with the thermodynamic data was satisfactory, at over 20 %.

The method was further applied for determining the interfacial properties and diffusivity rates of propylene glycol in CO_2 at 120 °C and 150 °C and at pressures ranging from 5 MPa up to 17.5 MPa. As expected, the high evaporation rate of propylene glycol allows for only a shorter drop shape observation time; consequently, a lower level of accuracy of the results is obtained, compared to that for the water- CO_2 system. Nevertheless, it was still established that diffusivity decreases with increasing pressure, meaning that solvent molecules are closer together, and increases with increasing temperature, predominately due to the higher kinetic energies of molecules that move more rapidly.

Additionally, the effect of argon as a co-contaminant in the CO_2 stream on the interfacial tension, storage capacity and diffusion coefficients was studied under conditions relevant to carbon sequestration, using the pendant drop method. A strong increase in isothermal interfacial tension at 45 °C and up to 20 MPa was observed with an increase in Ar co-contaminant from 5 vol. % to 100 vol. %. The densities of the equilibrated brine-rich phase for Ar+CO_2 mixtures were reduced in comparison to those in the absence of Ar. Since non-condensable Ar will be present in small concentrations up to 5 vol. % in most injected CO_2 streams and may considerably influence the physical properties in deep geological reservoirs, we focused on measuring the brine-CO_2 interfacial tension and brine mixture (CO_2 and Ar) interfacial tension with 5 vol. % and 10 vol. % of argon content at pressure (7.5-40 MPa) and temperature (40 - 80 °C) ranges that had not previously been investigated and that can be considered more practical for carbon sequestration. In the case of 5 vol. % and 10 vol. % Ar, the contamination buoyancy effect prevailed over the interfacial properties and decreased storage capacity.

It was found that the diffusivity of water in Ar is higher in comparison to water in CO_2. Small quantities of salt in the water had a minor effect on the diffusion coefficients of brine in supercritical CO_2. The experimentally obtained diffusion coefficients (D_{ab}) were correlated to obtain an effective diffusion coefficient (D_{eff}). It was found that, in the case of co-injection of Ar with CO_2, diffusive gas breakthrough could be enhanced.

4. Heat transfer at supercritical conditions

4.1 Theoretical part

Studying heat transfer in supercritical conditions is necessary for the design and optimization of trans-critical CO_2 power cycles in refrigeration systems [226], nuclear reactors [227], air-conditioning, and advance heat pumps [228], as well as in other technological applications of supercritical fluids, mainly extraction [229], reaction processes [230] and particle formation [40]. Each of those applications in its flowsheet involves heat exchangers that operate at high-pressures and temperatures. One of the most simple and applicable heat exchangers for high-pressure applications is the double pipe heat exchanger. It makes a significant contribution to pasteurizing, reheating, preheating, digester heating and the effluent heating process [231]. In supercritical extraction plants, the purpose of a heat exchanger can be to pre-heat supercritical fluids before they are fed to a high-pressure vessel, or to cool down supercritical fluids before compression or separation of the solubilized solutes [232]. In power cycles, among thermal-hydraulic performance, the heat exchangers have a significant effect on the total efficiency, compactness and operating cost of the system [233].

When the pressure and temperature of the fluid used in heat exchangers approach the critical point, its thermo-physical properties vary complexly [234]. The thermo-physical variations of CO_2 at 7.5 MPa and ethane at 5 MPa near critcal temperature are presented in Figures 4-1 and 4-2. The specific heat C_p increases greatly with increasing temperature and reaches peak value at 31.05 °C; thus, more heat is allowed to be removed, thermal conductivity λ, density ρ, and viscosity μ decrease rapidly with increasing temperature, and the flow velocity, as well as turbulence, are increased. Consequently, the heat transfer coefficient (in the following text HTC) near the critical point of fluids is expected to have much higher values. The major advantage of using supercritical fluids for heat transfer applications is that above the critical pressure no boiling will occur, eliminating the need for condensers, and situations where critical heat flux and burn out could occur. This makes for simplified plant design using fewer components, and therefore, reduced plant costs [235]. At high temperatures and low pressures, relative to the critical point, it behaves as a gas, while at low temperatures and high pressures it resembles a liquid. This results in low compressor work while maintaining gas-like behavior in the rest of the cycle [236]. There are many opportunities for the development of turbomachines for supercritical power cycles, in research of a heat transfer near the critical condensation and evaporation [237]. As a heat transfer fluid, supercritical fluids can be also integrated with solar energy in power cycles [238]. A lot of research on supercritical Brayton cycles [239] has been carried out. Thermal efficiency above 50% can be easily achieved.

Besides supercritical water, which has a relatively high critical point (T_c=374.14 °C, P_c=22.12 MPa), CO_2 has been the most often studied fluid at high pressures [53]. It is an easily accessible fluid with a relatively low critical point (T_c=31.05 °C, P_c=7.38 MPa), which means that the operating costs of many industrial applications can be reduced [240]. In recent years, CO_2 has also been reintroduced as an environmentally friendly refrigerant and used as a working fluid in heat pumps, car radiators and air conditioning systems. [42]. For instance, it has zero ozone depletion potential (ODE), a low global warming potential (GWP), and non-toxicity when compared to conventional chlorofluorocarbon (CFC) and hydro-chlorofluorocarbon (HCFC) freons.

Experimental and numerical studies of heat transfer at high pressure between water and CO_2 systems have been widely reported in the literature. Ma et al. [53] studied the heat transfer performance of supercritical CO_2 in a double pipe heat exchanger using a supercritical CO_2-water loop. They concluded that total and supercritical CO_2-side heat transfer coefficients near critical point behave similarly to specific heat, and the contribution of buoyancy force to the

heat transfer performance is large at small mass flux. Duffey et al. [241] presented a literature survey in which three heat transfer modes at supercritical pressures were surveyed: normal heat transfer deteriorated, heat transfer with lower values of the heat transfer coefficient (HTC) and improved heat transfer with higher values of the HTC compared to those of normal heat transfer. Song et al. [242] established that heat transfer had similar characteristic irrespective of heat transfer improvement or deterioration if the ratio of tube length to tube diameter and the ratio of heat flux to mass flux were kept constant. Liu et al. [243] performed numerical studies of heat transfer characteristic of supercritical CO_2 in a heated, helically coiled pipe. They showed that both the buoyancy force and the centrifugal force influence the circumferential heat transfer distribution in the helically coiled tube. The effect of flow direction was investigated by Li et al. [244] and Bruch et al. [245]. While Li et al. found that the heat transfer coefficients were better at downward flow than at upward flow; Bruch et al. came to the opposite conclusion in the pseudo-critical region. Lia and Zhao [246] investigated heat transfer in upward and horizontal flow. They observed that heat transfer in both horizontal and upward flow was enhanced, while heat transfer in downward flow was impaired significantly near the pseudo-critical region.

In all of the numerous investigations of heat transfer between supercritical CO_2 and water described above, there are still some variations and unknowns that need to be clarified. It is hard to say that heat transfer deterioration is caused by one factor alone. There is also a lack of information about other processing fluids that can be used as heat transfer fluids (HTF) in their critical state.

Negoescu and co-workers [247] studied heat transfer for supercritical nitrogen flowing vertically upward in a 2 mm diameter smooth tube. Their objective was to develop reliable prediction approaches regarding the heat transfer coefficient (HTC) in the large specific heat region. Zhang et al. [248] conducted experiments of heat transfer in supercritical Freon HFC-134a flowing upward in a circular tube. Jiang et al. [249] investigated transfer characteristics of HCFC-22 and ethanol at supercritical pressures in a vertical small tube. Recently, heat transfer of hydrogen and helium at supercritical pressures has been investigated by Hoa et al. [250, 251]. Harby [252] presents an overview of natural refrigerants, such as hydrocarbons. Halogenated refrigerants can be obtained from the natural hydrocarbons methane and ethane by replacing chlorine and fluorine atoms with hydrogen. Among the hydrocarbons that are most frequently investigated as refrigerants, ethane (HC-170) shows excellent thermodynamic properties together with suitable physical and chemical properties which are particularly energy-efficient. Besides, its critical pressure is relatively low; 4.87 MPa.

To the author's knowledge, there are no data on the heat transfer performance of an ethane and azeotrope mixture of ethane and CO_2 under supercritical conditions. Ethane was chosen for its ability to form an azeotropic blend with CO_2 with a minimum boiling point that could offer improved properties compared to pure CO_2. The azeotropic mixture of ethane and CO_2 can be found in large quantities in petrochemical processes as waste that needs to be further separated [253]. Therefore, one option instead of high-cost separation is to use the mixture as a heat medium in power cycles. To properly evaluate the potential and the performance of this azeotropic mixture in such systems, heat transfer coefficients (HTC) were first experimentally measured in a heat exchanger. Secondly, the Coefficients of Performance (*COP*) of the azeotropic blend were calculated for a simple heat pump cycle and compared to a system containing exclusively CO_2. The whole paper is dedicated to finding alternative sustainable energy solutions. The usage of environmentally harmful freons was therefore to be avoided.

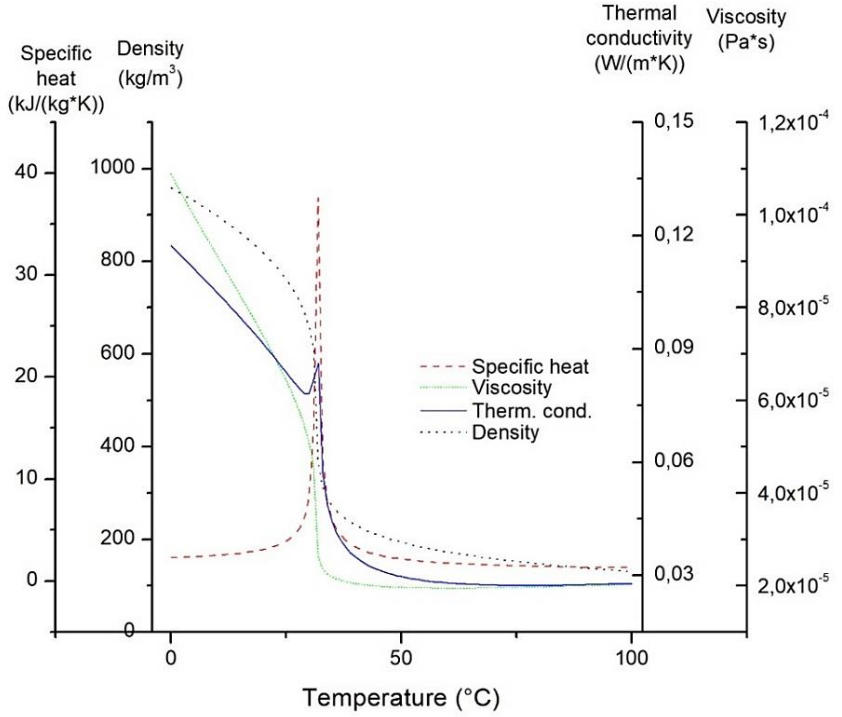

Figure 4-1: Variation in thermophysical properties of supercritical CO_2 at 7.5 MPa (obtained from NIST webbook) [109].

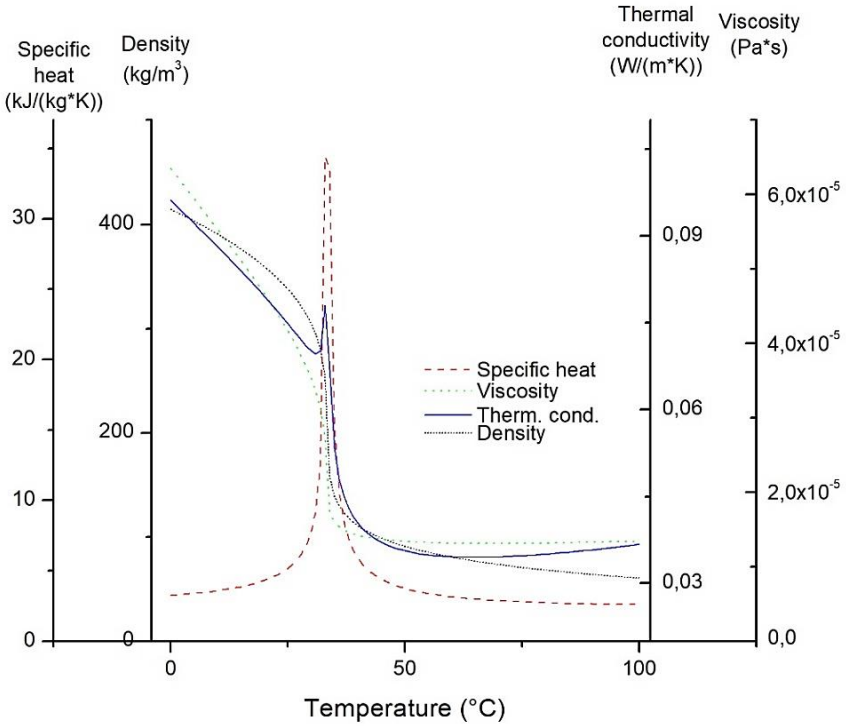

Figure 4-2: Variation in thermophysical properties of supercritical ethane at 5.0 MPa (obtained from NIST webbook) [109].

4.1.1 The Aims

In the present study, a double pipe heat exchanger was developed and set up to examine the effects of different operating parameters on heat transfer performance over a wide range of temperatures (25 °C to 90 °C) and pressures (6 MPa to 30 MPa). The heat transfer coefficients (HTC) of supercritical CO_2, ethane and their azeotropic mixture in a water loop were measured in order to make a good comparison. A brief evaluation is provided of the effect of mass flux, heat flux, pressure, temperature and bouncy force on heat transfer coefficients. Additionally, the performance and thermodynamic evaluation of a CO_2-ethane azeotropic mixture as a promising heat transfer fluid in heat power cycles are presented.

4.2 Experimental part

4.2.1 Materials

Carbon dioxide (3.5), ethane (4.5) and azeotropic mixtures with 75 wt. %, of CO_2 and 25 wt. of ethane content were obtained from Messer (Slovenia).

4.2.2 Test loops

Heat transfer coefficients (HTC) were determined using a new optimized experimental setup that enables measurements at high pressures (Figure 4-3). The experimental setup is comprised of two separate closed loops, i.e., a supercritical fluid (CO_2 and/or ethane) loop and a water loop. In the supercritical (high-pressure) fluid loop, gas released from the tank (CO_2 at 5 MPa, ethane at 3.7 MPa) was cooled to fully liquefy and was then compressed to desired pressures with a high-pressure liquid pump (NWA PM-101) that can operate at a maximum pressure of 60 MPa. To minimize fluid pulsation at the outlet of the high-pressure pump, gas was pumped into a 1 L buffer vessel and then preheated with a heating system (LAUDA E-300) to the desired working temperature. A digital differential pressure transmitter (WIKA-CHP 6200) was installed to measure the dense gas pressure at the inlet and outlet section of the heat exchanger. The accuracy of the transmitter is ±0.01 MPa. The inlet and outlet temperatures of both setup loops were controlled by the heaters, and K-type thermocouples with an accuracy of ±0.15 K. The supercritical fluids flow rate was measured using a Coriolis mass flow meter (RHEONIK RHM 03) equipped with a flow indicator (RHEONIK RHE 02) that is suitable for all flow applications from 0.038 kg/min up to 5 kg/min, with a measurement uncertainty of 0.1% up to 124 MPa and 623 K. In the water loop, the flow rate of water was measured with a needle valve rotameter (LZT-1002-M) with an accuracy ±2% of full scale. Water was circulated and a thermostat with a centrifugal pump (LAUDA E200) equipped with a heater.

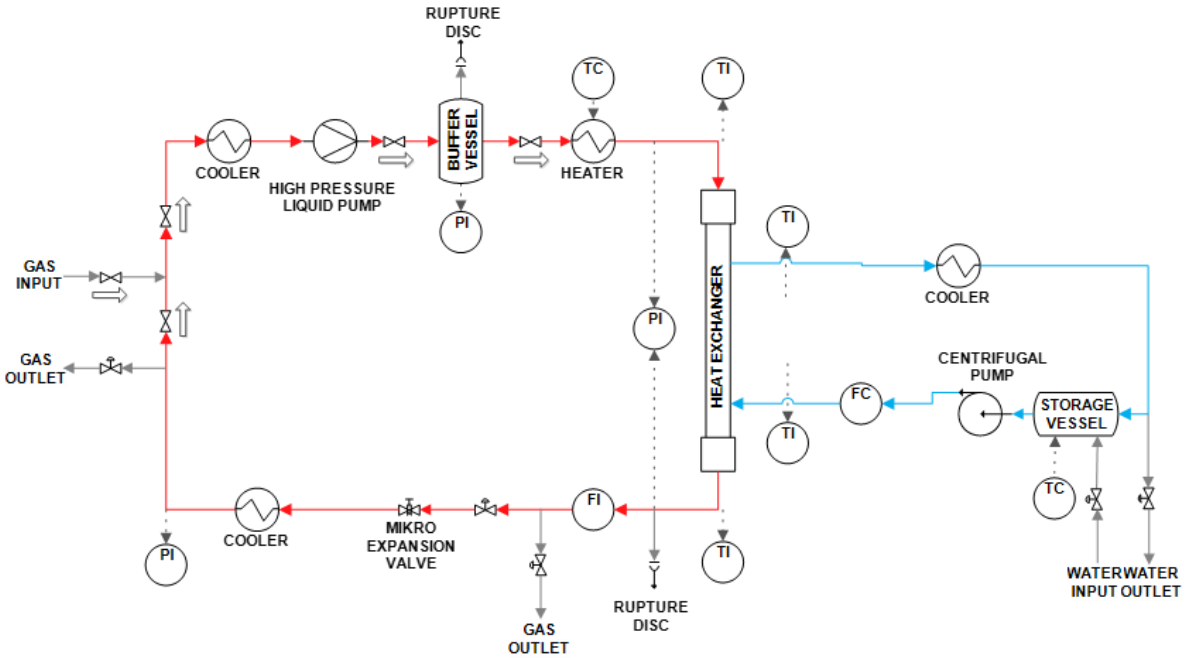

Figure 4-3: The experimental setup consisted of two separated closed loops, i.e. a supercritical fluid loop and a water loop. Acronyms: PI-pressure indicator, TC-temperature controller, TI-temperature indicator, FC-flow controller, FI-flow indicator.

4.2.3 Double pipe heat exchanger

Heat exchange was measured in a double-pipe tube setup with a countercurrent flow (Figure 4-4). The previously heated supercritical fluid flows horizontally through the inner tube made of stainless steel 304-L with an outer diameter 9.65 mm and a wall thickness of 2.07 mm, and liquid water flows counter-currently in the PVC annulus tube with an outer diameter of 20.00 mm and a wall thickness of 0.8 mm. To reduce heat loss from the heat exchanger and other pipes in the cycle-based system, ARMAFLEX thermal insulation with a 20 mm thickness was used. After the heat exchanger, a micro-expansion valve and cooling vessel were placed to reduce pressure and temperature in order to establish conditions enabling the dense gas to be fully recycled. An electronic pressure gauge (WIKA, Germany) measured the reduced pressure with an uncertainty of 0.01 MPa. The overall systematic error was 3.4% and was calculated by summarizing the accuracy of each individual piece of equipment used in the experiments

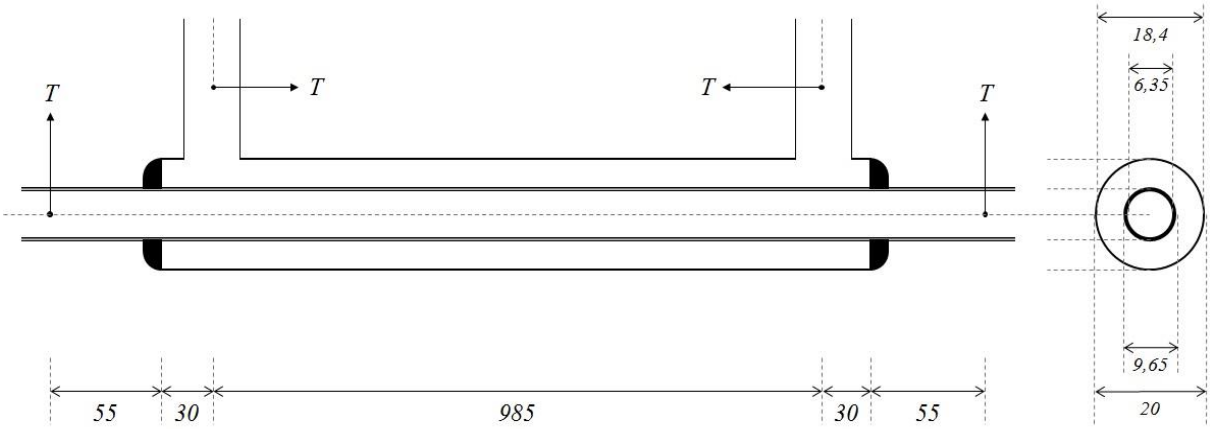

Figure 4-4: Double pipe heat exchanger with contraflow design.

4.2.4 Experimental evaluation

The total heat transfer coefficient U_{tot} on the supercritical fluid-side heat transfer area is calculated using the equation below:

$$U_{tot} = \frac{\dot{Q}_a}{A_{SCF}\,\Delta T}, \tag{4.1}$$

$$\Delta T = \frac{(T_{SCF,out} - T_{H2O,in}) - (T_{SCF,in} - T_{H2O,out})}{\ln\left(\frac{T_{SCF,out} - T_{H2O,in}}{T_{SCF,in} - T_{H2O,out}}\right)} \tag{4.2}$$

where Q_a is average heat transfer flux, A_{SCF} is the heat transfer area of the supercritical fluid side, and ΔT is the logarithmic mean temperature difference in the counter-current flow between the hot and cold sides. The average heat transfer flux is calculated by

$$\dot{Q}_a = \frac{(\dot{Q}_{SCF} + \dot{Q}_{water})}{2} \tag{4.3}$$

$$\dot{Q}_{water} = \dot{m}_{water}(H_{water,out} - H_{water,in}) \tag{4.4}$$

$$\dot{Q}_{SFC} = \dot{m}_{SCF}(H_{SCF,in} - H_{SCF,out}) \tag{4.5}$$

where, $\dot{Q}_{water}$ is the heat transfer flux on the water side, and $\dot{Q}_{SCF}$ is the heat transfer flux of the supercritical fluid (CO_2 or ethane) side, $H_{water,\,in}$, and $H_{water,out}$ are the enthalpies of water at the inlet and outlet, while $H_{SCF,in}$ and $H_{SCF,out}$ are the enthalpies of the supercritical fluid at the inlet and outlet. These equations are used when we deal with fluids that do not display constant values of specific heat capacity over the entire temperature range [254 48]. It has to be highlighted that in the case of the azeotropic mixture, it was necessary to determine the enthalpy by means of the enthalpy of pure components and the mass composition:

$$H_A(T,P) = \sum_{i=1}^{n} w_i * H_i(T,P) \tag{4.6}$$

where H_A is enthalpy of azeotropic mixture at the same pressure and temperature conditions in which azeotropic mixtures were measured, H_i is enthalpy of the i-th component in the mixture at pressure P and temperature T and w_i is the weight fraction of the i-th component in the mixture that was considered as constant for all measurements. The thermal physical properties of pure supercritical CO_2 and ethane under a wide range of pressures and temperatures have been obtained from the NIST database [109]. According to the thermal resistance network in the double pipe heat exchanger, the total heat transfer coefficient U_{tot} can be calculated by equation 4.7 [255] :

$$\frac{1}{U_{tot}} = \frac{1}{\alpha_{SCF}} + \frac{A_{SCF}\ln\left(\frac{D_{1,outer}}{D_{1,inner}}\right)}{2\pi\lambda L} + \frac{A_{SCF}}{\alpha_{water}A_{water}} \tag{4.7}$$

Therefore, heat transfer coefficients α_{SCF} on the supercritical fluid side are calculated by:

$$\alpha_{SCF} = 1/\left(\frac{1}{U_{tot}} - \frac{A_{SCF}\ln\left(\frac{D_{1,outer}}{D_{1,inner}}\right)}{2\pi\lambda L} - \frac{A_{SCF}}{\alpha_{water}A_{water}}\right) \tag{4.8}$$

where $D_{1,outer}$ is the outer diameter of the inner tube, $D_{1,inner}$ is the inner diameter of the inner tube, and λ is the thermal conductivity of the 304-L stainless steel inner tube. The heat transfer coefficient (α_{water}) in the annular space of the waterside is obtained by taking into account the equivalent diameter and Nusselt number for the annular cross-section [256]:

$$D_e = D_{2,inner} - D_{1,outer} \tag{4.9}$$

where, $D_{2,inner}$ is the inner diameter of the outer tube ("bigger tube"), $D_{1,outer}$ is the outer diameter of the inner tube ("small tube").

$$Nu_{De} = \frac{\alpha_{water} D_e}{\lambda} \tag{4.10}$$

From the equation 10 it is not possible to determine the values of heat transfer coefficient of water (α_{water}) directly, because the Nu number for the annular cross-section must be determined via well-known empirical correlations (equation 11):

$$Nu_{D_e} = 0.02\,\mathrm{Re}_{D_e}^{4/5}\,\mathrm{Pr}^{1/3}\left(\frac{D_{1,outer}}{D_{2,inner}}\right)^{0.53} \tag{4.11}$$

The Reynolds number represents the contribution of mass flux to the overall Nusselt value within the same annular cross-section. The dimensionless Prandtl number is the ratio of momentum diffusivity to thermal diffusivity and makes a smaller contribution to the total Nusselt value than the Reynolds number. The last parameter represents the decrease in the overall Nusselt number due to the introduction of an inner pipe to the flow of the fluid and was constant with a value of 0.7068. The above-mentioned correlation was used because the surface heat flux was not constant throughout the entire length of the heat exchanger and also to accommodate the influence of the double pipe design on the entire process of heat transfer [256]. Prandtl and Reynolds's number are calculated by:

$$\mathrm{Pr} = \frac{c_p \eta}{\lambda} \tag{4.12}$$

$$\mathrm{Re}_{De} = \frac{\rho v D_e}{\eta} \tag{4.13}$$

4.3 Results and discussion

The heat transfer coefficients (hereafter HTC) of supercritical CO_2 and ethane in a water loop were measured over a wide range of temperatures (25 °C to 90 °C) and pressures (6 MPa to 30 MPa). During the entire process, there was one phase present in the inner high-pressure tube. All measurements were performed at pressures higher than the critical pressure for a specific fluid. This ensured that there was no fluid in the vapor phase during the process. The vapor phase was not desirable as it would interfere with the operation of the high-pressure flowmeter on the Coriolis force. Additionally, a certain energy for the phase transition of the fluid from the liquid to the vapor phase would be needed, which would greatly impact the measurements. Based on these facts and the low specific heat of the gas phase, its presence in the operating system was omitted. In the displayed figures, bulk temperature T_b represents average values of the output and input temperatures of a fluid under specific pressure in the inner tube.
Measurements below the critical temperature were carried out at a constant inlet temperature of the fluid in the inner pipe (a few degrees below the critical temperature), while the outlet temperature was adjusted to the specific values by waterside temperature in the outer pipe of the double pipe heat exchanger. Therefore, the average value between the inlet and outlet temperature of a fluid could be increased near the critical temperature. Measurements above the critical temperature were carried out with an adjusted inlet temperature for the fluid and a constant outlet temperature (usually only a few degrees higher than the critical one). The constant outlet temperature was adjusted to the specific values by the temperature of the water side. All measurements were first carried out at a water flow rate of 1 L / min, and after each measurement, the water flow rate was increased to 2 L / min.

4.3.1 Effect of pressure and temperature on heat transfer coefficients

Total and supercritical-side HTC have the highest peaks near the critical point of the fluids being investigated (Figure 4-5). This is caused by a stronger change in thermo-physical properties, especially the greater increase in specific heat at pressures closer to the critical pressure [257]. The highest peak value of total HTC occurs at the location where the temperature is slightly higher than the critical point. A possible explanation could be that the temperature of supercritical fluid near the wall in the inner tube is lower than in the bulk, and the average temperature of the supercritical fluid in cross-section is not reduced to the critical temperature but shows values near the wall that are closer to the critical temperature [243]. The experimental data were obtained for five isobars: 7.5, 8.0, 10, 20 and 30 MPa. As shown in Figure 4-5, total HTC peaks of supercritical CO_2 decrease with the increasing pressure and have their maximum values above the critical temperature. Small variations in the bulk temperature T_b affected the HTC greatly. The highest peak was observed at 7.5 MPa; HTC points below critical temperature were raised to the highest point by increasing the bulk temperature and then, slightly above the critical temperature, began to decrease. When the pressure was increased from 7.5 to 10 MPa, the maximum total HTC near pseudo-critical temperature decreased significantly from 577 W/m^{2}K to 477 W/m^{2}K, and when the pressure was 30 MPa, the maximum HTC decreased to 345 W/m^{2}K.
The supercritical CO_2-side HTC (α_{SCF}) peaks reached much higher values compared to total (or overall) HTC (U_{tot}) under the same conditions (Figure 4-5 and Figure 4-6). The simple reason is that α_{SCF} takes into account the heat transfer from heating fluid into the wall of the pipe, while U_{tot} represents the heat transfer between the fluids being investigated. The simple reason is that α_{SCF} only takes into account the heat transfer from heating fluid into the wall of the pipe, while U_{tot} represents the heat transfer between the fluids being investigated thus considers both α_{SCF}, α_{water} and the thermal resistance of the inner pipe.

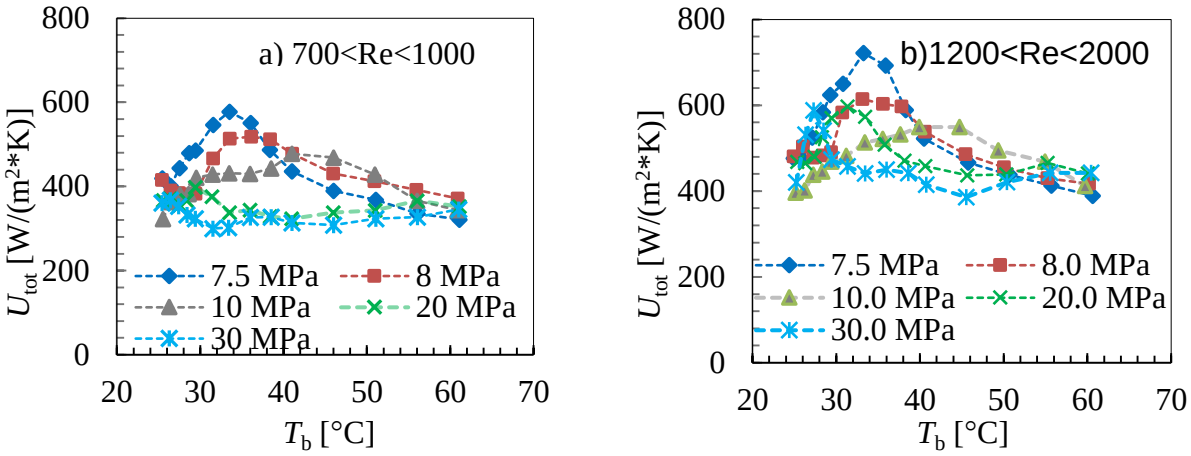

Figure 4-5: Effect of supercritical CO_2-side pressure and average temperature of heating fluid (T_b) on total heat transfer coefficient (U_{tot}).

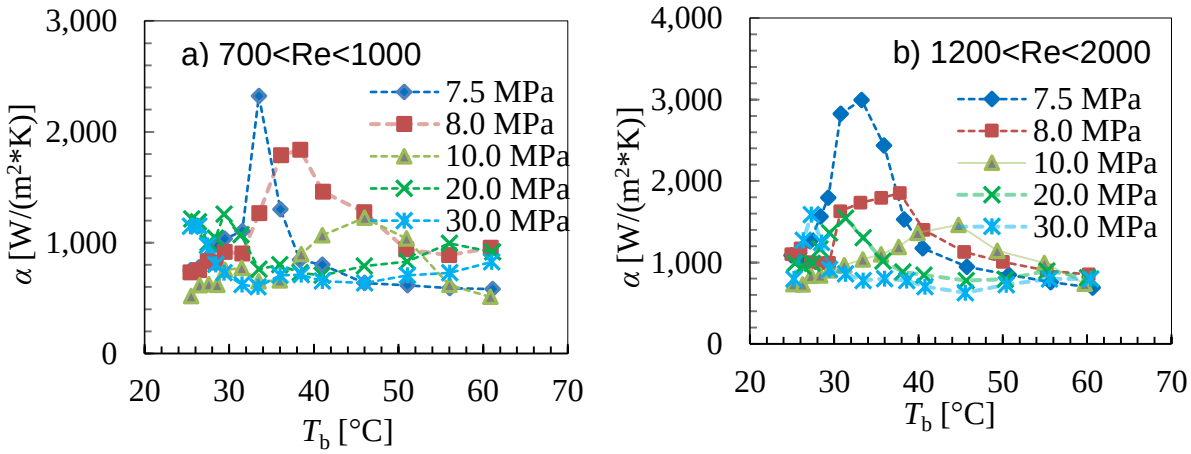

Figure 4-6: Effect of supercritical CO_2-side pressure and average temperature of heating fluid (T_b) on total heat transfer coefficient (U_{tot}).

4.3.2 Effect of mass flux

Since the effect of supercritical-side mass flux is significantly smaller than the effect of the water-side flux rate on HTC [243], the supercritical-side mass flux was kept constant at 0.08 kg/min for supercritical CO_2, and at 0.05 kg/min for supercritical ethane. The effect of the total heat transfer coefficients was investigated at two water volume flux rates of 1 L/min and 2 L/min for pressures around the pseudocritical temperature. The Re values obtained at the same water flow rate are expressed in a certain range because of its dependence on the density and dynamic viscosity in accordance with the temperature. As shown in Fig. 7, the total HTC increases by more than 25% when increasing the flux rate of water-side from 1 L/min ($700<Re_{water}<1000$) up to 2 L/min ($1200<Re_{water}<2000$). Increased heat transfer performance at the higher water flux rate could probably be related to turbulence phenomena [234]. At higher water flux rates in the vicinity of a critical temperature, some kind of local peak value occurs (Fig 5b). This peak, at pressures 20 MPa and 30 Mpa, could be attributed to the higher cooling intensity of water in contact with the inner fluid and as consequence of the local transition of a fluid from the supercritical phase to the liquid phase. Another possible explanation for this deviation could be the extremely small temperature difference between the water inlet and

outlet temperatures. Even an error of a tenth of a degree Celsius could contribute considerably to potential deviations.

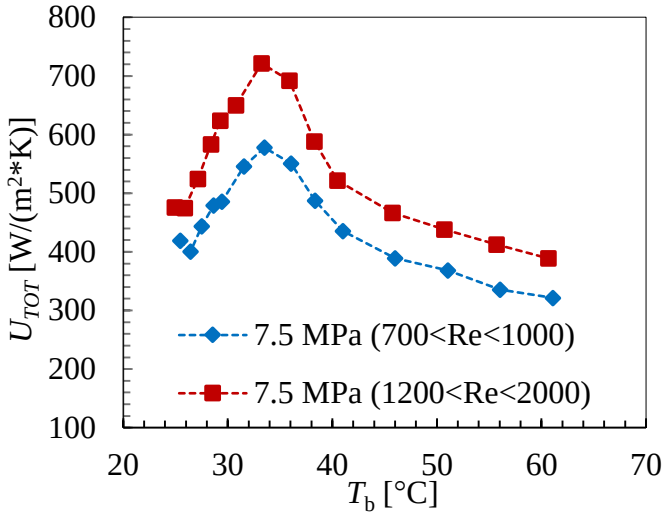

Figure 4-7: Effect of water-side mass flux average temperature of heating fluid (*T*b) on the total heat transfer coefficient (U_{tot}).

4.3.3 Heat transfer performance of supercritical CO_2 and ethane

The heat transfer performance of supercritical ethane (32.2 °C, 4.9 MPa) was compared to that of supercritical CO_2 (31.03 °C, 7.38 MPa). Ethane has a critical temperature near CO_2 and a critical pressure considerably lower than CO_2. Figure 4-8 represents, for the first time, a comparison of how supercritical CO_2-side pressure and supercritical ethane-side pressure influence the total heat transfer coefficients near the fluid critical point. In the case of supercritical CO_2-side pressure, HTC peaks result in higher values than in supercritical ethane-side pressure. One explanation could lie in the fact that the heat capacity of CO_2 near its critical point is greater than the heat capacity of ethane and therefore a larger quantity of heat was transferred (Figure 4-1 and Figure 4-2). The effect of supercritical ethane-side pressure on total and supercritical ethane-side HTC at an average temperature (T_b) of heating fluid and at a constant water flux of 1 L/min ($700<Re_{water}<1000$) and 2 L/min ($1200<Re_{water}<2000$) are presented in Figure 4-9 and Figure 4-10.

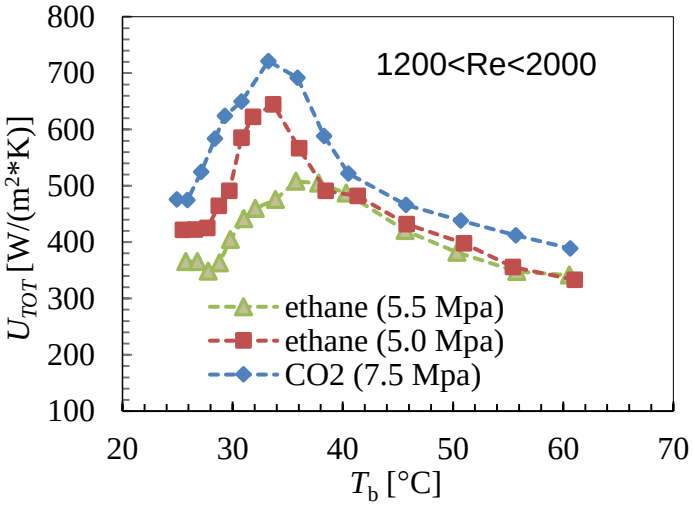

Figure 4-8: Influence of supercritical CO_2-side pressure and supercritical ethane-side pressure at different T_b on the total heat transfer coefficient.

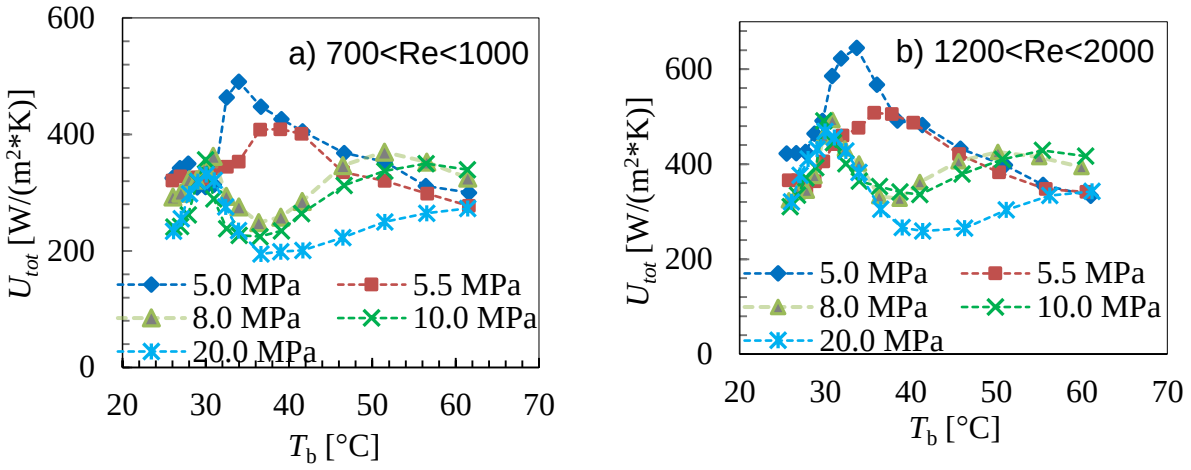

Figure 4-9: Effect of supercritical ethane-side pressure and average temperature of heating fluid (T_b) on the total heat transfer coefficient (U_{tot}).

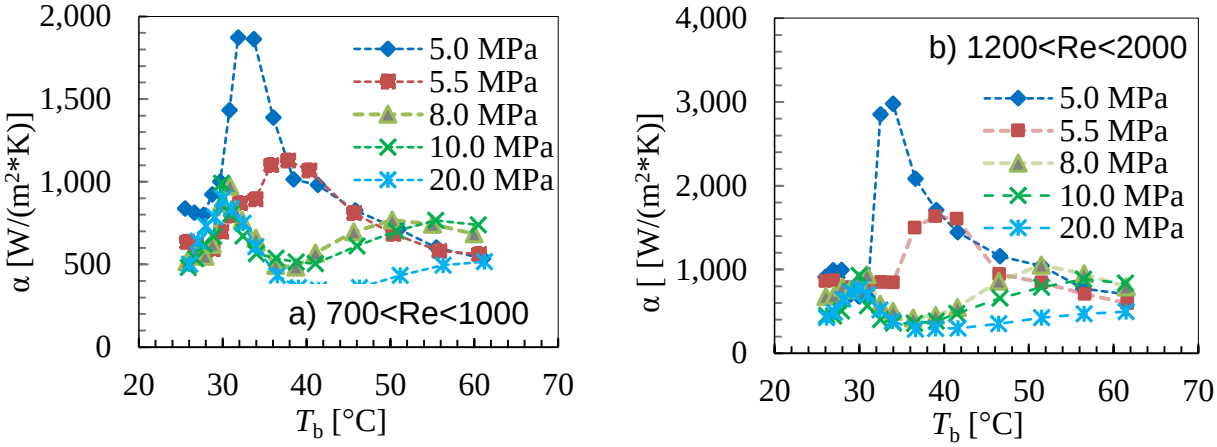

Figure 4-10: Effect of supercritical ethane-side pressure and average temperature of heating fluid (T_b) on the supercritical ethane-side heat transfer coefficient (α).

4.3.4 Heat transfer performance of the azeotropic mixture

The heat transfer performance of an azeotropic mixture of CO_2 and ethane (75 mass percent CO_2 and 25 mass percent of ethane) was compared to supercritical CO_2 and supercritical ethane. In order to ensure that there was one phase region throughout the inner high-pressure tube, it was necessary to know the exact critical point of the azeotropic mixture. Pseudocritical temperature T_c was calculated using the mole-fraction mixing method, called the Keys rule [258]:

$$T_c = \sum_{i=1}^{n} y_i T_{ci} \tag{4.12}$$

where the average mole fraction and pseudocritical temperature of the components were used in the calculation. For the pseudocritical pressure, P_c the modified rule of Prausnitz and Gunn was used [259]:

$$P_c = \frac{Z_c R T_c}{V_c} \tag{3.13}$$

where azeotrope pseudocritical Z_c, T_c and V_c are given by mole fraction average, and R is the gas constant (Table 4-1).
The calculated critical point of the azeotrope mixture (p_c=6.34 MPa and T_c=31.37 °C) was in good agreement with the experimentally observed critical point using a high-pressure visual cell (difference less than 1 %). Figure 4-11 represents a comparison between supercritical azeotropic mixture side, pure supercritical CO_2 and ethane side total heat transfer coefficients near the fluid critical point. Near the critical point, the HTC values of the azeotropic mixture fell between the HTC values for the pure CO_2 and those for ethane. In order to describe numerically the behavior of heat transfer fluids, the experimental values were interpolated. We focused mostly on the measurements taken at pressures slightly above the critical point (7.5 MPa for CO_2, 5.0 MPa for ethane), since these show the highest peaks of the heat transfer coefficient (U_{tot}). All the measurements were divided into two parts so that the interpolation could be more accurate over the entire measured region. A simple second order polynomic function was used to describe the trend:

$$U_{TOT}\left[W/(m^2K)\right] = A \cdot T_b^{\,2} + B \cdot T_b + C \tag{4-14}$$

For calculating the heat transfer coefficients of the aforementioned fluids below the critical temperature (33 °C), constants of the second order polynomial function are shown in Table 4- 2. For calculating the heat transfer coefficients above the critical temperature (33 °C), the constant parameters are shown in Table 4-3. The presented values were interpolated at the higher water flow rate (1200<Re<2000). It can be concluded that this azeotropic mixture, similarly to pure CO_2, absorbs a satisfactory amount of heat at a given temperature near the critical point and can be used as an alternative fluid in heat power cycles.

Table 4-1: Parameters for calculating the pseudocritical conditions of the CO_2-ethane mixture.

	CO_2	**ethane**
M [g/mol]	44	30
ω [-]	0.750	0.250
x [-]	0.672	0.328
T_c [°C]	30.98	32.18
P_c [MPa]	7.38	4.87
V_c [cm^3/mol]	94.07	145.50
Z_c [-]	0.274	0.279
pseudocritical conditions of the mixture		
T_{pc} [°C]	31.37	
P_{pc} [MPa]	6.34	

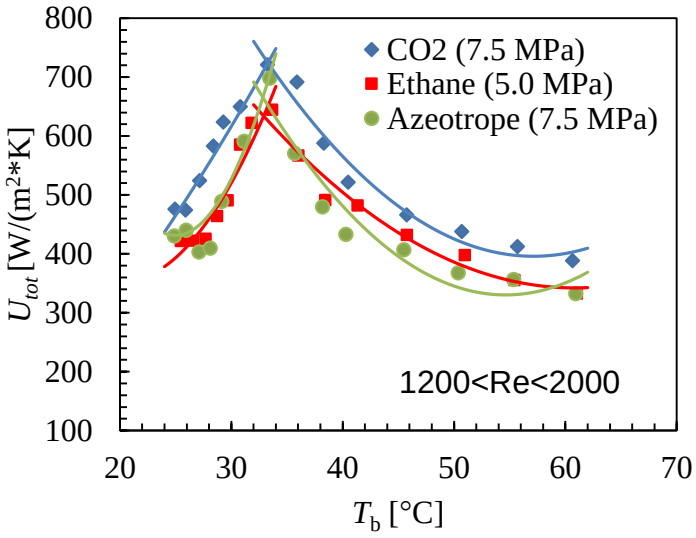

Figure 4-11: Influence of T_b on supercritical azeotropic mixture-side, supercritical CO_2-side and supercritical ethane-side total heat transfer coefficients. Lines represent calculated values.

Table 4-2: Constants of the second order polynomic function for calculation Utot below the critical temperature (T>Tc).

	A [W/(m²*K*°C²)]	**B [W/(m²*K*°C)]**	**C [W/(m²*K)]**	**R² [/]**
CO_2	0.31039	13.16429	-57.88965	0.98969
Ethane	1.72477	-69.44657	1051.54748	0.92235
Azeotrope	3.79058	-189.34642	2796.01254	0.99302

Table 4-3: Constants of the second order polynomic function for calculation Utot above the critical temperature (T<Tc).

	A [W/(m²*K*°C²)]	**B [W/(m²*K*°C)]**	**C [W/(m²*K)]**	**R² [/]**
CO_2	0.57756	-65.99777	2281.29139	0.97013
Ethane	0.37418	-45.51982	1726.57256	0.9652
Azeotrope	0.70655	-77.1818	2438.07248	0.92079

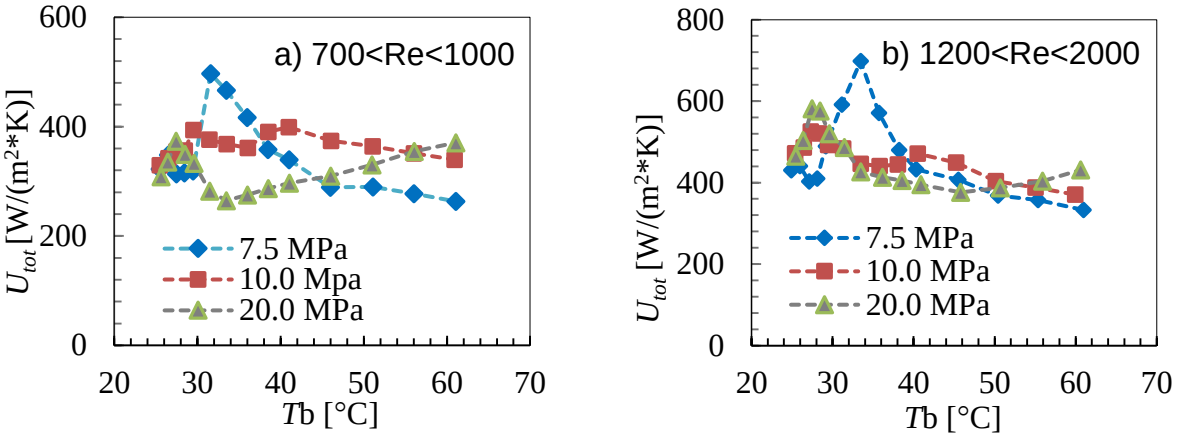

Figure 4-12: Effect of supercritical azeotropic mixture pressure and average temperature of heating fluid (T_b) on the total heat transfer coefficient (U_{tot}).

Figure 4-12: Effect of supercritical azeotropic mixture pressure and average temperature of heating fluid (T_b) on the total heat transfer coefficient (U_{tot}).

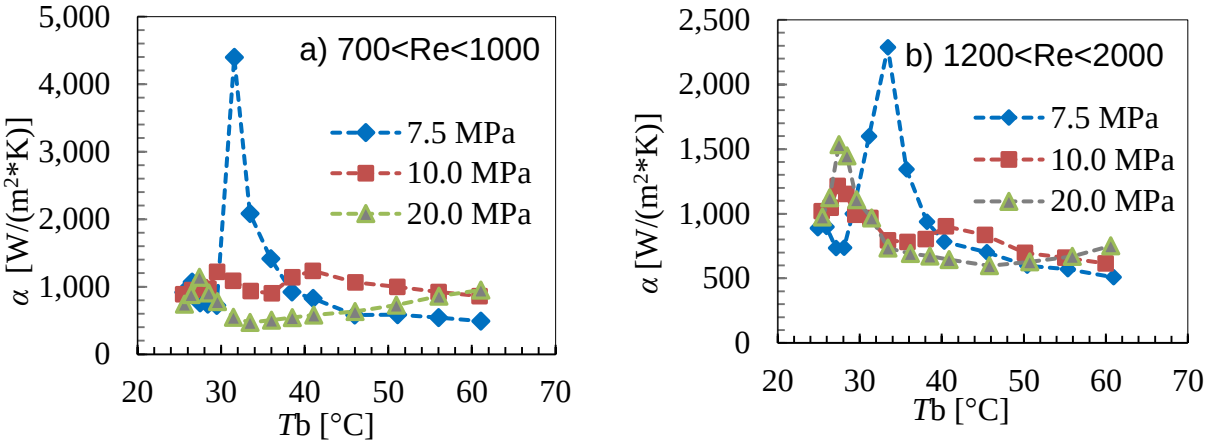

Figure 4-13: Effect of supercritical azeotropic mixture pressure and average temperature of heating fluid (T_b) on supercritical-side heat transfer coefficients (α).

4.3.5 Effect of buoyancy force

At supercritical pressures, either heat transfer improvement or heat transfer deterioration might take place. A lot of efforts to determine the onset of heat transfer deterioration can be observed in the literature. It might be caused by variation in the thermophysical properties and bouncy force (flow acceleration). Bouncy force may arise from non-uniform density distribution across the radial or axial direction [234]. Moreover, high flow rates can overcome the effects of density variation close to the tube wall and diminish the buoyancy effect [247].
Jackson et al. [260] derived a criterion for the onset of the buoyancy effect (*Bo*) in pipe flow by considering the modification of the turbulent shear stress profile across the viscous layer.

According to this criterion,

$$Bo = \frac{Gr_{Q_a}}{\mathrm{Re}_b^{3.5}\,\mathrm{Pr}_b^{0.8}} < 5.6\times10^{-7} \tag{15}$$

Where Gr_q is the Grashof number based on wall heat transfer calculated by:

$$Gr_{Q_a} = \frac{\rho_b^2 \beta_b D_{1,inner}^4 \dfrac{Q_a}{A_{SCF}}}{\lambda_b \mu_b^2} \tag{16}$$

The buoyancy force was evaluated for mass fluxes at the lowest pressure of 7.5 MPa, and the highest pressure of 30 MPa. All measured values were higher than 5.6 x 10^{-7}; therefore, the buoyancy effect did contribute to heat transfer performance.

4.3.6 Application of an azeotrope CO_2/ethane in heat pump power systems

The above-mentioned azeotropic mixture of CO_2 and ethane (at 75 % wt. CO_2 and 25 % wt. of ethane) can also be incorporated into a heat pump working cycle as the Heat Transferring Fluid (hereafter HTF).
Heat pump working cycles comprise four main components: the compressor, the condensation vessel, the expansion valve and the evaporation vessel [261]. The scheme *and T-S* diagram for such a simple heat pump cycle can be found in Figure 4-14. To achieve a cooling (or heating) effect, the HTF is pumped via the compressor to the condenser, where the gas phase condenses and releases heat at high temperatures because of the increase in pressure (point 2). The overheated gas then enters the condenser, where it is initially chilled to the phase boundary at point 3. From points 3 to 4, condensation of the gas phase occurs. Then the condensed liquid phase is led through the pressure relief expansion valve, which reduces the pressure of the liquid and partly evaporates it (point 5). The fluid in this state is at its saturation point when it arrives in the evaporation chamber, where it receives heat at low temperatures until it has completely evaporated (point 1). After this step, the gas is again compressed in the compressor, and the whole cycle is repeated.

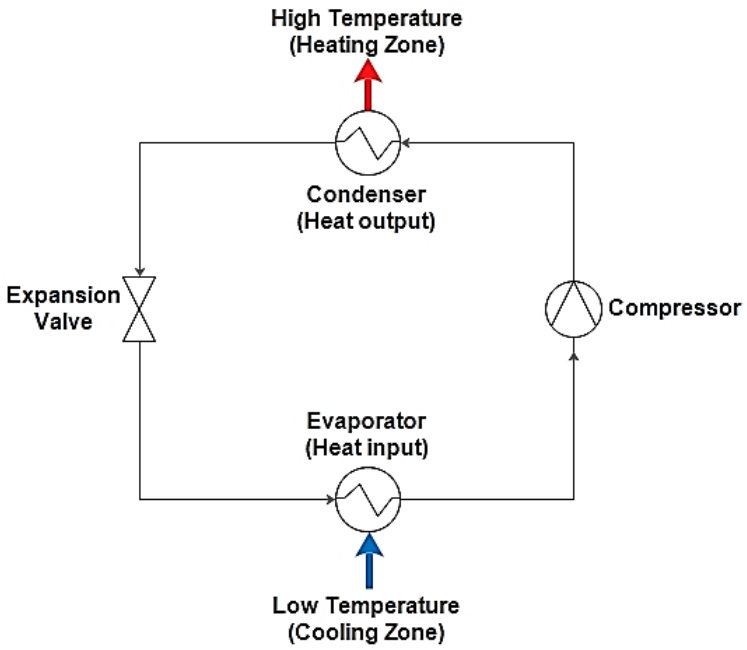

Figure 4-14: Scheme of the subcritical heat pump working cycle.

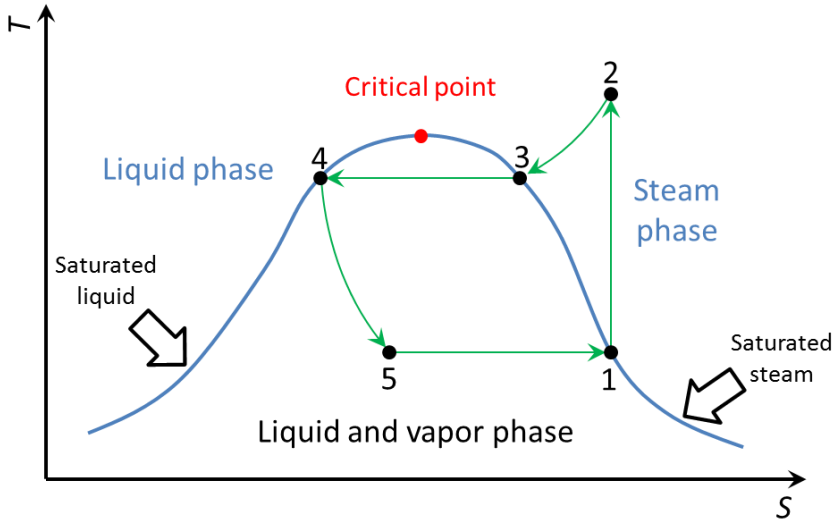

Figure 4-15: Scheme of T-S diagram for heat pump working cycle.

4.3.6.1 Boiling point diagram

The motivation for using an azeotropic mixture as the HTF in heat pump power cycles was the deviation of the boiling point of such fluids compared to its pure components. The hypothesis of this idea was that we could improve the performance of such systems only with the introduction of a different HTF.

It can clearly be seen from Figure 4-16 that, at a specific composition (75 wt. % CO_2 and 25 wt. % ethane), the mixture forms an azeotropic blend with a minimum boiling point that can be followed through the entire pressure range. We can also conclude that the composition of the azeotrope remains almost the same with increasing pressure (from 1 MPa to 4.5 MPa, it varies from 72 to 78 wt. % of CO_2). This feature also contributes to the immense potential that azeotropic blends have in heat pump cycles because their composition remains constant in both the gaseous and the liquid phase. This is also the key factor in ensuring composition consistency throughout the cycle. For example, if we were using a non-azeotropic blend of two cooling agents, we would not be able to sustain the same composition throughout the cycle, because of the separation of the fluids in the evaporator via distillation, on account of the different boiling points of the mixed fluids.

To properly assess such an azeotropic heat pump cycle, it was compared to a simple heat pump cycle system that contained pure CO_2 as the HTF. The research done in this paper is dedicated to finding alternative sustainable energy solutions.

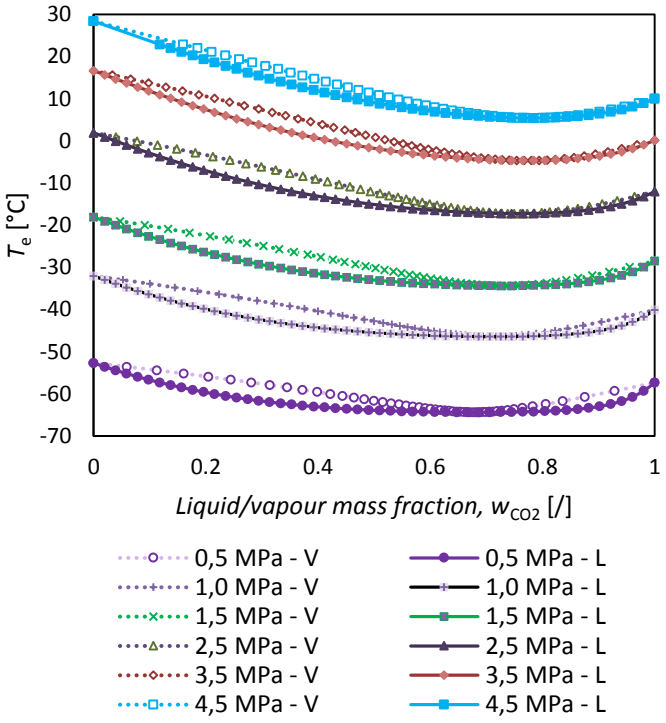

Figure 4-16: Phase diagram of CO_2 and ethane (filled points-boiling point line, empty points-dew point line).

4.3.6.2 Efficiency of the azeotropic mixture

The efficiency of heat pump cycles has been evaluated through the most commonly used parameters of heat pump system performance. To assess the potential of a binary azeotropic fluid system, we compared the Coefficients of Performance (COP in the following text) for a simple system using Aspen plus® software (REFPROP was used as the thermodynamic method).

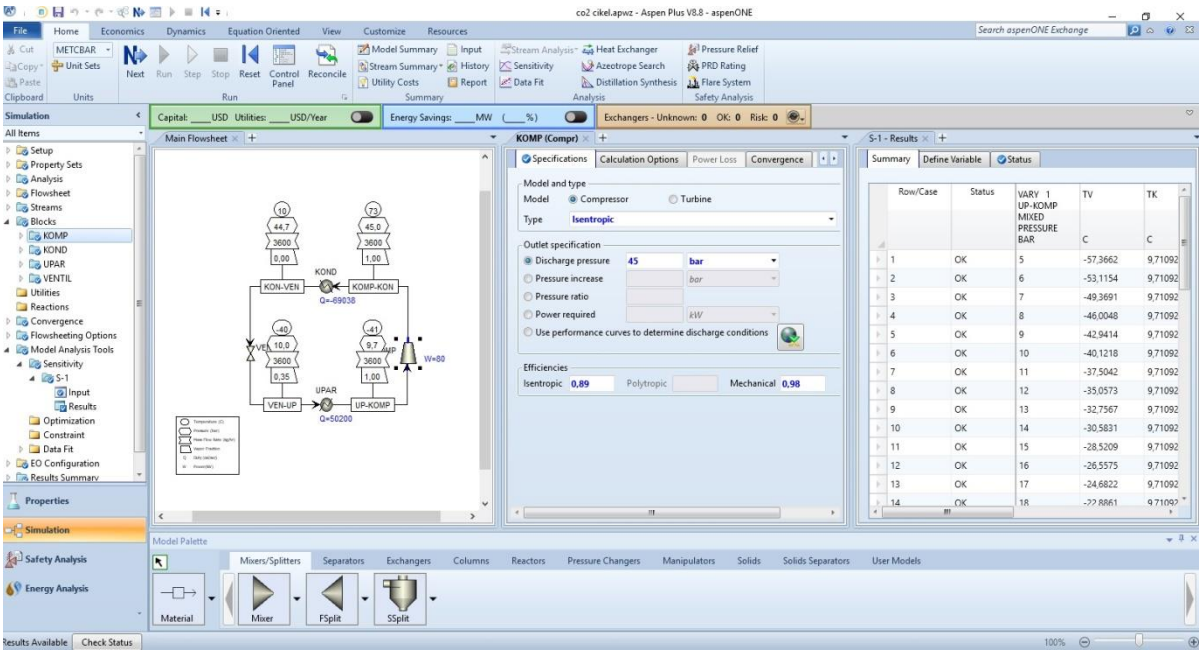

Figure 4-17: The efficiency of heat pump cycles has been evaluated using Aspen plus® software.

In Figure 4-18, the cooling COP of a simple CO_2 system is compared to the cooling COP of a system that contained the azeotropic blend of CO_2 and ethane. In the first segment of this figure (where the T_e (evaporation temperature) is lower than -25 °C) the COP of the azeotrope cycle is fairly similar to the COP of the simple CO_2 cycle. In this region, we do not encounter an increase in performance of the azeotrope cycle. In the second segment, however, (where the T_e is higher than -25 °C), we can clearly see that the COP values of the azeotrope cycle are significantly higher than those of the simple CO_2 cycle. For example, at T_e = 0 °C, the increase in COP of the compared cycles is close to 50 %.

This increase in efficiency can have a profound impact on the economy of the entire heat cycle process. Consequently, we can decrease the pressure ratio of the compressor and therefore decrease the required energy input to operate it, minimizing the operational cost by a significant extant. The condensation temperature (T_{con}) of the system shown in Figure 4-14 should also be considered. To properly compare the simple CO_2 cycle to the azeotrope cycle, the condensation pressure (P_{con}) of both simulations was held constant at 4.5 MPa. The corresponding T_{con} of the CO_2 cycle was 9.7 °C and it was 5.2 °C of the azeotrope cycle. This difference is due to the drop in boiling point of the azeotrope blend. It is usually common practice when comparing heat pump cycles to maintain the same T_{con} for all cases. Since we assumed that there were no technical restrictions regarding the temperature in the evaporator, we considered it as a variable parameter for this comparison.

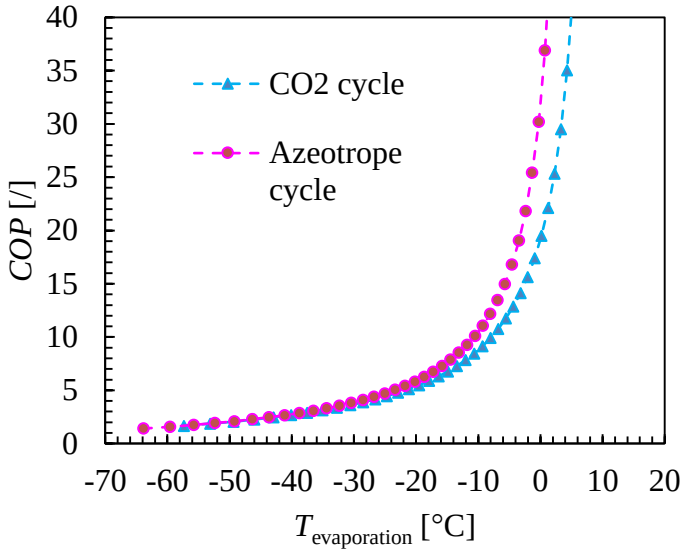

Figure 4-18: Coefficients of Performance (COP) of a simple CO_2 cycle system and the azeotropic cycle (CO_2/ethane).

In Figure 4-19, it can be seen that the optimal composition yielding the highest COP values is approximately 75 wt. % of CO_2 and 25 wt. % of ethane. These results are given in order to justify this composition as the optimal composition of the mixture to achieve the highest possible efficiency in heat pump cycles (not considering the possibility of using other fluids).

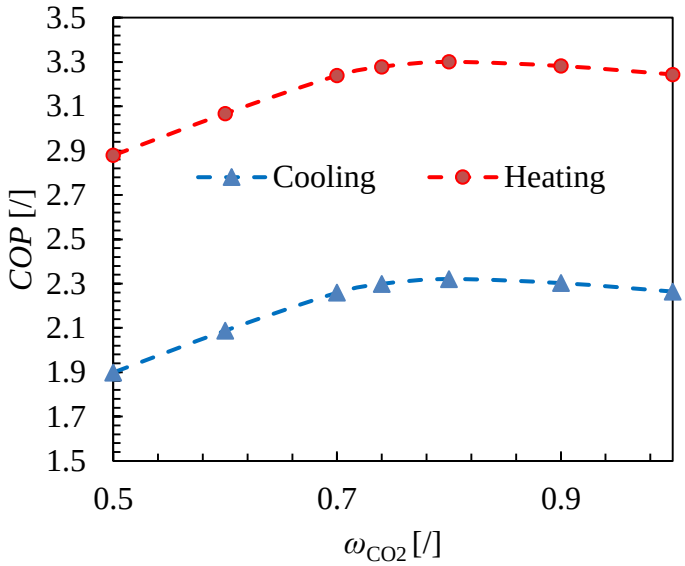

Figure 4-19: Coefficients of Performance (COP) of an azeotropic cycle depending on composition.

4.4 Conclusion

Heat transfer coefficients (HTC) have been determined using a new optimized experimental setup comprising two separate closed loops, i.e., a supercritical fluid loop and a water loop. For the first time, an azeotropic mixture of ethane and CO_2 as a potential new heat transfer fluid in heat power systems was investigated and compared to pure CO_2 and ethane. Measurements were performed at pressures above the pseudo-critical pressure and around the pseudo-critical temperature. It was found that total and supercritical-side HTC have the highest values near the pseudo-critical point of the given fluids. Such behaviour can be related to variations in the thermophysical properties of fluids. The influence of the water flux rate on the total and supercritical-side HTC was not to be neglected. The total HTC increased by more than 25 % when the flux rate of the water was increased from 1 L/min up to 2 L/min. Near the critical point, total HTC values for the azeotropic mixture fell between the total HTC values for the pure CO_2 and ethane. The heat transfer performance of the azeotropic mixture in the heat exchanger was satisfactorily high. Since it can be found in large quantities as a waste product in the petrochemical industry, its usage in heat power systems can be considered as a promising option.

The motivation to investigate an azeotropic mixture in a heat pump working cycle was the deviation of the boiling point compared to its pure components. We were able to successfully simulate a simple heat pump power cycle using Aspen V8.8 computer software. The main HTF used were CO_2 and a mixture of ethane and CO_2, since both of those fluids are considered refrigerants (R-744 and R-170) and form a well-known azeotropic blend. We concluded that the usage of such an azeotropic blend can result in lowering the evaporation temperature, which can potentiality decrease the operational costs if we are not bound by the condensation temperature, since it is also lowered with the introduction of the CO_2-ethane azeotrope.

The ideal azeotropic blend of fluids that could be used in heat pump cycles would be what is called a complex azeotrope, which has a maximum boiling point at high pressures and a minimum boiling point at low pressures. To the author's knowledge, such a complex azeotropic blend of fluids that can be used as a refrigerant has not yet been discovered.

5. Conclusion and future studies

This doctoral thesis was divided into several chapters, among them three main chapters which contained most of the research. At the beginning of each chapter, the theory and the current state of research regarding the topic were surveyed. Supercritical fluids (SCFs), used as green processing solvents in several high-pressure processes, comprised the connection between chapters.

The first chapter presents a contribution to the literature in a wide range, from early initial studies in developing simple and reliable methods for determination of thermodynamic and transport properties in polymeric systems with SCFs to pioneering experiments in adapting high-pressure technology to practical applications that are of great importance to the pharmaceutical industry. The PGSS^{TM} (Particles from Gas saturated Solution) process was applied to the biodegradable polymeric carriers polyoxyethylene stearyl ether **(**Brij 100 and Brij 52) and polyethylene glycol (PEG 4000) for the incorporation of insoluble drugs nimodipine, fenofibrate, o-vanillin, and esomeprazole with the purpose of improving their bioavailability and dissolution rate.

Before starting particle precipitation, preliminary thermodynamic experiments of water-soluble carriers polyoxyethylene stearyl with molar weights of 683 g/mol (Brij 52), 4670 g/mol (Brij 100) and polyethylene glycol of molar weights from 600 g/mol up to 1000 g/mol were carried out. The diffusion coefficient, density, interfacial tension and solubility of CO_2 saturated Brij 52 were studied at different pressure and temperature conditions. Similarly, for Brij 100, the melting points in the presence of various gases, CO_2 solubility in polymer matrixes and interfacial tension of gas-saturated solutions were determined. Influence of the polymer molar weight on the gas solubility and interfacial tension was measured in the system of PEG/CO_2 and PEG/Ar. Additionally, measured interfacial tension and viscosity of CO_2 saturated PEG 6000 at different spraying pressure and temperature conditions were correlated with particle shape and morphology. The results show that the Brij 100/CO_2 binary system has an S-L-G (solid-liquid-gas) curve with a negative *dP/dT* slope, which indicates high CO_2 solubility in the molten heavy component. Sorption of CO_2 in Brij 100 and Brij 52 is about 25 % higher than in PEG of different molar weights under similar conditions. In the case of argon saturated solutions of PEGs, the effect of pressure on interfacial tension was less pronounced in comparison with CO_2 saturated solutions of PEGs which resulted in up to 3 times higher values at pressures above 10 MPa. A possible explanation is that the solubility of carbon dioxide in the polymer was up to 10 times higher than the solubility of argon, most probably due to the differences in the molecular structures of the gases. The highest solubility and consequently densities of CO_2 and argon were determined in PEGs of lower molecular masses due to the fact that a PEG with a low molecular mass has a matrix with more empty spaces and can accept more gas molecules. Additionally, obtained data on interfacial tension and viscosity of CO_2 saturated solutions with PEG 6000 were for the first time correlated with particle size and particle morphology. With viscosity reduction, particles of the gas-saturated solution are expected to have smaller mean size. Increased pre-expansion temperature has a strong influence on PEG 6000 viscosity and morphology of obtaining particles. Higher interfacial tension boosts the formation of smaller particle droplets after spraying through the nozzle.

The second part of the first chapter presents particle precipitation and formulation of fenofibrate, nimodipine, o-vanillin, and esomeprazole with biodegradable Brij 100, Brij 52 and PEG 4000. In the case of Brij 100 and PEG 4000 the influence of the main process parameters (pressure, temperature and active substance/carrier ration) on the precipitated yield, mean the particle size distribution, loading efficiency, and dissolution rates are presented. With increasing pre-expansion pressure, the mean particle size of nimodipine/Brij S100, vanillin/Brij S100, and vanillin/PEG 4000 decrease. In the case of a mixture of fenofibrate/Brij S100,

anticipated effective surface areas were slightly reduced with pressure as a result of agglomeration. The loading efficiency of drugs in carriers observed by PGSS^{TM} was high in all experiments. It was observed that at lower pressure loading efficiency was greater than at higher pressures and that efficiency varies significantly with changing drug/carrier ratio. The morphology of particles obtained was irregular and, according to the ESEM pictures, porous. Combination of factors, including particle size reduction and interactions between drugs and hydrophilic carriers contribute to enhancing the dissolution rates of precipitated solid particles. On average, a 3.5 times greater amount of the dihydropyridine calcium channel blocker nimodipine was dissolved in 1 h from solid dispersions, compared to unprocessed nimodipine. Dissolution profiles were compared with a different f_1 factor and a similarity factor f_2. It was confirmed that the dissolution character of processed o-vanillin and nimodipine by PGSS^{TM} was different from that of unprocessed o-vanillin and nimodipine. On the other hand, micronization of Brij 52 without/with esomeprazole as the active compound has been carried out at one process condition (15 MPa and 60 °C), where the highest diffusion coefficients and CO_2 solubility in the polymer were measured. It was not possible to obtain particles with a well-defined structure since massive agglomeration of the particles took place. However, the formation mechanism of the cellular structure has been fully achieved and investigated from the viewpoint of the morphology and viscosity of the blend polymer Brij 52 and the mass-transfer rate of the physical foaming agent in polymer.

Processing of polymers with SCFs certainly has a bright future due to several beneficial effects considering ecological and economic feasibility. Substances are processed at lower temperatures, which is suitable in case of temperature labile compounds. CO_2 is still the most frequently applied processing media in novel engineering concepts. Future studies will focus on these concepts that include the use of supercritical CO_2 as an agent for production and formulation of fine particles with improved characteristics. New methods for estimation of thermodynamic and transport properties in systems with SCFs will be developed. The PGSS^{TM} will be applied for several unexplored water-soluble polymer surfactants like Gelucire^{R}, Imwitor^{R}, Miglyol^{R,} and TweenR to enhance solubility and impregnation affinity of desirable poorly water-soluble drugs. The optimization of the main process parameters, including the pre-expansion conditions, the size of the spray nozzle and polymer-drug ratio, on product characteristics such as the yield of collected particles, drug content, particle size distribution, morphology, and dissolution rate profile of the microparticle, will be carried out in a new comprehensive way using statistical design methods and fitting obtain data in multiple linear regressions.

In the second main chapter, a new experimental technique for obtaining diffusion coefficients and interfacial tension by means of pendant drop tensiometry was developed, and a mathematical model designed to fit the experimental data was used for determining the diffusion coefficients of binary systems at elevated pressured and temperatures. The experimental technique was validated by measuring the interfacial tension at water/CO_2 interface and diffusivity of water in CO_2 was measured at 25 °C and 45 °C in the pressure range from 0.1 MPa up to 60 MPa. Droplet geometry was examined by using a precise computer algorithm that fits Young–Laplace equation to the axisymmetric shape of a drop. The method was further applied for determining the interfacial properties and diffusivity rates of propylene glycol in CO_2 at 120 °C and 150 °C and at pressures ranging from 5 MPa up to 17.5 MPa. As expected, the high evaporation rate of propylene glycol allows for only a short drop shape observation time; consequently, a lower level of accuracy of the results is obtained, compared to that for the water- CO_2 system. Nevertheless, it was still established that diffusivity decreases with increasing pressure, meaning that solvent molecules are closer together, and increases with increasing temperature, predominately due to the higher kinetic energies of molecules that move more rapidly.

Additionally, the effect of argon as a co-contaminant in the CO_2 stream on the interfacial tension, storage capacity, and diffusion coefficients was studied under conditions relevant to carbon sequestration, using the pendant drop method. A strong increase in isothermal interfacial tension at 45 °C and up to 20 MPa was observed with an increase in Ar co-contaminant from 5 vol. % to 100 vol. %. The densities of the equilibrated brine-rich phase for Ar+CO_2 mixtures were reduced in comparison to those in the absence of Ar. Since non-condensable Ar will be present in small concentrations up to 5 vol. % in most injected CO_2 streams and may considerably influence the physical properties in deep geological reservoirs, we focused on measuring the brine-CO_2 interfacial tension and brine mixture (CO_2 and Ar) interfacial tension with 5 vol. % and 10 vol. % of argon content at pressure (7.5-40 MPa) and temperature (40-80 °C) ranges that had not previously been investigated and that can be considered more practical for carbon sequestration. In the case of 5 vol. % and 10 vol. % Ar, the contamination buoyancy effect prevailed over the interfacial properties and decreased storage capacity. It was found that the diffusivity of water in Ar is higher in comparison to water in CO_2. Small quantities of salt in the water had a minor effect on the diffusion coefficients of brine in supercritical CO_2. The experimentally obtained diffusion coefficients (D_{ab}) were correlated to obtain an effective diffusion coefficient (D_{eff}). It was found that, in the case of co-injection of Ar with CO_2, the diffusive gas breakthrough could be enhanced.

The method shows a wider applicability for estimation of mass transfer data in various systems of liquids in the presence of gases, which can be used as supercritical fluids at moderate and elevated pressures. Determination of mass transfer and thermodynamic properties is fundamental for a successful intensification and integration of separation processes. Properties of interest represent the first step to consider prior to processing of materials. These data are therefore crucial for high-pressure separation and formulation process optimization and to develop suitable analytical and separation methods for different systems of substances in alternative solvents such as supercritical fluids according to the green chemistry and sustainable technologies. However, the main disadvantage of this method for determining diffusivity is that it may be applied only to systems where evaporation of liquid droplet is more intensive than absorption. Therefore, this method is not suitable for substances like polymers or oils, where swelling of the droplet takes place. The aim of future studies will be to modify the method (mass – transfer model) and to perform measurements for these systems. Another disadvantage is that volatile compounds cannot be subjected to experiments at higher temperatures, since the deviation of the measurements is high as a result of the high evaporation rate.

In the third chapter, a double pipe heat exchanger was developed to study the effects of different operating parameters on heat transfer performance over a wide range of temperatures (25 °C to 90 °C) and pressures (6 MPa to 30 MPa). This chapter contributes to understanding and managing thermal properties at elevated conditions that are the topic of many new scientific breakthroughs. For the first time, an azeotropic mixture of ethane and CO_2 as a potential new heat transfer fluid in heat power systems was investigated and compared to pure CO_2 and ethane. Measurements were performed at pressures above the pseudo-critical pressure and around the pseudo-critical temperature. It was found that total and supercritical-side HTC have the highest values near the pseudo-critical point of the given fluids. Such behavior can be related to variations in the thermophysical properties of fluids. The influence of the water flux rate on the total and supercritical-side HTC is also an important parameter. The total HTC increased by more than 25% when the flux rate of the water was increased from 1 L/min up to 2 L/min. Near the critical point, total HTC values for the azeotropic mixture fell between the total HTC values for the pure CO_2 and ethane. The heat transfer performance of the azeotropic mixture in the heat exchanger was satisfactorily high. Since it can be found in large quantities as a waste product in the petrochemical industry, its usage in heat power systems can be considered as a promising option.

The motivation to investigate an azeotropic mixture in a heat pump power cycle was the deviation of the boiling point compared to its pure components. We were able to successfully simulate a simple heat pump power cycle using Aspen V8.8 computer software. The main HTF used were CO_2 and a mixture of ethane and CO_2, since both of those fluids are considered refrigerants (R-744 and R-170) and form a well-known azeotropic blend. We concluded that the usage of such an azeotropic blend can result in lowering the evaporation temperature, which can potentially decrease the operational costs if we are not bound by the condensation temperature, since it is also lowered with the introduction of the CO_2-ethane azeotrope.
Despite the numerous investigations of heat transfer properties under supercritical conditions, there are still variations among them and unknowns that need to be clarified. There is also a lack of information about many pure fluids and their mixtures which can be used as heat transfer fluids (HTF) in their critical state. For example, our test loop can be used to investigate heat transfer properties of hydrocarbon fuels in contact with a sub or supercritical CO_2 that are of a great importance in several industrial applications. Additionally, it would be interesting to observe the heat transfer in a co-current-flow regime using double pipe heat exchangers and to develop new test loops to study heat transfer at supercritical conditions in advanced refrigeration systems, advanced power cycles and solar collectors.

6. Reference

1. Knez, Ž.; Markočič, E.; Leitgeb, M.; Primožič, M.; Knez Hrnčič, M.; Škerget, M., Industrial applications of supercritical fluids: A review. *Energy* **2014,** 77, (Supplement C), 235-243.
2. Bolmatov, D.; Brazhkin, V.; Trachenko, K., Thermodynamic behavior of supercritical matter. *arXiv preprint arXiv:1303.3153* **2013**.
3. Knez, Ž.; Knez Hrnčič, M.; Škerget, M., Particle formation and product formulation using supercritical fluids. *Annual review of chemical and biomolecular engineering* **2015,** 6, 379-407.
4. Budisa, N.; Schulze-Makuch, D., Supercritical Carbon Dioxide and Its Potential as a Life-Sustaining Solvent in a Planetary Environment. *Life : Open Access Journal* **2014,** 4, (3), 331-340.
5. Brunner, G., Supercritical fluids: technology and application to food processing. *Journal of Food Engineering* **2005,** 67, (1), 21-33.
6. M, V. d. S., Supercritical fluids and its applications. In *In Current Trends in Chemical Engeneering*, Delgado, J. M. P. Q., Ed. Studium Press, : Houston, USA., 2010.
7. Haldorai, Y.; Shim, J.-J.; Lim, K. T., Synthesis of polymer–inorganic filler nanocomposites in supercritical CO2. *The Journal of Supercritical Fluids* **2012,** 71, (Supplement C), 45-63.
8. Hrnčič Knez, M.; Kravanja, G.; Knez, Ž., Hydrothermal treatment of biomass for energy and chemicals. *Energy* **2016,** 116, (Part 2), 1312-1322.
9. Hrnčič Knez, M.; Škerget, M.; Knez, Ž., Argon as a potential processing media for natural and synthetic substances. *The Journal of Supercritical Fluids* **2014,** 95, (Supplement C), 252-257.
10. Perrut, M., Supercritical fluid applications: industrial developments and economic issues. *Industrial & engineering chemistry research* **2000,** 39, (12), 4531-4535.
11. Centi, G.; Perathoner, S., Catalysis and sustainable (green) chemistry. *Catalysis Today* **2003,** 77, (4), 287-297.
12. Nakamura, K., Biochemical reactions in supercritical fluids. *Trends in Biotechnology* **1990,** 8, 288-292.
13. Smith, R. D., Method of making supercritical fluid molecular spray films, powder and fibers. In Google Patents: 1988.
14. Rao, J. P.; Geckeler, K. E., Polymer nanoparticles: preparation techniques and size-control parameters. *Progress in Polymer Science* **2011,** 36, (7), 887-913.
15. Engelmeier, L.; Pollak, S.; Weidner, E., Investigation of superheated liquid carbon dioxide jets for cutting applications. *The Journal of Supercritical Fluids* **2017**.
16. Lebedev, A. E.; Katalevich, A. M.; Menshutina, N. V., Modeling and scale-up of supercritical fluid processes. Part I: Supercritical drying. *The Journal of Supercritical Fluids* **2015,** 106, (Supplement C), 122-132.
17. Perrut, M., Sterilization and virus inactivation by supercritical fluids (a review). *The Journal of Supercritical Fluids* **2012,** 66, 359-371.
18. Scognamiglio, F.; Blanchy, M.; Borgogna, M.; Travan, A.; Donati, I.; Bosmans, J. W. A. M.; Foulc, M. P.; Bouvy, N. D.; Paoletti, S.; Marsich, E., Effects of supercritical carbon dioxide sterilization on polysaccharidic membranes for surgical applications. *Carbohydrate Polymers* **2017,** 173, (Supplement C), 482-488.
19. Yang, J.; Zhu, L.; Zhao, Y.; Xu, Y.; Sun, Q.; Liu, S.; Liu, C.; Ma, B., Separation of furostanol saponins by supercritical fluid chromatography. *Journal of Pharmaceutical and Biomedical Analysis* **2017,** 145, (Supplement C), 71-78.

20. Li, M.-J.; Zhu, H.-H.; Guo, J.-Q.; Wang, K.; Tao, W.-Q., The development technology and applications of supercritical CO2 power cycle in nuclear energy, solar energy and other energy industries. *Applied Thermal Engineering* **2017,** 126, (Supplement C), 255-275.
21. López-Padilla, A.; Ruiz-Rodriguez, A.; Reglero, G.; Fornari, T., Supercritical extraction of solid materials: A practical correlation related with process scaling. *Journal of Food Engineering* **2017**.
22. Marrone, P. A., Supercritical water oxidation—current status of full-scale commercial activity for waste destruction. *The Journal of Supercritical Fluids* **2013,** 79, 283-288.
23. Ramsey, E.; Qiubai, S.; Zhang, Z.; Zhang, C.; Wei, G., Mini-Review: Green sustainable processes using supercritical fluid carbon dioxide. *Journal of Environmental Sciences* **2009,** 21, (6), 720-726.
24. Herrero, M.; Cifuentes, A.; Ibañez, E., Sub-and supercritical fluid extraction of functional ingredients from different natural sources: Plants, food-by-products, algae and microalgae: A review. *Food chemistry* **2006,** 98, (1), 136-148.
25. Erkey, C., Supercritical carbon dioxide extraction of metals from aqueous solutions: a review. *The Journal of Supercritical Fluids* **2000,** 17, (3), 259-287.
26. Herrero, M.; Mendiola, J. A.; Cifuentes, A.; Ibáñez, E., Supercritical fluid extraction: Recent advances and applications. *Journal of Chromatography A* **2010,** 1217, (16), 2495-2511.
27. Sharif, K.; Rahman, M.; Azmir, J.; Mohamed, A.; Jahurul, M.; Sahena, F.; Zaidul, I., Experimental design of supercritical fluid extraction–A review. *Journal of Food Engineering* **2014,** 124, 105-116.
28. Tsivintzelis, I.; Sanxaridou, G.; Pavlidou, E.; Panayiotou, C., Foaming of polymers with supercritical fluids: A thermodynamic investigation. *The Journal of Supercritical Fluids* **2016,** 110, 240-250.
29. Costeux, S., CO2-blown nanocellular foams. *Journal of Applied Polymer Science* **2014,** 131, (23).
30. Tomasko, D. L.; Burley, A.; Feng, L.; Yeh, S.-K.; Miyazono, K.; Nirmal-Kumar, S.; Kusaka, I.; Koelling, K., Development of CO 2 for polymer foam applications. *The Journal of Supercritical Fluids* **2009,** 47, (3), 493-499.
31. Knez, Ž.; Markočič, E.; Novak, Z.; Hrnčič, M. K., Processing Polymeric Biomaterials using Supercritical CO2. *Chemie Ingenieur Technik* **2011,** 83, (9), 1371-1380.
32. Paisana, M. C.; Müllers, K. C.; Wahl, M. A.; Pinto, J. F., Production and stabilization of olanzapine nanoparticles by rapid expansion of supercritical solutions (RESS). *The Journal of Supercritical Fluids* **2016,** 109, (Supplement C), 124-133.
33. Lőrincz, L.; Bánsághi, G.; Zsemberi, M.; de Simón Brezmes, S.; Szilágyi, I. M.; Madarász, J.; Sohajda, T.; Székely, E., Diastereomeric salt precipitation based resolution of ibuprofen by gas antisolvent method. *The Journal of Supercritical Fluids* **2016,** 118, (Supplement C), 48-53.
34. Prosapio, V.; Reverchon, E.; De Marco, I., Formation of PVP/nimesulide microspheres by supercritical antisolvent coprecipitation. *The Journal of Supercritical Fluids* **2016,** 118, (Supplement C), 19-26.
35. Dal Magro, C.; Aguiar, G. P. S.; Veneral, J. G.; dos Santos, A. E.; de Chaves, L. M. P. C.; Oliveira, J. V.; Lanza, M., Co-precipitation of trans-resveratrol in PHBV using Solution Enhanced Dispersion by Supercritical Fluids technique. *The Journal of Supercritical Fluids* **2017,** 127, (Supplement C), 182-190.
36. Bleich, J.; Müller, B. W.; Waßmus, W., Aerosol solvent extraction system — a new microparticle production technique. *International Journal of Pharmaceutics* **1993,** 97, (1), 111-117.

37. Lévai, G.; Albarelli, J. Q.; Santos, D. T.; Meireles, M. A. A.; Martín, Á.; Rodríguez-Rojo, S.; Cocero, M. J., Quercetin loaded particles production by means of supercritical fluid extraction of emulsions: Process scale-upstudy and thermo-economic evaluation. *Food and Bioproducts Processing* **2017,** 103, (Supplement C), 27-38.
38. Martín, Á.; Weidner, E., PGSS-drying: Mechanisms and modeling. *The Journal of Supercritical Fluids* **2010,** 55, (1), 271-281.
39. Lack, E.; Weidner, E.; Knez, Z.; Gruner, S.; Weinreich, B.; Seidlitz, H., *Particle generation with supercritical CO2*. na: 2005.
40. Weidner, E., High pressure micronization for food applications. *The Journal of Supercritical Fluids* **2009,** 47, (3), 556-565.
41. Brunner, G., Supercritical process technology related to energy and future directions–An introduction. *The Journal of Supercritical Fluids* **2015,** 96, 11-20.
42. Oignet, J.; Hoang, H. M.; Osswald, V.; Delahaye, A.; Fournaison, L.; Haberschill, P., Experimental study of convective heat transfer coefficients of CO2 hydrate slurries in a secondary refrigeration loop. *Applied Thermal Engineering* **2017,** 118, 630-637.
43. Chen, H.; Goswami, D. Y.; Rahman, M. M.; Stefanakos, E. K., A supercritical Rankine cycle using zeotropic mixture working fluids for the conversion of low-grade heat into power. *Energy* **2011,** 36, (1), 549-555.
44. Iverson, B. D.; Conboy, T. M.; Pasch, J. J.; Kruizenga, A. M., Supercritical CO 2 Brayton cycles for solar-thermal energy. *Applied Energy* **2013,** 111, 957-970.
45. Craig, M. T.; Jaramillo, P.; Zhai, H.; Klima, K., The Economic Merits of Flexible Carbon Capture and Sequestration as a Compliance Strategy with the Clean Power Plan. *Environmental Science & Technology* **2017,** 51, (3), 1102-1109.
46. Agarwal, A.; Parsons, J., Commercial Structures for Integrated CCS-EOR Projects. *Energy Procedia* **2011,** 4, 5786-5793.
47. Carpenter, S. M.; Koperna, G., Development of the First Internationally Accepted Standard for Geologic Storage of Carbon Dioxide utilizing Enhanced Oil Recovery (EOR) under the International Standards Organization (ISO) Technical Committee TC-265. *Energy Procedia* **2014,** 63, 6717-6729.
48. Zhang, Z.; Huisingh, D., Carbon dioxide storage schemes: Technology, assessment and deployment. *Journal of Cleaner Production* **2017,** 142, 1055-1064.
49. Fozer, D.; Sziraky, F. Z.; Racz, L.; Nagy, T.; Tarjani, A. J.; Toth, A. J.; Haaz, E.; Benko, T.; Mizsey, P., Life cycle, PESTLE and Multi-Criteria Decision Analysis of CCS process alternatives. *Journal of Cleaner Production* **2017,** 147, 75-85.
50. von der Assen, N.; Jung, J.; Bardow, A., Life-cycle assessment of carbon dioxide capture and utilization: avoiding the pitfalls. *Energy & Environmental Science* **2013,** 6, (9), 2721-2734.
51. Cuéllar-Franca, R. M.; Azapagic, A., Carbon capture, storage and utilisation technologies: A critical analysis and comparison of their life cycle environmental impacts. *Journal of CO2 Utilization* **2015,** 9, 82-102.
52. Pavlovič, I.; Knez, Ž.; Škerget, M., Hydrothermal Reactions of Agricultural and Food Processing Wastes in Sub- and Supercritical Water: A Review of Fundamentals, Mechanisms, and State of Research. *Journal of Agricultural and Food Chemistry* **2013,** 61, (34), 8003-8025.
53. Hrnčič Knez, M.; Kravanja, G.; Knez, Ž., Hydrothermal treatment of biomass for energy and chemicals. *Energy* **2016,** 116, 1312-1322.
54. Gao, Y.; Wang, X.-H.; Yang, H.-P.; Chen, H.-P., Characterization of products from hydrothermal treatments of cellulose. *Energy* **2012,** 42, (1), 457-465.

55. Stemann, J.; Erlach, B.; Ziegler, F., Hydrothermal Carbonisation of Empty Palm Oil Fruit Bunches: Laboratory Trials, Plant Simulation, Carbon Avoidance, and Economic Feasibility. *Waste and Biomass Valorization* **2013,** 4, (3), 441-454.
56. DeYoung, J. P.; McClain, J. B.; Gross, S. M., Processes for cleaning and drying microelectronic structures using liquid or supercritical carbon dioxide. In Google Patents: 2003.
57. Bray, D., Critical point drying of biological specimens for scanning electron microscopy. *Supercritical Fluid Methods and Protocols* **2000**, 235-243.
58. Aegerter, M.; Leventis, N.; Koebel, M. M., *Aerogels handbook*. Springer Science & Business Media: 2011.
59. Baetens, R.; Jelle, B. P.; Gustavsen, A., Aerogel insulation for building applications: a state-of-the-art review. *Energy and Buildings* **2011,** 43, (4), 761-769.
60. Veronovski, A.; Tkalec, G.; Knez, Ž.; Novak, Z., Characterisation of biodegradable pectin aerogels and their potential use as drug carriers. *Carbohydrate polymers* **2014,** 113, 272-278.
61. Tkalec, G.; Knez, Ž.; Novak, Z., Formation of polysaccharide aerogels in ethanol. *RSC Advances* **2015,** 5, (94), 77362-77371.
62. Ulker, Z.; Erkey, C., An emerging platform for drug delivery: Aerogel based systems. *Journal of Controlled Release* **2014,** 177, 51-63.
63. Nalawade, S. P.; Picchioni, F.; Janssen, L. P. B. M., Supercritical carbon dioxide as a green solvent for processing polymer melts: Processing aspects and applications. *Progress in Polymer Science* **2006,** 31, (1), 19-43.
64. Marizza, P.; Pontoni, L.; Rindzevicius, T.; Alopaeus, J. F.; Su, K.; Zeitler, J. A.; Keller, S. S.; Kikic, I.; Moneghini, M.; De Zordi, N.; Solinas, D.; Cortesi, A.; Boisen, A., Supercritical impregnation of polymer matrices spatially confined in microcontainers for oral drug delivery: Effect of temperature, pressure and time. *The Journal of Supercritical Fluids* **2016,** 107, (Supplement C), 145-152.
65. Trupej, N.; Hrnčič, M. K.; Škerget, M.; Knez, Ž., Solubility and binary diffusion coefficient of argon in polyethylene glycols of different molecular weights. *The Journal of Supercritical Fluids* **2015,** 103, (Supplement C), 10-17.
66. da Ponte, M., High pressure phase equilibria for poly (ethylene glycol) s+ CO 2: experimental results and modelling. *Physical Chemistry Chemical Physics* **1999,** 1, (23), 5369-5375.
67. Hrnčič Knez, M.; Markočič, E.; Trupej, N.; Škerget, M.; Knez, Ž., Investigation of thermodynamic properties of the binary system polyethylene glycol/CO 2 using new methods. *The Journal of Supercritical Fluids* **2014,** 87, 50-58.
68. Trupej, N.; Hrnčič, M. K.; Škerget, M.; Knez, Ž., Solubility and binary diffusion coefficient of argon in polyethylene glycols of different molecular weights. *The Journal of Supercritical Fluids* **2015,** 103, 10-17.
69. Fanovich, M. A.; Jaeger, P., Sorption and diffusion of compressed carbon dioxide in polycaprolactone for the development of porous scaffolds. *Materials Science and Engineering: C* **2012,** 32, (4), 961-968.
70. Sato, Y.; Fujiwara, K.; Takikawa, T.; Takishima, S.; Masuoka, H., Solubilities and diffusion coefficients of carbon dioxide and nitrogen in polypropylene, high-density polyethylene, and polystyrene under high pressures and temperatures. *Fluid phase equilibria* **1999,** 162, (1), 261-276.
71. Khosravi-Darani, K.; Vasheghani-Farahani, E.; Yamini, Y.; Bahramifar, N., Solubility of poly (β-hydroxybutyrate) in supercritical carbon dioxide. *Journal of Chemical & Engineering Data* **2003,** 48, (4), 860-863.

72. Cravo, C.; Duarte, A. R. C.; Duarte, C. M., Solubility of carbon dioxide in a natural biodegradable polymer: Determination of diffusion coefficients. *The Journal of supercritical fluids* **2007,** 40, (2), 194-199.
73. Dimitrov, K.; Boyadzhiev, L.; Tufeu, R.; Cansell, F.; Barth, D., Solubility of poly (ethylene glycol) nonylphenyl ether in supercritical carbon dioxide. *The Journal of supercritical fluids* **1998,** 14, (1), 41-47.
74. Weidner, E.; Wiesmet, V.; Knez, Ž.; Škerget, M., Phase equilibrium (solid-liquid-gas) in polyethyleneglycol-carbon dioxide systems. *The Journal of Supercritical Fluids* **1997,** 10, (3), 139-147.
75. Knez, Ž.; Škerget, M.; Mandžuka, Z., Determination of S–L phase transitions under gas pressure. *The Journal of Supercritical Fluids* **2010,** 55, (2), 648-652.
76. Kegl, T.; Kravanja, G.; Knez, Ž.; Knez Hrnčič, M., Effect of addition of supercritical CO2 on transfer and thermodynamic properties of biodegradable polymers PEG 600 and Brij52. *The Journal of Supercritical Fluids* **2017,** 122, (Supplement C), 10-17.
77. Trupej, N.; Škerget, M.; Knez, Ž., Thermodynamic data for processing polyethylene glycol with non-conventional fluids. *The Journal of Supercritical Fluids* **2016,** 118, (Supplement C), 39-47.
78. Hrnčič Knez, M.; Markočič, E.; Trupej, N.; Škerget, M.; Knez, Ž., Investigation of thermodynamic properties of the binary system polyethylene glycol/CO2 using new methods. *The Journal of Supercritical Fluids* **2014,** 87, (Supplement C), 50-58.
79. Hrnčič Knez, M.; Škerget, M.; Knez, Ž., Density and viscosity of the binary polyethylene glycol/CO2 systems. *The Journal of Supercritical Fluids* **2014,** 95, (Supplement C), 641-668.
80. Nalawade, S. P.; Picchioni, F.; Janssen, L., Supercritical carbon dioxide as a green solvent for processing polymer melts: Processing aspects and applications. *Progress in Polymer Science* **2006,** 31, (1), 19-43.
81. Mahmood, S.; Ameli, A.; Hossieny, N.; Park, C., The interfacial tension of molten polylactide in supercritical carbon dioxide. *The Journal of Chemical Thermodynamics* **2014,** 75, 69-76.
82. Carbone, M. G. P.; Di Maio, E.; Scherillo, G.; Mensitieri, G.; Iannace, S., Solubility, mutual diffusivity, specific volume and interfacial tension of molten PCL/CO 2 solutions by a fully experimental procedure: effect of pressure and temperature. *The Journal of Supercritical Fluids* **2012,** 67, 131-138.
83. Gutiérrez, C.; Rodríguez, J.; Gracia, I.; De Lucas, A.; García, M., Preparation and characterization of polystyrene foams from limonene solutions. *The Journal of Supercritical Fluids* **2014,** 88, 92-104.
84. Enders, S.; Kahl, H.; Winkelmann, J., Interfacial properties of polystyrene in contact with carbon dioxide. *Fluid phase equilibria* **2005,** 228, 511-522.
85. Silva, S. S.; Duarte, A. R. C.; Carvalho, A. P.; Mano, J. F.; Reis, R. L., Green processing of porous chitin structures for biomedical applications combining ionic liquids and supercritical fluid technology. *Acta biomaterialia* **2011,** 7, (3), 1166-1172.
86. Krykin, M., Sorption and diffusion of gas mixtures in polymers at high pressures. Mutual effects of components. *Polymer Science USSR* **1990,** 32, (2), 301-307.
87. Markočič, E.; Škerget, M.; Knez, Z. e., Effect of temperature and pressure on the behavior of poly (ε-caprolactone) in the presence of supercritical carbon dioxide. *Industrial & Engineering Chemistry Research* **2013,** 52, (44), 15594-15601.
88. Nalawade, S. P.; Picchioni, F.; Janssen, L., Batch production of micron size particles from poly (ethylene glycol) using supercritical CO 2 as a processing solvent. *Chemical Engineering Science* **2007,** 62, (6), 1712-1720.

89. Pestieau, A.; Krier, F.; Lebrun, P.; Brouwers, A.; Streel, B.; Evrard, B., Optimization of a PGSS (particles from gas saturated solutions) process for a fenofibrate lipid-based solid dispersion formulation. *International Journal of Pharmaceutics* **2015,** 485, (1), 295-305.
90. Jug, M.; Hafner, A.; Lovrić, J.; Kregar, M. L.; Pepić, I.; Vanić, Ž.; Cetina-Čižmek, B.; Filipović-Grčić, J., An overview of in vitro dissolution/release methods for novel mucosal drug delivery systems. *Journal of Pharmaceutical and Biomedical Analysis* **2017**.
91. Kawabata, Y.; Wada, K.; Nakatani, M.; Yamada, S.; Onoue, S., Formulation design for poorly water-soluble drugs based on biopharmaceutics classification system: Basic approaches and practical applications. *International Journal of Pharmaceutics* **2011,** 420, (1), 1-10.
92. Huang, Z.; Sun, G.-B.; Chiew, Y. C.; Kawi, S., Formation of ultrafine aspirin particles through rapid expansion of supercritical solutions (RESS). *Powder Technology* **2005,** 160, (2), 127-134.
93. Weidner, E.; Petermann, M.; Knez, Z., Multifunctional composites by high-pressure spray processes. *Current Opinion in Solid State and Materials Science* **2003,** 7, (4), 385-390.
94. Couto, R.; Alvarez, V.; Temelli, F., Encapsulation of Vitamin B2 in solid lipid nanoparticles using supercritical CO2. *The Journal of Supercritical Fluids* **2017,** 120, (Part 2), 432-442.
95. Weidner, E.; Steiner, R.; Knez, Z., Powder generation from polyethyleneglycols with compressible fluids. In *Process Technology Proceedings*, von Rohr, P. R.; Trepp, C., Eds. Elsevier: 1996; Vol. 12, pp 223-228.
96. Chen, W.; Hu, X.; Hong, Y.; Su, Y.; Wang, H.; Li, J., Ibuprofen nanoparticles prepared by a PGSS™-based method. *Powder Technology* **2013,** 245, (Supplement C), 241-250.
97. Kerč, J.; Srčič, S.; Knez, Ž.; Senčar-Božič, P., Micronization of drugs using supercritical carbon dioxide. *International Journal of Pharmaceutics* **1999,** 182, (1), 33-39.
98. Senčar-Božič, P.; Srčič, S.; Knez, Z.; Kerč, J., Improvement of nifedipine dissolution characteristics using supercritical CO2. *International Journal of Pharmaceutics* **1997,** 148, (2), 123-130.
99. Marizza, P.; Keller, S. S.; Müllertz, A.; Boisen, A., Polymer-filled microcontainers for oral delivery loaded using supercritical impregnation. *Journal of Controlled Release* **2014,** 173, (Supplement C), 1-9.
100. García-González, C. A.; Argemí, A.; Sousa, A. R. S. d.; Duarte, C. M. M.; Saurina, J.; Domingo, C., Encapsulation efficiency of solid lipid hybrid particles prepared using the PGSS® technique and loaded with different polarity active agents. *The Journal of Supercritical Fluids* **2010,** 54, (3), 342-347.
101. Knez, Ž.; Cretnik, L.; Škerget, M., MICRONISATION OF VANILLINS BY PGSS TM USING VARIOUS COMPRESSED GASES.
102. Kravanja, G.; Knez, Ž.; Kotnik, P.; Ljubec, B.; Knez Hrnčič, M., Formulation of nimodipine, fenofibrate, and o-vanillin with Brij S100 and PEG 4000 using the PGSS™ process. *The Journal of Supercritical Fluids* **2018,** 135, 245-253.
103. Sampaio de Sousa, A. R.; Simplício, A. L.; de Sousa, H. C.; Duarte, C. M. M., Preparation of glyceryl monostearate-based particles by PGSS®—Application to caffeine. *The Journal of Supercritical Fluids* **2007,** 43, (1), 120-125.
104. Varona, S.; Martín, Á.; Cocero, M. J.; Duarte, C. M. M., Encapsulation of Lavandin Essential Oil in Poly-(ϵ-caprolactones) by PGSS Process. *Chemical Engineering & Technology* **2013,** 36, (7), 1187-1192.

105. de Paz, E.; Martín, Á.; Duarte, C. M. M.; Cocero, M. J., Formulation of β-carotene with poly-(ε-caprolactones) by PGSS process. *Powder Technology* **2012,** 217, (Supplement C), 77-83.
106. Sato, Y.; Takikawa, T.; Takishima, S.; Masuoka, H., Solubilities and diffusion coefficients of carbon dioxide in poly (vinyl acetate) and polystyrene. *The journal of Supercritical fluids* **2001,** 19, (2), 187-198.
107. Škerget, M.; Mandžuka, Z.; Aionicesei, E.; Knez, Ž.; Ješe, R.; Znoj, B.; Venturini, P., Solubility and diffusivity of CO 2 in carboxylated polyesters. *The Journal of Supercritical Fluids* **2010,** 51, (3), 306-311.
108. Čuček, D.; Perko, T.; Ilić, L.; Znoj, B.; Venturini, P.; Knez, Ž.; Škerget, M., Phase equlibiria and diffusivity of dense gases in various polyethylenes. *The Journal of Supercritical Fluids* **2013,** 78, 54-62.
109. (NIST), T. N. I. o. S. a. T., In U.S. department of commerce: https://www.nist.gov/.
110. Mamaliga, I.; Schabel, W.; Kind, M., Measurements of sorption isotherms and diffusion coefficients by means of a magnetic suspension balance. *Chemical Engineering and Processing: Process Intensification* **2004,** 43, (6), 753-763.
111. Hrnčič, M. K.; Škerget, M.; Knez, Ž., Density and viscosity of the binary polyethylene glycol/CO 2 systems. *The Journal of Supercritical Fluids* **2014,** 95, 641-668.
112. Kravanja, G.; Knez, Ž.; Knez Hrnčič, M., The effect of argon contamination on interfacial tension, diffusion coefficients and storage capacity in carbon sequestration processes. *International Journal of Greenhouse Gas Control* **2018,** 71, 142-154.
113. Chun, B. S., Interfacial-tension in high-pressure carbon-dioxide mixtures. *Industrial and Engineering Chemistry Research* **1996,** 34 (12), 4371–4377.
114. Godina, A.; Vuherer, T.; Acko, B., Possibilities for minimising uncertainty of dissimilar materials gauge blocks calibration by mechanical comparison. *Measurement* **2012,** 45, (3), 517-524.
115. Liao, X.; Li, Y. G.; Park, C. B.; Chen, P., Interfacial tension of linear and branched PP in supercritical carbon dioxide. *The Journal of Supercritical Fluids* **2010,** 55, (1), 386-394.
116. Weidner, E.; Knez, Z.; Novak, Z., Process for the production of particles or powders. In Google Patents: 2000.
117. Cocero, M. J.; Martín, Á.; Mattea, F.; Varona, S., Encapsulation and co-precipitation processes with supercritical fluids: Fundamentals and applications. *The Journal of Supercritical Fluids* **2009,** 47, (3), 546-555.
118. Kravanja, G.; Hrnčič, M. K.; Škerget, M.; Knez, Ž., Interfacial tension and gas solubility of molten polymer polyethylene glycol in contact with supercritical carbon dioxide and argon. *The Journal of Supercritical Fluids* **2016,** 108, 45-55.
119. Markočič, E.; Škerget, M.; Knez, Ž., Solubility and diffusivity of CO 2 in poly (l-lactide)–hydroxyapatite and poly (d, l-lactide-co-glycolide)–hydroxyapatite composite biomaterials. *The Journal of Supercritical Fluids* **2011,** 55, (3), 1046-1051.
120. Kvamme, B.; Kuznetsova, T.; Hebach, A.; Oberhof, A.; Lunde, E., Measurements and modelling of interfacial tension for water + carbon dioxide systems at elevated pressures. *Computational Materials Science* **2007,** 38, (3), 506-513.
121. Akutsu, T.; Yamaji, Y.; Yamaguchi, H.; Watanabe, M.; Smith Jr, R. L.; Inomata, H., Interfacial tension between water and high pressure CO2 in the presence of hydrocarbon surfactants. *Fluid Phase Equilibria* **2007,** 257, (2), 163-168.
122. Kravanja, G.; Hrnčič, M. K.; Škerget, M.; Knez, Ž., Interfacial tension and gas solubility of molten polymer polyethylene glycol in contact with supercritical carbon dioxide and argon. *The Journal of Supercritical Fluids* **2016,** 108, (Supplement C), 45-55.

123. Hrnčič, M. K.; Škerget, M.; Knez, Ž., Argon as a potential processing media for natural and synthetic substances. *The Journal of Supercritical Fluids* **2014,** 95, 252-257.
124. Wiesmet, V.; Weidner, E.; Behme, S.; Sadowski, G.; Arlt, W., Measurement and modelling of high-pressure phase equilibria in the systems polyethyleneglycol (PEG)–propane, PEG–nitrogen and PEG–carbon dioxide. *The Journal of Supercritical Fluids* **2000,** 17, (1), 1-12.
125. Lin, H.; Freeman, B. D., Gas solubility, diffusivity and permeability in poly (ethylene oxide). *Journal of Membrane Science* **2004,** 239, (1), 105-117.
126. Kappler, P.; Leiner, W.; Petermann, M.; Weidner, E. In *Size and morphology of particles generated by spraying polymer-melts with carbon dioxide*.
127. Ilieva, P.; Kilzer, A.; Weidner, E., Measurement of solubility, viscosity, density and interfacial tension of the systems tristearin and CO2 and rapeseed oil and CO2. *The Journal of Supercritical Fluids* **2016,** 117, (Supplement C), 40-49.
128. Avelino, H. M. N. T.; Fareleira, J. M. N. A.; Gourgouillon, D.; Igreja, J. M.; Nunes da Ponte, M., Viscosity of poly(ethyleneglycol) 200 [PEG 200] saturated with supercritical carbon dioxide. *The Journal of Supercritical Fluids* **2017,** 128, (Supplement C), 300-307.
129. Gourgouillon, D.; Avelino, H. M. N. T.; Fareleira, J. M. N. A.; Nunes da Ponte, M., Simultaneous viscosity and density measurement of supercritical CO2-saturated PEG 400. *The Journal of Supercritical Fluids* **1998,** 13, (1), 177-185.
130. Harrison, K. L.; Johnston, K. P.; Sanchez, I. C., Effect of Surfactants on the Interfacial Tension between Supercritical Carbon Dioxide and Polyethylene Glycol. *Langmuir* **1996,** 12, (11), 2637-2644.
131. Yeo, S.-D.; Kiran, E., Formation of polymer particles with supercritical fluids: a review. *The Journal of Supercritical Fluids* **2005,** 34, (3), 287-308.
132. Strumendo, M.; Bertucco, A.; Elvassore, N., Modeling of particle formation processes using gas saturated solution atomization. *The Journal of Supercritical Fluids* **2007,** 41, (1), 115-125.
133. Hiendrawan, S.; Veriansyah, B.; Tjandrawinata, R. R., Micronization of fenofibrate by rapid expansion of supercritical solution. *Journal of Industrial and Engineering Chemistry* **2014,** 20, (1), 54-60.
134. Magalhães, A. L.; Lito, P. F.; Da Silva, F. A.; Silva, C. M., Simple and accurate correlations for diffusion coefficients of solutes in liquids and supercritical fluids over wide ranges of temperature and density. *The Journal of Supercritical Fluids* **2013,** 76, 94-114.
135. Ratnakar, R. R.; Dindoruk, B., On the Exact Representation of Pressure Decay Tests: New Modeling and Experimental Data for Diffusivity Measurement in Gas - Oil/Bitumen Systems. In Society of Petroleum Engineers.
136. Robb, W. L.; Drickamer, H. G., Diffusion in CO2 up to 150-Atmospheres Pressure. *The Journal of Chemical Physics* **1951,** 19, (12), 1504-1508.
137. Takahashi, S.; Hongo, M., DIFFUSION COEFFICIENTS OF GASES AT HIGH PRESSURES IN THE C0₂-C₂H₄ SYSTEM. *Journal of Chemical Engineering of Japan* **1982,** 15, (1), 57-59.
138. Karaiskakis, G.; Gavril, D., Determination of diffusion coefficients by gas chromatography. *Journal of Chromatography A* **2004,** 1037, (1), 147-189.
139. Riazi, M. R., A new method for experimental measurement of diffusion coefficients in reservoir fluids. *Journal of Petroleum Science and Engineering* **1996,** 14, (3), 235-250.
140. Sachs, W., The diffusional transport of methane in liquid water: method and result of experimental investigation at elevated pressure. *Journal of Petroleum Science and Engineering* **1998,** 21, (3), 153-164.

141. Azin, R.; Mahmoudy, M.; Raad, S. M. J.; Osfouri, S., Measurement and modeling of CO2 diffusion coefficient in Saline Aquifer at reservoir conditions. *Central European Journal of Engineering* **2013,** 3, (4), 585-594.
142. Jamialahmadi, M.; Emadi, M.; Müller-Steinhagen, H., Diffusion coefficients of methane in liquid hydrocarbons at high pressure and temperature. *Journal of Petroleum Science and Engineering* **2006,** 53, (1), 47-60.
143. Wen, Y. W.; Kantzas, A., Monitoring Bitumen−Solvent Interactions with Low-Field Nuclear Magnetic Resonance and X-ray Computer-Assisted Tomography. *Energy & Fuels* **2005,** 19, (4), 1319-1326.
144. Guerrero Aconcha, U. E.; Kantzas, A., Diffusion of Hydrocarbon Gases in Heavy Oil and Bitumen. In Society of Petroleum Engineers.
145. Moganty, S. S.; Baltus, R. E., Diffusivity of Carbon Dioxide in Room-Temperature Ionic Liquids. *Industrial & Engineering Chemistry Research* **2010,** 49, (19), 9370-9376.
146. Espinoza, D. N.; Santamarina, J. C., Water-CO2-mineral systems: Interfacial tension, contact angle, and diffusion—Implications to CO2 geological storage. *Water Resources Research* **2010,** 46, (7), n/a-n/a.
147. Yang, C.; Gu, Y., Diffusion coefficients and oil swelling factors of carbon dioxide, methane, ethane, propane, and their mixtures in heavy oil. *Fluid Phase Equilibria* **2006,** 243, (1–2), 64-73.
148. ; Bellan, J. O., K. High Pressure, Transport Properties of Fluids: Theory and Data from Levitated Fluid-Drops at Combustion-Relevant Temperatures. 2001.
149. Hirai, S.; Okazaki, K.; Yazawa, H.; Ito, H.; Tabe, Y.; Hijikata, K., Measurement of CO2 diffusion coefficient and application of LIF in pressurized water. *Energy* **1997,** 22, (2–3), 363-367.
150. Erbil, H. Y.; Dogan, M., Determination of Diffusion Coefficient−Vapor Pressure Product of Some Liquids from Hanging Drop Evaporation. *Langmuir* **2000,** 16, (24), 9267-9273.
151. Hrnčič, M. K.; Kravanja, G.; Škerget, M.; Sadiku, M.; Knez, Ž., Investigation of interfacial tension of the binary system polyethylene glycol/CO2 by a capillary rise method. *The Journal of Supercritical Fluids* **2015,** 102, 9-16.
152. Akutsu, T.; Yamaji, Y.; Yamaguchi, H.; Watanabe, M.; Smith, R. L.; Inomata, H., Interfacial tension between water and high pressure CO2 in the presence of hydrocarbon surfactants. *Fluid Phase Equilibria* **2007,** 257, (2), 163-168.
153. Qin, K.; Wang, K.; Luo, R.; Li, Y.; Wang, T., Interfacial tension and wetting properties of 1-ethyl-3-methylimidazolium tetrafluoroborate in carbon dioxide, from atmospheric pressure to supercritical state. *The Journal of Supercritical Fluids* **2016,** 116, (Supplement C), 83-89.
154. Kvamme, B.; Kuznetsova, T.; Hebach, A.; Oberhof, A.; Lunde, E., Measurements and modelling of interfacial tension for water+carbon dioxide systems at elevated pressures. *Computational Materials Science* **2007,** 38, (3), 506-513.
155. Chun, B.-S.; Wilkinson, G. T., Interfacial tension in high-pressure carbon dioxide mixtures. *Industrial & engineering chemistry research* **1995,** 34, (12), 4371-4377.
156. Chen, H.; Muros-Cobos, J. L.; Holgado-Terriza, J. A.; Amirfazli, A., Surface tension measurement with a smartphone using a pendant drop. *Colloids and Surfaces A: Physicochemical and Engineering Aspects* **2017,** 533, 213-217.
157. Korenko, M.; Šimko, F. e., Measurement of Interfacial Tension in Liquid− Liquid High-Temperature Systems. *Journal of Chemical & Engineering Data* **2010,** 55, (11), 4561-4573.

158. Zang, D.; Yu, Y.; Chen, Z.; Li, X.; Wu, H.; Geng, X., Acoustic levitation of liquid drops: Dynamics, manipulation and phase transitions. *Advances in Colloid and Interface Science* **2017**.
159. Raza, A.; Gholami, R.; Rezaee, R.; Bing, C. H.; Nagarajan, R.; Hamid, M. A., Assessment of CO2 residual trapping in depleted reservoirs used for geosequestration. *Journal of Natural Gas Science and Engineering* **2017,** 43, 137-155.
160. Saraji, S.; Piri, M.; Goual, L., The effects of SO2 contamination, brine salinity, pressure, and temperature on dynamic contact angles and interfacial tension of supercritical CO2/brine/quartz systems. *International Journal of Greenhouse Gas Control* **2014,** 28, 147-155.
161. Akbarabadi, M.; Piri, M., Co-sequestration of SO2 with supercritical CO2 in carbonates: An experimental study of capillary trapping, relative permeability, and capillary pressure. *Advances in Water Resources* **2015,** 77, 44-56.
162. Georgiadis, A.; Maitland, G.; Trusler, J. P. M.; Bismarck, A., Interfacial Tension Measurements of the (H2O + CO2) System at Elevated Pressures and Temperatures. *Journal of Chemical & Engineering Data* **2010,** 55, (10), 4168-4175.
163. Chiquet, P.; Daridon, J.-L.; Broseta, D.; Thibeau, S., CO2/water interfacial tensions under pressure and temperature conditions of CO2 geological storage. *Energy Conversion and Management* **2007,** 48, (3), 736-744.
164. Aggelopoulos, C. A.; Robin, M.; Vizika, O., Interfacial tension between CO2 and brine (NaCl + CaCl2) at elevated pressures and temperatures: The additive effect of different salts. *Advances in Water Resources* **2011,** 34, (4), 505-511.
165. Arif, M.; Al-Yaseri, A. Z.; Barifcani, A.; Lebedev, M.; Iglauer, S., Impact of pressure and temperature on CO2–brine–mica contact angles and CO2–brine interfacial tension: Implications for carbon geo-sequestration. *Journal of Colloid and Interface Science* **2016,** 462, 208-215.
166. Pereira, L. M. C.; Chapoy, A.; Burgass, R.; Tohidi, B., Interfacial tension of CO2 + brine systems: Experiments and predictive modelling. *Advances in Water Resources* **2017,** 103, 64-75.
167. Yang, Z.; Liu, X.; Hua, Z.; Ling, Y.; Li, M.; Lin, M.; Dong, Z., Interfacial tension of CO2 and crude oils under high pressure and temperature. *Colloids and Surfaces A: Physicochemical and Engineering Aspects* **2015,** 482, 611-616.
168. Chalbaud, C.; Robin, M.; Lombard, J. M.; Martin, F.; Egermann, P.; Bertin, H., Interfacial tension measurements and wettability evaluation for geological CO2 storage. *Advances in Water Resources* **2009,** 32, (1), 98-109.
169. Li, X.; Boek, E. S.; Maitland, G. C.; Trusler, J. P. M., Interfacial Tension of (Brines + CO2): CaCl2(aq), MgCl2(aq), and Na2SO4(aq) at Temperatures between (343 and 423) K, Pressures between (2 and 50) MPa, and Molalities of (0.5 to 5) mol·kg–1. *Journal of Chemical & Engineering Data* **2012,** 57, (5), 1369-1375.
170. Talman, S., Subsurface geochemical fate and effects of impurities contained in a CO2 stream injected into a deep saline aquifer: What is known. *International Journal of Greenhouse Gas Control* **2015,** 40, 267-291.
171. Al-Yaseri, A.; Sarmadivaleh, M.; Saeedi, A.; Lebedev, M.; Barifcani, A.; Iglauer, S., N2+CO2+NaCl brine interfacial tensions and contact angles on quartz at CO2 storage site conditions in the Gippsland basin, Victoria/Australia. *Journal of Petroleum Science and Engineering* **2015,** 129, 58-62.
172. Shah, V.; Broseta, D.; Mouronval, G.; Montel, F., Water/acid gas interfacial tensions and their impact on acid gas geological storage. *International Journal of Greenhouse Gas Control* **2008,** 2, (4), 594-604.

173. Masterton, W.; Bianchi, J.; Slowinski Jr, E., Surface tension and adsorption in gas—liquid systems at moderate pressures1. *The Journal of Physical Chemistry* **1963,** 67, (3), 615-618.
174. Massoudi, R.; King Jr, A., Effect of pressure on the surface tension of water. Adsorption of low molecular weight gases on water at 25. deg. *The Journal of Physical Chemistry* **1974,** 78, (22), 2262-2266.
175. Wiegand, G.; Franck, E., Interfacial tension between water and non-polar fluids up to 473 K and 2800 bar. *Berichte der Bunsengesellschaft für physikalische Chemie* **1994,** 98, (6), 809-817.
176. Chow, Y. T. F., Interfacial properties of reservoir fluids and carbon dioxide with impurities. **2016**.
177. Chow, Y. F.; Maitland, G. C.; Trusler, J. M., Interfacial tensions of the (CO 2+ N 2+ H 2 O) system at temperatures of (298 to 448) K and pressures up to 40MPa. *The Journal of Chemical Thermodynamics* **2016,** 93, 392-403.
178. Chow, Y. F.; Eriksen, D. K.; Galindo, A.; Haslam, A. J.; Jackson, G.; Maitland, G. C.; Trusler, J. M., Interfacial tensions of systems comprising water, carbon dioxide and diluent gases at high pressures: Experimental measurements and modelling with SAFT-VR Mie and square-gradient theory. *Fluid Phase Equilibria* **2016,** 407, 159-176.
179. Change), P. I. P. o. C., Special Report on Carbon Dioxide Capture and Storage. In Cambridge University Press, Cambridge, UK, and
New York, NY, USA, 2005.
180. Canada), T. P. T. A., In Alberta CO2 Purity Project, 2014; p 160 p.
181. Oosterkamp, A., Ramsen, J, State of the art overview of CO2 pipeline transport with relevance to offshore pipelines. In Polytec Report number: POL-O-2007, 2008.
182. Škerget, M.; Čuček, D.; Knez, Ž., Phase equilibria of the propylene glycol/CO2 and propylene glycol/ethanol/CO2 systems. *The Journal of Supercritical Fluids* **2014,** 95, 129-136.
183. Berry, J. D.; Neeson, M. J.; Dagastine, R. R.; Chan, D. Y. C.; Tabor, R. F., Measurement of surface and interfacial tension using pendant drop tensiometry. *Journal of Colloid and Interface Science* **2015,** 454, 226-237.
184. Saad, S. M. I.; Neumann, A. W., Axisymmetric Drop Shape Analysis (ADSA): An Outline. *Advances in Colloid and Interface Science*.
185. Andrade, M. A. R.; Favarin, B.; Derradi, R.; Bolean, M.; Simão, A. M. S.; Millán, J. L.; Ciancaglini, P.; Ramos, A. P., Pendant-drop method coupled to ultraviolet-visible spectroscopy: A useful tool to investigate interfacial phenomena. *Colloids and Surfaces A: Physicochemical and Engineering Aspects* **2016,** 504, 305-311.
186. Saad, S. M. I.; Policova, Z.; Neumann, A. W., Design and accuracy of pendant drop methods for surface tension measurement. *Colloids and Surfaces A: Physicochemical and Engineering Aspects* **2011,** 384, (1–3), 442-452.
187. Ilieva, P.; Kilzer, A.; Weidner, E., Measurement of solubility, viscosity, density and interfacial tension of the systems tristearin and CO2 and rapeseed oil and CO2. *The Journal of Supercritical Fluids* **2016,** 117, 40-49.
188. Fonseca, J. M. S.; Dohrn, R.; Peper, S., High-pressure fluid-phase equilibria: Experimental methods and systems investigated (2005–2008). *Fluid Phase Equilibria* **2011,** 300, (1–2), 1-69.
189. Dohrn, R.; Brunner, G., High-pressure fluid-phase equilibria: Experimental methods and systems investigated (1988–1993). *Fluid Phase Equilibria* **1995,** 106, (1), 213-282.
190. Škerget, M.; Knez, Ž.; Knez-Hrnčič, M., Solubility of Solids in Sub- and Supercritical Fluids: a Review. *Journal of Chemical & Engineering Data* **2011,** 56, (4), 694-719.

191. Kegl, T.; Kravanja, G.; Knez, Ž.; Knez Hrnčič, M., Effect of addition of supercritical CO2 on transfer and thermodynamic properties of biodegradable polymers PEG 600 and Brij52. *The Journal of Supercritical Fluids* **2017,** 122, 10-17.
192. Hrnčič, M. K.; Venderbosch, R. H.; Škerget, M.; Ilić, L.; Knez, Ž., Phase equilibrium data of hydrogen in pyrolysis oil and hydrogenated pyrolysis oil at elevated pressures. *The Journal of Supercritical Fluids* **2013,** 80, 86-89.
193. Hoorfar, M.; Neumann, A., Axisymmetric drop shape analysis (ADSA) for the determination of surface tension and contact angle. *The Journal of Adhesion* **2004,** 80, (8), 727-743.
194. Stalder, A. F.; Melchior, T.; Müller, M.; Sage, D.; Blu, T.; Unser, M., Low-bond axisymmetric drop shape analysis for surface tension and contact angle measurements of sessile drops. *Colloids and Surfaces A: Physicochemical and Engineering Aspects* **2010,** 364, (1), 72-81.
195. Hoorfar, M.; W. Neumann, A., Recent progress in Axisymmetric Drop Shape Analysis (ADSA). *Advances in Colloid and Interface Science* **2006,** 121, (1), 25-49.
196. Canny, J., A computational approach to edge detection. *IEEE Transactions on pattern analysis and machine intelligence* **1986**, (6), 679-698.
197. Jennings, J. W.; Pallas, N. R., An efficient method for the determination of interfacial tensions from drop profiles. *Langmuir* **1988,** 4, (4), 959-967.
198. Fletcher, R., A modified Marquardt subroutine for non-linear least squares. **1971**.
199. Takahashi, M.; Kobayashi, Y.; Takeuchi, H., Diffusion coefficients and solubilities of carbon dioxide in binary mixed solvents. *Journal of Chemical & Engineering Data* **1982,** 27, (3), 328-331.
200. He, C.-H.; Yu, Y.-S., New Equation for Infinite-Dilution Diffusion Coefficients in Supercritical and High-Temperature Liquid Solvents. *Industrial & Engineering Chemistry Research* **1998,** 37, (9), 3793-3798.
201. Zhao, H.; Lvov, S. N., Phase behavior of the CO2–H2O system at temperatures of 273–623 K and pressures of 0.1–200 MPa using Peng-Robinson-Stryjek-Vera equation of state with a modified Wong-Sandler mixing rule: An extension to the CO2–CH4–H2O system. *Fluid Phase Equilibria* **2016,** 417, 96-108.
202. Duan, Z.; Zhang, Z., Equation of state of the H2O, CO2, and H2O–CO2 systems up to 10 GPa and 2573.15 K: Molecular dynamics simulations with ab initio potential surface. *Geochimica et Cosmochimica Acta* **2006,** 70, (9), 2311-2324.
203. Cadogan, S. P.; Maitland, G. C.; Trusler, J. P. M., Diffusion Coefficients of CO2 and N2 in Water at Temperatures between 298.15 K and 423.15 K at Pressures up to 45 MPa. *Journal of Chemical & Engineering Data* **2014,** 59, (2), 519-525.
204. Pizarro, C.; Suárez-Iglesias, O.; Medina, I.; Bueno, J. L., Binary Diffusion Coefficients of 2-Ethyltoluene, 3-Ethyltoluene, and 4-Ethyltoluene in Supercritical Carbon Dioxide. *Journal of Chemical & Engineering Data* **2009,** 54, (5), 1467-1471.
205. Pallas, N. R.; Harrison, Y., An automated drop shape apparatus and the surface tension of pure water. *Colloids and Surfaces* **1990,** 43, (2), 169-194.
206. Hebach, A.; Oberhof, A.; Dahmen, N.; Kögel, A.; Ederer, H.; Dinjus, E., Interfacial tension at elevated pressures measurements and correlations in the water+ carbon dioxide system. *Journal of Chemical & Engineering Data* **2002,** 47, (6), 1540-1546.
207. Bikkina, P. K.; Shoham, O.; Uppaluri, R., Equilibrated interfacial tension data of the CO2–water system at high pressures and moderate temperatures. *Journal of Chemical & Engineering Data* **2011,** 56, (10), 3725-3733.
208. Park, J.-Y.; Lim, J. S.; Yoon, C. H.; Lee, C. H.; Park, K. P., Effect of a fluorinated sodium bis (2-ethylhexyl) sulfosuccinate (aerosol-OT, AOT) analogue surfactant on the

interfacial tension of CO2+ water and CO2+ Ni-plating solution in near-and supercritical CO2. *Journal of Chemical & Engineering Data* **2005,** 50, (2), 299-308.
209. Da Rocha, S. R.; Harrison, K. L.; Johnston, K. P., Effect of surfactants on the interfacial tension and emulsion formation between water and carbon dioxide. *Langmuir* **1999,** 15, (2), 419-428.
210. Hebach, A.; Oberhof, A.; Dahmen, N., Density of Water + Carbon Dioxide at Elevated Pressures: Measurements and Correlation. *Journal of Chemical & Engineering Data* **2004,** 49, (4), 950-953.
211. Efika, E. C.; Hoballah, R.; Li, X.; May, E. F.; Nania, M.; Sanchez-Vicente, Y.; Trusler, J. M., Saturated phase densities of (CO 2+ H 2 O) at temperatures from (293 to 450) K and pressures up to 64MPa. *The Journal of Chemical Thermodynamics* **2016,** 93, 347-359.
212. Medina, I., Determination of diffusion coefficients for supercritical fluids. *Journal of Chromatography A* **2012,** 1250, 124-140.
213. Stievano, M.; Elvassore, N., High-pressure density and vapor–liquid equilibrium for the binary systems carbon dioxide–ethanol, carbon dioxide–acetone and carbon dioxide–dichloromethane. *The Journal of Supercritical Fluids* **2005,** 33, (1), 7-14.
214. Bachu, S., Screening and ranking of sedimentary basins for sequestration of CO2 in geological media in response to climate change. *Environmental Geology* **2003,** 44, (3), 277-289.
215. Lu, W.; Guo, H.; Chou, I. M.; Burruss, R. C.; Li, L., Determination of diffusion coefficients of carbon dioxide in water between 268 and 473 K in a high-pressure capillary optical cell with in situ Raman spectroscopic measurements. *Geochimica et Cosmochimica Acta* **2013,** 115, 183-204.
216. Kravanja, G.; Škerget, M.; Knez, Ž.; Knez Hrnčič, M., Diffusion coefficients of water and propylene glycol in supercritical CO2 from pendant drop tensiometry. *The Journal of Supercritical Fluids* **2018,** 133, (Part 1), 1-8.
217. Arif, M.; Barifcani, A.; Iglauer, S., Solid/CO2 and solid/water interfacial tensions as a function of pressure, temperature, salinity and mineral type: Implications for CO2-wettability and CO2 geo-storage. *International Journal of Greenhouse Gas Control* **2016,** 53, 263-273.
218. Khaksar Manshad, A.; Olad, M.; Taghipour, S. A.; Nowrouzi, I.; Mohammadi, A. H., Effects of water soluble ions on interfacial tension (IFT) between oil and brine in smart and carbonated smart water injection process in oil reservoirs. *Journal of Molecular Liquids* **2016,** 223, 987-993.
219. Leslie Zhang, D.; Liu, S.; Puerto, M.; Miller, C. A.; Hirasaki, G. J., Wettability alteration and spontaneous imbibition in oil-wet carbonate formations. *Journal of Petroleum Science and Engineering* **2006,** 52, (1–4), 213-226.
220. Ameri, A.; Kaveh, N. S.; Rudolph, E. S. J.; Wolf, K. H.; Farajzadeh, R.; Bruining, J., Investigation on Interfacial Interactions among Crude Oil–Brine–Sandstone Rock–CO2 by Contact Angle Measurements. *Energy & Fuels* **2013,** 27, (2), 1015-1025.
221. Wang, J.; Ryan, D.; Anthony, E. J.; Wildgust, N.; Aiken, T., Effects of impurities on CO2 transport, injection and storage. *Energy Procedia* **2011,** 4, 3071-3078.
222. Xu, B.; Nagashima, K.; DeSimone, J. M.; Johnson, C. S., Diffusion of Water in Liquid and Supercritical Carbon Dioxide: An NMR Study. *The Journal of Physical Chemistry A* **2003,** 107, (1), 1-3.
223. Li, D.; Duan, Z., The speciation equilibrium coupling with phase equilibrium in the H2O–CO2–NaCl system from 0 to 250 °C, from 0 to 1000 bar, and from 0 to 5 molality of NaCl. *Chemical Geology* **2007,** 244, (3), 730-751.

224. Shojai Kaveh, N.; Barnhoorn, A.; Wolf, K. H., Wettability evaluation of silty shale caprocks for CO2 storage. *International Journal of Greenhouse Gas Control* **2016,** 49, 425-435.
225. Busch, A.; Alles, S.; Gensterblum, Y.; Prinz, D.; Dewhurst, D. N.; Raven, M. D.; Stanjek, H.; Krooss, B. M., Carbon dioxide storage potential of shales. *International Journal of Greenhouse Gas Control* **2008,** 2, (3), 297-308.
226. Sawalha, S.; Karampour, M.; Rogstam, J., Field measurements of supermarket refrigeration systems. Part I: Analysis of CO2 trans-critical refrigeration systems. *Applied Thermal Engineering* **2015,** 87, 633-647.
227. Lee, W. W.; Bae, S. J.; Jung, Y. H.; Yoon, H. J.; Jeong, Y. H.; Lee, J. I., Improving power and desalination capabilities of a large nuclear power plant with supercritical CO2 power technology. *Desalination* **2017,** 409, 136-145.
228. Jin, Z.; Eikevik, T. M.; Nekså, P.; Hafner, A.; Wang, R., Annual energy performance of R744 and R410A heat pumping systems. *Applied Thermal Engineering* **2017,** 117, 568-576.
229. Lim, S.; Lee, K. T., Investigation of impurity tolerance and thermal stability for biodiesel production from Jatropha curcas L. seeds using supercritical reactive extraction. *Energy* **2014,** 68, 71-79.
230. Chen, B.; Hoffmann, R.; Cammi, R., The Effect of Pressure on Organic Reactions in Fluids—a New Theoretical Perspective. *Angewandte Chemie International Edition* **2017,** 56, (37), 11126-11142.
231. Omidi, M.; Farhadi, M.; Jafari, M., A comprehensive review on double pipe heat exchangers. *Applied Thermal Engineering* **2017,** 110, (Supplement C), 1075-1090.
232. Simões, P. C.; Afonso, B.; Fernandes, J.; Mota, J. P. B., Static mixers as heat exchangers in supercritical fluid extraction processes. *The Journal of Supercritical Fluids* **2008,** 43, (3), 477-483.
233. Ahn, Y.; Bae, S. J.; Kim, M.; Cho, S. K.; Baik, S.; Lee, J. I.; Cha, J. E., Review of supercritical CO2 power cycle technology and current status of research and development. *Nuclear Engineering and Technology* **2015,** 47, (6), 647-661.
234. Huang, D.; Wu, Z.; Sunden, B.; Li, W., A brief review on convection heat transfer of fluids at supercritical pressures in tubes and the recent progress. *Applied Energy* **2016,** 162, 494-505.
235. Zhao, Z.; Su, S.; Si, N.; Hu, S.; Wang, Y.; Xu, J.; Jiang, L.; Chen, G.; Xiang, J., Exergy analysis of the turbine system in a 1000 MW double reheat ultra-supercritical power plant. *Energy* **2017,** 119, 540-548.
236. Xiong, T.; Yan, X.; Huang, S.; Yu, J.; Huang, Y., Modeling and analysis of supercritical flow instability in parallel channels. *International Journal of Heat and Mass Transfer* **2013,** 57, (2), 549-557.
237. Linares, J. I.; Cantizano, A.; Arenas, E.; Moratilla, B. Y.; Martín-Palacios, V.; Batet, L., Recuperated versus single-recuperator re-compressed supercritical CO2 Brayton power cycles for DEMO fusion reactor based on dual coolant lithium lead blanket. *Energy* **2017,** 140, 307-317.
238. Osorio, J. D.; Hovsapian, R.; Ordonez, J. C., Effect of multi-tank thermal energy storage, recuperator effectiveness, and solar receiver conductance on the performance of a concentrated solar supercritical CO2-based power plant operating under different seasonal conditions. *Energy* **2016,** 115, 353-368.
239. Bai, Z.; Zhang, G.; Li, Y.; Xu, G.; Yang, Y., A supercritical CO2 Brayton cycle with a bleeding anabranch used in coal-fired power plants. *Energy* **2018,** 142, 731-738.
240. Knez, Ž.; Markočič, E.; Leitgeb, M.; Primožič, M.; Knez Hrnčič, M.; Škerget, M., Industrial applications of supercritical fluids: A review. *Energy* **2014,** 77, 235-243.

241. Duffey, R. B.; Pioro, I. L., Experimental heat transfer of supercritical carbon dioxide flowing inside channels (survey). *Nuclear Engineering and Design* **2005,** 235, (8), 913-924.
242. Song, J. H.; Kim, H. Y.; Kim, H.; Bae, Y. Y., Heat transfer characteristics of a supercritical fluid flow in a vertical pipe. *The Journal of Supercritical Fluids* **2008,** 44, (2), 164-171.
243. Liu, X.; Xu, X.; Liu, C.; Ye, J.; Li, H.; Bai, W.; Dang, C., Numerical study of the effect of buoyancy force and centrifugal force on heat transfer characteristics of supercritical CO2 in helically coiled tube at various inclination angles. *Applied Thermal Engineering* **2017,** 116, 500-515.
244. Li, Z.-H.; Jiang, P.-X.; Zhao, C.-R.; Zhang, Y., Experimental investigation of convection heat transfer of CO2 at supercritical pressures in a vertical circular tube. *Experimental Thermal and Fluid Science* **2010,** 34, (8), 1162-1171.
245. Bruch, A.; Bontemps, A.; Colasson, S., Experimental investigation of heat transfer of supercritical carbon dioxide flowing in a cooled vertical tube. *International Journal of Heat and Mass Transfer* **2009,** 52, (11–12), 2589-2598.
246. Liao, S. M.; Zhao, T. S., An experimental investigation of convection heat transfer to supercritical carbon dioxide in miniature tubes. *International Journal of Heat and Mass Transfer* **2002,** 45, (25), 5025-5034.
247. Negoescu, C. C.; Li, Y.; Al-Duri, B.; Ding, Y., Heat transfer behaviour of supercritical nitrogen in the large specific heat region flowing in a vertical tube. *Energy* **2017**.
248. Zhang, S.; Gu, H.; Cheng, X.; Xiong, Z., Experimental study on heat transfer of supercritical Freon flowing upward in a circular tube. *Nuclear Engineering and Design* **2014,** 280, 305-315.
249. Jiang, P.-X.; Zhao, C.-R.; Liu, B., Flow and heat transfer characteristics of r22 and ethanol at supercritical pressures. *The Journal of Supercritical Fluids* **2012,** 70, 75-89.
250. Hoa, C.; Lagier, B.; Rousset, B.; Bonnay, P.; Michel, F., Heat Load Estimator for Smoothing Pulsed Heat Loads on Supercritical Helium Loops. *Physics Procedia* **2015,** 67, 1147-1152.
251. Ge, Z.; Jin, H.; Guo, L., Hydrogen production by catalytic gasification of coal in supercritical water with alkaline catalysts: Explore the way to complete gasification of coal. *International Journal of Hydrogen Energy* **2014,** 39, (34), 19583-19592.
252. Harby, K., Hydrocarbons and their mixtures as alternatives to environmental unfriendly halogenated refrigerants: An updated overview. *Renewable and Sustainable Energy Reviews* **2017,** 73, 1247-1264.
253. Lastari, F.; Pareek, V.; Trebble, M.; Tade, M. O.; Chinn, D.; Tsai, N. C.; Chan, K. I., Extractive distillation for CO2–ethane azeotrope separation. *Chemical Engineering and Processing: Process Intensification* **2012,** 52, 155-161.
254. Levenspiel, O., *Engineering flow and heat exchange*. Springer: 2014.
255. Ma, T.; Chu, W.-x.; Xu, X.-y.; Chen, Y.-t.; Wang, Q.-w., An experimental study on heat transfer between supercritical carbon dioxide and water near the pseudo-critical temperature in a double pipe heat exchanger. *International Journal of Heat and Mass Transfer* **2016,** 93, 379-387.
256. Bergman, T. L.; Incropera, F. P., *Fundamentals of heat and mass transfer*. John Wiley & Sons: 2011.
257. Rao, N. T.; Oumer, A. N.; Jamaludin, U. K., State-of-the-art on flow and heat transfer characteristics of supercritical CO2 in various channels. *The Journal of Supercritical Fluids* **2016,** 116, 132-147.
258. Kay, W., Gases and Vapors At High Temperature and Pressure - Density of Hydrocarbon. *Industrial & Engineering Chemistry* **1936,** 28, (9), 1014-1019.

259. Prausnitz, J. M.; Gunn, R. D., Volumetric properties of nonpolar gaseous mixtures. *AIChE Journal* **1958,** 4, (4), 430-435.
260. Jackson, J. D.; Cotton, M. A.; Axcell, B. P., Studies of mixed convection in vertical tubes. *International Journal of Heat and Fluid Flow* **1989,** 10, (1), 2-15.
261. Jouhara, H.; Chauhan, A.; Nannou, T.; Almahmoud, S.; Delpech, B.; Wrobel, L. C., Heat pipe based systems - Advances and applications. *Energy* **2017,** 128, 729-754.

7. Appendix

7.1 Appendix 1-Chapter 2

Table A1-1: Melting points of Brij S100.

p/ MPa	T_1/ °C	T_2/ °C	p/ MPa	T_1/ °C	T_2/ °C
0.51	57.8	59.6	8.56	38.00	40.50
0.49	57.5	59.3	9.25	38.80	41.50
1.00	54.90	56.00	9.27	38.80	41.60
0.98	55.00	56.60	10.25	38.80	42.20
2.19	53.10	59.00	10.13	39.60	42.60
2.10	52.50	54.00	12.15	24.80	25.80
2.14	52.20	54.30	12.20	39.50	41.90
3.08	50.80	53.80	12.24	39.20	41.90
3.07	50.70	53.50	15.15	31.90	33.00
4.09	53.60	55.40	15.10	39.20	41.50
4.06	49.50	51.90	15.14	39.30	41.10
4.05	49.40	52.00	17.23	39.10	43.00
5.10	51.20	52.50	17.10	39.10	41.60
5.20	50.30	51.50	17.29	38.20	40.00
5.16	46.30	50.70	20.15	27.10	27.60
5.07	38.30	40.40	20.10	37.80	39.10
6.13	45.50	49.60	20.08	37.50	39.20
6.12	45.50	49.70	25.26	36.50	37.70
6.73	44.00	48.40	25.25	36.40	37.70
6.73	42.00	46.30	28.50	36.50	38.70
7.15	39.90	46.50	28.55	36.40	38.80
7.11	40.00	42.30	30.25	36.30	39.30
7.19	39.80	43.70	30.57	37.00	39.10
7.18	41.90	46.20	32.70	36.50	38.80
7.12	40.50	43.50	32.50	36.40	38.60
7.05	42.50	44.70	35.00	35.90	36.80
7.88	39.70	43.20	35.00	35.70	37.00
7.86	39.50	43.00	39.75	38.20	40.20
8.55	37.30	38.90	40.20	36.50	40.50

Table A1-2: Solubility of CO_2 in PEG 600.

PEG 600/CO_2, 60 °C		**PEG 600/CO_2, 80 °C**	
p /MPa	*S* / g/g	*p* /MPa	*S* / g/g
0.00	0.00	0.00	0.00
5.17	0.10	5.47	0.08
10.47	0.10	10.67	0.14
15.18	0.21	15.48	0.15
19.43	0.35	19.94	0.29
23.80	0.49	24.80	0.44
28.94	0.59	29.05	0.56

Table A1-3: Solubility of CO_2 in Brij 52.

Brij 52/CO_2, 60 °C		**PEG 600/CO_2, 80 °C**	
p /MPa	*S* / g/g	*p* /MPa	*S* / g/g
0.00	0.00	0.00	0.00
6.08	0.15	5.81	0.13
10.30	0.17	10.79	0.25
15.14	0.41	15.65	0.31
20.09	0.57	20.21	0.51
24.00	0.67	25.09	0.62
29.03	0.77	29.76	0.73

Table A1-4: Solubility of CO_2 in Brij 100.

Brij 100/CO_2, 60 °C		**PEG 600/CO_2, 80 °C**	
p /MPa	*S* / g/g	*p* /MPa	*S* / g/g
0.00	0.00	0	0.00
5.18	0.08	5.87	0.12
10.57	0.20	10.29	0.29
15.08	0.32	15.33	0.32
20.23	0.43	20.25	0.45
25.04	0.53	25.37	0.61
29.90	0.56	30.07	0.67
34.87	0.58	34.91	0.67

Table A1-5: Diffusion coefficient in CO_2/ PEG 600 system.

PEG 600/CO_2, 60 °C		**PEG 600/CO_2, 80 °C**	
p /MPa	*D* /cm²/s	*p* /MPa	*D* /cm²/s
0.00	0.0	0.0	0.0
5.17	5.78E-05	5.47	7.09E-05
10.47	1.93E-04	10.7	1.29E-04
15.18	8.10E-04	15.48	5.14E-04
19.43	4.69E-04	19.94	4.53E-04
23.80	4.53E-04	24.8	5.10E-04
28.94	2.07E-04	29.05	4.82E-04

Table A1-6: Diffusion coefficient in CO_2/ Brij 52 system.

Brij 52/CO_2, 60 °C		**Brij 52/CO_2, 80 °C**	
p /MPa	*D* /cm²/s	*p* /MPa	*D* /cm²/s
0.00	0.00	0.00	0.00
6.08	1.63E-04	5.81	1.25E-04
10.30	8.15E-04	10.79	6.35E-04
15.14	1.93E-03	15.65	1.32E-03
20.09	1.06E-03	20.21	1.45E-03
24.00	3.10E-04	25.09	4.73E-04
29.03	1.69E-04	29.76	1.77E-04

Table A1-7: Density of CO_2 saturated PEG 600 solution.

PEG 600/CO_2 (g/mL), 60 °C		**PEG 600/CO_2 (g/mL), 80 °C**	
p (MPa)	*ρ* (g/mL)	*p* (MPa)	ρ (g/mL)
0	1.0749	0.18	1.0761
1.37	1.0913	2.69	1.0769
2.65	1.1062	3.85	1.0778
3.25	1.1130	4.77	1.0783
4.43	1.1261	4.96	1.0780
5.43	1.1369	6.55	1.0787
6.83	1.1516	7.31	1.0796
7.33	1.1567	8.02	1.0798
8	1.1633	10.61	1.0807
9.36	1.1767	11.85	1.0813
12.26	1.2034	13.5	1.0822
13.87	1.2173	15.26	1.0832
18.3	1.2522	17.32	1.0843
20.36	1.2668	18.06	1.0846
21.95	1.2773	21.75	1.0864
25.83	1.3017	22.77	1.0867
26.71	1.3063	24.33	1.0876
28.62	1.3162	27.45	1.0890
29.03	1.3191	27.94	1.0890
31.53	1.3294	30.64	1.0906

Table A1-8: Density of CO_2 saturated Brij 52 solution.

Brij 52/CO_2, 60 °C		**Brij 52/CO_2, 80 °C**	
p (MPa)	ρ (g/mL),	p (MPa)	ρ (g/mL)
0.0	0.8649	0.00	0.8582
1.6	0.8862	1.25	0.8587
2.5	0.8948	2.54	0.8596
3.6	0.9057	3.13	0.8594
4.4	0.9128	4.13	0.8591
5.0	0.9175	5.05	0.8595
7.8	0.9408	5.41	0.8601
8.5	0.9474	7.01	0.8608
10.2	0.9594	8.77	0.8618
10.4	0.9611	11.13	0.8630
13.8	0.9851	11.95	0.8629
15.6	0.9970	14.12	0.8644
16.8	1.0042	14.67	0.8649
17.5	1.0082	17.13	0.8659
18.0	1.0110	17.68	0.8660
19.7	1.0206	18.38	0.8662
20.3	1.0239	20.18	0.8674
22.5	1.0352	20.58	0.8674
23.9	1.0417	25.15	0.8694
24.9	1.0457	27.75	0.8705
28.9	1.0622	28.26	0.8705
34.3	1.0805	35.25	0.8730

Table A1-9: Density of CO_2 saturated Brij 100 solution.

p [MPa]	ρ [g/mL]	p [bar]	ρ [g/mL]
0.10	1.0629	0.10	1.0460
0.56	1.0633	1.58	1.0470
1.05	1.0635	2.03	1.0473
1.53	1.0639	2.53	1.0476
2.04	1.0641	3.02	1.0479
2.52	1.0644	3.56	1.0482
3.06	1.0647	4.01	1.0485
3.55	1.0649	4.53	1.0488
4.02	1.0651	5.00	1.0490
4.30	1.0652	5.52	1.0493
5.11	1.0657	6.05	1.0496
5.52	1.0658	6.52	1.0498
6.00	1.0662	7.60	1.0504
7.30	1.0668	8.07	1.0506
7.89	1.0672	8.77	1.0510
8.53	1.0675	9.00	1.0511
9.18	1.0679	9.51	1.0514
9.75	1.0682	10.00	1.0516
10.27	1.0684	10.50	1.0519
10.81	1.0686	10.99	1.0521
11.32	1.0689	11.51	1.0524
11.88	1.0692	12.03	1.0526
12.76	1.0696	12.53	1.0529
13.15	1.0697	13.05	1.0531
13.54	1.0698	13.55	1.0534
14.04	1.0701	14.05	1.0536
14.50	1.0703	14.55	1.0538
14.99	1.0706	15.11	1.0540
15.90	1.0709	15.51	1.0543
16.70	1.0713	16.04	1.0545
17.06	1.0715	16.69	1.0548
17.49	1.0716	17.03	1.0550
18.19	1.0719	17.73	1.0553
18.51	1.0721	17.99	1.0554
19.17	1.0724	18.47	1.0556
19.51	1.0726	19.02	1.0559
20.06	1.0727	19.53	1.0561
20.59	1.0730	20.04	1.0563
21.02	1.0732	20.46	1.0565
21.50	1.0733	21.03	1.0568
22.01	1.0735	21.80	1.0571
22.44	1.0738	22.55	1.0575
23.08	1.0740	23.02	1.0576

p [MPa]	ρ [g/mL]	p [bar]	ρ [g/mL]
23.56	1.0743	23.52	1.0578
24.00	1.0744	24.00	1.0580
24.48	1.0746	24.47	1.0583
24.97	1.0748	25.05	1.0584
25.49	1.0751	25.57	1.0586
26.00	1.0753	26.08	1.0590
26.48	1.0754	26.47	1.0591
26.97	1.0756	26.98	1.0594
27.53	1.0759	27.50	1.0596
27.96	1.0761	28.02	1.0598
28.52	1.0763	28.52	1.0600
28.97	1.0765	29.04	1.0603
29.49	1.0767	29.54	1.0605
30.04	1.0770	30.04	1.0607

Table A1-9: Interfacial tension of CO_2 saturated PEG 600 solution.

PEG 600/CO_2, 60 °C		**PEG 600/CO_2, 80 °C**	
p (bar)	γ (mN/m)	p (bar)	γ (mN/m)
0.10	40.33	0.10	38.39
2.37	37.70	2.11	36.23
4.07	33.46	4.08	31.55
6.07	29.17	6.27	28.29
8.26	24.38	8.31	24.25
10.22	21.64	10.09	21.01
12.16	17.84	12.12	18.05
13.98	15.18	14.01	15.36
15.79	13.75	15.83	13.19
17.89	12.84	17.84	11.64
19.81	12.33	20.01	10.29
25.00	11.54	25.00	10.29

Table A1-10: Interfacial tension of CO_2 saturated Brij 52 solution.

Brij 52/CO_2, 60 °C		**Brij 52/CO_2, 80 °C**	
p (bar)	γ (mN/m)	p (bar)	γ (mN/m)
1.00	22.66	1.00	15.77
20.30	20.12	20.60	14.25
41.50	16.06	40.40	12.48
61.50	13.27	60.80	10.86
82.00	10.22	81.60	9.31
102.50	7.37	100.80	7.68
121.10	5.65	120.90	5.93
141.20	4.30	140.30	5.01
159.10	3.63	159.60	4.08
179.30	3.09	179.80	3.32

Table A1-11: Interfacial tension of CO_2 saturated Brij 100 solution.

Brij 100/CO_2, 60 °C		**Brij 100/CO_2, 80 °C**	
p (bar)	γ (mN/m)	p (bar)	γ (mN/m)
1.00	29.11	1.00	28.00
20.70	24.03	20.40	23.07
41.70	19.43	41.30	18.25
58.80	16.34	62.00	13.88
82.60	11.90	81.60	11.11
102.60	9.56	105.00	8.17
120.40	7.99	123.40	6.80
138.90	5.99	141.90	5.56
158.10	5.10	159.80	4.90
179.80	4.47	179.90	4.30
199.60	4.05	199.20	3.83
217.10	3.87	220.10	3.27
238.60	3.53	239.50	3.04
260.60	3.10	261.40	2.80
279.40	3.03	280.50	2.62

Table A1-12: interfacial tension and solubility measurements for the (CO_2 + PEG)

p (MPa)	T (°C)	ρ_{PEG} (g/mL)	ρ_{CO2} (g/mL)	S (g/g)	γ (mN/m)
CO_2 + PEG 1000					
0.00	70 ± 0.25	1.1421	0.0000	0.0000	40.3885
0.98	70 ± 0.25	1.0910	0.0153	0.0323	37.3516
1.87	70 ± 0.25	1.0944	0.0307	0.0769	33.8688
4.16	70 ± 0.25	1.1493	0.0741	0.0769	28.1326
8.00	70 ± 0.25	1.1582	0.1746	0.1246	19.3943
12.13	70 ± 0.25	1.1383	0.3524	0.1556	14.6412
16.87	70 ± 0.25	1.1952	0.5785	0.2623	12.5057
20.18	70 ± 0.25	1.3051	0.6621	0.3308	10.3414
24.37	70 ± 0.25	1.5831	0.7293	0.4361	11.3874
30.30	70 ± 0.25	1.6175	0.7906	0.5170	13.0278
CO_2 + PEG 1500					
0.00	55 ± 0.25	1.2000	0.0000	0.0000	47.8727
2.05	55 ± 0.25	1.1858	0.0357	0.0555	38.8302
4.10	55 ± 0.25	1.1782	0.0786	0.1272	30.2673
6.06	55 ± 0.25	1.2059	0.1318	0.1268	25.5111
8.12	55 ± 0.25	1.2356	0.2087	0.1020	18.6277
10.06	55 ± 0.25	1.2425	0.3289	0.0256	15.6127
12.20	55 ± 0.25	1.2883	0.5190	0.1605	12.9652
16.10	55 ± 0.25	1.3001	0.6840	0.2229	10.0582
20.12	55 ± 0.25	1.4332	0.7566	0.3999	10.5683
24.00	55 ± 0.25	1.4535	0.8014	0.4446	10.9649
28.00	55 ± 0.25	1.5231	0.8357	0.4317	11.5573
30.55	55 ± 0.25	1.5161	0.8540	0.4671	11.2393
0.00	70 ± 0.25	1.1900	0.0000	0.0000	41.1240
1.00	70 ± 0.25	1.1758	0.0161	0.0152	34.4760
2.02	70 ± 0.25	1.1682	0.0333	0.0323	31.1846
4.52	70 ± 0.25	1.1959	0.0827	0.0769	25.0798
6.00	70 ± 0.25	1.2056	0.1170	0.0932	23.8877
8.00	70 ± 0.25	1.2025	0.1746	0.1123	21.1355
12.09	70 ± 0.25	1.2001	0.3497	0.1556	15.0136
14.52	70 ± 0.25	1.2463	0.4843	0.1954	11.8085
20.01	70 ± 0.25	1.4232	0.6590	0.3308	11.7523
24.42	70 ± 0.25	1.4435	0.7300	0.4039	10.7394
30.25	70 ± 0.25	1.4535	0.7901	0.4468	11.2289
0.00	80 ± 0.25	1.0765	0.0000	0.0000	39.5709
2.05	80 ± 0.25	1.0791	0.0314	0.0052	32.8012
4.10	80 ± 0.25	1.0820	0.0667	0.0223	26.5187
6.06	80 ± 0.25	1.0858	0.1060	0.0669	20.9202
8.12	80 ± 0.25	1.0890	0.1526	0.0832	15.5323

p (MPa)	T (°C)	ρ_{PEG} (g/mL)	ρ_{CO2} (g/mL)	S (g/g)	γ (mN/m)
10.06	80 ± 0.25	1.0913	0.2043	0.1023	13.0682
12.20	80 ± 0.25	1.0965	0.2713	0.1456	13.0292
16.10	80 ± 0.25	1.1016	0.4122	0.1853	11.1998
20.12	80 ± 0.25	1.1066	0.5369	0.3207	10.7298
24.00	80 ± 0.25	1.1111	0.6196	0.3939	11.4340
30.55	80 ± 0.25	1.1219	0.7093	0.4368	11.7534
CO_2 + PEG 3000					
0	70 ± 0.25	1.1900	0.0016	0.0000	43.2404
1.14	70 ± 0.25	1.1681	0.0159	0.0166	36.8457
2.01	70 ± 0.25	1.1614	0.0330	0.0338	29.8411
5.21	70 ± 0.25	1.2263	0.0818	0.0940	25.7872
8.07	70 ± 0.25	1.2003	0.1736	0.0970	21.8730
11.93	70 ± 0.25	1.2371	0.3350	0.1003	15.5701
12.68	70 ± 0.25	1.2130	0.3792	0.1030	14.2523
14.93	70 ± 0.25	1.2334	0.5013	0.1130	12.1876
17.69	70 ± 0.25	1.3332	0.6067	0.1443	12.1007
19.89	70 ± 0.25	1.3963	0.6507	0.1738	12.4195
25.01	70 ± 0.25	1.4914	0.7393	0.1829	12.5273
29.86	70 ± 0.25	1.5464	0.7880	0.2411	12.6334
CO_2 + PEG 4000					
0	70 ± 0.25	1.1950	0.0000	0.0000	43.258
2.08	70 ± 0.25	1.0850	0.0340	0.0333	35.385
4.58	70 ± 0.25	1.1300	0.0832	0.0747	25.426
8.06	70 ± 0.25	1.1580	0.1761	0.0849	18.128
10.06	70 ± 0.25	1.1492	0.2514	0.0947	15.960
12.01	70 ± 0.25	1.1205	0.3453	0.1180	13.760
15.05	70 ± 0.25	1.1985	0.5082	0.1823	12.050
17.66	70 ± 0.25	1.3304	0.6027	0.2433	11.550
20.01	70 ± 0.25	1.4124	0.6594	0.3049	11.860
23.96	70 ± 0.25	1.5076	0.7240	0.3631	12.250
27.97	70 ± 0.25	1.5661	0.7695	0.3916	12.490
30.07	70 ± 0.25	1.6006	0.7884	0.4085	12.730
CO_2 + PEG 6000					
0.00	70 ± 0.25	1.1853	0.0000	0.0000	44.8785
1.04	70 ± 0.25	1.0789	0.0168	0.0068	39.1179
2.01	70 ± 0.25	1.1248	0.0331	0.0168	35.6528
4.51	70 ± 0.25	1.1772	0.0821	0.0353	30.6295
6.00	70 ± 0.25	1.1362	0.1173	0.0763	25.6064
7.50	70 ± 0.25	1.1180	0.1588	0.0912	22.9370
10.00	70 ± 0.25	1.0986	0.2471	0.0102	18.0181
11.34	70 ± 0.25	1.2199	0.3107	0.1147	15.5472
12.52	70 ± 0.25	1.1524	0.3759	0.1046	13.1845
15.40	70 ± 0.25	1.1869	0.5236	0.1379	11.5888
19.84	70 ± 0.25	1.3110	0.6553	0.1786	11.4834
24.95	70 ± 0.25	1.4042	0.7361	0.2206	11.8567

p (MPa)	T (°C)	ρ_{PEG} (g/mL)	ρ_{CO2} (g/mL)	S (g/g)	γ (mN/m)
CO_2 + PEG 10 000					
0.00	70 ± 0.25	1.2034	0.0000	0.0000	45.3103
2.05	70 ± 0.25	1.2023	0.0340	0.0309	36.5937
4.26	70 ± 0.25	1.1967	0.0767	0.0691	31.9305
6.00	70 ± 0.25	1.2037	0.1173	0.0791	27.1518
8.00	70 ± 0.25	1.2107	0.1745	0.0907	22.6476
10.53	70 ± 0.25	1.2647	0.2716	0.1185	19.3248
13.23	70 ± 0.25	1.2452	0.4154	0.0676	14.9966
14.99	70 ± 0.25	1.2699	0.5059	0.0779	13.0148
20.04	70 ± 0.25	1.2967	0.6604	0.1639	12.6195
22.42	70 ± 0.25	1.3418	0.7018	0.1840	12.9754
28.06	70 ± 0.25	1.4001	0.7700	0.2099	12.7923
30.01	70 ± 0.25	1.4128	0.7880	0.2156	12.9044

Table A1-13: Liquid - vapour interfacial tension and solubility for the (Argon + PEG).

p (MPa)	T (°C)	ρ_{PEG} (g/mL)	ρ_{Ar} (g/mL)	S (g/g)	γ (mN/m)
Argon + PEG 400					
0.00	70 ± 0.25	1.1621	0.0000	0.0000	41.0318
2.04	70 ± 0.25	1.1880	0.0281	0.0102	40.1079
4.08	70 ± 0.25	1.2373	0.0565	0.0152	38.6452
6.01	70 ± 0.25	1.2202	0.0850	0.0153	36.0890
8.09	70 ± 0.25	1.2336	0.1136	0.0159	34.5273
10.15	70 ± 0.25	1.2305	0.1422	0.0162	32.9922
12.04	70 ± 0.25	1.2264	0.1706	0.0164	31.9563
16.20	70 ± 0.25	1.2258	0.2265	0.0172	30.1266
20.12	70 ± 0.25	1.2624	0.2808	0.0196	28.6749
24.20	70 ± 0.25	1.2698	0.3328	0.0233	28.0544
27.82	70 ± 0.25	1.2575	0.3820	0.0237	26.6011
29.90	70 ± 0.25	1.2866	0.4043	0.0249	27.6366
Argon + PEG 1000					
0.00	70 ± 0.25	1.1154	0.0000	0.0000	45.0329
2.02	70 ± 0.25	1.1539	0.0282	0.0139	42.1185
4.04	70 ± 0.25	1.1815	0.0574	0.0163	39.9522
6.11	70 ± 0.25	1.2061	0.0882	0.0186	38.2913
8.09	70 ± 0.25	1.2165	0.1140	0.0235	36.6281
10.10	70 ± 0.25	1.2263	0.1419	0.0217	35.7442
12.03	70 ± 0.25	1.2421	0.1718	0.0206	34.2771
16.13	70 ± 0.25	1.2150	0.2266	0.0206	32.6994
20.14	70 ± 0.25	1.2204	0.2824	0.0039	30.9212
24.10	70 ± 0.25	1.2324	0.3338	0.0240	30.2548
28.00	70 ± 0.25	1.2458	0.3819	0.0260	29.5910
30.10	70 ± 0.25	1.2679	0.4061	0.0286	28.7323
			0.0000		
Argon + PEG 1500					
0.00	55 ± 0.25	1.1719	0.0000	0.0000	47.5603
2.15	55 ± 0.25	1.1927	0.0318	0.0038	46.0778
4.04	55 ± 0.25	1.2272	0.0603	0.0066	45.7157
6.17	55 ± 0.25	1.2291	0.0920	0.0099	44.5489
8.02	55 ± 0.25	1.2290	0.1201	0.0125	43.4439
10.18	55 ± 0.25	1.2253	0.1527	0.0161	42.0199
12.03	55 ± 0.25	1.2502	0.1807	0.0234	40.5203
16.12	55 ± 0.25	1.2431	0.2412	0.0301	37.7250
20.12	55 ± 0.25	1.2424	0.2990	0.0370	35.5217
24.06	55 ± 0.25	1.2967	0.3535	0.0446	34.5197
27.99	55 ± 0.25	1.2967	0.4042	0.0525	32.6635
30.01	55 ± 0.25	1.2967	0.4289	0.0556	32.6744

p (MPa)	T (°C)	ρ_{PEG} (g/mL)	ρ_{Ar} (g/mL)	S (g/g)	γ (mN/m)
0.00	70 ± 0.25	1.1911	0.0000	0.0000	46.6079
2.01	70 ± 0.25	1.1895	0.0281	0.0028	45.2242
4.06	70 ± 0.25	1.1887	0.0565	0.0056	43.7438
6.20	70 ± 0.25	1.1880	0.0850	0.0086	41.4014
8.02	70 ± 0.25	1.1868	0.1136	0.0115	39.8028
9.98	70 ± 0.25	1.1861	0.1422	0.0151	38.4250
12.10	70 ± 0.25	1.1847	0.1706	0.0224	36.7107
16.00	70 ± 0.25	1.1810	0.2265	0.0291	34.2389
20.10	70 ± 0.25	1.1797	0.2808	0.0360	32.3696
24.02	70 ± 0.25	1.1466	0.3328	0.0436	29.9955
28.01	70 ± 0.25	1.1834	0.3820	0.0515	29.9129
30.05	70 ± 0.25	1.1915	0.4055	0.0546	30.0945
			0.0000		
0.00	80 ± 0.25	1.0935	0.0000	0.0000	40.9160
2.02	80 ± 0.25	1.0952	0.0266	0.0002	39.2308
4.05	80 ± 0.25	1.1305	0.0540	0.0179	38.5135
6.11	80 ± 0.25	1.1729	0.0815	0.0169	37.9228
8.08	80 ± 0.25	1.1056	0.1076	0.0153	36.7588
10.06	80 ± 0.25	1.1979	0.1342	0.0168	36.7096
12.09	80 ± 0.25	1.1661	0.1607	0.0189	34.6984
16.01	80 ± 0.25	1.1923	0.2115	0.0164	33.8500
20.01	80 ± 0.25	1.1786	0.2620	0.0174	31.6322
24.10	80 ± 0.25	1.1715	0.3112	0.0315	30.1764
28.05	80 ± 0.25	1.1731	0.3568	0.0167	30.1628
30.01	80 ± 0.25	1.1741	0.3784	0.0190	29.3994
			0.0000		
Argon + PEG 4000					
0	70 ± 0.25	1.1044	0.0000	0.0000	44.8959
2.05	70 ± 0.25	1.1250	0.0290	0.0022	44.3250
4.02	70 ± 0.25	1.1345	0.0569	0.0024	43.5817
6.11	70 ± 0.25	1.1353	0.0863	0.0022	40.2092
8.05	70 ± 0.25	1.1280	0.1144	0.0012	38.8548
9.97	70 ± 0.25	1.1317	0.1417	0.0012	37.9515
11.95	70 ± 0.25	1.1351	0.1696	0.0013	37.0121
16.04	70 ± 0.25	1.1263	0.2273	0.0015	34.4598
20.02	70 ± 0.25	1.1458	0.2812	0.0076	33.1410
24.04	70 ± 0.25	1.1138	0.3335	0.0081	30.1681
28.05	70 ± 0.25	1.1945	0.3824	0.0119	29.3009
30.13	70 ± 0.25	1.2011	0.4072	0.0187	30.6935
Argon + PEG 6000					
0	70 ± 0.25	1.1525	0.0000	0.0000	46.8520
2.04	70 ± 0.25	1.1680	0.0290	0.0014	46.0639
4.02	70 ± 0.25	1.1742	0.0569	0.0057	42.5666
6.01	70 ± 0.25	1.1781	0.0849	0.0086	41.9062
8.05	70 ± 0.25	1.1720	0.1144	0.0042	39.5504

p (MPa)	T (°C)	ρ_{PEG} (g/mL)	ρ_{Ar} (g/mL)	S (g/g)	γ (mN/m)
Argon + PEG 6000					
0	70 ± 0.25	1.1525	0.0000	0.0000	46.8520
2.04	70 ± 0.25	1.1680	0.0290	0.0014	46.0639
4.02	70 ± 0.25	1.1742	0.0569	0.0057	42.5666
6.01	70 ± 0.25	1.1781	0.0849	0.0086	41.9062
8.05	70 ± 0.25	1.1720	0.1144	0.0042	39.5504
9.97	70 ± 0.25	1.1799	0.1417	0.0035	38.8228
11.95	70 ± 0.25	1.1813	0.1696	0.0025	36.7185
16.06	70 ± 0.25	1.1976	0.2273	0.0022	33.6693
20.04	70 ± 0.25	1.1672	0.2812	0.0075	30.7407
24.06	70 ± 0.25	1.1772	0.3335	0.0081	30.3022
28.01	70 ± 0.25	1.1852	0.3824	0.0119	29.0970
30.01	70 ± 0.25	1.1992	0.4055	0.0177	29.0292
Argon + PEG 10 000					
0.00	70 ± 0.25	1.1925	0.0000	0.0000	47.6673
2.00	70 ± 0.25	1.1580	0.0283	0.0012	44.8407
4.00	70 ± 0.25	1.1642	0.0569	0.0014	43.1202
6.10	70 ± 0.25	1.1681	0.0863	0.0012	40.9604
8.02	70 ± 0.25	1.1620	0.1137	0.0002	39.1542
10.18	70 ± 0.25	1.1699	0.1445	0.0002	35.6010
12.00	70 ± 0.25	1.1713	0.1703	0.0003	34.1706
16.10	70 ± 0.25	1.1876	0.2280	0.0005	33.8830
20.12	70 ± 0.25	1.1572	0.2826	0.0066	30.8807
24.00	70 ± 0.25	1.1672	0.3329	0.0071	30.0442
28.00	70 ± 0.25	1.1752	0.3824	0.0109	29.1063
30.10	70 ± 0.25	1.1892	0.4066	0.0177	29.4650

Table A1-14: Density of CO_2 saturated PEG 6000 solution.

T [°C]	p [MPa]	ρ [g/mL]
60	0.17	1.0928
60	1.05	1.0931
60	2.32	1.0934
60	3.52	1.0938
60	4.10	1.0941
60	5.16	1.0945
60	6.80	1.0950
60	7.55	1.0952
60	9.35	1.0959
60	10.97	1.0965
60	11.37	1.0966
60	11.76	1.0967
60	12.33	1.0969
60	12.98	1.0972
60	13.45	1.0973
60	14.21	1.0976
60	14.93	1.0979
60	15.84	1.0982
60	16.56	1.0985
60	17.40	1.0989
60	18.74	1.0995
60	19.70	1.0998
60	20.64	1.1002
60	21.17	1.1004
60	22.31	1.1009
60	23.07	1.1012
60	24.13	1.1017
60	24.74	1.1019
60	25.84	1.1023
60	26.88	1.1028
60	27.82	1.1032
60	28.90	1.1037
60	29.33	1.1038
60	30.09	1.1041
60	31.50	1.1047
60	32.05	1.1050
60	33.04	1.1054
60	34.15	1.1059
60	35.10	1.1063
70	0.10	1.0851
70	1.25	1.0855
70	2.10	1.0857
70	3.30	1.0861
70	4.05	1.0864
70	5.40	1.0871
70	6.11	1.0873
70	6.96	1.0877
70	7.90	1.0881
70	8.70	1.0888
70	10.29	1.0897
70	11.64	1.0907
70	12.62	1.0913
70	13.38	1.0918
70	14.55	1.0926
70	15.37	1.0931
70	16.06	1.0937
70	17.13	1.0944
70	18.03	1.0950
70	18.95	1.0957
70	19.85	1.0964
70	20.52	1.0969
70	22.24	1.0983
70	23.53	1.0993
70	24.95	1.1005
70	26.27	1.1016
70	27.45	1.1026
70	27.87	1.1029
70	29.24	1.1040
70	30.55	1.1050
70	31.12	1.1054
70	32.69	1.1062
70	33.65	1.1073
70	34.14	1.1076
70	35.39	1.1085
80	0.10	1.0753
80	1.25	1.0759
80	2.20	1.0765
80	3.05	1.0770
80	4.31	1.0777
80	5.42	1.0782
80	6.21	1.0787
80	14.75	1.0822
80	15.20	1.0823
80	15.88	1.0827
80	16.52	1.0829
80	16.93	1.0831
80	17.53	1.0833
80	18.27	1.0836

T [°C]	p [MPa]	ρ [g/mL]
80	19.10	1.0839
80	19.89	1.0842
80	20.98	1.0846
80	22.13	1.0851
80	23.00	1.0854
80	23.88	1.0857
80	24.73	1.0860
80	25.63	1.0863
80	25.99	1.0864
80	26.80	1.0867
80	27.66	1.0870
80	28.33	1.0872
80	29.09	1.0874
80	29.96	1.0877
80	30.74	1.0880
80	31.44	1.0881
80	32.41	1.0886
80	33.64	1.0891
80	34.63	1.0894
80	35.97	1.0900
90	0.10	1.0711
90	0.36	1.0712
90	2.12	1.0722
90	3.25	1.0729
90	4.12	1.0734
90	5.63	1.0743
90	6.15	1.0746
90	6.75	1.0750
90	9.71	1.0764
90	12.02	1.0779
90	13.69	1.0788
90	15.15	1.0797
90	15.91	1.0800
90	16.99	1.0807
90	17.59	1.0810
90	18.68	1.0816
90	19.77	1.0823
90	20.97	1.0831
90	21.80	1.0836
90	22.86	1.0843
90	23.79	1.0848
90	24.10	1.0850
90	24.92	1.0855
90	25.72	1.0859
90	26.40	1.0864
90	27.18	1.0867
90	28.23	1.0875
90	29.13	1.0880
90	30.26	1.0887
90	31.52	1.0894
90	32.17	1.0897
90	32.92	1.0901
90	34.10	1.0908

Table A1-15: Interfacial tension of CO_2 saturated PEG 6000 solution

T [°C]	p [MPa]	γ [nM/m]
60	0.1	32.34
60	1.96	27.03
60	4.31	22.54
60	6.18	18.48
60	8.42	15.20
60	10.28	13.43
60	12.15	12.20
60	13.92	10.28
60	15.94	8.55
60	18.00	7.04
60	20.06	6.53
60	22.24	5.77
60	24.01	5.55
60	26.04	5.03
60	28.19	4.69
60	30.08	4.57
60	32.30	4.36
60	34.20	4.06
60	36.43	3.93
70	0.10	32.32
70	2.06	26.51
70	4.27	21.28
70	6.16	17.91
70	8.31	14.40
70	10.30	12.53
70	12.05	10.39
70	14.24	8.59
70	16.00	7.47
70	17.82	6.67
70	19.93	5.86
70	22.16	5.30
70	23.94	4.90
70	25.97	4.35
70	28.05	3.92
70	30.22	3.46
80	0.10	31.64
80	2.07	24.51
80	4.17	20.28
80	6.02	16.92
80	8.08	13.90
80	10.09	11.58
80	12.02	9.61
80	14.01	8.21
80	16.03	6.56
80	18.01	5.74
80	20.14	5.33
80	22.16	4.58
80	24.05	4.24
80	26.28	3.75
80	27.97	3.53
80	29.97	3.09
90	0.10	30.55
90	2.06	23.67
90	4.25	19.75
90	6.27	16.18
90	8.49	12.27
90	10.62	9.99
90	12.27	8.45
90	14.21	7.20
90	16.03	6.08
90	17.91	4.93
90	20.05	4.33
90	21.86	3.81
90	24.08	3.52
90	26.12	3.30
90	27.92	3.09
90	30.06	2.92

Table A1-16: Viscosity of CO_2 saturated PEG 6000 solution.

T/ °C	p/Mpa	η/mPas
60	0.10	652.00
60	5.17	3.10
60	10.95	2.80
60	15.39	2.51
60	20.54	2.32
60	25.69	2.00
60	30.10	1.95
60	35.60	1.70
60	0.10	3.02
70	4.77	2.82
70	10.38	2.61
70	15.35	2.20
70	19.77	2.06
70	25.75	1.79
70	30.56	1.60
70	35.67	1.41
80	0.10	2.91
80	5.43	2.64
80	10.46	2.33
80	15.52	2.02
80	20.50	1.90
80	25.27	1.62
80	30.35	1.40
80	35.30	1.32
90	0.10	2.53
90	5.49	2.04
90	10.56	1.87
90	16.13	1.72
90	20.60	1.42
90	25.20	1.25
90	29.86	1.05
90	36.25	0.95

7.2 Appendix 2-Chapter 3

Table A2-1: Water-CO_2 interfacial tension at 25 °C and 45 °C in pressure range up to 20 MPa.

T (°C)	p (MPa)	$\Delta\rho$ (kg/m^3)	γ (mN/m)
25 ± 0.10	0.10	997.05	71.86 ± 0.11
	2.05	962.12	59.00 ±0.59
	3.94	907.06	47.30 ±0.16
	6.00	799.89	34.87 ±0.22
	7.98	221.32	29.32 ±0.17
	10.01	183.87	27.60 ±0.74
	12.00	156.83	27.21 ±0.47
	14.04	136.08	25.60 ±0.28
	16.02	119.01	25.08 ±0.48
	18.06	104.44	24.88 ±0.45
	19.90	92.21	24.37 ±0.55
45 ± 0.10	0.10	990.21	67.32 ± 0.43
	2.01	954.70	57.90 ± 0.10
	4.02	910.72	48.80 ± 0.27
	5.58	851.17	41.98 ± 0.32
	8.07	752.59	35.72 ± 0.20
	10.00	496.24	28.84 ± 0.51
	12.01	337.61	28.08 ± 0.36
	14.05	275.73	27.99 ± 0.25
	16.20	237.06	27.60 ± 0.24
	18.32	208.65	26.35 ± 0.27
	20.01	186.04	25.34 ± 0.29

Table A2-2: Density of propylene glycol saturated solution with CO_2 and density of pure CO_2, $\Delta\rho = \rho_{PG} - \rho_{(CO2)}$, interfacial tension of propylene glycol saturated solution with CO_2.

p (MPa)	T (K)	ρ_{PG} (kg/m^3)	ρ_{CO2} (kg/m^3)	$\Delta\rho$ (kg/m^3)	γ (mN/m)
5.00	398.15	1002.81	39.53	963.28	25.25 ±26
7.52	398.15	1004.40	59.32	945.08	22.18 ±62
10.00	398.15	1006.83	79.07	927.76	19.91 ±42
12.51	398.15	1008.83	98.74	910.09	16.76 ±45
14.99	398.15	1010.85	118.28	892.57	14.08 ±12
17.50	398.15	1012.58	137.67	874.91	12.57 ±14
5.02	423.15	976.70	67.43	909.27	22.00 ±48
7.49	423.15	978.45	105.11	873.34	19.67 ±62
10.00	423.15	980.20	145.56	834.64	17.54 ±42
12.50	423.15	981.95	188.66	793.29	13.96 ±45
15.02	423.15	983.70	233.93	749.77	11.88 ±12
17.50	423.15	985.45	280.48	704.97	10.78 ±13

Table A2 - 3: Effect of Ar contaminant on densities and interfacial tension at 45 °C.

System at 45 °C	p (MPa)	ρ_{Brine} (kg/m^3)	ρ_{CO2} (kg/m^3)	$\Delta\rho$ (kg/m^3)	γ (mN/m)
Brine/CO_2					
	1.98	1011.42	36.34	975.08	58.35 ± 0.10
	4.01	1012.19	81,195	930.99	50.00 ± 0.08
	6.04	1012.95	141.61	871.34	42.62 ± 0.11
	7.98	1013.72	241.05	772.67	36.22 ± 0.32
	10.04	1014.49	498.25	516.24	32.24 ± 0.80
	11.95	1015.24	655.58	359.66	27.82 ± 0.11
	13.98	1016.03	720.47	295.56	27.23 ± 0.81
	16.02	1016.8	759.98	256.82	26.24 ± 0.18
	18.00	1017.56	789.24	228.32	26.82 ± 0.26
	19.98	1018.33	812.69	205.64	26.36 ± 0.17
Brine/CO_2+5% Ar					
	2.05	1011.03	36.05	974.98	61.74 ± 0.17
	4.05	1011.78	81.45	930.33	51.90 ± 0.21
	6.03	1012.62	142.75	869.88	43.98 ± 0.99
	8.10	1013.41	242.25	771.16	37.87 ± 0.39
	10.05	1014.27	488.18	526.09	30.91 ±0. 54
	11.98	1015.1	634.21	380.89	29.35 ± 0.94
	13.99	1015.87	695.37	320.50	28.64 ± 0.18
	15.97	1016.71	734.46	282.26	28.68 ± 0.16
	18.00	1017.51	763.77	253.74	28.30 ± 0.33
	20.00	1018.34	787.54	230.80	28.74 ± 0.56
Brine/CO_2+10% Ar					
	2.50	1011.16	35.75	975.40	55.52 ± 0.50
	3.98	1011.88	73.69	938.19	49.54 ± 0.16
	6.04	1012.7	130.03	882.67	40.75 ± 0.60
	7.96	1013.47	215.02	798.45	34.33 ± 0.20
	10.05	1014.3	449.98	564.32	27.47 ± 0.54
	12.08	1015.11	595.75	419.36	26.18 ± 0.10
	13.98	1015.86	650.61	365.26	26.33 ±0 .46
	16.02	1016.68	686.48	330.20	25.76 ± 0.35
	17.98	1017.46	713.12	304.34	26.84 ± 0.23
	20.00	1018.26	734.52	283.74	26.32 ± 0.18
Brine/CO_2+ 50% Ar					
	2.01	1001.74	33.40	968.34	65.32 ±0.26
	4.10	1002.57	72.31	930.26	63.67 ±0.39
	5.95	1003.4	119.75	883.65	59.55 ±0.29
	8.08	1004.23	187.04	817.20	54.58 ±0.39
	10.06	1005.06	331.06	674.00	46.99 ±0.27
	12.02	1005.89	422.48	583.42	42.44 ±0.31
	13.95	1006.72	469.5	537.23	39.05 ±0.31
	16.13	1007.55	504.73	502.82	36.54 ±0.54
	17.96	1008.38	534.59	473.80	36.47 ±0.25
	20.11	1009.21	561.23	447.98	35.41 ±0.25

System Brine/Ar at 45 °C	p (MPa)	ρ_{Brine} (kg/m^3)	ρ_{CO2} (kg/m^3)	$\Delta\rho$ (Kg/m^3)	γ (mN/m)
	2.01	992.09	30.46	961.63	65.55 ± 0.64
	4.01	993.00	62.15	930.85	63.52 ± 0.40
	6.10	993.96	94.20	899.76	62.26 ± 0.34
	8.05	994.87	125.69	869.18	61.35 ± 029

Table A2-4: Calculated storage capacity form brine-CO_2 interfacial properties relevant.

T [°C]	*p* [MPa]	ρ_{brine} [kg/m^3]	ρ_{CO2} [kg/m^3]	$\Delta\rho$ [kg/m^3]	γ [mN/m]	*cosΦ*	*H* (m)	*M* (Mt/km^2)	*Depth* (km)
25	7.22	1016.78	751.22	265.56	32.07	0.9728	239.48	25.19	0.72
40	7.91	1017.17	267.07	750.1	34.3	0.9726	90.68	3.39	0.79
40	9.12	1017.66	510.38	507.28	33.32	0.9724	130.23	9.31	0.91
40	10	1018.57	628.61	389.96	32.82	0.9723	166.83	14.68	1
40	11.3	1018.57	695.15	323.42	32.01	0.972	196.14	19.09	1.13
40	12.21	1018.88	723.36	295.52	31.58	0.9719	211.76	21.44	1.22
40	13.08	1019.33	745.25	274.08	31.1	0.9717	224.79	23.45	1.31
40	13.9	1019.67	761.41	258.26	30.8	0.9716	236.22	25.18	1.39
40	15	1020.13	780.23	239.9	30.32	0.9713	250.29	27.34	1.5
50	10.02	1010.85	387.15	623.7	32.06	0.9723	101.9	5.52	1
50	12.1	1011.65	590.85	420.8	31.04	0.9719	146.14	12.09	1.21
50	14	1012.38	672.17	340.21	30.14	0.9715	175.47	16.51	1.4
50	16.15	1013.22	725.1	288.12	29.43	0.9711	202.26	20.53	1.62
50	18.22	1014	760.13	253.87	29.01	0.9707	226.13	24.06	1.82
50	20.17	1014.76	787.31	227.45	28.94	0.9704	251.75	27.75	2.02
60	13.51	1009.02	535.26	473.76	29.91	0.9716	125.06	9.37	1.35
60	14.77	1009.67	596.41	413.26	29.03	0.9714	139.12	11.62	1.48
60	17	1010.74	664.59	346.15	28.71	0.971	164.21	15.28	1.7
60	19.11	1011.74	708.48	303.26	28.38	0.9706	185.18	18.37	1.91
60	20.98	1012.62	738.78	273.84	28.32	0.9702	204.54	21.16	2.1
60	23	1013.54	763.55	249.99	28.1	0.9698	222.25	23.76	2.3
60	25.1	1014.44	786.55	227.89	27.89	0.9694	241.91	26.64	2.51
70	16.82	1003.37	576.27	427.1	29.62	0.971	137.29	11.08	1.68
70	19.92	1004.9	657.01	347.89	28.62	0.9704	162.78	14.97	1.99
70	22.07	1005.96	696.7	309.26	28.42	0.97	181.71	17.72	2.21
70	24	1006.92	725.55	281.37	27.93	0.9697	196.24	19.93	2.4
70	26.07	1007.94	749.73	258.21	27.66	0.9693	211.71	22.22	2.61
70	27.92	1008.87	768.6	240.27	27.27	0.9689	224.22	24.13	2.79
70	30.04	1009.9	788.41	221.49	27.09	0.9685	241.47	26.65	3
80	20	996.74	595.09	401.65	29.19	0.9704	143.8	11.98	2
80	24.1	998.1	672.83	325.27	28.23	0.9696	171.57	16.16	2.41
80	27.93	999.39	723.23	276.16	27.9	0.9689	199.59	20.21	2.79
80	32.01	1000.71	764.37	236.34	27.36	0.9681	228.46	24.45	3.2
80	35.02	1001.71	788.97	212.74	27.02	0.9675	250.5	27.67	3.5

T **[°C]**	***p*** **[MPa]**	ρ_{brine} **[kg/m^3]**	ρ_{CO2} **[kg/m^3]**	$\Delta\rho$ **[kg/m^3]**	γ **[mN/m]**	***cosΦ***	***H*** **(m)**	***M*** **(Mt/km^2)**	***Depth*** **(km)**
90	22.98	993.71	600.71	393	28.49	0.9698	143.36	12.06	2.3
90	26	995.01	651.66	343.35	28.22	0.9693	162.42	14.82	2.6
90	30	996.73	703.27	293.46	27.64	0.9685	185.95	18.31	3
90	34	998.45	743.18	255.27	26.97	0.9677	208.44	21.69	3.4
90	38	1000.17	775.57	224.6	26.67	0.9669	234.11	25.42	3.8
90	40.03	1001.04	789.73	211.31	26.7	0.9665	248.98	27.53	4

Table A2-5: Calculated storage capacity form brine-CO_2+5 vol. % Ar interfacial properties.

	***p* [MPa]**	***ρ*** $_{brine}$**[kg/m^3]**	***ρ*** $_{CO2+Ar}$ **[kg/m^3]**	**Δ*ρ*** **[kg/m^3]**	***γ*** **[mN/m]**	***cosΦ***	***H* (m)**	***M*** **(Mt/km^2)**	***Depth*** **(km)**
30	10.2	1017.75	741.19	276.56	29.94	0.9722	214.61	22.27	1.02
40	6.75	1016.71	182.77	833.63	36.17	0.9729	86.06	2.2	0.68
40	8.01	1017.22	269.56	747.4	34.82	0.9726	92.39	3.49	0.8
40	10.5	1018.22	635.48	382.56	33	0.9722	170.97	15.21	1.05
40	12.06	1018.85	694.2	324.55	31.74	0.9719	193.78	18.83	1.21
40	13.21	1019.31	720.55	298.67	31.07	0.9717	206.06	20.79	1.32
40	14.25	1019.73	740.73	279	30.2	0.9715	214.41	22.23	1.43
40	15.03	1020.04	753.95	266.11	28.45	0.9713	211.69	22.34	1.5
50	9.98	1010.53	372.75	637.9	31.33	0.9723	97.35	5.08	1
50	12.1	1011.37	564.65	446.75	30.73	0.9719	136.31	10.78	1.21
50	14.4	1012.27	660.8	351.46	28.41	0.9715	160.08	14.81	1.44
50	15.98	1012.9	698.21	314.69	28.22	0.9712	177.57	17.36	1.6
50	17.99	1013.69	732.98	280.67	27.83	0.9708	196.27	20.14	1.8
50	20.23	1014.57	762.69	251.79	27.65	0.9704	217.22	23.19	2.02
60	13.56	1007.48	523.75	484.16	28.47	0.9716	116.48	8.54	1.36
60	15.3	1008.47	595.43	413.28	28.32	0.9713	135.69	11.31	1.53
60	17	1009.44	649.68	359.94	27.8	0.971	152.89	13.91	1.7
60	18.98	1010.56	685.23	325.22	27.16	0.9706	165.26	15.85	1.9
60	20.83	1011.61	714.24	297.07	26.96	0.9703	179.52	17.95	2.08
60	23.02	1012.86	743.11	269.22	26.79	0.9698	196.78	20.47	2.3
60	25.1	1014.04	765.15	248.13	26.67	0.9694	212.44	22.76	2.51
70	17	1001.46	565.66	435.95	28.61	0.971	129.93	10.29	1.7
70	30	1009.82	768.85	240.38	27.02	0.9685	221.97	23.89	3
80	20	996.33	577.74	417.52	29.14	0.9704	138.08	11.17	2
80	22.97	997.21	637.56	358.89	28.45	0.9699	156.74	13.99	2.3
80	26	998.1	718.58	279.11	27.39	0.9693	193.92	19.51	2.6
80	29.03	998.99	711.58	287.26	27.19	0.9687	186.93	18.62	2.9
80	32	999.87	746.83	253.25	27.13	0.9681	211.47	22.11	3.2
80	35	1000.76	771.82	229.41	27.07	0.9675	232.75	25.15	3.5
90	22.98	993.2	585.57	407.63	28.72	0.9698	139.31	11.42	2.3
90	26	994.66	635.76	358.9	28.14	0.9693	154.94	13.79	2.6
90	30	996.2	687.01	309.19	27.97	0.9685	178.6	17.18	3
90	34	998	727.02	270.98	27.37	0.9677	199.27	20.28	3.4
90	38	999.6	759.79	239.81	27.25	0.9669	223.98	23.82	3.8
90	40.03	1000.8	774.19	226.61	26.72	0.9665	232.32	25.18	4

Table A2-6: Calculated storage capacity form brine-CO_2+10 vol. % Ar interfacial properties.

T [°C]	*p* [MPa]	ρ_{brine} [kg/m^3]	ρ_{CO2+Ar} [kg/m^3]	$\Delta\rho$ [kg/m^3]	γ [mN/m]	*cosΦ*	*H* (m)	*M* (Mt/km^2)	*Depth* (km)
30	10	1018	710.89	307.11	19.4	0.97	125.24	12.46	1
									0
40	7.98	1017.22	262.76	754.46	34.82	0.97	91.53	3.37	0.8
40	10.5	1018.08	585.01	433.07	33	0.97	151.03	12.37	1.05
40	12.02	1018.82	665.09	353.73	31.74	0.97	177.79	16.55	1.2
40	13.03	1019.23	689.44	329.79	31.07	0.97	186.62	18.01	1.3
40	15.03	1020.03	726.1	293.93	30.2	0.97	203.49	20.69	1.5
50	10.11	1010.54	372.12	638.42	32.11	0.97	99.69	5.19	1.01
50	12.04	1011.33	547.49	463.84	30.8	0.97	131.59	10.09	1.2
50	14.02	1012.12	626.37	385.75	29.83	0.97	153.18	13.43	1.4
50	15.98	1012.94	674.33	338.61	28.96	0.97	169.36	15.99	1.6
50	18.1	1013.65	710.34	303.31	28.23	0.97	184.2	18.32	1.81
50	20.12	1014.48	737.44	277.04	27.72	0.97	197.98	20.44	2.01
60	13.62	1007.5	506.73	500.77	28.93	0.97	114.45	8.12	1.36
60	15.35	1008.47	577.57	430.9	28.04	0.97	128.86	10.42	1.54
60	17	1009.44	624.24	385.2	27.91	0.97	143.45	12.54	1.7
60	18.95	1010.57	662.89	347.68	27.74	0.97	157.88	14.65	1.9
60	21.02	1011.71	695.44	316.27	27.52	0.97	172.14	16.76	2.1
60	23.05	1012.84	722.09	290.75	27.18	0.97	184.81	18.68	2.31
60	25.01	1013.98	743.76	270.23	27.02	0.97	197.61	20.58	2.5
70	16.95	1001.43	538.02	463.41	28.93	0.97	123.6	9.31	1.7
70	19	1002.75	600.34	402.41	28.04	0.97	137.88	11.59	1.9
70	21.1	1004.03	639.72	364.31	27.91	0.97	151.55	13.57	2.11
70	23.04	1005.32	671.34	333.99	27.74	0.97	164.23	15.44	2.3
70	24.95	1006.57	697.15	309.42	27.52	0.97	175.81	17.16	2.5
70	26.97	1007.83	719.98	287.85	27.18	0.97	186.53	18.8	2.7
70	30	1009.82	749.72	260.1	27.02	0.97	205.1	21.53	3
80	20.02	996.33	561.56	434.77	28.77	0.97	130.93	10.29	2
80	23.01	997.22	620.22	377	28.05	0.97	147.13	12.78	2.3
80	26.12	998.1	665.77	332.33	27.51	0.97	163.57	15.25	2.61
80	29.03	999	699.82	299.18	27.24	0.97	179.79	17.61	2.9
80	31.98	999.87	729.26	270.61	26.91	0.97	196.27	20.04	3.2
80	35	1000.76	754.61	246.15	26.65	0.97	213.59	22.56	3.5
90	22.98	993.2	570.44	422.76	28.35	0.97	132.61	10.59	2.3
90	26	994.2	619.85	374.35	28.14	0.97	148.54	12.89	2.6
90	30	994.7	670.74	323.96	27.8	0.97	169.44	15.91	3
90	34	997.77	710.86	286.91	27.37	0.97	188.21	18.73	3.4

7.3 Appendix 3-Chapter 4

7.3.1 Heat transfer coefficients of the CO_2 - water system

Table A3-1: CO_2-water system at 7.5 MPa and 1 L/min water flux.

Water		**CO_2**					
T_{in} [°C]	T_{out} [°C]	T_{in} [°C]	T_{out} [°C]	Q_m [kg/min]	ΔT_{log} [K]	α [W/(m²*K)]	U [W/(m²*K)]
18.00	18.90	30.90	22.00	0.083	8.21	1765.51	400.70
20.00	21.00	31.10	23.90	0.080	7.28	2662.99	443.55
22.60	23.50	31.00	26.30	0.082	6.52	3744.10	479.19
25.60	26.20	31.00	27.90	0.079	5.38	3327.13	485.81
14.40	17.20	35.00	28.10	0.082	3.40	6028.24	545.98
24.50	25.80	35.00	32.00	0.083	15.66	23236.24	577.81
26.20	27.40	40.10	32.00	0.070	8.32	12985.42	550.57
25.00	26.40	44.90	31.80	0.069	8.80	3437.56	487.10
23.40	25.20	49.90	32.10	0.074	11.69	1987.57	435.70
21.70	24.00	60.00	32.00	0.070	15.33	1342.87	389.27
20.50	23.20	70.10	32.00	0.072	20.54	1149.60	368.05
20.00	22.80	80.00	32.10	0.072	25.18	891.68	335.67
18.90	22.10	90.10	32.10	0.071	29.03	811.81	321.46
18.00	18.90	30.90	22.00	0.083	33.43	1765.51	400.70

Table A3-2: CO_2-water system at 7.5 MPa and 2 L/min water flux.

Water		**CO_2**					
T_{in} [°C]	T_{out} [°C]	T_{in} [°C]	T_{out} [°C]	Q_m [kg/min]	ΔT_{log} [K]	α [W/(m²*K)]	U [W/(m²*K)]
15.60	16.20	31.00	18.90	0.083	7.66	1087.24	476.03
17.70	18.20	31.00	20.80	0.083	6.84	1046.20	474.76
20.20	20.70	31.10	23.20	0.081	5.95	1262.73	524.37
23.20	23.70	30.90	25.90	0.080	4.59	1565.79	583.47
25.60	26.00	30.90	27.70	0.078	3.30	1796.68	623.98
14.80	16.50	35.10	26.50	0.082	14.88	2825.48	649.91
24.88	25.70	35.00	31.50	0.084	7.88	2995.53	721.47
26.30	27.10	40.10	31.70	0.076	8.65	2438.92	691.87
25.30	26.20	45.00	31.60	0.074	11.43	1530.41	588.21
23.70	24.70	49.90	31.10	0.075	14.53	1176.15	521.93
21.60	23.00	60.10	31.40	0.076	20.51	948.62	466.34
20.50	22.10	70.10	31.30	0.078	24.94	847.83	438.02
20.10	21.90	80.00	31.40	0.075	28.58	758.91	412.33
19.00	20.90	90.20	31.10	0.076	32.77	689.74	388.83

Table A3-3: CO_2-water system at 8 MPa and 1 L/min water flux.

Water		**CO_2**					
T_{in} [°C]	T_{out} [°C]	T_{in} [°C]	T_{out} [°C]	Q_m [kg/min]	ΔT_{log} [K]	α [W/(m^2*K)]	U [W/(m^2*K)]
19.00	19.80	31.00	21.90	0.074	6.14	1521.23	390.16
21.70	22.30	30.90	24.00	0.073	4.78	1313.60	383.88
23.90	24.40	30.90	25.90	0.071	3.82	1208.11	381.24
26.50	26.80	30.90	28.00	0.089	2.59	1148.09	382.65
20.90	22.40	35.00	28.10	0.083	9.65	3419.84	466.36
24.50	26.20	35.00	32.10	0.087	8.19	5639.44	513.67
20.80	23.00	40.10	32.10	0.086	14.00	11880.28	518.08
18.20	21.10	44.90	31.90	0.090	18.29	18378.48	511.78
17.40	20.60	50.00	32.10	0.086	21.21	5599.63	477.53
15.40	19.10	60.00	31.90	0.083	26.88	2748.51	430.39
13.30	17.70	69.90	31.90	0.084	32.56	2375.99	412.15
12.50	17.20	79.90	32.00	0.085	36.99	1881.75	391.50
11.80	16.80	89.90	31.90	0.082	41.05	1528.75	371.49
19.00	19.80	31.00	21.90	0.074	6.14	1521.23	390.16

Table A3-4: CO_2-water system at 8 MPa and 2 L/min water flux.

Water		**CO_2**					
T_{in} [°C]	T_{out} [°C]	T_{in} [°C]	T_{out} [°C]	Q_m [kg/min]	ΔT_{log} [K]	α [W/(m^2*K)]	U [W/(m^2*K)]
16.20	16.80	30.90	19.00	0.077	6.99	1099.22	480.39
19.00	19.50	30.90	21.20	0.074	5.59	1172.11	503.78
21.60	22.00	30.90	23.60	0.073	4.62	1001.93	477.35
24.30	24.60	31.00	25.80	0.069	3.38	990.73	482.64
26.60	26.80	31.00	27.80	0.087	2.39	993.63	489.78
20.90	21.80	34.90	26.60	0.086	8.89	1627.75	582.35
24.90	25.80	35.10	31.20	0.090	7.70	1733.90	614.16
20.80	22.10	40.10	31.10	0.090	13.79	1793.90	602.79
18.20	19.90	45.00	30.60	0.095	18.01	1850.47	596.98
17.40	19.20	50.10	31.10	0.092	21.15	1400.09	537.73
15.50	17.50	60.00	30.90	0.093	26.70	1126.42	485.52
13.30	15.60	70.00	30.10	0.090	32.00	1006.89	455.29
12.50	15.00	80.00	30.50	0.090	36.60	899.21	429.86
11.80	14.50	90.00	30.40	0.090	40.61	851.81	417.06

Table A3-5: CO_2-water system at 10 MPa and 1 L/min water flux.

Water		**CO_2**					
T_{in} [°C]	T_{out} [°C]	T_{in} [°C]	T_{out} [°C]	Q_m [kg/min]	ΔT_{log} [K]	α [W/(m²*K)]	U [W/(m²*K)]
16.90	17.60	31.00	20.00	0.087	7.04	879.66	322.95
19.90	20.50	31.00	22.00	0.083	5.22	1149.78	362.85
22.40	22.90	31.10	24.00	0.081	4.04	1253.20	380.70
24.70	25.10	31.20	26.00	0.081	3.10	1188.48	381.61
27.20	27.50	31.00	28.00	0.07	1.83	1542.67	420.81
25.90	26.60	35.00	27.90	0.078	4.46	1713.09	428.39
31.00	31.30	35.00	31.90	0.08	1.98	1513.57	431.60
28.70	29.60	40.00	31.90	0.085	6.11	1580.03	429.94
25.80	27.30	45.00	32.00	0.088	10.96	1951.88	443.12
21.80	24.30	50.00	32.00	0.096	16.77	3650.51	477.63
18.00	21.60	60.00	32.00	0.091	24.18	4237.78	469.07
17.10	20.90	70.00	31.90	0.086	28.60	2381.43	428.19
18.40	21.90	80.00	32.00	0.07	30.65	1187.45	366.36
21.70	25.10	89.90	31.80	0.053	29.43	912.26	343.87

Table A3-6: CO_2-water system at 10 MPa and 2 L/min water flux.

Water		**CO_2**					
T_{in} [°C]	T_{out} [°C]	T_{in} [°C]	T_{out} [°C]	Q_m [kg/min]	ΔT_{log} [K]	α [W/(m²*K)]	U [W/(m²*K)]
17.00	17.40	31.10	19.20	0.083	6.29	733.42	396.05
19.90	20.20	31.00	21.50	0.081	4.82	729.98	401.52
22.20	22.50	31.00	23.50	0.081	3.83	836.20	437.56
24.70	24.90	31.10	25.60	0.07	2.75	841.58	445.14
27.30	27.40	31.00	27.80	0.078	1.57	902.22	468.13
26.10	26.40	35.00	27.40	0.08	3.86	966.34	481.81
31.40	31.50	34.90	31.90	0.085	1.51	1037.53	513.54
28.70	29.20	40.00	31.10	0.088	5.58	1101.50	521.47
25.90	26.70	44.90	30.40	0.096	9.80	1190.20	531.84
21.90	23.20	50.00	29.80	0.091	15.47	1362.82	549.25
17.90	19.90	60.10	29.40	0.086	22.93	1460.85	549.04
17.00	19.00	70.00	28.70	0.07	26.69	1145.23	494.33
18.30	20.60	80.10	29.80	0.053	29.20	993.64	468.29
22.60	24.40	89.80	29.60	0.056	26.13	738.87	411.86

Table A3-7: CO_2-water system at 20 MPa and 1 L/min water flux.

Water		**CO_2**					
T_{in} [°C]	T_{out} [°C]	T_{in} [°C]	T_{out} [°C]	Q_m [kg/min]	ΔT_{log} [K]	α [W/(m²*K)]	U [W/(m²*K)]
19.20	19.70	31.10	20.00	0.067	3.99	1212.92	366.45
21.20	21.60	30.90	21.80	0.066	3.17	1186.78	370.33
23.40	23.70	30.90	24.10	0.085	2.79	996.16	355.57
25.40	25.60	30.90	25.80	0.083	1.90	1040.71	366.68
27.80	27.90	30.90	27.90	0.067	0.85	1255.41	397.65
27.10	27.50	34.90	27.90	0.074	2.97	1071.33	375.58
31.80	31.90	35.00	32.00	0.073	1.06	758.73	337.61
31.00	31.40	40.00	31.90	0.071	3.41	799.64	344.12
30.40	31.00	44.90	31.90	0.072	5.57	727.21	329.01
29.70	30.50	49.90	32.00	0.078	8.02	704.19	323.07
28.40	29.70	60.00	31.90	0.078	12.42	789.37	337.64
27.50	29.20	70.00	32.00	0.078	16.47	829.96	343.26
26.20	28.60	80.10	31.90	0.077	20.81	993.40	365.79
25.30	27.90	90.10	32.10	0.079	25.03	914.31	352.47

Table A3-8: CO_2-water system at 20 MPa and 2 L/min water flux.

Water		**CO_2**					
T_{in} [°C]	T_{out} [°C]	T_{in} [°C]	T_{out} [°C]	Q_m [kg/min]	ΔT_{log} [K]	α [W/(m²*K)]	U [W/(m²*K)]
19.20	19.50	31.00	19.70	0.07	3.51	991.33	467.47
21.00	21.30	31.00	21.60	0.07	3.27	954.60	464.45
23.40	23.60	31.00	23.80	0.08	2.40	989.51	479.57
25.50	25.60	31.00	25.60	0.08	1.33	1168.34	524.94
27.80	27.90	31.00	27.90	0.06	0.87	1363.89	569.72
27.20	27.50	35.00	27.70	0.09	2.58	1543.00	596.70
31.80	31.90	35.00	31.90	0.06	0.87	1304.12	572.66
31.00	31.30	40.00	31.60	0.07	3.03	1017.38	507.77
30.50	30.90	44.90	31.40	0.08	4.77	883.46	471.03
29.80	30.40	50.00	31.30	0.07	7.04	843.87	458.21
29.00	29.80	60.00	31.30	0.08	10.84	778.32	436.74
27.40	28.50	70.00	30.60	0.08	14.95	793.32	438.31
26.30	27.80	80.10	30.40	0.08	18.93	894.33	465.24
25.40	27.00	89.90	30.20	0.08	22.58	814.29	440.66

Table A3-9: CO_2-water system at 30 MPa and 1 L/min water flux.

Water		**CO_2**					
T_{in} [°C]	T_{out} [°C]	T_{in} [°C]	T_{out} [°C]	Q_m [kg/min]	ΔT_{log} [K]	α [W/(m²*K)]	U [W/(m²*K)]
19.20	19.70	30.90	19.90	0.063	3.79	1147.88	360.28
21.40	21.80	30.90	21.90	0.061	2.96	1148.38	367.14
23.50	23.80	30.90	23.90	0.060	2.33	973.81	352.95
25.60	25.80	30.90	25.90	0.060	1.69	803.86	332.66
27.70	27.80	30.90	27.90	0.076	1.06	727.42	323.11
27.60	27.80	35.00	28.00	0.069	2.35	620.80	300.12
31.70	31.80	34.90	31.90	0.066	1.06	599.89	301.87
31.90	32.00	40.00	32.00	0.068	1.80	704.38	326.59
31.40	31.80	45.00	32.00	0.066	4.08	710.04	327.15
30.60	31.20	50.00	32.00	0.078	6.70	652.36	313.12
29.80	30.70	60.10	31.90	0.076	10.34	635.44	308.05
29.30	30.60	70.10	32.00	0.075	13.72	705.73	323.10
28.90	30.50	80.00	32.10	0.075	16.91	728.40	327.27
28.50	30.50	90.00	32.00	0.075	19.77	826.88	345.33

Table A3-10: CO_2-water system at 30 MPa and 2 L/min water flux.

Water		**CO_2**					
T_{in} [°C]	T_{out} [°C]	T_{in} [°C]	T_{out} [°C]	Q_m [kg/min]	ΔT_{log} [K]	α [W/(m²*K)]	U [W/(m²*K)]
19.30	19.50	30.90	19.60	0.071	3.05	798.45	419.79
21.70	21.90	30.90	21.80	0.055	1.98	1273.02	531.25
23.60	23.80	30.90	23.70	0.054	1.64	1589.63	587.85
25.70	25.90	31.00	26.00	0.065	1.69	1245.69	540.89
27.70	27.80	31.00	27.90	0.075	1.08	916.79	473.04
27.60	27.70	35.00	27.70	0.077	1.68	859.76	457.15
31.80	31.90	34.90	32.00	0.055	1.03	776.66	441.11
31.90	32.00	40.00	32.00	0.077	1.80	803.08	449.71
31.50	31.80	45.10	32.10	0.080	4.10	779.13	441.52
30.60	31.00	50.00	31.50	0.078	5.93	703.39	414.63
29.90	30.40	60.00	31.10	0.077	8.86	627.00	385.84
29.20	30.00	70.00	30.80	0.076	11.93	728.69	421.04
29.00	30.10	80.10	31.00	0.075	14.91	796.43	442.70
28.60	29.90	90.00	30.90	0.074	17.71	796.87	442.20

7.3.2 Heat transfer coefficients of the ethane-water system

Table A3-11: Ethane -water system at 5.0 MPa and 1 L/min water flux.

Water		**Ethane**					
T_{in} [°C]	T_{out} [°C]	T_{in} [°C]	T_{out} [°C]	Q_m [kg/min]	ΔT_{log} [K]	α [W/(m^2*K)]	U [W/(m^2*K)]
16.20	17.10	32.10	19.90	0.040	8.07	908.20	325.07
18.80	19.60	31.90	21.90	0.040	6.68	989.86	342.37
21.30	22.00	31.80	24.00	0.039	5.51	993.62	349.86
23.50	24.00	31.90	26.00	0.039	4.69	698.89	309.12
26.20	26.50	32.00	27.90	0.042	3.24	677.10	310.04
28.70	28.90	32.00	29.90	0.043	2.00	673.23	313.96
23.10	24.30	35.00	30.00	0.045	8.66	2851.51	463.84
28.20	29.30	35.00	32.90	0.044	5.18	2978.21	491.05
25.60	26.80	40.10	33.10	0.044	10.12	2082.67	448.08
25.10	26.50	45.00	33.10	0.044	12.52	1709.32	426.44
24.40	26.00	50.10	33.10	0.045	15.11	1444.76	405.71
20.50	22.90	60.10	33.10	0.048	22.72	1158.03	368.43
19.50	22.20	70.00	33.00	0.049	27.13	1042.02	353.32
17.50	20.60	79.90	32.90	0.043	32.56	770.77	311.36

Table A3-12: Ethane -water system at 5.0 MPa and 2 L/min water flux.

Water		**Ethane**					
T_{in} [°C]	T_{out} [°C]	T_{in} [°C]	T_{out} [°C]	Q_m [kg/min]	ΔT_{log} [K]	α [W/(m^2*K)]	U [W/(m^2*K)]
16.00	16.60	32.00	19.00	0.040	7.58	836.99	422.00
18.80	19.30	31.90	21.30	0.040	6.24	811.57	422.50
21.40	21.80	31.90	23.50	0.039	5.09	799.18	425.39
23.50	23.90	32.00	25.50	0.039	4.36	923.78	464.13
26.50	26.70	32.00	27.40	0.042	2.48	1000.31	491.11
28.80	29.00	32.00	29.60	0.043	1.66	1432.33	585.31
23.20	24.00	35.00	28.70	0.045	7.93	1872.56	622.14
28.30	28.80	35.00	32.40	0.044	5.08	1861.73	644.60
25.60	26.40	40.10	32.00	0.044	9.59	1387.18	566.72
25.10	25.90	45.00	31.90	0.044	11.91	1014.10	491.22
24.50	25.50	50.10	32.60	0.045	14.85	981.30	481.97
20.60	22.00	59.90	31.70	0.048	21.82	826.43	432.24
19.70	21.20	70.00	32.00	0.049	26.49	714.54	397.68
17.30	19.10	79.80	31.10	0.043	31.66	600.98	355.77

Table A3-13: Ethane -water system at 5.5 MPa and 1 L/min water flux.

Water		**Ethane**					
T_{in} [°C]	T_{out} [°C]	T_{in} [°C]	T_{out} [°C]	Q_m [kg/min]	ΔT_{log} [K]	α [W/(m²*K)]	U [W/(m²*K)]
17.10	17.80	32.00	20.00	0.049	7.11	859.24	320.68
19.30	19.90	32.00	21.90	0.051	6.18	869.98	327.85
21.70	22.20	32.00	24.00	0.049	5.17	764.05	317.09
24.10	24.50	32.00	25.90	0.049	3.99	787.27	326.56
26.50	26.80	32.10	28.00	0.050	3.01	745.71	324.32
29.10	29.30	32.00	30.00	0.050	1.64	808.08	341.35
27.50	28.00	35.10	30.00	0.050	4.41	846.51	344.65
31.50	31.80	35.00	32.90	0.046	2.18	844.84	353.22
24.00	25.60	40.20	32.90	0.049	11.52	1497.24	408.31
21.50	23.50	45.00	32.90	0.050	15.92	1634.02	409.13
19.60	22.20	50.10	32.90	0.048	19.71	1605.73	401.25
17.30	20.00	60.10	32.90	0.045	25.95	943.43	335.10
16.60	19.70	69.90	33.10	0.043	30.29	844.51	320.42
16.60	19.90	80.00	33.20	0.039	33.81	705.11	298.29

Table A3-14: Ethane -water system at 5.5 MPa and 2 L/min water flux.

Water		**Ethane**					
T_{in} [°C]	T_{out} [°C]	T_{in} [°C]	T_{out} [°C]	Q_m [kg/min]	ΔT_{log} [K]	α [W/(m²*K)]	U [W/(m²*K)]
16.80	17.20	32.20	19.30	0.050	6.98	636.68	365.62
19.50	19.80	32.10	21.50	0.051	5.67	621.11	365.47
22.00	22.20	32.00	23.60	0.053	4.52	563.01	348.55
24.10	24.30	32.10	25.50	0.049	3.73	592.42	363.14
26.40	26.60	32.00	27.60	0.046	2.79	698.31	404.90
29.30	29.40	32.10	29.90	0.057	1.40	795.04	441.85
27.50	27.80	34.90	29.20	0.050	3.78	870.00	460.03
31.50	31.70	35.00	32.80	0.049	2.15	893.57	475.95
24.10	25.00	40.10	31.40	0.048	10.73	1101.97	507.92
21.30	22.60	45.00	30.60	0.046	14.90	1128.19	504.75
19.60	21.10	50.10	30.50	0.049	18.50	1067.40	487.01
17.50	19.20	60.10	31.20	0.049	24.87	811.05	420.58
16.60	18.40	70.00	30.70	0.045	28.91	685.35	382.24
16.60	18.50	80.00	31.60	0.042	32.96	581.22	347.60

Table A3-15: CO_2-water system at 8.0 MPa and 1 L/min water flux.

Water		**Ethane**					
T_{in} [°C]	T_{out} [°C]	T_{in} [°C]	T_{out} [°C]	Q_m [kg/min]	ΔT_{log} [K]	α [W/(m²*K)]	U [W/(m²*K)]
17.80	18.40	32.10	20.00	0.05	6.29	676.83	292.78
20.20	20.70	32.00	22.00	0.05	5.17	686.21	299.63
22.30	22.80	32.10	23.90	0.05	4.37	787.65	322.51
24.60	25.00	31.90	25.90	0.05	3.35	755.50	322.08
27.00	27.30	32.00	27.90	0.05	2.30	862.31	345.80
29.30	29.50	31.90	29.90	0.04	1.30	937.20	362.94
29.00	29.20	35.00	29.90	0.05	2.63	584.70	293.75
32.50	32.60	35.00	32.90	0.04	1.12	501.81	275.88
31.60	31.80	39.90	32.80	0.05	3.61	421.47	248.80
30.60	31.10	45.00	33.00	0.04	6.55	452.02	258.14
29.70	30.50	50.10	33.00	0.04	9.15	546.06	285.18
26.70	28.50	59.90	33.00	0.04	15.63	861.61	346.77
24.90	27.50	69.90	33.00	0.04	20.72	1051.00	370.05
23.60	26.50	80.00	33.00	0.04	25.36	946.35	353.04

Table A3-16: Ethane-water system at 8.0 MPa and 2 L/min water flux.

Water		**Ethane**					
T_{in} [°C]	T_{out} [°C]	T_{in} [°C]	T_{out} [°C]	Q_m [kg/min]	ΔT_{log} [K]	α [W/(m²*K)]	U [W/(m²*K)]
17.70	18.00	32.10	19.40	0.05	5.86	516.72	323.92
20.10	20.40	32.00	21.50	0.04	4.82	551.06	341.00
22.60	22.80	32.00	23.70	0.05	3.81	549.14	344.12
24.70	24.90	31.90	25.60	0.05	2.97	620.64	374.61
27.00	27.20	31.90	27.70	0.05	2.10	870.43	458.81
29.50	29.60	31.90	29.80	0.05	0.98	974.27	492.69
28.90	29.10	35.00	29.60	0.05	2.44	768.82	432.91
32.50	32.60	34.90	33.00	0.05	1.18	658.19	401.30
31.60	31.80	39.90	32.70	0.04	3.51	493.63	332.59
30.70	31.00	45.00	32.40	0.04	5.83	483.17	326.88
29.60	30.10	50.10	32.00	0.04	8.30	567.59	362.07
27.00	27.90	59.80	31.40	0.04	13.88	695.74	405.85
25.00	26.30	69.90	30.50	0.04	18.40	767.40	425.36
23.50	25.00	80.00	30.00	0.04	22.71	742.75	414.69

Table A3-17: Ethane -water system at 10.0 MPa and 1 L/min water flux.

Water		**Ethane**					
T_{in} [°C]	T_{out} [°C]	T_{in} [°C]	T_{out} [°C]	Q_m [kg/min]	ΔT_{log} [K]	α [W/(m²*K)]	U [W/(m²*K)]
18.20	18.70	32.10	20.20	0.04	15.07	451.95	241.44
20.30	20.70	32.00	21.90	0.04	14.76	444.65	242.25
22.40	22.80	31.90	23.90	0.04	14.19	504.44	262.31
24.80	25.20	32.10	25.90	0.04	13.22	737.12	319.13
27.20	27.50	32.00	27.90	0.04	12.22	928.36	356.46
29.60	29.70	32.00	29.90	0.04	10.21	564.44	289.41
29.00	29.20	35.00	30.00	0.05	13.70	399.99	238.43
32.50	32.60	35.00	33.00	0.04	11.11	360.88	227.12
32.00	32.20	40.00	33.00	0.04	16.19	355.88	224.74
31.20	31.60	45.00	33.10	0.04	19.97	383.54	234.79
30.30	31.00	50.00	33.00	0.04	23.08	472.42	264.41
29.30	30.40	60.10	33.10	0.05	27.62	657.62	312.45
28.10	29.70	70.00	33.00	0.05	31.94	788.56	337.16
26.40	28.60	80.00	32.90	0.05	35.79	884.45	350.16

Table A3-18: Ethane -water system at 10.0 MPa and 2 L/min water flux.

Water		**Ethane**					
T_{in} [°C]	T_{out} [°C]	T_{in} [°C]	T_{out} [°C]	Q_m [kg/min]	ΔT_{log} [K]	α [W/(m²*K)]	U [W/(m²*K)]
18.30	18.60	32.10	19.70	0.04	15.40	481.30	310.47
20.30	20.60	31.90	21.60	0.04	15.02	532.83	334.24
22.40	22.70	31.90	23.60	0.04	14.48	620.44	370.56
25.00	25.20	32.10	25.70	0.05	13.60	669.04	392.27
27.20	27.40	32.00	27.70	0.04	12.60	990.17	490.61
29.50	29.60	32.10	29.80	0.04	10.67	804.31	445.12
29.00	29.20	35.00	29.80	0.05	14.89	672.09	400.63
32.50	32.60	35.00	33.00	0.04	11.71	564.54	364.44
32.00	32.20	40.00	32.70	0.04	17.15	537.89	352.60
31.30	31.60	45.10	32.40	0.04	20.76	514.18	341.50
30.40	30.80	50.00	32.10	0.04	23.21	504.24	336.10
29.50	30.10	60.00	32.00	0.05	27.98	610.68	379.06
27.80	28.70	70.10	31.30	0.05	31.72	702.42	409.63
26.60	27.80	80.00	30.80	0.05	35.60	766.90	428.55

Table A3-19: Ethane -water system at 20.0 MPa and 1 L/min water flux.

Water		Ethane					
T_{in} [°C]	T_{out} [°C]	T_{in} [°C]	T_{out} [°C]	Q_m [kg/min]	ΔT_{log} [K]	α [W/(m²*K)]	U [W/(m²*K)]
19.00	19.40	32.10	20.10	0.03	423.31	423.3125	234.03
21.10	21.50	32.00	22.10	0.03	487.29	487.2877	255.61
23.50	23.80	32.10	24.00	0.04	646.87	646.8673	298.31
25.80	26.00	32.00	26.10	0.04	726.53	726.5324	319.05
27.90	28.00	32.10	28.00	0.04	769.51	769.5074	331.59
29.80	29.90	32.00	30.00	0.04	698.53	698.5279	321.39
29.40	29.60	34.90	29.90	0.04	516.18	516.1801	275.96
32.50	32.60	34.90	32.90	0.04	382.15	382.1535	235.36
32.80	32.90	40.10	33.10	0.03	285.20	285.2025	194.81
32.40	32.60	45.00	33.00	0.03	294.76	294.7627	198.99
32.20	32.50	50.20	33.10	0.03	299.45	299.4528	201.01
31.40	32.00	60.00	32.90	0.03	352.05	352.0545	222.86
31.30	32.20	70.00	33.00	0.03	424.85	424.8532	250.03
31.30	32.40	80.00	33.00	0.03	468.46	468.4607	264.65

Table A3-20: Ethane -water system at 20.0 MPa and 2 L/min water flux.

Water		Ethane					
T_{in} [°C]	T_{out} [°C]	T_{in} [°C]	T_{out} [°C]	Q_m [kg/min]	ΔT_{log} [K]	α [W/(m²*K)]	U [W/(m²*K)]
19.30	19.50	30.90	19.60	0.071	3.05	798.45	419.79
21.70	21.90	30.90	21.80	0.055	1.98	1273.02	531.25
23.60	23.80	30.90	23.70	0.054	1.64	1589.63	587.85
25.70	25.90	31.00	26.00	0.065	1.69	1245.69	540.89
27.70	27.80	31.00	27.90	0.075	1.08	916.79	473.04
27.60	27.70	35.00	27.70	0.077	1.68	859.76	457.15
31.80	31.90	34.90	32.00	0.055	1.03	776.66	441.11
31.90	32.00	40.00	32.00	0.077	1.80	803.08	449.71
31.50	31.80	45.10	32.10	0.080	4.10	779.13	441.52
30.60	31.00	50.00	31.50	0.078	5.93	703.39	414.63
29.90	30.40	60.00	31.10	0.077	8.86	627.00	385.84
29.20	30.00	70.00	30.80	0.076	11.93	728.69	421.04
29.00	30.10	80.10	31.00	0.075	14.91	796.43	442.70
28.60	29.90	90.00	30.90	0.074	17.71	796.87	442.20

7.3.3 Heat transfer coefficients of the azeotrope-water system

Table A3-21: Azeotrope-water system at 6.5 MPa and 1 L/min water flux.

Water		**Azeotrope**					
T_{in} [°C]	T_{out} [°C]	T_{in} [°C]	T_{out} [°C]	Q_m [kg/min]	ΔT_{log} [K]	α [W/(m^2*K)]	U [W/(m^2*K)]
10.40	12.10	31.00	19.90	0.06	13.67	475.66	449.24
15.40	16.70	30.90	22.20	0.06	10.05	475.66	531.48
20.10	20.90	31.00	24.20	0.06	6.66	475.66	639.53
23.30	23.90	30.90	26.00	0.06	4.51	475.66	797.01
26.20	26.70	30.90	27.90	0.06	2.76	1453.23	410.75
25.40	25.90	35.00	27.90	0.06	5.11	475.66	287.82
31.00	31.20	34.90	31.90	0.05	1.98	475.66	265.99
30.10	30.40	39.90	32.00	0.05	4.72	370.68	228.82
28.90	29.40	45.10	32.10	0.05	7.86	359.26	223.39
28.20	28.80	50.00	32.00	0.05	10.12	374.98	228.71
27.30	28.10	59.90	31.90	0.05	14.07	364.76	224.08
26.70	27.80	69.90	32.00	0.05	17.76	372.92	226.67
25.00	26.30	80.00	32.00	0.05	22.92	350.94	216.80
24.10	25.70	90.00	32.00	0.05	26.90	365.67	221.55

Table A3-22: Azeotrope-water system at 6.5 MPa and 2 L/min water flux.

Water		**Azeotrope**					
T_{in} [°C]	T_{out} [°C]	T_{in} [°C]	T_{out} [°C]	Q_m [kg/min]	ΔT_{log} [K]	α [W/(m^2*K)]	U [W/(m^2*K)]
10.50	11.50	31.00	18.40	0.06	12.84	1490.08	518.15
16.00	16.70	31.00	21.70	0.06	9.35	1979.49	595.48
20.80	21.20	31.00	23.80	0.06	5.74	4383.21	748.66
23.50	23.80	30.90	25.50	0.06	4.03	25741.26	899.66
26.70	26.90	30.90	27.60	0.06	2.08	979.13	486.50
25.20	25.60	35.00	27.40	0.06	4.96	720.33	409.98
30.70	30.90	34.90	31.80	0.04	2.25	613.91	381.83
29.80	30.10	39.90	31.60	0.06	4.72	524.53	344.18
28.70	29.10	45.10	31.20	0.05	7.27	466.28	316.96
28.00	28.50	50.10	31.20	0.05	9.64	460.70	313.66
27.20	27.80	59.90	31.00	0.05	13.26	418.55	292.80
26.80	27.60	70.10	31.30	0.05	16.92	419.99	293.21
24.70	25.70	80.00	30.70	0.05	21.93	417.25	289.86
24.10	25.30	90.00	30.50	0.05	25.20	422.61	291.91

Table A3-23: Azeotrope-water system at 7.5 MPa and 1 L/min water flux.

Water		**Azeotrope**					
T_{in} [°C]	T_{out} [°C]	T_{in} [°C]	T_{out} [°C]	Q_m [kg/min]	ΔT_{log} [K]	α [W/(m²*K)]	U [W/(m²*K)]
14.70	15.90	31.00	20.00	0.05	9.36	0.05	322.65
17.50	18.60	31.00	22.00	0.05	7.79	0.05	348.06
20.10	20.90	30.90	24.00	0.05	6.48	0.05	313.52
22.90	23.50	31.00	25.80	0.05	4.84	0.05	315.74
26.00	26.40	30.90	28.00	0.05	3.08	0.05	319.23
24.20	25.00	35.00	28.10	0.05	6.48	0.05	496.78
30.90	31.20	35.00	31.90	0.05	2.10	0.05	542.20
28.90	29.40	40.00	31.90	0.05	6.02	0.05	416.77
27.90	28.60	45.00	31.90	0.05	8.79	0.05	358.04
26.40	27.40	50.10	31.90	0.05	12.13	0.05	339.35
26.60	27.80	60.00	31.90	0.05	14.91	0.05	289.47
25.80	27.20	70.10	32.10	0.05	19.08	0.05	289.55
24.60	26.30	80.00	32.00	0.05	23.36	0.05	277.36
24.80	26.80	90.10	32.00	0.05	25.81	0.05	263.31

Table A3-24: Azeotrope-water system at 7.5 MPa and 2 L/min water flux.

Water		**Azeotrope**					
T_{in} [°C]	T_{out} [°C]	T_{in} [°C]	T_{out} [°C]	Q_m [kg/min]	ΔT_{log} [K]	α [W/(m²*K)]	U [W/(m²*K)]
14.50	15.30	31.00	18.80	0.05	8.80	887.34	430.44
17.30	18.00	30.90	21.00	0.05	7.37	896.37	440.44
20.10	20.60	31.00	23.20	0.05	6.03	733.30	403.20
22.80	23.20	30.90	25.30	0.05	4.62	736.05	409.90
25.90	26.20	30.90	27.40	0.05	2.80	998.48	489.10
23.90	24.40	35.10	27.20	0.05	6.29	1599.07	591.11
30.30	30.50	35.00	31.90	0.05	2.80	2286.37	698.51
29.00	29.40	40.00	31.40	0.05	5.52	1343.18	570.92
28.00	28.50	45.10	31.30	0.05	8.23	937.45	479.78
26.70	27.30	50.00	30.60	0.05	10.67	782.86	433.05
26.40	27.20	60.10	30.90	0.05	14.28	702.91	407.03
25.70	26.60	70.00	30.80	0.05	17.89	597.03	368.08
24.70	25.80	80.10	30.60	0.05	21.81	571.57	356.85
26.00	27.20	90.20	31.70	0.05	23.85	508.17	332.85

Table A3-25: Azeotrope-water system at 10.00 MPa and 1 L/min water flux.

Water		**Azeotrope**					
T_{in} [°C]	T_{out} [°C]	T_{in} [°C]	T_{out} [°C]	Q_m [kg/min]	ΔT_{log} [K]	α [W/(m²*K)]	U [W/(m²*K)]
18.90	19.40	31.00	19.90	0.04	4.32	889.21	329.34
20.80	21.30	31.00	22.00	0.05	4.07	950.50	342.70
23.10	23.50	30.90	24.00	0.05	3.09	994.85	354.70
25.20	25.50	31.00	25.90	0.05	2.33	967.75	356.79
27.60	27.80	31.00	28.00	0.05	1.35	1222.55	393.83
26.70	27.20	34.90	27.90	0.05	3.50	1088.75	376.69
31.50	31.70	35.00	32.00	0.05	1.48	936.89	368.23
30.70	31.20	40.10	32.00	0.05	3.95	902.75	361.33
29.10	30.10	45.00	32.00	0.05	7.33	1141.46	390.53
28.40	29.60	50.10	31.80	0.05	9.52	1235.81	399.19
26.20	28.00	60.10	32.00	0.05	15.37	1065.03	374.23
25.40	27.60	70.00	32.10	0.05	19.35	998.45	364.04
24.30	26.90	80.00	32.00	0.05	23.51	922.15	351.05
23.10	26.00	89.90	31.90	0.05	27.79	861.42	339.27

Table A3-26: Azeotrope-water system at 10.00 MPa and 2 L/min water flux.

Water		**Azeotrope**					
T_{in} [°C]	T_{out} [°C]	T_{in} [°C]	T_{out} [°C]	Q_m [kg/min]	ΔT_{log} [K]	α [W/(m²*K)]	U [W/(m²*K)]
18.80	19.20	31.10	19.60	0.04	4.11	1018.22	472.26
21.40	21.70	30.90	22.00	0.05	3.15	1046.13	486.37
23.10	23.40	30.90	23.70	0.05	2.73	1213.47	525.79
25.30	25.50	31.00	25.70	0.05	1.95	1151.56	521.03
27.70	27.80	31.00	27.90	0.05	1.08	991.80	492.25
26.80	27.10	35.00	27.60	0.05	3.10	967.16	483.94
31.60	31.70	35.00	31.90	0.05	1.25	792.53	445.79
30.50	30.80	40.10	31.50	0.05	3.72	782.04	440.46
29.00	29.50	45.10	31.00	0.05	6.62	804.02	444.39
28.20	28.90	50.10	30.90	0.05	8.98	902.47	471.19
26.80	27.70	60.10	30.40	0.05	13.11	835.36	449.23
25.30	26.40	69.90	30.40	0.05	17.91	697.07	403.22
24.10	25.40	80.00	30.10	0.05	22.01	659.14	388.20
22.80	24.30	90.00	29.90	0.05	26.34	615.45	370.54

Table A3-27: Azeotrope-water system at 20.00 MPa and 1 L/min water flux.

Water		**Azeotrope**					
T_{in} [°C]	T_{out} [°C]	T_{in} [°C]	T_{out} [°C]	Q_m [kg/min]	ΔT_{log} [K]	α [W/(m²*K)]	U [W/(m²*K)]
19.80	20.10	31.10	20.10	0.04	2.97	740.72	308.43
21.80	22.00	30.90	21.90	0.04	1.96	882.10	335.61
23.80	24.00	30.90	23.90	0.04	1.61	1139.02	373.31
25.70	25.90	31.10	25.90	0.04	1.53	908.96	349.64
27.90	28.00	31.10	28.00	0.04	0.87	778.85	333.31
27.60	27.80	35.00	27.90	0.04	2.17	549.47	282.40
31.70	31.80	35.00	31.90	0.04	1.08	469.55	264.87
31.40	31.70	40.00	32.00	0.04	2.93	503.03	274.94
31.40	31.80	45.00	32.00	0.04	4.08	544.04	286.83
31.20	31.70	50.10	32.00	0.05	5.61	581.31	296.63
31.00	31.80	59.90	32.10	0.05	8.33	634.33	309.76
30.80	31.80	70.00	31.90	0.05	10.46	727.14	330.16
30.40	31.90	80.10	32.00	0.05	13.68	858.77	354.52
30.70	32.50	90.10	32.00	0.04	14.85	951.65	370.49

Table A3-28: Azeotrope-water system at 20.00 MPa and 2 L/min water flux.

Water		**Azeotrope**					
T_{in} [°C]	T_{out} [°C]	T_{in} [°C]	T_{out} [°C]	Q_m [kg/min]	ΔT_{log} [K]	α [W/(m²*K)]	U [W/(m²*K)]
19.70	19.90	31.10	19.80	0.04	2.35	974.10	464.96
21.70	21.90	30.90	21.80	0.04	1.98	1122.87	503.17
23.80	24.00	31.00	23.90	0.04	1.62	1533.57	580.86
25.70	25.90	31.00	25.90	0.04	1.51	1447.00	575.66
27.90	28.00	31.20	28.00	0.04	0.89	1107.00	519.68
27.70	27.90	35.00	27.90	0.04	1.93	966.51	486.08
31.70	31.80	35.00	31.90	0.04	1.08	733.80	426.77
31.90	32.10	40.10	32.20	0.04	2.35	692.94	413.04
31.80	32.00	45.10	32.00	0.04	3.08	671.01	404.98
31.30	31.60	50.10	31.70	0.05	4.72	644.86	394.61
31.10	31.50	60.00	31.60	0.05	6.93	597.18	376.01
31.00	31.50	69.90	31.50	0.05	8.73	626.69	387.43
30.70	31.50	80.20	31.60	0.05	11.98	670.54	403.50
30.50	31.50	89.90	31.30	0.04	13.43	750.45	430.93

8. Bibliographic information about the candidate

PERSONAL INFORMATION

Gregor Kravanja

Ulica Moše Pijada 23 c, 2000, Maribor, Slovenija

+386 41/ 908 199

gregor.kravanja@um.si

www.linkedin.com/in/gregor-kravanja-389972133

Sex Male | Date of birth 03/04/1990 | Nationality Slovenian

JOB APPLIED FOR
POSITION
PREFERRED JOB
STUDIES APPLIED FOR
PERSONAL STATEMENT

Doctor of Science

WORK EXPERIENCE

11/2014 – 5/2018

Young Researcher and Assistant

University of Maribor, Faculty of Chemistry and Chemical Engineering, Laboratory of Separation Processes and Production Design

- research and project work, mentoring students, publishing in JCR indexed journals

EDUCATION AND TRAINING

9/2012 - 9/2014

Masters' Degree in Chemical Engineering

University of Maribor, Faculty of Chemistry and Chemical Engineering

9/2012 - 9/2014

Bachelor's Degree in Chemical Engineering

University of Maribor, Faculty of Chemistry and Chemical Engineering

6/2014–8/2014

Practical Training

Marine Biology Station Piran that operates within the framework of National Institute of Biology (NIB)

7/2015–8/2015

The European Summer School in High Pressure Technology

Graz University of Technology, Austria

PERSONAL

SKILLS

Mother tongue(s) Slovenian

Other language(s)

	UNDERSTANDING		SPEAKING		WRITING
	Listening	Reading	Spoken interaction	Spoken production	
English	C1	C1	C1	C1	C1
	Replace with name of language certificate. Enter level if known.				
Germany	B1	B1	B1	B1	B1
	Replace with name of language certificate. Enter level if known.				

Communication skills
- Good communication skills gained through my experience as student representative,
- lectured at international conferences (SEEP, PRES).

Organisational / managerial skills
- Representative in the Senate and Student Council, Faculty of Chemistry and Chemical Technology.

Job-related skills
- Solution orientated, teamwork, ability to manage and delegate to others, building positive working relationships, commercial awareness.

Digital skills

SELF-ASSESSMENT				
Information processing	Communication	Content creation	Safety	Problem solving
Proficient user	Proficient user	Proficient user	Proficient user	Proficient user

Levels: Basic user - Independent user - Proficient user
Digital competences - Self-assessment grid

Replace with name of ICT-certificates

- Good command of Microsoft office suite ((Word, Excel, PowerPoint).

Other skills
- Advance Open Water Diver,
- guitarist.

Driving licence B

ADDITIONAL INFORMATION

Projects
- Part of the research program group P2 – 0046: Separation processes and production design (*Pricipal researcher: Prof. Dr. Željko Knez*).

Honours and awards
- Henkel award for the best Masters' Degree thesis
- The Journal of Supercritical Fluids Editor-in-Chiefs Featured Article, Volume 102, July 2015, and Pages 9-16.

Memberships
- Member of the Commission for Scientific Research Affairs at the University of Maribor,
- Member of the Commission for a Sustainable and Socially Responsible University

9. Scientific bibliography of the candidate

Original scientific article:

1. KRAVANJA, Gregor, ZAJC, Gašper, KNEZ, Željko, ŠKERGET, Mojca, MARČIČ, Simon, KNEZ HRNČIČ, Maša. Heat transfer performance of CO_2, ethane and their azeotropic mixture under supercritical conditions. *Energy*, ISSN 0360-5442. [Print ed.], June 2018, vol. 152, str. 190-201., doi: 10.1016/j.energy.2018.03.146. [COBISS.SI-ID 21310230], [JCR, SNIP]

2. KRAVANJA, Gregor, KNEZ, Željko, KNEZ HRNČIČ, Maša. The effect of argon contamination on interfacial tension, diffusion coefficients and storage capacity in carbon sequestration processes. *International journal of greenhouse gas control*, ISSN 1750-5836, April 2018, vol. 71, str. 142-154, doi: 10.1016/j.ijggc.2018.02.016. [COBISS.SI-ID 21211670], [JCR, SNIP, Scopus do 10. 3. 2018: št. citatov (TC): 0, čistih citatov (CI): 0]

3. KRAVANJA, Gregor, ŠKERGET, Mojca, KNEZ, Željko, KNEZ HRNČIČ, Maša. Diffusion coefficients of water and propylene glycol in supercritical CO2 from pendant drop tensiometry. *The Journal of supercritical fluids*, ISSN 0896-8446. [Print ed.], March 2018, vol. 133, part. 1, str. 1-8, doi: 10.1016/j.supflu.2017.09.022. [COBISS.SI-ID 20803094], [JCR, SNIP, WoS do 23. 3. 2018: št. citatov (TC): 0, čistih citatov (CI): 0, Scopus do 29. 3. 2018: št. citatov (TC): 1, čistih citatov (CI): 0]

4. KRAVANJA, Gregor, KNEZ, Željko, KOTNIK, Petra, LJUBEC, Barbara, KNEZ HRNČIČ, Maša. Formulation of nimodipine, fenofibrate, and o-vanillin with Brij S100 and PEG 4000 using the PGSSTM process. *The Journal of supercritical fluids*, ISSN 0896-8446. [Print ed.], May 2018, vol. 135, str. 245-253, doi: 10.1016/j.supflu.2018.01.021. [COBISS.SI-ID 21211414], [JCR, SNIP, WoS do 6. 4. 2018: št. citatov (TC): 0, čistih citatov (CI): 0, Scopus do 17. 3. 2018: št. citatov (TC): 0, čistih citatov (CI): 0]

5. KNEZ HRNČIČ, Maša, **KRAVANJA, Gregor**, KNEZ, Željko. Minimizing energy requirements for polymer processing by the means of supercritical fluids. *Chemical engineering transactions*, ISSN 2283-9216. [Online ed.], 2017, vol. 61, str. 1657-1662, doi: 10.3303/CET1761274. [COBISS.SI-ID 20879382], [SNIP, Scopus do 21. 10. 2017: št. citatov (TC): 0, čistih citatov (CI): 0]

6. KEGL, Tina, **KRAVANJA, Gregor**, KNEZ, Željko, KNEZ HRNČIČ, Maša. Effect of addition of supercritical CO2 on transfer and thermodynamic properties of biodegradable polymers PEG 600 and Brij52. *The Journal of supercritical fluids*, ISSN 0896-8446. [Print ed.], April 2017, vol. 122, str. 10-17, doi: 10.1016/j.supflu.2016.11.011. [COBISS.SI-ID 20059670], [JCR, SNIP, WoS do 2. 4. 2018: št. citatov (TC): 1, čistih citatov (CI): 0, Scopus do 29. 3. 2018: št. citatov (TC): 2, čistih citatov (CI): 0]

7. KNEZ HRNČIČ, Maša, **KRAVANJA, Gregor**, KNEZ, Željko. Hydrothermal treatment of biomass for energy and chemicals. *Energy*, ISSN 0360-5442. [Print ed.], Dec. 2016, vol. 116, part 2, str. 1312-1322, doi: 10.1016/j.energy.2016.06.148. [COBISS.SI-ID 19682838], [JCR, SNIP, WoS do 2. 4. 2018: št. citatov (TC): 7, čistih citatov (CI): 6, Scopus do 29. 3. 2018: št. citatov (TC): 10, čistih citatov (CI): 9]

8. KRAVANJA, Gregor, KNEZ HRNČIČ, Maša, ŠKERGET, Mojca, KNEZ, Željko. Interfacial tension and gas solubility of molten polymer polyethyleneglycol in contact with supercritical carbon dioxide and argon. *The Journal of supercritical fluids*, ISSN 0896-8446. [Print ed.], Feb. 2016, vol. 108, str. 45-55, doi: 10.1016/j.supflu.2015.10.013. [COBISS.SI-ID 19233814], [JCR, SNIP, WoS do 2. 4. 2018: št. citatov (TC): 5, čistih citatov (CI): 2, Scopus do 29. 3. 2018: št. citatov (TC): 8, čistih citatov (CI): 2]

9. KNEZ HRNČIČ, Maša, **KRAVANJA, Gregor**, ŠKERGET, Mojca, SADIKU, Makfire, KNEZ, Željko. Investigation of interfacial tension of the binary system polyethylene glycol/CO2 by a capillary rise method. *The Journal of supercritical fluids*, ISSN 0896-8446. [Print ed.], Jul. 2015, vol. 102, str. 9-16, doi: 10.1016/j.supflu.2015.03.015. [COBISS.SI-ID 18658582], [JCR, SNIP, WoS do 2. 4. 2018: št. citatov (TC): 5, čistih citatov (CI): 1, Scopus do 12. 11. 2017: št. citatov (TC): 5, čistih citatov (CI): 1] nagrada: The Journal of supercritical fluids Editor-in-chief's featured article, July 2015

Published scientific conference contribution

10. KRAVANJA, Gregor, ZAJC, Gašper, KNEZ, Željko, ŠKERGET, Mojca, KNEZ HRNČIČ, Maša. An experimental study on heat transfer of CO_2 at supercritical conditions. V: KROPE, Jurij (ur.), et al. *Energy efficiency: (conference proceedings)*. Maribor: University of Maribor Press: Faculty of Chemistry and Chemical Engineering. 2017, str. 195-203. http://press.um.si/index.php/ump/catalog/view/241/203/428-1. [COBISS.SI-ID 20899094]

11. KNEZ HRNČIČ, Maša, KRAVANJA, Gregor, KNEZ, Željko. Low energy processing of polymeric materials. V: KROPE, Jurij (ur.), et al. *Materials : (conference proceedings)*. Maribor: University of Maribor Press: Faculty of Chemistry and Chemical Engineering. 2017, str. 13-22, ilustr. [COBISS.SI-ID 20674838]

Published scientific conference contribution (invited lecture)

12. KNEZ, Željko, KNEZ HRNČIČ, Maša, KRAVANJA, Gregor. Thermodyamic and transport data for the systems of polymers and subcritical and supercritical gases. V: *16th European meeting on Supercritical fluids, EMSF 2017, 25-28 April 2017, Lisbon: [book of abstracts]*. [S. l.: s. n. 2017], str. 34. [COBISS.SI-ID 20671766]

13. KNEZ, Željko, CÖR, Darija, KNEZ HRNČIČ, Maša, KRAVANJA, Gregor. Thermodynamic and transport data for the sstems polymer/dense gases. V: *Physics and chemistry of elementary chemical processes : book of abstracts : dedicated to the 100-th anniversary of academician Vladislav Voevodsky,* IX International Voevodsky conference, June 25-30, 2017, Akademgorodok, Novosibirsk, Russia. [S. l.: s. n. 2017], str. 19. [COBISS.SI-ID 20666902]

14. KNEZ, Željko, KNEZ HRNČIČ, Maša, CÖR, Darija, KRAVANJA, Gregor. *Processing of polymer material using sub and supercritical gases: keynote lecture at the 10th International conference on supercritical fluids Supergreen 2017, December 1-3, 2017, Nagoya, Japan*. [COBISS.SI-ID 21021718]

15. KNEZ, Željko, KNEZ HRNČIČ, Maša, MARKOČIČ, Elena, KRAVANJA, Gregor, TRUPEJ, Nina, ŠKERGET, Mojca. *Design of processes using supercritical fluids : keynote*

lecture at ISSF 2015, 11th International symposium on supercritical fluids, October 11-14 2015, Seoul, Korea. 2015. [COBISS.SI-ID 19085846]

Published scientific conference contribution abstract

16. KRAVANJA, Gregor, KNEZ, Željko, ŠKERGET, Mojca, KNEZ HRNČIČ, Maša. Current status and contribution of carbon capture and storage (CSS) processes to sustainable development. V: ARAVOSSIS, Konstantinos (ur.). *Book of abstracts of the 18th European roundtable on sustainable consuption and production - Towards a greener challenge & evolution in the framework of the circular economy, October 1-5, 2017, Skiathos Islands, Greece*. Thessaloniki: Grafima Publ. cop. 2017, str. 220. [COBISS.SI-ID 20880406]

17. LJUBEC, Barbara, KNEZ HRNČIČ, Maša, KRAVANJA, Gregor, CÖR, Darija, KNEZ, Željko. Mikroenkapsulacija farmacevtskih učinkovin s PGSSTM postopkom. V: KAUČIČ, Venčeslav (ur.). *Zbornik referatov in povzetkov*, Slovenski kemijski dnevi 2017, 20.-22. september 2017, Portorož. Ljubljana: Slovensko kemijsko društvo. 2017, str. [1]. [COBISS.SI-ID 20809238]

18. KRAVANJA, Gregor, ZAJC, Gašper, KNEZ HRNČIČ, Maša, ŠKERGET, Mojca, KNEZ, Željko. Prenos toplote pri superkritičnih pogojih. V: KAUČIČ, Venčeslav (ur.). *Zbornik referatov in povzetkov*, Slovenski kemijski dnevi 2017, 20.-22. september 2017, Portorož. Ljubljana: Slovensko kemijsko društvo. 2017, str. [1]. [COBISS.SI-ID 20804886]

19. KRAVANJA, Gregor, KNEZ HRNČIČ, Maša, ŠKERGET, Mojca, KNEZ, Željko. Polymer processing with supercritical fluids : from fundamental data to special polymeric structures. V: MLAKAR, Damir (ur.). *1st AARC PhD Students Conference on Environment and Sustainable Energy, November 24th - 25th 2016, Maribor, Slovenia*. Maribor: University. 2016, str. 73-74. [COBISS.SI-ID 20061974]

20. KNEZ, Željko, KRAVANJA, Gregor, CÖR, Darija, KNEZ HRNČIČ, Maša, TRUPEJ, Nina, ŠKERGET, Mojca. Supercritical fluids for process intensification. V: *Book of abstracts*, 15th European meeting on Supercritical fluids, EMSF 2016, 8-11 May 2016, Essen, Germany. [S. l.: s. n. 2016], str. 31. [COBISS.SI-ID 19578902]

21. KRAVANJA, Gregor, FAKIN, Gregor, KEGL, Tina, KNEZ HRNČIČ, Maša, KNEZ, Željko. Gostote dvofaznih sistemov v okolici kritične točke. V: KAUČIČ, Venčeslav (ur.), BEŠTER-ROGAČ, Marija (ur.), GANTAR, Marjana (ur.). *Zbornik referatov in povzetkov*, 22. Slovenski kemijski dnevi, Portorož, 28.-30. september 2016 = 22. Slovenian Chemical Days Portorož, September 28-30, 2016. Ljubljana: Slovensko kemijsko društvo. 2016, str. [1], ilustr. [COBISS.SI-ID 19921174]

22. KRAVANJA, Gregor, KNEZ HRNČIČ, Maša, ŠKERGET, Mojca, KNEZ, Željko. Pomen medfazne napetosti in difuzijskih koeficientov pri geološkem shranjevanju toplogrednih plinov. V: KAUČIČ, Venčeslav (ur.), BEŠTER-ROGAČ, Marija (ur.), GANTAR, Marjana (ur.). *Zbornik referatov in povzetkov*, 22. Slovenski kemijski dnevi, Portorož, 28.-30. september 2016 = 22. Slovenian Chemical Days Portorož, September 28-30, 2016. Ljubljana: Slovensko kemijsko društvo. 2016, str. [1], ilustr. [COBISS.SI-ID 19914262]

MONOGRAPHS AND OTHER COMPLETED WORK

Master's thesis

23. KRAVANJA, Gregor. *Določitev površinske napetosti z metodo kapilarnega dviga dvofaznih sistemov : magistrsko delo študijskega programa II. stopnje*. Maribor: [G. Kravanja], 2014. XI, 77 str., ilustr. http://dkum.uni-mb.si/IzpisGradiva.php?id=45415. [COBISS.SI-ID 18248214]

Undergraduate thesis

24. KRAVANJA, Gregor. *Toplotne izgube zaradi odlaganja vodnega kamna na grelcih gospodinjskih naprav : diplomsko delo univerzitetnega študijskega programa*. Maribor: [G. Kravanja], 2012. VIII, 51 str., ilustr. http://dkum.uni-mb.si/Dokument.php?id=50899. [COBISS.SI-ID 16718870]

SECONDARY AUTHORITY

25. FILIPIČ, Uroš. *Formuliranje farmacevtskih učinkovin s PGSS procesom : diplomsko delo visokošolskega strokovnega študijskega programa I. stopnje*. Maribor: [U. Filipič], 2017. X, 50 str., ilustr. https://dk.um.si/IzpisGradiva.php?id=67667. [COBISS.SI-ID 21040150]

26. ŠUŠEK, Lovro. *Preučevanje skladiščenja in shranjevanja toplogrednega CO2 z uporabo visokotlačnih tehnologij : kemija, kemijska tehnologija : raziskovalna naloga*. Maribor: II. gimnazija,2016.33f.,ilustr.http://zpmmb.si/wpcontent/uploads/2016/06/SŠ_Kemija_Preučevanje_skladiščenja_in_shranjevanja.pdf. [COBISS.SI-ID 93828865]

UNIVERZA V MARIBORU

FAKULTETA ZA KEMIJO IN KEMIJSKO TEHNOLOGIJO

Izjava doktorskega kandidata

Podpisani-a **Gregor Kravanja**, vpisna številka **K3000724**

izjavljam,

da je doktorska disertacija z naslovom **Načrtovanje visokotlačnih procesov za predelavo polimerov in izboljšave prenosa toplote**

- rezultat lastnega raziskovalnega dela,
- da predložena disertacija v celoti ali v delih ni bila predložena za pridobitev kakršnekoli izobrazbe po študijskih programih drugih fakultet ali univerz,
- da so rezultati korektno navedeni in
- da nisem kršil-a avtorskih pravic in intelektualne lastnine drugih.

Podpis doktorskega kandidata